UCLA
School
of
Engineering
and
Applied
Science

ONR Final Report:
Grant N00014-93-1383

*STUDIES IN THE CONTROL OF EMISSIONS
IN SMALL-SCALE INCINERATION SYSTEMS*

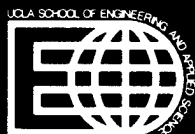*Ann R. Karagozian, Frank E. Marble, and Owen I. Smith*

UCLA, ENG-97-174

July 1997

DTIC QUALITY INSPECTED 4

19970723 094

REPORT DOCUMENTATION PAGE

Public reporting burden for this collection of information is estimated to average 1 hour per response, including the time for reviewing instructions, searching existing data sources, gathering and maintaining the data needed, and completing and reviewing the collection of information. Send comments regarding this burden estimate or any other aspect of this collection of information, including suggestions for reducing this burden, to Washington Headquarters Services, Directorate for Information Operations and Reports, 1215 Jefferson Davis Highway, Suite 1204, Arlington, VA 22202-4302, and to the Office of Management and Budget, Paperwork Reduction Project (0704-0188), Washington, DC 20503.

1. AGENCY USE ONLY (Leave Blank)	2. REPORT DATE July 1997	3. REPORT TYPE AND DATES COVERED Final Technical, 9/30/93 - 3/31/97

4. TITLE AND SUBTITLE

STUDIES IN THE CONTROL OF EMISSIONS IN SMALL-SCALE INCINERATION SYSTEMS

5. FUNDING NUMBERS

G: N00014-93-1-1383

6. AUTHORS

ANN R. KARAGOZIAN

7. PERFORMING ORGANIZATION NAME(S) AND ADDRESS(ES)

UNIVERSITY OF CALIFORNIA, LOS ANGELES
MECHANICAL AND AEROSPACE ENGINEERING DEPARTMENT
420 WESTWOOD PLAZA, BOX 159710
LOS ANGELES, CA 90095-1597

8. PERFORMING ORGANIZATION REPORT NUMBER

UCLA, ENG-97-174

9. SPONSORING / MONITORING AGENCY NAME(S) AND ADDRESS(ES)

OFFICE OF NAVAL RESEARCH
BALLSTON CENTER TOER ONE
800 NORTH QUINCY STREET
ARLINGTON, VA 22217-5660

10. SPONSORING / MONITORING AGENCY REPORT NUMBER

11. SUPPLEMENTARY NOTES

12a. DISTRIBUTION / AVAILABILITY STATEMENT

APPROVED FOR PUBLIC RELEASE; DISTRIBUTION UNLIMITED.

12b. DISTRIBUTION CODE

13. ABSTRACT (Maximum 200 words)

The two research projects undertaken at UCLA under this grant have focused on the analysis and control of mixing and reaction processes during the destruction of hazardous waste surrogates as well as pyrolysis gas surrogates from a primary treatment system such as plasma arc pyrolysis. Both projects have relevance to the thermal treatment and destruction of shipboard wastes generated on Navy vessels, and both projects have demonstrated extremely high degrees of efficiency and toxic emissions reduction. The first project, the resonant incinerator/afterburner or "trapped vortex" combustor, produced waste surrogate destruction efficiencies (DREs) which exceeded U.S. EPA standards by four orders of magnitude under appropriate conditions of external acoustical forcing. Detailed laser diagnostics and numerical simulation of the device enabled insight into the physical processes behind such excellent performance. The second project, the lobed injector/burner, is a concept which provides a means of rapid initial mixing of fuel/waste/off-gas and air in a thermal destruction device via passive flow control. Experiments as well as numerical modeling demonstrated a significant degree of mixing enhancement in lobed injector flowfields, in addition to the potential for ignition delay and the associated reduction in toxic emissions.

14. SUBJECT TERMS

COMBUSTION, MIXING, INCINERATION, AFTERBURNING

15. NUMBER OF PAGES

193 (11 w/out appendices)

16. PRICE CODE

17. SECURITY CLASSIFICATION OF REPORT UNCLASSIFIED	18. SECURITY CLASSIFICATION OF THIS PAGE UNCLASSIFIED	19. SECURITY CLASSIFICATION OF ABSTRACT UNCLASSIFIED	20. LIMITATION OF ABSTRACT UNLIMITED

NSN 7540-01-280-5500

Standard Form 298 (Rev. 2-89)
Prescribed by ANSI Std. Z39-1
298-102

ONR Final Report:

Grant N00014-93-1183

STUDIES IN THE CONTROL OF EMISSIONS IN SMALL-SCALE INCINERATION SYSTEMS

Ann R. Karagozian, Frank E. Marble, and Owen I. Smith

Department of Mechanical and Aerospace Engineering
University of California, Los Angeles

Contents

STUDIES IN THE CONTROL OF EMISSIONS IN SMALL-SCALE INCINERATION SYSTEMS

Ann R. Karagozian, Frank E. Marble, and Owen I. Smith

Department of Mechanical and Aerospace Engineering

University of California, Los Angeles

June 30, 1997

The two research projects undertaken at UCLA under this grant have focused on the analysis and control of mixing and reaction processes during the destruction of hazardous waste surrogates as well as pyrolysis gas surrogates from a primary treatment system such as plasma arc pyrolysis. Both projects have relevance to the thermal treatment and destruction of shipboard wastes generated on Navy vessels, and both projects have demonstrated extremely high degrees of efficiency and toxic emissions reduction.

1   The Resonant Incinerator/Afterburner

The first project, the **resonant incinerator/afterburner or "trapped vortex" combustor**, is a concept designed to achieve higher volumetric heat release rates, improved mixing and surrogate destruction, and real time **active or passive** control in a compact device under strong acoustical excitation.

The UCLA resonant incinerator/afterburner is based on the dump combustor concept, which is typically used in aerospace applications (e.g., in a ramjet engine) to maintain high rates of heat release in a relatively compact, lightweight combustion chamber. In the present application, fluid waste/pyrolysis gas surrogates are injected into the recirculation zones of the device's combustion cavity, where they are trapped for relatively long periods of time under high temperature and/or high radical concentration conditions, and thus can be destroyed to a high degree. A schematic of the dump combustor device used in the present study, with a blow-up view of the recirculation ·
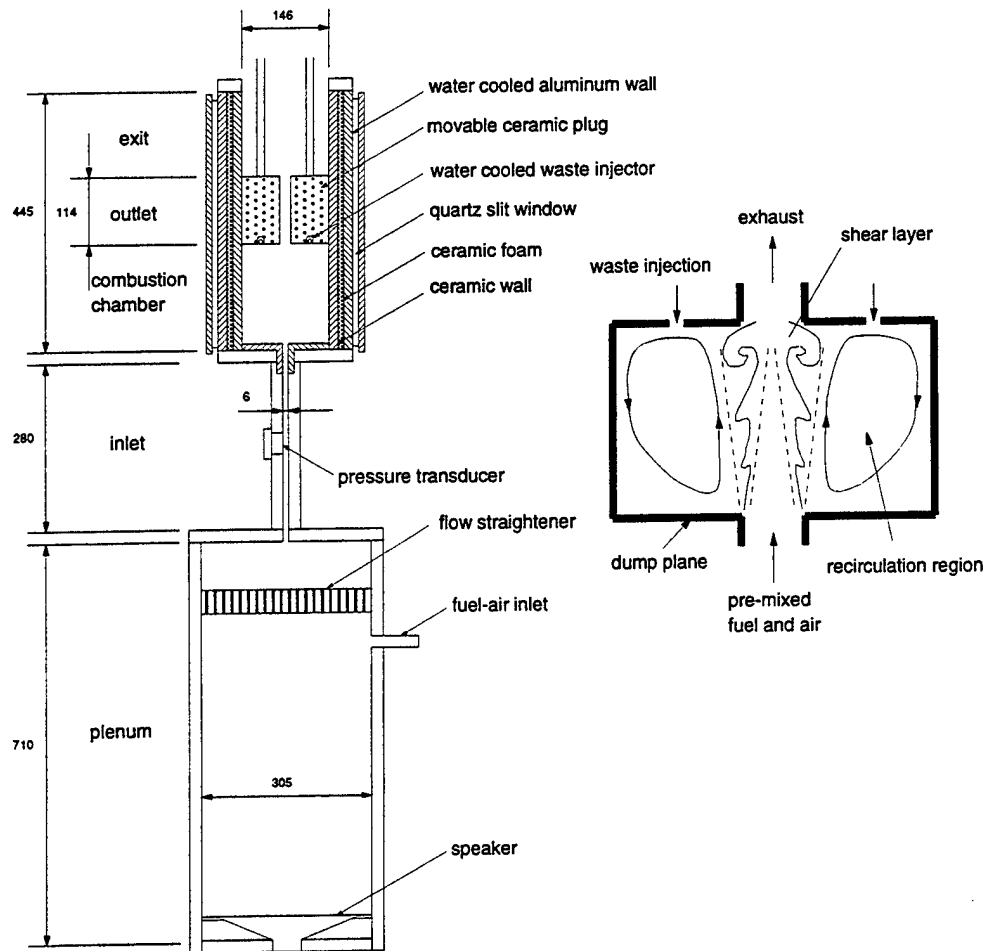zones, is shown in Figure 1.

Figure 1. Schematic of the dump combustor, including features of the combustion chamber cavity. Dimensions are given in units of mm.

The integrity of the recirculation cells, and thus the destruction and removal efficiency of the incinerator/afterburner, are strongly correlated with natural or externally forced acoustic resonances excited in the device. Both types of excitation were studied experimentally in the present device; computational studies focused on natural (unforced) operation. Major accomplishments of the dump combustor research are outlined below, with specific details provided in the papers included in the Appendix to this report.

1.1 Experimental Results: Natural (Unforced) Operation

Upon the recommendations of our grant monitor, Dr. Klaus Schadow, the initial focus of the experimental research here was on the **natural** operation of the dump combustor (acoustically

3

resonant as well as quiet). Both gaseous and liquid waste surrogates were tested in this device. Sulfur hexafluoride (in the gaseous phase) as well as acetonitrile (in the liquid phase) were used in these experiments as surrogates, and the relationships among waste destruction, acoustic characteristics, equivalence ratio, flow rates, and geometry were determined. Destruction and removal efficiencies (DREs) of 99.9999% and above were measured for optimal (resonant as well as quiet) acoustic conditions; this compares with DREs of 99.99% required by the EPA for hazardous waste incinerators, **an improvement of four orders of magnitude above conventional thermal destruction devices.**

Details of these studies are provided in two journal papers, [1] and [2], and in the Ph.D. thesis of J. Willis[3]. Specific destruction rate results, for example, are provided in Figures 3 and 5 in [1] and in Figures 2ab in [2], which are included in the Appendix.

1.2 Experimental Results: Externally Forced Operation

Later experimental studies focused on the ability of the dump combustor to destroy surrogates under **externally forced** acoustic excitation by placing a loudspeaker in the plenum section of the device (see Figure 1). Both hazardous waste and pyrolysis gas surrogates were examined, the latter study being conducted at the request of Dr. Schadow in light of the potential for this device as an afterburner for a plasma arc pyrolysis system. Destruction of waste surrogates SF_6 and methyl chloride (CH_3Cl) and a pyrolysis gas surrogate (a mixture of ethylene (C_2H_4), benzene (C_6H_6), and nitrogen (N_2)) were examined, with results described in two journal papers, [2] and [4], and in the M.S. thesis of G. Pont[5].

By applying acoustic forcing at specific high frequency natural modes of the device, increases in DREs of two to four orders of magnitude were obtained, again exceeding EPA requirements by several orders of magnitude. These results are shown in Figures 3 and 4 in [2] and in Figures 2 and 3ab in [4]. Simultaneously, NO emissions as well as unburned hydrocarbons are seen to diminish by up to 60% and by several orders of magnitude, respectively; these are shown in Figures 5ab and 6ab in [4].

Future studies include using the dump combustor input/output data (pressures, DREs, chemiluminescence images) in the development of active control algorithms for dump combustor flowfields. This work is being conducted in collaboration with Professor Richard Murray of Caltech.

1.3 Experimental Results: Reactive Flow Diagnostics

Fundamental studies of the underlying mechanisms of this remarkable operation were conducted by performing detailed flow diagnostics in the dump combustor.

Chemiluminescence imaging of electronically excited OH^* was performed in the combustor under naturally excited as well as external forcing conditions. These studies indicated that, with acoustical forcing at natural frequencies, the flame structure broadens and is slightly lifted, suggesting increases in recirculation zone temperatures with acoustic forcing. These results, shown, for example, in Figures 5 and 6 in [2], are consistent with dramatically increased DREs of the surrogate SF_6.

Thermocouple as well as NO planar laser-induced fluorescence (PLIF) imaging (from which temperature fields are estimated) indicated enhancement of energy transport to the recirculation zones during acoustic excitation at natural modes, again consistent with DRE measurements. Thermocouple results are shown, for example, in Figure 7 in [4], while the NO PLIF results are included in the Ph.D. thesis of C. Cadou[6].

Particle image velocimetry (PIV) in the device was used to quantify the two-dimensional velocity field in the dump combustor under cold flow conditions. These results indicated that external forcing at desirable frequencies broadens the jet/core flow substantially and strongly enhances the transport of momentum between the recirculation regions and the core, quantitatively represented by an entrainment factor. These results are documented in Y. Kang's Ph.D. thesis[7]. The results are currently being written up, together with the NO PLIF results, for journal submission ([8]).

1.4   Computational Results

In terms of computational studies, we have completed several studies of relevance to the dump combustor configuration shown in Figure 1. 2D, steady state numerical simulation of the dump combustor was initially performed, using methane as the waste surrogate. The SIMPLER algorithm is used here, with a finite-rate reduced methane-air mechanism for seven species. An examination of the effects of oxygen enrichment was also conducted, with good correspondence to experimental observations. Results from this study are described in [9].

Further simulations, also using SIMPLER, were conducted for the case in which a liquid surrogate jet is injected into a chamber such as the dump combustor cavity. These results, which have reasonable correspondence with turbulent spray characteristics seen in experiments, are described in the M.S. thesis of M. Mitchell[10].

Finally, 2D transient simulations of the behavior of reacting flows in a dump combustor cavity (such as in Figure 1) were performed by collaborators in the Department of Mathematics at UCLA. This study, while not explicitly funded by the present ONR grant, involved a significant amount of input from our group and resulted in a useful simulation of the evolution of the shear layers and recirculation zones in the dump combustor with complex chemistry. The results of this transient simulation were published in the Ph.D. thesis of R. Fedkiw[11] and in a journal paper ([12]).

2   The Lobed Injector/Burner

The second project, the **lobed injector/burner**, is a concept which provides a means of rapid initial mixing of fuel/waste/off-gas and air in a thermal destruction device via **passive flow control**.

The lobed injector consists of two sinusoidally loaded plates, as shown in Figure 2, between which fuel and waste are injected into coflowing air and strongly mixed due to the formation of streamwise vortical structures.
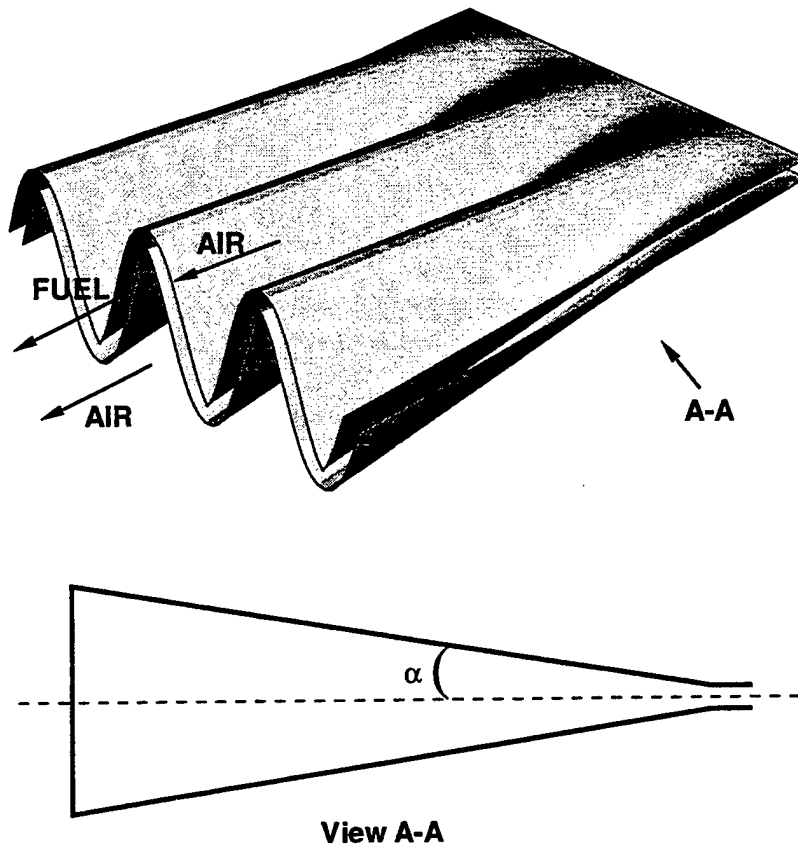
Figure 2. Schematic of the general lobed injector geometry.

Very rapid initial mixing of reactants occurs through streamwise vorticity generation, producing high strain rates which can enhance mixing yet delay ignition. Further downstream of the rapid mixing region, the flowfield produces a reduced effective strain rate, thus allowing ignition of a turbulent flame to occur in a premixed mode, allowing for a more complete combustion/incineration process and where it is possible for combustion to take place under very lean (or very rich) conditions, thus potentially reducing toxic emissions from the burner.

Major accomplishments of the lobed injector research are outlined below, with specific details provided in the papers included in the Appendix to this report.

2.1 Experimental Results: Lobed Injector Mixing Studies

Non-reactive mixing experiments were conducted at UCLA in order to quantify the benefits of the lobed injector configuration for molecular mixing enhancement. All mixing experiments were

completed using CO_2 as a fuel/waste surrogate (injected between the lobed plates in Figure 2), with PLIF imaging of acetone seeded in the CO_2. Two alternative lobed injector configurations were examined, in addition to a straight injector as a baseline geometry.

Results for the lobed injector mixing studies were published recently in [13] and are included in the M.S. theses of A. Majamaki[14] and I. Lam[15]. Acetone PLIF data (e.g., see Figures 4-9 in [13]) were used to quantify mixing by the injectors and scalar dissipation rate fields, the latter being related to the local strain rate in the flowfield. Mixing by the lobed injectors was quantified (using the "unmixedness" parameter suggested by Dimotakis and Miller) under a variety of flow conditions, in some cases improving mixing by 60% over the straight (non-lobed) injector mixing; examples are shown in Figures 10a-d in [13]. Scalar dissipation rates, especially for a rounded square wave lobed injector, were also found to be large near injection and to decay downstream, as would be expected (see Figures 11a-d in [13]). Strain rates near injection were estimated from these mixing experiments to exceed 500 sec^{-1}, sufficiently high, according to asymptotic analysis, to delay ignition and promote mixing.

Further mixing studies for the lobed injector, including high speed flight tests, are being continued under NASA sponsorship.

2.2 Experimental Results: Lobed Injector Combustion Studies

Experiments which test the ignition and burning characteristics of the lobed injector have been conducted, with propane used as the fuel/waste surrogate. Differences between flame structure for lobed and non-lobed (straight) fuel injectors are remarkable. For identical flow conditions, the lobed injector flames effectively are highly turbulent, relatively short (less than 0.5 m in length), and bright blue in color, indicating the presence of a lean premixed flame, while the flames associated with the straight injector are very long (greater than 1.5 m in length), laminar strips, and blue and yellow in color, exhibiting significant sooting characteristics. Even the visible flame characteristics indicate a substantial degree of mixing and entrainment of air into the lobed fuel jet, creating locally lean premixed or partially premixed flame structures.

Preliminary measurements demonstrate that NO emissions from the lobed injector/burner can be reduced substantially, especially with air and injectant velocity mismatches which further assist mixing through spanwise vorticity generation. Sample results are shown in Figures 4-6 of a recent conference paper, [16]. Further testing of the lobed injector is continuing under NASA sponsorship, and will be a part of the Ph.D. thesis of M. Mitchell[17].

2.3 Computational Studies

Computational studies relevant to the lobed injector were of two types: the first examining the ignition and burning properties of a strained fuel strip, a component of the lobed injector flowfield, and the second type of study examining the evolution of the full lobed injector flowfield, with and without reaction.

Computational studies of the ignition of a strained fuel strip were completed using single step activation energy asymptotics and numerical solution of governing equations; these were

published in the M.S. thesis of T. Gerk[18] and in the recent *Twenty-Sixth Symposium (International) on Combustion* Volume[19]. New modes of ignition, involving substantial thermal feedback between species interfaces, were identified in this study; these are shown, for example, in Figure 2 of [19]. Simulation of this same flowfield was recently completed using a full kinetic mechanism for the propane-air reaction. The different modes of ignition which were identified in the asymptotic analysis are also seen using the full simulation, as seen in Figures 5-8 in a paper recently submitted for publication, [20]. The full simulation also enables computation of the processes of stable combustion and extinction as well as prediction of NO_x formation; this is shown in Figures 11-12 in [20]. This full kinetics simulation will be a part of the Ph.D. thesis of T. Selerland[21]. These studies provide substantial evidence that ignition delay may be enhanced for the lobed injector flowfield, that is, occurring at lower strain rates than for conventional injectors, resulting in lowered NO_x emissions.

Simulations of the evolution of the flowfield created by the lobed injector were conducted in collaboration with Dr. J. Strickland of Sandia National Laboratories, Albuquerque. Through mutual research interests, Dr. Strickland developed a numerical scheme to simulate the mixing processes for the sinusoidal lobed injector flowfield using 2D, transient vortex elements. This simulation has provided remarkable predictions of the evolution of vortical structures associated with the lobed fuel injector. Modifications to this scheme were made by T. Selerland at UCLA in order to extract streamtube evolution as well as flow simulation for the rounded square wave lobed geometry. These results compare very well with mixing evolution quantified in [13], and the modeling study of mixing will be written up soon for publication ([22]). This code is also being used for the design of future lobed injectors.

Modifications to the vortex element code are also underway which include a single step reaction to simulate the combustion process. Additional features such as heat release, baroclinic vorticity generation, species diffusion, and volume expansion are being included and will be part of the Ph.D. thesis of T. Selerland[21] before being written up and submitted for publication ([23]). This future work is being supported through a separate grant from NASA.

3 References

References

[1] Willis, J. W., Cadou, C., Mitchell, M., Karagozian, A. R., and Smith, O. I., "Destruction of Liquid and Gaseous Waste Surrogates in an Acoustically Excited Dump Combustor", *Combustion and Flame* 99:280-287 (1994).

[2] Pont, G., Willis, J. W., Karagozian, A. R., and Smith, O. I., "Effects of External Acoustic Excitation on Enhanced Transport in a Resonant Incinerator", *26th Symposium (Intl.) on Combustion* 2463-2470 (1996).

[3] Willis, J. W., "Acoustic Behavior and Waste Surrogate Destruction in a Resonant Combustor", Ph.D. Thesis, University of California, Los Angeles, 1994.

[4] G. Pont, C. P. Cadou, A. R. Karagozian, and O. I. Smith, "Emissions Reduction and Pyrolysis Gas Destruction in an Acoustically Driven Dump Combustor", to appear in *Combustion and Flame*.

[5] Pont, G., "Effects of External Acoustic Excitation on Waste Surrogate Destruction in a Resonant Combustor", M.S. Thesis, University of California, Los Angeles, 1996.

[6] Cadou, C. P., "Two-Dimensional, Time Resolved Temperature Measurements in a Resonant Incinerator using Planar Laser-Induced Fluorescence", Ph.D. thesis, University of California, Los Angeles (1996).

[7] Kang, Yungmo, "Dump Combustor Flowfield Investigation using Particle Image Velocimetry", Ph.D. thesis, University of California, Los Angeles (1997).

[8] Cadou, C., Kang, Y., Karagozian, A. R., and Smith, O. I., "Enhancement of Transport in Acoustically Excited, Reactive Cavity Flows", paper in preparation.

[9] Hepler, W. and Smith, O., "Numerical Simulation of Steady-State Dump Combustor Performance", *Combustion Science and Technology* 107:31 (1995).

[10] Mitchell, M., "A Numerical Model for Turbulent Jets and Sprays", M.S. Thesis, University of California, Los Angeles, 1996.

[11] Fedkiw, R., "A Survey of Chemically Reacting, Compressible Flows", Ph.D. thesis, Department of Mathematics, UCLA, 1996.

[12] Fedkiw, R. P., Merriman, B., and Osher, S., "High accuracy numerical methods for thermally perfect gas flows with chemistry", *J. Computational Physics*, 132 (2), pp. 175-190 (1997).

[13] Smith, L. L., Majamaki, A. J., Lam, I. T., Delabroy, O., Karagozian, A. R., Marble, F. E., and Smith, O. I., "Mixing enhancement in a lobed injector", *The Physics of Fluids* 9, pp. 667-678 (1997).

[14] Majamaki, A. J., "A Mixing Enhancement Study in a Lobed Fuel Injector", M.S. Thesis, University of California, Los Angeles (1996).

[15] Lam, I., "A Computational Procedure for the Interrogation of Mixing and Reacting Layers", M.S. Thesis, University of California, Los Angeles (1996).

[16] Mitchell, M. G., Smith, L. L., Karagozian, A. R., and Smith, O. I., "NO_x emissions from a lobed fuel injector/burner", Paper 96F-075, Western States Section/The Combustion Institute Fall Meeting, October, 1996.

[17] Mitchell, M., "An Experimental Investigation of Combustion in a Lobed Injector/Burner", Ph.D. Thesis, University of California, Los Angeles (1998, expected).

[18] Gerk, T. J., "Mixing, Ignition, and Burning Processes in Strained Fuel Layers", M.S. Thesis, University of California, Los Angeles (1996).

[19] Gerk, T. J. and Karagozian, A. R., "Ignition delay associated with a strained fuel strip", *Twenty-Sixth Symposium (International) on Combustion*, The Combustion Institute, Pittsburgh, PA, pp. 1095-1102 (1996).

[20] T. Selerland and A. R. Karagozian, "Ignition, Burning, and Extinction of a Strained Fuel Strip with Complex Kinetics", submitted to *Combustion Science and Technology*, June, 1997.

[21] Selerland, T., "Numerical simulation of strained flames associated with a lobed fuel injector", Ph.D. Thesis, University of California, Los Angeles (1997, expected).

[22] Strickland, J., Selerland, T., Mitchell, M., and Karagozian, A. R., "Numerical Simulations of Mixing in a Lobed Injector Flowfield", to be submitted for publication.

[23] Selerland, T. and Karagozian, A. R., "Numerical Simulations of Combustion in a Lobed Injector Flowfield", to be submitted for publication.

10

4 Appendix

The papers which follow are numbered according to the scheme used in the References section of this document.

REFERENCE [1]

Destruction of Liquid and Gaseous Waste Surrogates in an Acoustically Excited Dump Combustor

J. W. WILLIS, C. CADOU, M. MITCHELL, and A. R. KARAGOZIAN*

Department of Mechanical, Aerospace and Nuclear Engineering

O. I. SMITH

Department of Chemical Engineering, University of California, Los Angeles, CA 90024-1597

Destruction of gaseous and liquid waste surrogates is studied in a two-dimensional dump combustor configuration. Two different waste surrogates are examined: sulfur hexafluoride, which is injected in the gaseous phase and pyrolyzed at high temperatures, and acetonitrile, which is injected in the liquid phase and can be burned in the presence of high concentrations of oxidizing species. Waste surrogates are injected through movable ceramic plugs into the recirculation zones within the dump combustor cavity. The movable plugs allow the combustor cavity length to be altered, in turn exciting or damping various acoustic modes of the device. Strong coupling among the fluid mechanics, acoustics, and combustion/incineration processes are observed in this device; these processes are representative of dump combustors in general. Among the important observations in this study is that waste destruction is strongly affected by the flame and recirculation zone stability. When the flame is perturbed by large vortical structures corresponding to low-frequency "chugging" oscillations, or when it is chaotically destabilized (while acoustically quiet), the recirculation zones into which waste is injected can be destabilized, and DREs for the surrogate are reduced. When the flame is stabilized under conditions which are acoustically quiet, or when the flame is only slightly wrinkled or disturbed, as under high-frequency mode conditions, the recirculation zones are stable and waste is usually destroyed well. Waste destruction itself, however, is also observed to affect recirculation zone and flame stability in addition to affecting the device's acoustic signature.

INTRODUCTION

Increasing restrictions on hazardous waste streams and their destruction in recent years [1] has led to a strengthening of interest in the development of highly efficient, controllable incinerators. In particular, as waste minimization practices such as separation and recycle become more widely used, waste streams are expected to shrink in volume and become more highly distributed, increasing the demand for smaller-scale incinerators that can be transported to the site of waste generation and which are potentially more acceptable to the public.

Over the past few years our research has focused on the development and investigation of a small-scale, two-dimensional dump combustor (or "resonant incinerator") capable of destroying hazardous waste surrogates to a high

degree [2–6]. The acoustic character of the incinerator is found to be strongly dependent on operating conditions (combustor cavity size, gas speeds, equivalence ratios, etc.) and is correlated with combustion instabilities evident from images of flame deformations [2, 4]. The degree of gaseous waste surrogate (SF_6) destruction in the device is also correlated with its acoustic character [3, 5], thus suggesting the potential for use of the acoustic signature as a real-time monitor of destruction efficiency. Acoustically resonant conditions appear to materially increase the rate of heat-release, resulting in very high volumetric heat release rates, i.e., high power in a very compact, lightweight device. Other research groups have also been exploring the potential of pulse combustion systems in designing more efficient incinerators [7, 8].

The goals of the present experimental study are fourfold: (1) to examine the destruction of a liquid waste surrogate (acetonitrile) in the resonant incinerator and to compare its performance with that for gaseous waste destruction, (2) to examine the effects of the fluid mechan-

---

ics and acoustics of the device on waste destruction in general, (3) to examine the effects of waste injection and destruction on the fluid mechanics and acoustics of the device, and (4) to attempt to understand the strong coupling among fluid mechanics, acoustics, and combustion in an acoustically excited combustor. Goals 1–3 clearly have a direct impact on the use of the device as a practical hazardous waste incinerator, and also have implications for current generation incinerators.

Goal 4 is one which has been pursued by a number of research groups examining dump combustors that are used, for example, in ramjet engines [9–11]. These researchers have found that acoustical excitation in a dump combustor is strongly coupled to the vortices shed in the combustor that are coincident with premixed flame structures. Zukoski and coworkers [10, 12] found that after a vortical structure impinges on the combustor wall, the intense heat pulse produces a pressure wave which triggers the shedding of another vortex. It is this coupling between the acoustics and combustion processes that is responsible for sustaining the combustion instability, according to Rayleigh's criterion [13]. According to Rayleigh's criterion, when the phase difference between the periodic heat addition and the pressure oscillations lies between plus and minus one quarter of a period, energy is supplied to specific acoustic modes of the device, resulting in acoustic resonances. The coupling between vortex shedding and acoustic oscillations in a combustor has been characterized by Yu et al. [11] as a mixed acoustic-convective mode. In the present study, waste injection has the potential for altering the convective processes in the combustor in addition to changing local sound speeds and, in turn, the acoustic character. Hence, the present study can shed new light on this complex fluid mechanics-acoustics-combustion coupling in a dump combustor environment.

EXPERIMENTAL APPARATUS AND PROCEDURE

The dump combustor used in the present experiments is shown schematically in Fig. 1, with an expanded view of flow/reaction processes in the combustion cavity also shown. The combustor's basic features have been described previously, and will only be summarized here. The reader is referred to Refs. 4 and 5 for additional details.

Propane and air at room temperature are introduced into the two-dimensional plenum section of the combustor after first passing through calibrated rotameters. The gases are accelerated through an inlet section, then enter the combustion cavity at a sudden expansion or "dump plane," where premixed flames may be stabilized due to the formation of high temperature recirculation regions at the dump plane [14]. The spanwise depth of the inlet, combustion cavity, outlet and exit sections (30.5 cm) is usually sufficient to produce a visually two-dimensional flame over the entire span, although under certain experimental conditions the flow in the cavity becomes turbulent and the flame/flow structures become three-dimensional. The inlet in the present configuration has been narrowed to 0.69 cm, compared with 2.0 cm in the device described in Ref. 5. This narrowing of the inlet allows high frequency acoustic modes to be generated with greater ease. Quartz windows bound each end of the system in the spanwise direction, allowing appropriate optical access; additional quartz window slits are installed in the side walls to allow the introduction of a sheet of laser light for optical diagnostics.

The set of movable ceramic plugs which define the outlet section is a novel feature of this combustor. It is through the movable plugs that waste injection occurs, as indicated in the figure. Injection into the recirculation zones allows wastes to be trapped for relatively long residence times under high temperature conditions so that they may be destroyed more efficiently. Different injectors are used for gaseous and liquid waste surrogates. Water cooled stainless steel injectors are used to introduce gaseous waste surrogates into the cavity (described in Ref. 5); there are roughly forty 0.3-mm-diameter holes in the spanwise direction along each injector. Liquid wastes are injected through stainless steel spray atomizers (0.40 GPH Delevan 60° WDA) which are placed in a water-cooled box embedded in the ceramic plugs. Cooling the liquid prior to injec-
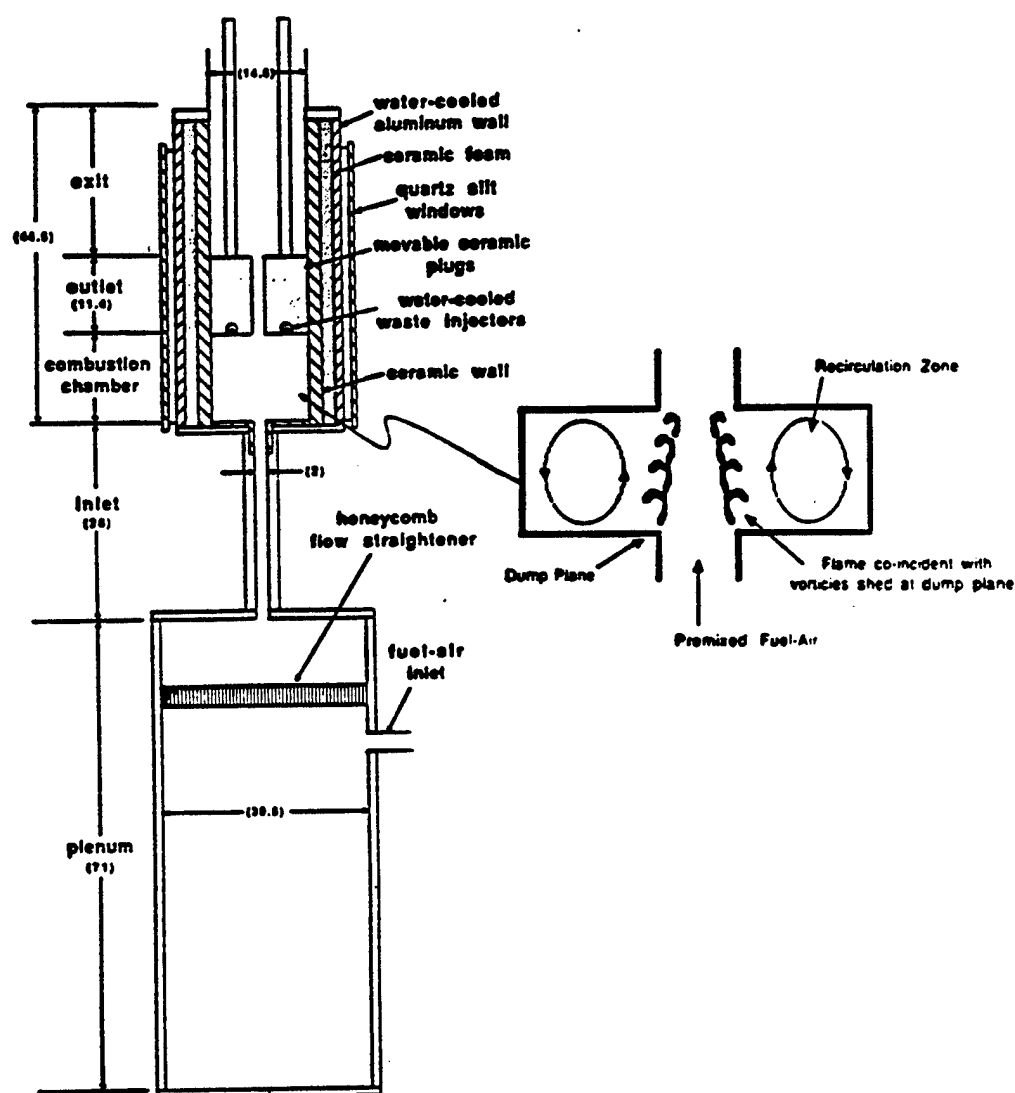
Fig. 1. Schematic of the dump combustor, including features of the combustion chamber cavity. Dimensions are given in units of cm.

tion prevents vaporization and possible pyrolysis of the waste in the injectors, which could clog them. There are three liquid injectors situated on each ceramic plug, allowing waste surrogate to be injected in a very roughly two-dimensional span of the combustion cavity.

Acoustic data are taken using a pressure transducer located in the plenum. In prior studies of a smaller dump combustor [2], three different acoustic modes were identified with combustor operation: two high-frequency oscillations in the 400–700 Hz range and an oscillation in the 30–50 Hz range described as the "chugging" mode. The high-frequency modes

are observed (from shadowgraph images) to correspond to flame wrinkling or even small-scale periodic vortex shedding from the dump plane, in which several vortex pairs may be present in the combustion cavity at a given time. The chugging mode corresponds to the formation of a large vortex pair at the dump plane which grows to fill the entire cavity before dissipating, probably destroying the coherent recirculation regions. A "quiet" mode, in which stable flame structures are formed and the recirculation cells remain stabilized, is also observed to occur under certain conditions. The larger combustor studied in Ref. 5 is the

one used in present context except with a different inlet width, as noted above. In the device in Ref. 5, only chugging and quiet modes were observed to occur; with the altered inlet width, high frequency modes are also excited. These different modes have different implications with respect to waste destruction in the cavity, as noted in Refs. 3 and 5, and as will be described below.

SURROGATE WASTE INJECTION AND DETECTION

To evaluate the performance of this dump combustor as an incinerator, two different waste surrogates are injected into the combustion cavity: sulfur hexafluoride (SF_6), injected in the gaseous phase with additional nitrogen, and acetonitrile (CH_3CN), injected in the liquid phase. SF_6 is an extremely refractory compound, which shows no degradation at temperatures below 1000°C [15]. Thus SF_6 is a good surrogate for studying waste destruction processes which may be susceptible to thermal by-passing. Acetonitrile is selected as a waste surrogate because of its resistance to incineration and its liquid state at room temperatures [16]. It has been ranked as one of the twenty RCRA Appendix VIII compounds that are most difficult to destroy, primarily because of its requirement of high concentrations of oxidizing radicals for destruction. Hence, destruction of acetonitrile should verify the existence of acceptable oxygen concentrations in the recirculation zones of the combustor. Detection of waste destruction in the device is made using a gas chromatograph. The GC is equipped with an electron capture detector for SF_6 measurements sensitive to < 1 ppb; for acetonitrile measurements, a flame ionization detector is used, with a detection limit of the order of 1 ppm.

RESULTS

As noted above, the acoustic character of the device is correlated with its ability to destroy injected wastes. Hence the acoustic signature without waste destruction is important to determine for the present operation. The acoustic behavior for the current device is shown in

Fig. 2. This mode map indicates that a "chugging" mode ($\approx$ 50 Hz) typically occurs at low equivalence ratios and longer combustion cavity lengths, that low frequency oscillations ($\approx$ 150 Hz) tend to be excited under rich burning and long cavity conditions, and that high-frequency oscillations ($\approx$ 500–600 Hz) dominate at shorter cavity lengths and equivalence ratios close to unity. Another characteristic mode, at 284 Hz (close to the 250-Hz hydrodynamic instability mode under these conditions) occurs for a variety of cavity lengths and equivalence ratios, yet is sensitive to the length of the plenum. Data points for the quiet mode are not shown here; the mode tends to occur at a variety of cavity lengths and equivalence ratios. Again we note that only chugging and quiet modes could be generated in the earlier version of this combustor [5] with a wider inlet area.

We now explore the destruction of SF_6 in the present device. Typical results are shown in Fig. 3 for the destruction and removal efficiency (DRE) of the incinerator, given in number of nines (e.g., 4 nines is equal to 99.99% DRE of SF_6), as a function of the global volumetric heat release rate or power density in the cavity. Clearly, there is a strong dependence of destruction efficiency on the acoustic character; under chugging (very low frequency) conditions, DREs are unacceptably poor, under high-frequency conditions DREs are moderately good, yet under quiet mode conditions the DREs are good to excellent.

These results indicate that waste destruction, and hence the stability and local temperature of the recirculation regions, are correlated with the different acoustic modes which are excited. Under quiet mode conditions with high power densities, and to a lesser extent, under high-frequency modes, the recirculation zones are sufficiently stable and contain gases at high enough temperatures for SF_6 to be pyrolyzed efficiently. Under chugging mode conditions, as noted above, large vortical structures are shed periodically from the dump plane, coincident with the premixed flames, which grow and perturb the recirculation zones. Hence, under these conditions the recirculation zones are subject to periodic destruction, so that the temperature field in the cavity varies periodi-
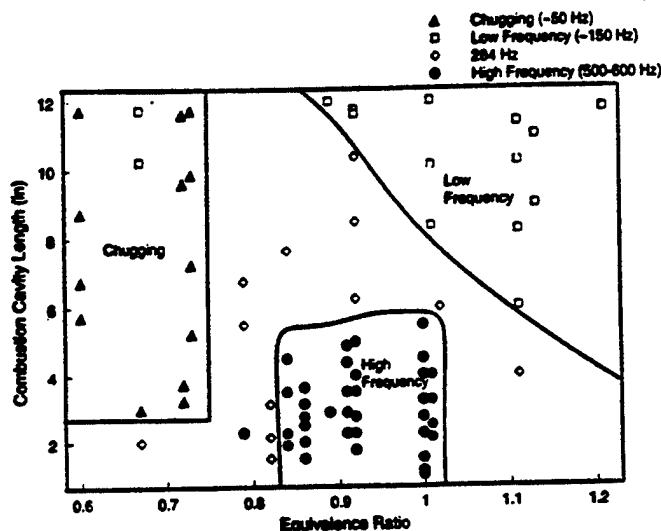
Fig. 2. Acoustic character of resonant incinerator without waste injection: acoustic modes excited for various cavity lengths and equivalence ratios of core flow. Inlet (core) flow rates vary between 5 and 12 m/s.

cally in time as well, possibly producing temperatures during its cycle which fall below the limit for SF₆ destruction. These conclusions are verified by planar laser-induced fluorescence (PLIF) images of OH in the cavity, shown in Fig. 4. Details of this diagnostic technique may be found in [4]. High concentrations of OH, which is an indicator of flame location, appear in the shapes of two-dimensional vortex pairs under chugging mode conditions, penetrating well into the recirculation zones of the cavity. Under quiet mode conditions, also shown in Fig. 4, the stabilized flames do not significantly disturb the recirculation zones.
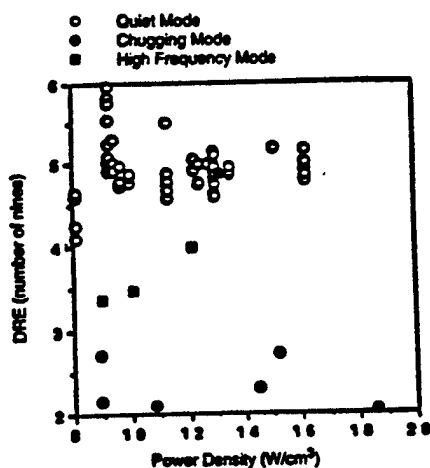

Fig. 3. Destruction and Removal Efficiencies (DREs) of SF₆ in the resonant incinerator for quiet, high frequency, and chugging acoustic modes as a function of power density in the combustion cavity.

It should also be noted that when SF₆ is injected into the combustion cavity under resonant conditions, the acoustic characteristics do not change. Neither the amplitude nor the frequency of the oscillations change from the values obtained without waste injection (Fig. 2), and when the combustor is operating under conditions which would produce a quiet mode without injection, the combustor remains quiet with SF₆ injection. The flame characteristics are also unaltered with the injection of SF₆; the mass flow rate of injected gas (SF₆ and nitrogen) is low enough, less than 8% of the inlet flow rate (which ranges from 0.7 to 2.0 kg/min), so that the recirculation region stability is relatively unchanged when compared with cases without injection in the cavity. There is also no appreciable release of heat in the recirculation zones due to pyrolysis of SF₆, and of course no additional flame structures are present in those regions due to the nature of SF₆ destruction. Hence these results concerning the acoustics and flame characteristics would clearly be expected for this type of waste surrogate.

Destruction of acetonitrile, the liquid waste surrogate, is summarized in Fig. 5. Acetonitrile is injected through water-cooled atomizers at roughly the same mass flow rate as that of SF₆ and nitrogen used above. Here DREs are evaluated as a function of the overall equivalence ratio for the combustor, which considers fuel injection through the inlet core (propane) as well as injection in the cavity (acetonitrile).
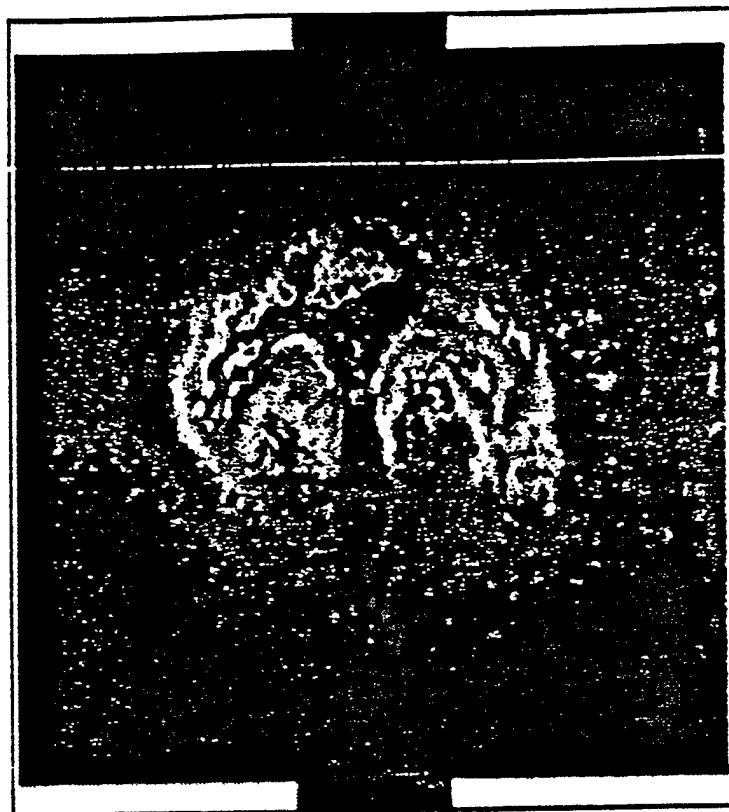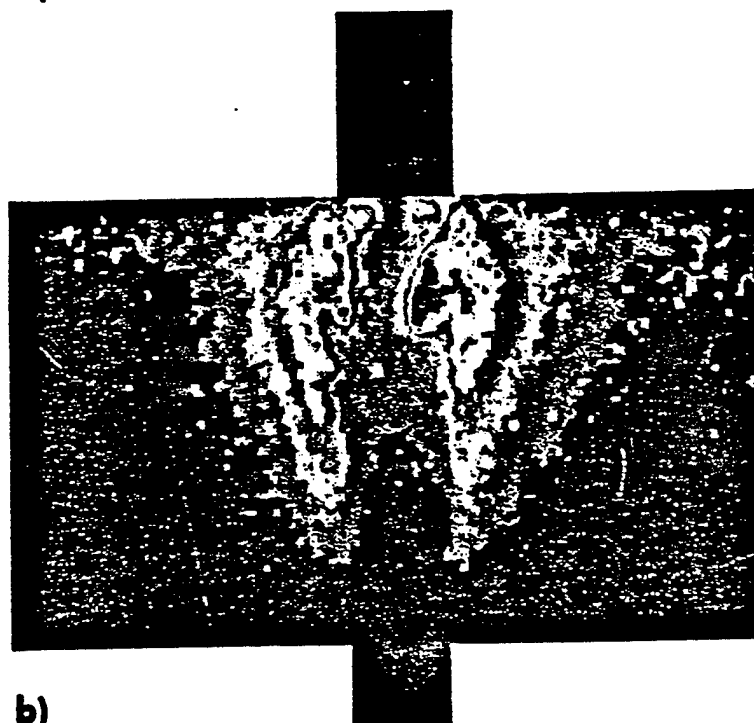
Fig. 4. Instantaneous images of deformed flame structures in the incinerator under (a) chugging mode oscillations (43 Hz) and (b) quiet mode conditions. Planar laser-induced fluorescence (PLIF) of the OH radical is·used to produce images of OH concentrations (from Ref. 4); the color sequence red-yellow-green-blue-black depicts decreasing OH concentration.

This definition of overall ϕ is appropriate since there can be combustion (and a secondary flame) occurring in the recirculation regions. Equivalence ratios computed using only the core flow are also shown in the figure.

The filled triangle symbols represent experimental conditions run in which the core flow contains enriched oxygen; this allows excess oxygen to be transported to the recirculation regions to assist with acetonitrile destruction. As would be expected, the cases with enriched oxygen provide the lowest overall equivalence ratio and the highest overall DREs for acetonitrile. The circles refer to experimental conditions without use of enriched oxygen in the core. The open circles correspond to quiet mode conditions observed for waste injection, occurring mostly under lean conditions in the core flow. The closed circles correspond to conditions which produce a high-frequency oscillation in the combustor with acetonitrile injection; these cases occur under nearly stoichiometric core conditions and produce the worst DREs of all cases considered.

The data described in Fig. 5 are quite revealing with respect to fluid mechanical, acoustic, and combustion processes in the dump combustor. First of all, most of the experimental conditions which produce nonoscillating (quiet) combustor operation *with* waste injection actually correspond to conditions producing chugging (≈ 50 Hz) or low-frequency (≈ 150 Hz)
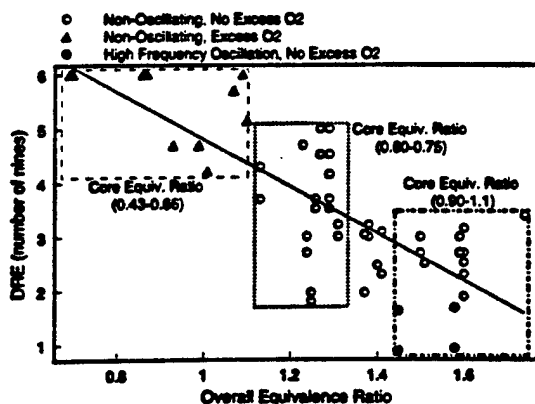

Fig. 5. Destruction and Removal Efficiencies (DREs) of acetonitrile in the resonant incinerator for cases with and without the enrichment of oxygen in the core (inlet) flow. DREs are evaluated for different overall equivalence ratios as well as equivalence ratios of flow in the core only.

modes *without* waste injection, shown in Fig. 2. This is particularly true for the data given by open circles in Fig. 5. Injection of acetonitrile appears to completely dampen these low-frequency oscillations. In addition, when acetonitrile is injected under conditions which produce a high-frequency mode without injection, the resulting high frequency mode with injection is significantly weakened in intensity (filled circles in Fig. 5). The frequency of the high-frequency oscillation remains the same with waste injection as without injection, however.

These observations concerning the waste destruction and the acoustic alteration may be explained as follows. For liquid waste injection with high core equivalence ratios (0.90–1.1), there is clearly not much oxygen transported through the primary flames into the recirculation zones. Thus acetonitrile injected into these zones is not exposed to enough oxygen to burn; the waste simply vaporizes and pyrolyzes, probably reducing the overall temperature of the recirculation zones. Destruction of the acetonitrile is poor under these conditions because of the reduction of oxidizing radical concentration in the recirculation zones; the resonant modes are probably damped due to the removal of heat in these zones. Hence, a lesser degree of energy is put into the acoustic oscillations at these conditions, and the oscillations are either damped (as in the high-frequency case) or not excited at all (as in the low-frequency case). In terms of Rayleigh's criterion, this means that the acetonitrile injection not only reduces the magnitude of the oscillations in heat release at the dump plane, but also appears to change the phase of the low-frequency oscillations such that the acoustic instability is not sustained.

This conclusion is further verified by experiments in which water is injected into the combustor cavity instead of acetonitrile. Water only vaporizes in the cavity, without pyrolysis or formation of any secondary flame, thus removing latent heat from the recirculation zones and cooling the region significantly. What is interesting in the case of water injection is that when operating conditions are chosen which produce acoustic oscillations *without* cavity injection (either chugging or high-frequency modes), when water is injected there is no

appreciable acoustic output at all. There is a removal of energy from the system by the vaporization in addition to an alteration of the phase of the oscillations, thus damping rather than exciting acoustic oscillations. In addition, because the recirculation regions become much cooler with water injection, it becomes much more difficult to achieve flame attachment at the dump plane. This reduction in the flame-holding ability of the combustor is also seen with acetonitrile injection at the higher equivalence ratios; the flame appears attached to the dump plane only in the center (spanwise) region of the device.

A less straightforward result is the observation that for low core equivalence ratios (0.60–0.75), the chugging mode is damped by acetonitrile injection while the flames appear to be far more stable than without injection. Clearly, under these lean conditions, there is sufficient oxygen transported into the recirculation zones to accomplish burning of acetonitrile; there is actually a visible secondary flame structure present in the zones. Hence, the improvement in waste destruction here is to be expected. The fact that there is energy release in the recirculation zones with acetonitrile injection, however, means that energy is being put into the system and that the zones are becoming much hotter than cases without injection. These hotter recirculation zones assist in stabilizing the flames, as one would expect, but the additional energy input does not appear to enhance acoustic oscillations in the device at all. It appears that pulses of heat released by vortical structures at the dump plane are altered in phase due to the addition of heat in the recirculation zones such that Rayleigh's criterion is no longer satisfied and the instability is not sustained. These same conclusions hold for the experimental conditions run with oxygen enrichment in the core flow (filled triangles, Fig. 5) and a secondary combustion process occurring in the recirculation zones.

CONCLUSIONS

The foregoing comparison of gaseous and liquid waste surrogate destruction in a resonant dump combustor leads to the following conclusions. First, we observe a strong correlation between the fluid mechanical distortions of the premixed flame structures and the destruction of both gaseous and liquid waste streams. In both cases, when the flame oscillates (as in the chugging mode during SF_6 injection) or when it is detached in a chaotic fashion (as in the high core equivalence ratio cases with acetonitrile injection), the DREs are poor. Of course, in the latter case the poor destruction is mostly an outcome of the reduced oxygen concentrations in the recirculation zones, but it is this reduced concentration that causes lower temperatures and a reduction in flame stability. When the flames are stabilized, as in the quiet and high-frequency modes for SF_6 destruction or the lean conditions for acetonitrile destruction, the DREs are good to excellent, exceeding RCRA requirements of 99.99% destruction. In the case of SF_6, waste is destroyed well if there are high temperatures in the recirculation cells and as a consequence the flame structures are stabilized by the hot zones. In the case of acetonitrile, waste is destroyed well if there are high concentrations of oxidizing radicals in the recirculation cells, and the heat release in the cells *subsequent* to the combustion of acetonitrile allows flame stabilization to be maintained.

The contrast between destruction of gaseous and liquid wastes in a pulse combustion system is also apparent in the present study. The gaseous waste surrogate used here does not significantly add or remove energy from the system such that the acoustic oscillations are affected or the stability of the flame is influenced. Although other gaseous waste streams could produce additional heat release and higher temperatures in the recirculation zones, the only effects they should have on this and other pulse combustor devices is to improve flame stability (and hence improve waste destruction) while possibly damping acoustic oscillations. Thus, flame stability and ultimately, DREs for gaseous waste injection, should not worsen when the combustor is operating in the quiet or high-frequency modes.

For liquid waste injection, we have seen that the vaporization process may be important if the waste only undergoes pyrolysis and not combustion in the cavity. Heat removal may be

significant enough to cool recirculation regions in the cavity and cause flame detachment. Under these conditions, poor DREs result both from a lack of excess oxygen (and hence lack of a secondary combustion process) in the cavity as well as an unstable flame structure. As with any process (gaseous or liquid) in which secondary combustion could take place in the recirculation zones, an alteration in the phase of the heat release at the dump plane may occur, potentially dampening acoustical oscillations.

While early studies of waste destruction in the present dump combustor configuration indicated a strong correlation, almost a cause-and-effect relationship, between the acoustic character of the device and waste destruction, the present studies suggest a much more complex process. Under most conditions, a chugging acoustic mode is correlated with poor waste destruction, mainly because these conditions produce strong fluctuations in flame structure and recirculation zone stability. Under "quiet" conditions, waste destruction may be very good (SF$_6$, Fig. 3) or relatively poor (acetonitrile in the absence of oxygen enrichment, Fig. 5). The differences in DREs between the two figures have mainly to do with the stability of the primary flames and the presence of hot gases in the recirculation zones to assist with flame stabilization, processes which are more fluid mechanical than acoustic in nature. Finally, under high-frequency mode conditions, we observe both adequate waste destruction (SF$_6$) and poor waste destruction (acetonitrile). Again the differences appear to result from flame stability rather than acoustic effects.

Based on the present experiments, it appears that the acoustic signature can only be an indicator of resonant incinerator performance when accounting for the character of the primary flame structures. Future studies will focus on active control of the device as a means of generating acoustic disturbances

while keeping the flame structure stable and allowing proper destruction of waste to occur.

REFERENCES

1. Oppelt, T., *J. Air Pollut. Control Assoc.* 37:558 (1987).
2. Logan, P., Lee, J. W., Lee, L. M., Karagozian, A. R., and Smith, O. I., *Combust. Flame* 84:93-109 (1991).
3. Smith, O. I., Marchant, R., Willis, J., Lee, L. M., Logan, P., and Karagozian, A. R., *Combust. Sci. Technol.* 74:199-210 (1990).
4. Cadou, C., Logan, P., Karagozian, A., Marchant, R., and Smith, O., *Environ. Sensing Combust Diagn.*, SPIE Proc. Ser. 1434:67-77 (1991).
5. Marchant, R., Hepler, W., Smith, O. I., Willis, J., Cadou, C., Logan, P., and Karagozian, A. R., *Combust. Sci. Technol.* 82:1-12 (1992).
6. Willis, J., Lee, L.-M., Karagozian, A. R., and Smith, O. I., *Combust. Sci. Technol.* 94:469-481 (1993).
7. Zinn, B. T., *Twenty-Fourth Symposium (International) on Combustion*, The Combustion Institute, Pittsburgh, 1992, pp. 1297-1305.
8. Schadow, K., private communication.
9. Poinsot, T. J., Trouve, A. C., Veynante, D. P., Candel, S. M., and Esposito, E. J., *J. Fluid Mech.* 177:265-292 (1987).
10. Smith, D. A., and Zukoski, E. E., Twenty-first Joint Propulsion Conference, Monterey, CA. Paper 1248, 1985.
11. Yu, K. H., Trouve, A., and Daily, J. W., *J. Fluid Mech.* 232:47-72 (1991).
12. Sterling, J. D., and Zukoski, E. E., Twenty-fifth Aerospace Sciences Meeting, Reno, NV, Paper 0220, 1987.
13. Rayleigh, Lord, *The Theory of Sound*, Dover, New York, 1945, Vol. II, p. 227.
14. Zukoski, E. E., and Marble, F. E., Proceedings of the Symposium on Gas Dynamics, Northwestern University, August 22-24, 1955.
15. Proctor, C. L., Berger, M. C., Fourier, J. R., and Roychoudhury, S., Report ESL-TR-86-47, Air Force Engineering and Services Laboratory, Tyndall AFB (1987).
16. Chang, D. P. Y., and Sorbo, N. W., Final Report, California Air Resources Board Contract, A6-221-45 (1988).

REFERENCE [2]

EFFECTS OF EXTERNAL ACOUSTIC EXCITATION ON ENHANCED TRANSPORT IN A RESONANT INCINERATOR

G. PONT, J. W. WILLIS, A. R. KARAGOZIAN AND O. I. SMITH

Department of Mechanical and Aerospace Engineering
University of California
Los Angeles, CA 90095-1597, USA

The research described here focuses on the enhancement of energy transport and waste surrogate destruction in an acoustically resonant dump combustor. While prior studies focused on flow field interrogation and the nature of waste destruction under conditions of natural acoustic excitation, the present study focuses on the device's behavior under externally forced acoustical conditions. External forcing was accomplished here using a loudspeaker situated in the plenum section of the device, allowing strong excitation of acoustic resonances. The effect of this external forcing on waste destruction in the device was found to be significant. Results show that, for specific forcing frequencies (coincident with the system natural modes), marked improvement in destruction and removal efficiencies (DREs) of the waste surrogate SF_6, by four orders of magnitude and perhaps higher, could be achieved. When the device was forced at frequencies other than natural modes, little improvement over the nonforced combustor performance was achieved. External forcing at very high frequency natural modes yielded some improvement in waste destruction, but to a lesser extent than at lower frequency natural modes. OH* chemiluminescence images indicated that the enhancement of waste destruction at certain natural modes coincided with flame shortening and broadening, likely arising due to vortex shedding during the acoustical excitation. This alteration in flame structure during excitation of specific natural modes appeared to materially enhance energy transport to the regions in which waste was injected, as evidenced by reduced flame liftoff under such conditions. These observations suggest that acoustically resonant combustor conditions can render this device extremely efficient as well as highly controllable.

Introduction

The dump combustor is a device that has been studied extensively over the past half century because of its ability to burn fuel and contain heat in a relatively compact configuration. Acoustically driven combustion instabilities are known to occur in such devices when pressure oscillations and periodic heat release associated with the combustion are in phase [1]. Transverse acoustic modes are associated with periodic, transversely alternating vortices shed coincident with flame structures, the so-called screech phenomenon [2]. Longitudinal acoustic modes are also associated with vortex shedding in such combustors; a number of research groups over the years have sought to control such combustion instabilities through the use of externally applied acoustical forcing [3–6]. Acoustically excited combustion processes have also been studied in pulse combustor systems [7–10]. Local extinction by flame stretch is observed to delay ignition; later relaxation of strain allows thermal ignition to take place in a volumetric fashion, significantly increasing heat and mass transfer rates. Numerical simulations of acoustically resonant combustion systems [10–12] have indicated the importance of periodic vortex shedding in sustaining the acoustical excitation [1,13].

Over the past few years, our research has focused on the development and investigation of a small-scale, two-dimensional dump combustor (or "resonant incinerator") which has been found to be capable of destroying hazardous waste surrogates to a high degree [14–19]. The acoustic character of the incinerator is found to be correlated with classical combustion instabilities according to the Rayleigh criterion [1,13] in which energy input occurs nearly in phase with pressure oscillations to sustain the acoustic resonance. The degree of waste surrogate destruction in the device has been found to correlate somewhat with naturally occurring acoustic conditions [15,17,19]. Destruction and removal efficiencies (DREs) for the gaseous waste surrogate sulfur hexafluoride (SF_6) are observed to be as high as 99.999999% ("8 nines") under quiet conditions and occasionally under acoustically resonant conditions [19]. This is four orders of magnitude above the EPA requirement of 99.99% DRE for hazardous waste incinerators [20]. Liquid waste surrogate (acetonitrile) destruction in the device, in contrast, is not only found to be less dependent on the acoustic character of the device, but is actually found to
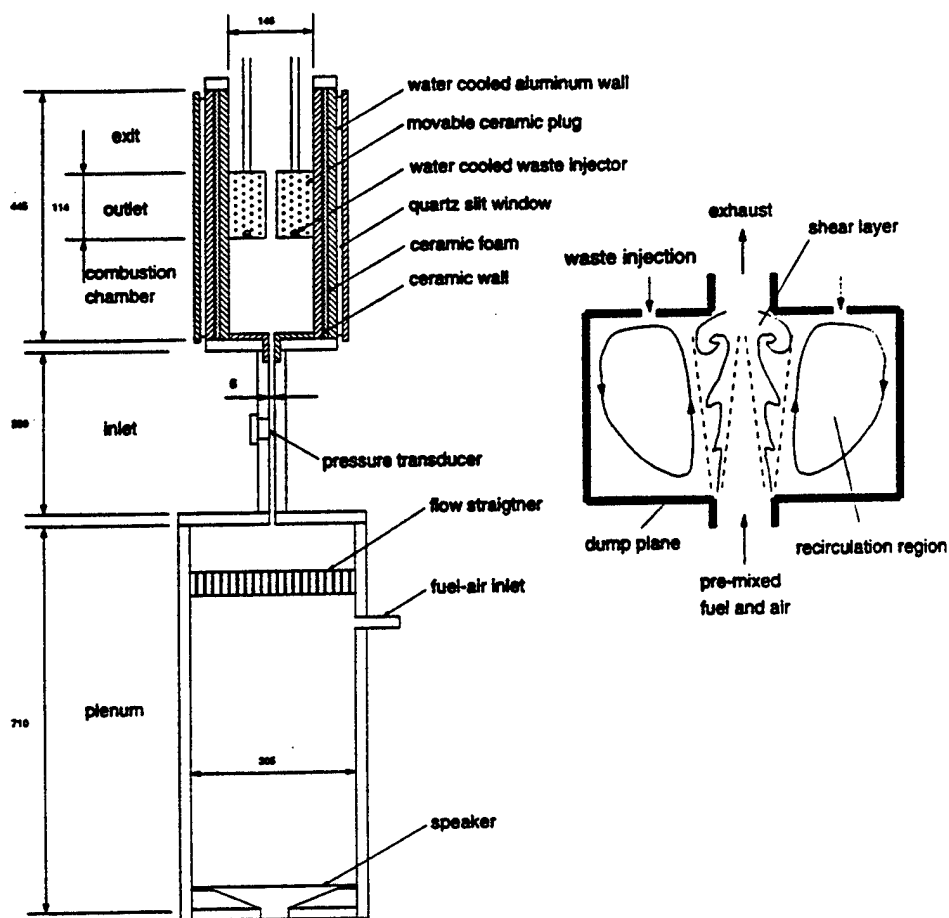
FIG. 1. Schematic of the dump combustor, including features of the combustion chamber cavity. Dimensions are given in millimeters.

dampen preexisting natural acoustic modes due to the heat removal process associated with vaporization [19]. Nevertheless, DREs for acetonitrile can be quite high (greater than 6 nines, the detection limit of the diagnostic equipment) if sufficient excess oxygen is available for combustion of the waste surrogate.

The present experiments focus on the ability of the resonant incinerator to destroy waste surrogates under externally forced (not naturally occurring) acoustical conditions. Based on prior results, it may be desirable to excite acoustical modes in the device in order to improve waste destruction without having to alter the equivalence ratio, cavity length, flow velocity, or other parameters necessary to excite natural modes. The present work also seeks to understand the advantages of exciting certain acoustic modes over others with respect to waste destruction and energy transport, using chemiluminescence im-

aging of the reaction zone. This study opens the possibility of active rather than passive control of the resonant incinerator, that is, actively forcing the combustor at a frequency that optimizes waste destruction.

Experimental Apparatus and Procedure

The two-dimensional dump combustor used in the present experiments is shown schematically in Fig. 1, with an expanded view of flow/reaction processes in the combustion cavity. The combustor's basic features have been described previously, and will only be summarized here. The reader is referred to Refs. 17 and 19 for additional details.

Propane and air at room temperature were introduced into the plenum section of the combustor, then were mixed and accelerated through an inlet

section before entering the combustion cavity at a sudden expansion or "dump plane." Premixed flames could be stabilized due to the formation of high temperature recirculation regions downstream of the dump plane [21], but as noted above, vortex shedding coincident with the flames could occur under conditions of natural acoustic excitation [14–19]. The spanwise depth of the inlet, combustion cavity, outlet, and exit sections (30.5 cm) were usually sufficient to produce a visually two-dimensional flame over the entire span, although under certain experimental conditions the flow in the cavity became turbulent and the flame/flow structures became three-dimensional. The inlet width in the present configuration was the same as that in Ref. 19 (0.6 cm), as compared with 2.0 cm in the device described in Ref. 17. This narrowing of the inlet allowed high-frequency acoustic modes to be naturally excited with greater ease. Quartz windows bounded each end of the system in the spanwise direction, allowing appropriate optical access; additional quartz window slits were installed in the side walls to allow the introduction of a sheet of laser light for optical diagnostics [16].

A set of movable ceramic plugs defined the outlet section of this combustor. Waste surrogate was introduced through injectors embedded in these plugs as indicated in Fig. 1. Injection into the recirculation zones allowed wastes to be trapped for relatively long residence times under high-temperature conditions so that they could be destroyed more efficiently. Water-cooled stainless steel injectors were used to introduce gaseous waste surrogates into the cavity [15,17]; there were forty 0.3-mm-diameter holes in the spanwise direction along each injector.

Acoustic data were taken using pressure transducers located in the plenum and inlet. In recent studies of the present combustor [19], a low-frequency "chugging" mode (at approximately 50 Hz) typically occurred at low equivalence ratios and longer combustion cavity lengths; this acoustic mode tended to create large vortex structures at the dump plane which expanded periodically to disturb the recirculation zones, hence waste destruction under these conditions was poor [17,19]. Other low-frequency oscillations ($\approx$150 Hz) tended to be excited under rich-burning and long cavity conditions. High frequency natural modes ($\approx$500–600 Hz) dominated at shorter cavity lengths and equivalence ratios close to unity; these conditions could yield excellent waste destruction [19]. Another characteristic acoustic mode, near 290 Hz (close to the 250-Hz hydrodynamic instability mode under these conditions), appeared to be sensitive to plenum conditions only. These high-frequency modes all depended on the presence of a standing wave in the system and were observed from shadowgraph images to correspond to flame wrinkling and small-scale periodic vortex shedding from the dump plane. An acoustically

"quiet" mode in which flames and recirculation cells were stabilized and no significant acoustic output was detected occurred for a variety of cavity lengths and equivalence ratios, and also was found to produce excellent conditions for waste destruction [15,17,19].

To continue to evaluate the performance of this dump combustor as an incinerator, the waste surrogate SF_6 was injected in the present study in the gaseous phase with additional nitrogen. SF_6 is an extremely refractory compound, which shows no degradation at temperatures below 1000°C [22]. It has been ranked as one of the twenty RCRA Appendix VIII compounds that are most difficult to destroy. Thus, SF_6 is a good surrogate for studying waste destruction processes that may be susceptible to thermal bypassing. Detection of waste destruction in the present device was made using a gas chromatograph equipped with an electron capture detector for SF_6, measurements sensitive to ≤ 1 ppb, yielding a detection limit for SF_6 of nearly 8 nines.

External acoustical forcing was accomplished in the present experiment using a loudspeaker situated at the bottom of the plenum section of the device. Using a signal generator, it was possible to produce a sine wave of varying frequency, then to amplify the signal and pass it to the speaker. This enabled a sweep through a range of input forcing frequencies from 0 to 1000 Hz to be performed, with forcing amplitude variation up to 150 dB, although frequencies below 200 Hz were difficult to attain consistently with the present speaker. Thus, it became possible to force the loudspeaker at frequencies corresponding to the natural modes of the device as well as other frequences, and to determine the effects of this forcing on DREs.

It was of interest to determine differences in flame characteristics within the combustor under different acoustical forcing conditions. The technique of OH* chemiluminescence was used here in order to image the reaction zone in a time-dependent manner. OH* chemiluminescence is thought [23] to result from the radiative decay of electronically excited radicals produced within the reaction zone by the reaction

$$CH + O_2 \rightarrow CO + OH^*$$
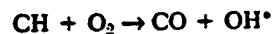
The chemiluminescence image thus depicts the heart of the reaction zone, the only region with significant concentrations of CH. Persistence of species is not a problem here (as compared with OH planar laser-induced fluorescence imaging) because CH is destroyed by rapid bimolecular reactions, not the much slower termolecular processes that dominate OH removal in the postflame region. Therefore, one may expect to obtain a well-defined image of the flame zone, both spatially and temporally. For most conditions explored here, the two-dimensional nature of the flow structures rendered OH*
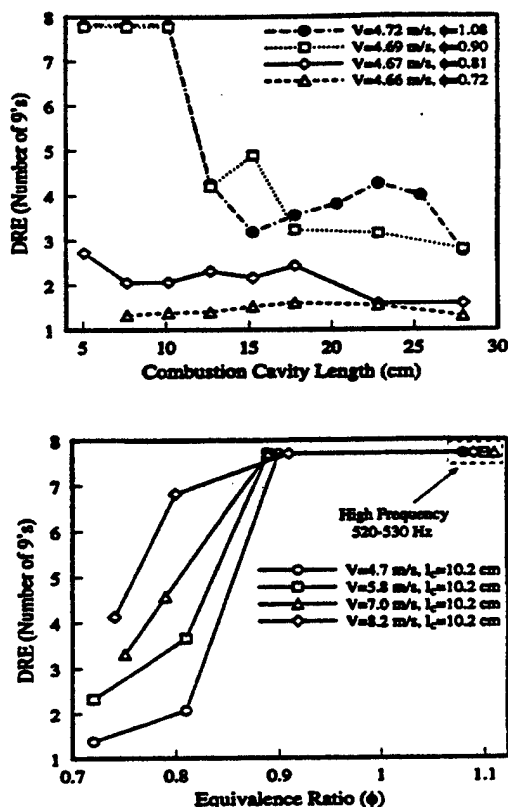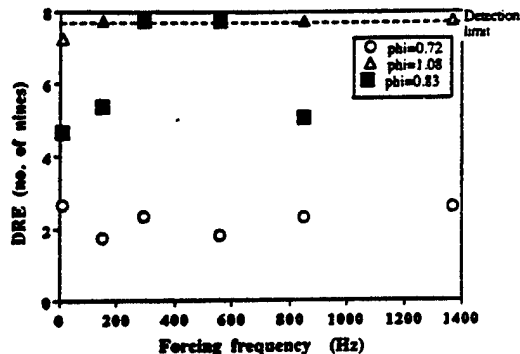
FIG. 3. Destruction and removal efficiencies (DREs) of SF$_6$ in the resonant incinerator during externally forced acoustical excitation for equivalence ratios of 0.72 (circles), 0.83 (filled squares), and 1.08 (triangles). For no external forcing (zero frequency), the only naturally resonant condition is for $\phi = 1.08$.

FIG. 2. (a) Destruction and removal efficiencies (DREs) of SF$_6$ in the resonant incinerator as a function of combustor cavity length for inlet velocities $V \approx 4.7$ m/s and for various equivalence ratios. Acoustic resonance occurs only at the highest equivalence ratio ($\phi = 1.08$) for cavity lengths below 11 cm. (b) Destruction and removal efficiencies (DREs) of SF$_6$ in the resonant incinerator as a function of equivalence ratio for a cavity length $l_c = 10.2$ cm and various inlet velocities. Acoustic resonances occur at the equivalence ratios above 1.

Results and Discussion

Recent results for the destruction of SF$_6$ in the resonant incinerator *without* external forcing are shown in Fig. 2a,b. DREs, given in numbers of nines, varied with the length of the combustion cavity (Fig. 2a) and with the equivalence ratio ϕ of the core flow (Fig. 2b). SF$_6$ destruction or pyrolysis, and hence the stability and local temperature of the recirculation regions, became quite high, increasing by four or more orders of magnitude, as the length of the combustor cavity was reduced or the equivalence ratio was increased. It is important to note that in Fig. 2a the combustor was not operating in an acoustically excited mode except when $\phi = 1.08$ at short cavity lengths, while in Fig. 2b the combustor operated in an acoustically resonant high frequency mode when ϕ was near unity. As seen before [19], very high DREs, nearly to 8 nines (the detection limit of the GC), were attained under quiet or certain acoustically resonant conditions that were made to occur naturally.

External acoustical forcing was applied via the loudspeaker in the plenum to produce oscillations at natural as well as other frequencies. Figure 3 shows the effects of forcing at various frequencies on DREs for the combustor, for several different operating conditions. For lower equivalence ratio conditions which produced poor DREs when the combustor was naturally quiet ($\phi = 0.72$, the circles), external forcing did little to significantly increase DREs. Under certain naturally resonant conditions that produced high DREs without external forcing ($\phi = 1.08$, the triangles), forcing from the loudspeaker did relatively little to improve the destruction, although the DREs measured (exceeding 8 nines) were at the detection limit of the GC and actually could be much higher than shown with external forcing. When
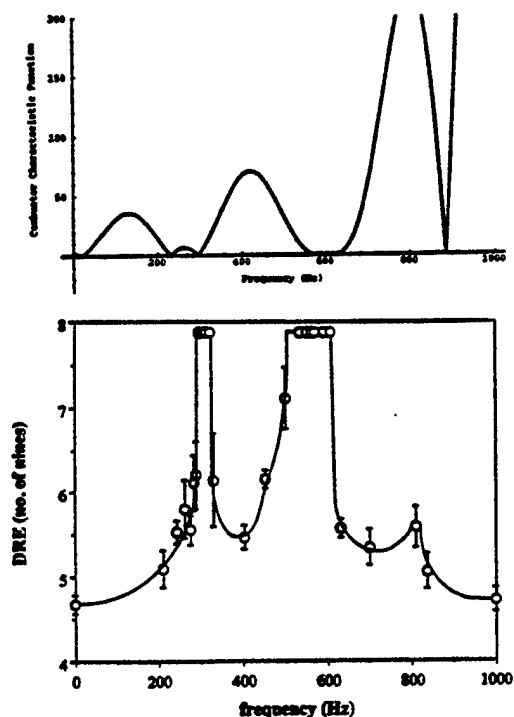
chemiluminescence images reasonably clear depictions of 2-D flame oscillations.

The OH* chemiluminescence measurements were made with a subset of the equipment used for PLIF imaging, described in Refs. 16 and 19. An intensified CCD camera was synchronized to the pressure oscillations detected in the inlet to be able to capture variations in OH* chemiluminescence within the combustion cavity over a period of oscillation. The integration time of the image intensifier was 250 μs, long enough to provide adequate signal-to-noise, but short with respect to the period of even the highest frequency modes observed. A bandpass filter centered around 312 nm was used in an attempt to isolate fluorescence from the $X^2 \Pi(v = 0)$ $\leftarrow A^2\Sigma(v = 0)$ states of OH.

FIG. 4. The lower plot shows destruction and removal efficiencies (DREs) of SF_6 in the resonant incinerator during externally forced acoustical excitation for the case where equivalence ratio $\phi = 0.83$. Comparison is made with characteristic function of the system (shown in the upper plot), computed from the 1-D model described in Refs. 14, 18; system zeroes correspond to natural modes.

external forcing was applied under conditions associated with an intermediate ϕ and no natural excitation ($\phi = 0.83$, the filled squares), it was seen that certain forcing frequencies significantly increased DREs, by four orders of magnitude or more, compared with conditions without external forcing. DREs were also found to increase monotonically with forcing amplitude at these optimal frequencies. It is of interest to understand precisely *why* such a profound increase in waste destruction can occur at these specific frequencies, that is, to understand what material changes occur in the reaction processes to cause such an augmentation.

This question was answered in part by examining in greater detail the changes in DREs with frequency for the $\phi = 0.83$ case; this is shown in the lower part of Fig. 4. Clearly, at specific frequencies (roughly $\Omega \approx 300$ Hz, 500–600 Hz, 800 Hz), significant augmentation in incinerator performance could be achieved, while between these modes, performance returned nearly to the unforced behavior. The forcing frequencies that caused this augmentation were close to the natural acoustic modes that,

theoretically, could occur under the given operating conditions. This is demonstrated in the upper portion of Fig. 4 in the plot of the characteristic function of the system as a function of frequency, computed from a one-dimensional acoustic model as described in Refs. 14 and 18. The model represents the various elements of the incinerator (plenum, inlet, cavity, etc.) as separate components of an acoustical system, and represents the oscillatory heat release initiated by vortex shedding in the combustion cavity as a sinusoidal volume source. The zeroes of the acoustical system's characteristic function in general correspond to system resonant modes or eigenvalues. It is clear from this comparison, however, that certain natural modes ($\Omega \approx 295$ Hz, 560 Hz) were superior to others ($\Omega \approx 830$ Hz) in terms of their effect on combustor performance. It is interesting to note that there were actually two natural modes that occurred between 500 and 600 Hz; these apparently caused the very broad peak in the DREs in this frequency range. If the detection limit of our GC were higher than 8 nines, it is likely that two peaks in DREs would be observed in this range.

OH* chemiluminescence images, which indicate the oscillatory behavior of the flame/reaction zone, supplied further information with respect to the advantages of forcing at specific frequencies. Fig. 5 shows the differences in OH* chemiluminescence in the combustion cavity for a number of different cases explored, with consistently normalized chemiluminescence intensities. Figure 5a shows a temporally averaged OH* chemiluminescence image for the case without external forcing, while Fig. 5b–e shows instantaneous chemiluminescence images for the cases with external forcing at increasing frequencies for similar positions within the acoustic cycle. The flame structure in the absence of acoustical excitation (Fig. 5a) appeared elongated and was stabilized fairly closely to the dump plane, yet it appeared much more diffuse and in fact more three-dimensional (visually) than the acoustically resonant flames. External forcing at the natural frequencies producing high DREs ($\Omega = 295$ Hz and 560 Hz) showed flame structures that were significantly more compact and visibly more two-dimensional (Fig. 5b and d, respectively), with some degree of lifting at the dump plane. These flames appeared to be more coherent compared with those in the unforced case; some flame broadening was observed, likely due to the deformation of the flames by small-scale vortices, as evidenced in OH PLIF images [16]. External forcing at a nonnatural frequency ($\Omega = 430$ Hz, Fig. 5c) produced flame structures that appeared thinner than those forced at natural modes; these in fact were visually more similar to the unforced case (Fig. 5a), although the flame was much more lifted in the OH* images and periodically jumped to very high positions within the cavity. Excitation at a high-frequency natural mode ($\Omega = 830$ Hz, Fig. 5e)
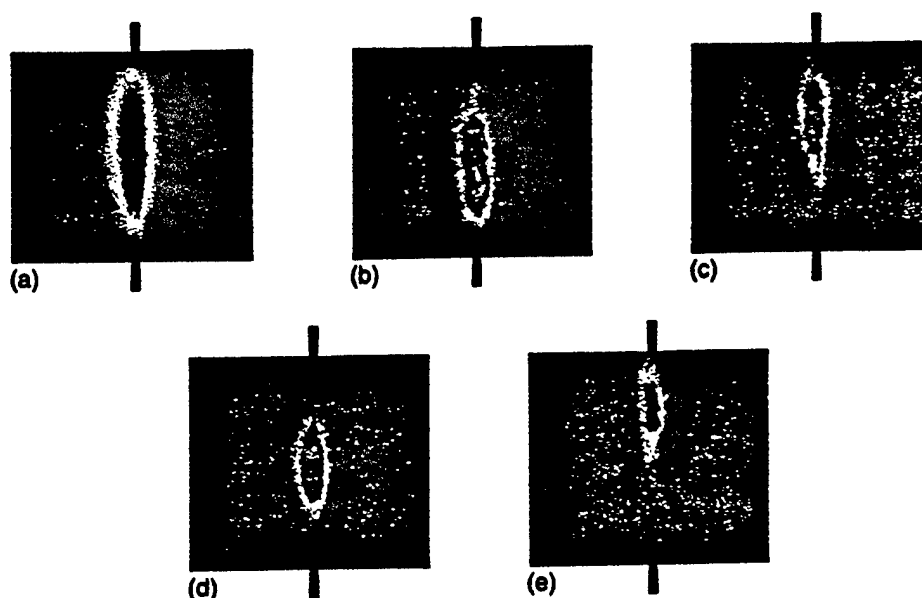
FIG. 5. OH* chemiluminescence images of the combustion cavity for an equivalence ratio $\phi = 0.83$. Highest chemiluminescence intensity is indicated by red; lowest by blue. Cases shown are for conditions of (a) no external forcing. (b) external forcing at 295 Hz (a natural mode), (c) external forcing at 430 Hz, (d) external forcing at 560 Hz (a natural mode), and (e) external forcing at 830 Hz (a natural mode).
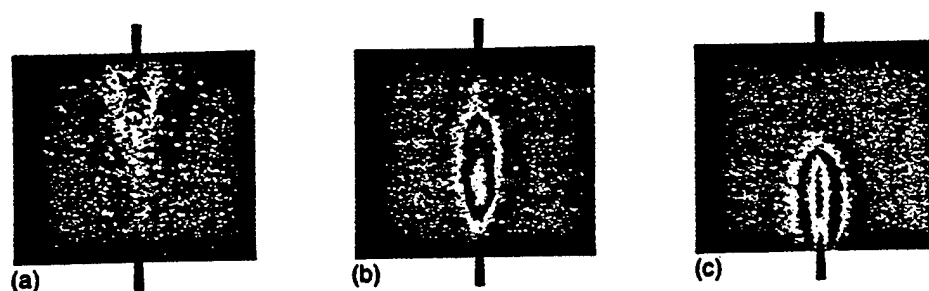

FIG. 6. OH* chemiluminescence images of the combustion cavity for external forcing at 295 Hz. Highest chemiluminescence intensity is indicated by red; lowest by blue. Cases shown are for equivalence ratios (a) $\phi = 0.72$. (b) $\phi = 0.92$, and (c) $\phi = 1.08$.

similarly produced a thinner and much more highly lifted flame structure than seen in Fig. 5b or d.

It was first recognized by Marble and Adamson [24] that the flame liftoff distance from a bluff-body flameholder increases with decreasing recirculation zone temperature. The present observations of liftoff suggest that the temperatures within the recirculation zones for the cases in Fig. 5c,e could be much lower than in Fig. 5b,d. These temperature differences could explain the enhancement of SF_6 destruction in the latter two cases where high temperatures are required for acceptable waste destruction rates. The increased recirculation zone temperatures under optimal acoustic excitation were also

suggested by recent temperature field measurements in the resonant incinerator [26]. The lessened broadening of the flame in Fig. 5e as compared with the other natural modes (Fig. 5b,d) also indicated that the flame had trouble keeping up with oscillations that occur at such a high frequency. as suggested by Egolfopoulos [25].

If there was not sufficient chemical energy input to the system during the reaction process. acoustic excitation. even at naturally resonant frequencies. did not materially affect combustor performance. as indicated by the $\phi = 0.72$ case in Fig. 3. These differences in global energy input were borne out inthe OH* chemiluminescence images shown in
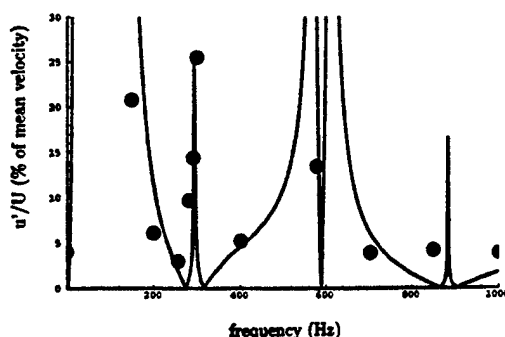
FIG. 7. The symbols represent hot-wire measurements of velocity fluctuations at the dump plane for cold flow conditions as a function of forcing frequency; comparison is made with 1-D model predictions of velocity perturbations at the dump plane [14,18] under cold conditions.

Fig. 6a–c, for fixed external forcing at 295 Hz (at or near a natural resonance) with increasing values of ϕ. As equivalence ratio was successively increased in Fig. 6a–c (see also Figure 5b, the case where ϕ = 0.83), the flame became less and less lifted. The case where ϕ = 1.08 (Fig. 6c) appeared to have the most coherent 2-D flame structure, the highest relative concentration of OH* in the flame zone, and likely had the most efficient energy transport to the recirculation zones, although the detection limit of the GC restricted the extent to which this transport could be completely quantified. The moderate equivalence ratio cases, however (ϕ = 0.83 and ϕ = 0.92 in Figs. 5b and 6b, respectively), appeared to have enough enhancement of energy transport from the flame zone due to acoustic excitation to produce the same high DREs. From the point of view of combustor performance, then, acoustic excitation could perform a similar function to increasing equivalence ratio by providing a greater rate of energy transport to optimal locations.

The nature of flame liftoff may be studied further by measuring velocity fluctuations at the dump plane using a hot-wire anemometer under different acoustic forcing conditions for cold flow conditions. The experimental results are shown as the symbols in Fig. 7. Calculations of the velocity perturbation at the dump plane are also shown in the figure; these were made using a one-dimensional model with volumetric forcing downstream of the dump plane to represent energy addition via forcing [18]. Scaling between experimental and theoretical results was achieved by matching the velocity fluctuations at a single frequency (295 Hz). The experimental peaks in velocity fluctuations at the dump plane occurred at the natural frequencies that produced the peaks in DREs; forcing off-resonance or at a very high frequency mode (~830 Hz) yielded relatively small velocity perturbations. The model showed similar be-

havior, consistent with the presence of a standing wave in the system under resonant conditions. These observations suggest that high-amplitude velocity fluctuations were associated with the flame instability that broadens the flame zone while enhancing energy transport to and temperatures within the recirculating regions.

Concluding Remarks

This study demonstrates that externally forced as well as naturally occurring acoustical oscillations can have a dramatic effect on the present combustor when operating as an incinerator. DREs for a temperature-sensitive waste surrogate (SF_6) were found to increase by four orders of magnitude (perhaps more) when acoustical forcing was imposed at system characteristic frequencies, as long as there was enough global energy available in the chemical reaction, that is, a high enough equivalence ratio for the reaction. With external forcing at natural modes of the system, flame structures were made more compact and broadened, likely due to vortex shedding which materially enhanced the transport of energy to the recirculation zones where waste destruction occurred. Flame liftoff characteristics as evidenced by OH* chemiluminescence images were consistent with higher recirculation zone temperatures during external forcing at desirable natural modes. Forcing at natural modes appeared also to significantly increase velocity fluctuations at the dump plane for the geometry studied.

While the present studies reinforce the desirability of acoustically resonant combustion for enhanced energy transport [8,9], there is new evidence here for the desirability of *specific* natural acoustic mode excitation over other modes. Acoustic excitation at specific natural modes can be viewed as performing a similar function to increasing equivalence ratio by providing a greater rate of energy transport to optimal locations into which waste is injected. This can have important implications for practical use of this device in that one can achieve excellent incinerator performance even with reduced flow rates of auxiliary (core) fuel, as long as appropriate acoustic excitation is maintained.

The study also suggests the possibility of actively controlling the behavior of a resonant combustor for incineration applications; this could be particularly useful in ensuring recovery from incinerator upset conditions, for example, that could occur due to sudden changes in waste characteristics. It is hoped that future studies in this device will explore in more detail the ability of the external forcing to actively control waste destruction.

REFERENCES

1. Rayleigh, Lord, The Theory of Sound, Vol II, Dover Publications, New York, 1945, p. 227.
2. Rogers, D. E. and Marble, F. E., *Jet Propulsion* 26:456–462 (1956).
3. Yu, K., Trouve, A. and Candel, S., AIAA Paper No. 91-0367, 1991.
4. Schadow, K., Gutmark, E., and Wilson, K. J., AIAA Paper No. 90-2447, 1990.
5. McManus, K. R., Vandsburger, U., and Bowman, C. T., *Combust. Flame* 82:75–92 (1990).
6. McManus, K. R., Poinsot, T., and Candel, S. M., *Prog. Energy Combust. Sci.* 19:1–12 (1993).
7. Stewart, C. R., Lemieux, P. M., and Zinn, B. T., *Combust. Sci. Technol.* 94:427–446 (1993).
8. Bai, T., Cheng, X. C., Daniel, B. R., Jagoda, J. I., and Zinn, B. T., *Combust. Sci. Technol.* 94:245–258 (1993).
9. Keller, J. O., Barr, P. K., and Gemmen, R. S., *Combust. Flame* 99:29–42 (1994).
10. Barr, P. K. and Keller, J. O., *Combust. Flame* 99:43–52 (1994).
11. Kailasanath, K., Gardner, J., Boris, J., and Oran, E., AIAA Paper No. 87-1065 (1987).
12. Najm, H. N. and Ghoniem, A. F., *Combust. Sci. Technol.* 94:259–278 (1993).
13. Putnam, A. A., *Combustion-Driven Oscillations in Industry*, American Elsevier, New York, 1971.
14. Logan, P., Lee, J. W., Lee, L. M., Karagozian, A. R., and Smith, O. I., *Combust. Flame* 84:93–109 (1991).
15. Smith, O. I., Marchant, R., Willis, J., Lee, L. M., Logan, P., and Karagozian, A. R., *Combust. Sci. Technol.* 74:199–210 (1990).
16. Cadou, C., Logan, P., Karagozian, A., Marchant, R., and Smith, O., *Environ. Sensing Combust. Diagn. SPIE Proc. Ser.* 1434:67–77 (1991).
17. Marchant, R., Hepler, W., Smith, O. I., Willis, J., Cadou, C., Logan, P., and Karagozian, A. R., *Combust. Sci. Technol.* 82:1–12 (1992).
18. Willis, J. W., Lee, L. -M., Karagozian, A. R., and Smith, O. I., *Combust. Sci. Technol.* 94:469–481 (1993).
19. Willis, J. W., Cadou, C., Mitchell, M., Karagozian, A. R., and Smith, O. I., *Combust. Flame* 99:280–287 (1994).
20. Oppelt, T., *J. Air Pollut. Control Assoc.* 37:555 (1987).
21. Zukoski, E. E. and Marble, F. E., *Proceedings of the Gas Dynamics Symposium on Aerothermochemistry*, Northwestern University Press, Evanston, IL, 1956, pp. 205–210.
22. Proctor, C. L., Berger, M. C., Fournier, J. R., and Roychoudhury, S., *Sulfur Hexafluoride as a Tracer for the Verification of Waste Destruction Levels in an Incinerator*, Report ESL-TR-86-47, Air Force Engineering and Services Laboratory, Tyndall AFB, 1987.
23. Gaydon, A. G., *The Spectroscopy of Flames*, 2nd Ed., John Wiley & Sons, New York, 1974, p. 287.
24. Marble, F. E. and Adamson, T. C., *Jet Propulsion* 24:85 (1954).
25. Egolfopoulos, F. N., *Twenty-Fifth Symposium (International) on Combustion*, The Combustion Institute, Pittsburgh, 1994, pp. 1381–1402.
26. Cadou, C. P., Karagozian, A. R., and Smith, O. I., *Bull. Am. Phys. Soc.* 40:2002 (1995).

COMMENTS

Bo Leckner, Chalmers University of Technology, Sweden. You have presented results from a research reactor of small size. Can you scale up your results to a unit of larger size?

Author's Reply. We have pointed out previously [14–19] that the most logical application of the technology described here is for incineration on the site of small waste generators. We actually have investigated reactors of two sizes. The results reported here were obtained in a device four times larger than that used in our original investigations [14–15]. Although the firing rates reported here are all around 30 kW due to the capacity of the laboratory compressed air supply, experiments with the smaller device suggest that firing rates in excess of 80 kW should be achievable. For a typical organic waste with high heating value (e.g., benzene), this corresponds to a feed rate of approximately 2 gal/hr. Thus, in terms of firing rate, a large degree of scale-up may not be necessary for some applications.

The principal difficulty with simply enlarging the device geometrically is that it becomes increasingly difficult to prevent bifurcation of the recirculation cell within the cavity, especially at high waste injection rates. Where difficult-to-destroy, low heating value wastes are concerned (SF_6 being an extreme example), it is highly desirable to maximize the residence time by stabilizing a single, large recirculation cell. At the present scale, this limits the cavity aspect ratio to no more than two and the waste mass flowrate to less than 10% of the core mass flowrate. Here our present two-dimensional device would best be scaled up by increasing the spanwise dimension, e.g. the depth.

In other applications involving readily burnable wastes, adequate mixing between the fuel-lean core flow and the rich recirculation region is more important than residence time distribution. Here the DRE is optimized at aspect ratios above two, where the interfacial area between the two regions is larger, and we find that the capacity at fixed DRE can be increased simply by increasing the aspect ratio.

REFERENCE [3]

UNIVERSITY OF CALIFORNIA
Los Angeles

Acoustic Behavior and Waste Surrogate Destruction
in a
Resonant Combustor

A dissertation submitted in partial satisfaction of the
requirements for the degree Doctor of Philosophy
in Aerospace Engineering

by

Jeffrey William Willis

1994

REFERENCE [4]

EMISSIONS REDUCTION AND PYROLYSIS GAS DESTRUCTION IN AN ACOUSTICALLY DRIVEN DUMP COMBUSTOR

G. Pont, C. P. Cadou, A. R. Karagozian, and O. I. Smith
Department of Mechanical and Aerospace Engineering
University of California
Los Angeles, CA 90095-1597

Corresponding Author:

Professor A. R. Karagozian
Department of Mechanical and Aerospace Engineering
46-147D Engineering IV, UCLA
Los Angeles, CA 90095-1597
U.S.A.
Phone: (310) 825-5653; FAX: (310) 206-4830
E-mail: ark@seas.ucla.edu

1

EMISSIONS REDUCTION AND PYROLYSIS GAS DESTRUCTION IN AN ACOUSTICALLY DRIVEN DUMP COMBUSTOR

G. Pont, C. P. Cadou, A. R. Karagozian, and O. I. Smith
Mechanical and Aerospace Engineering Department
University of California, Los Angeles

1 Abstract

The research described here focuses on the enhancement of hazardous waste and pyrolysis gas surrogate destruction and the reduction in nitric oxide and unburned hydrocarbon emissions in an acoustically resonant dump combustor. While several prior studies have focused on flowfield interrogation and hazardous waste surrogate destruction under conditions of natural acoustic excitation, the present study focuses on the device's behavior under externally forced acoustic excitation. The effect of this external forcing on hazardous waste surrogate destruction in the device was recently found to be significant, yielding destruction rates for the surrogate SF_6 that increased by as much as four orders of magnitude with acoustic forcing at specific resonant modes[1]. The present study also indicates a significant improvement in performance with external forcing at the same acoustic modes as those explored earlier. Emissions of NO are seen to decrease by nearly 60%, unburned hydrocarbons are seen to drop by over two orders of magnitude, and waste and pyrolysis gas surrogate destruction is seen to increase by nearly three orders of magnitude, all with external forcing at a specific acoustic mode of the device. The present observations further support the idea that acoustically resonant conditions can render the dump combustor device extremely efficient as well as highly controllable as a small scale thermal treatment system.

2 Introduction

Dump combustors have been studied extensively because of their ability to burn fuel and contain heat in a relatively compact configuration. Acoustically driven combustion instabilities are known to occur in such devices when pressure oscillations and periodic heat release associated with the combustion are in phase[2–4]. Acoustically excited combustion processes are also generated in pulse combustor systems[5–8]. Local extinction by flame stretch is observed to delay ignition; later relaxation of strain allows thermal ignition to take place in a volumetric fashion, significantly increasing heat and mass transfer rates. Emissions of NO_x are also seen to drop during optimal pulse combustion performance[7, 9]; this is largely attributed to short gas residence times at high temperatures caused by rapid mixing with cooler residual gases.

Over the past few years our research has focused on the development and investigation of a small scale, two-dimensional dump combustor which has been found to be capable of destroying hazardous waste surrogates to a high degree[10–15]. The degree of waste surrogate destruction in the device has been found to correlate with naturally occurring acoustic conditions[11,13,15]. Destruction and removal efficiencies or DREs for the temperature-sensitive waste surrogate sulfur hexafluoride (SF_6), for example, are observed to be as high as 99.999999% ("8 nines") under quiet conditions and occasionally under acoustically resonant conditions[15]. The DRE is defined as

$$DRE \equiv \frac{(\dot{m}_{in} - \dot{m}_{out})100\%}{\dot{m}_{in}} \qquad (1)$$

where $\dot{m}_{in}$ and $\dot{m}_{out}$ are the mass flow rates of the principal organic hazardous constituent entering and leaving the system, respectively. SF_6 destruction of eight nines is four orders of magnitude above the EPA requirement of 99.99% DRE for hazardous waste incinerators[16].

More recent experiments have focused on the ability of the resonant combustor to destroy waste surrogates under externally forced acoustical conditions using a loud speaker[1]. DREs for SF_6 under fixed flow conditions are found to increase by four orders of magnitude or more, to 8 nines DRE, when acoustical forcing is imposed at system characteristic frequencies of 295 and 550-600 Hz. With external forcing at these natural modes of the system, OH^* chemiluminescence images indicate that periodically excited flame structures become more compact and somewhat broadened, likely due to flame deformation by vortex shedding from the entrance to the combustion cavity. In addition, average flame liftoff distances appear to decrease with external acoustical forcing at desirable modes, suggesting that higher recirculation zone temperatures may be associated with on-resonance forcing.

The purpose of the present study is to further quantify and understand the benefits of external acoustical excitation on dump combustor performance for an incinerator/afterburner application. Two additional surrogate species were examined here, methyl chloride (CH_3Cl) and a mixture of ethylene (C_2H_4), benzene (C_6H_6), and nitrogen (N_2), each of which has different destruction characteristics from surrogates previously examined. Nitric oxide (NO) and unburned hydrocarbon (HC) emissions were also measured under resonant and non-resonant operating conditions. In order to understand and further quantify transport processes associated with acoustical excitation, thermocouple measurements were made in the present study to examine the temperature distributions within the flowfield.

3 Experimental Apparatus and Procedure

The two-dimensional dump combustor used in the present experiments is shown schematically in Figure 1, with an expanded view of flow/reaction processes in the combustion cavity. The combustor's basic features have been described previously, and will only be summarized here. The reader is referred to [13,15] for additional details.

In general in these dump combustor experiments, propane (C_3H_8) and air at room temperature were introduced into the plenum/mixing section of the combustor, then were ac-

3

celerated through an inlet section before entering the combustion cavity at the sudden expansion or "dump plane". Premixed flames can be stabilized due to the formation of high temperature recirculation regions downstream of the dump plane[17], but as noted above, vortex shedding coincident with the flames may occur under conditions of natural acoustic excitation[10–15]. The spanwise depth of the inlet, combustion cavity, outlet and exit sections (30.5 cm) was usually sufficient to produce a visually two-dimensional flame over the entire span, although under certain experimental conditions the flow in the cavity became turbulent and the flame/flow structures became three-dimensional. Quartz windows bounded each end of the system in the spanwise direction, allowing appropriate optical access; additional quartz window slits were installed in the side walls to allow the introduction of a sheet of laser light for optical diagnostics[12].

A set of movable ceramic plugs defined the outlet section of this combustor. Waste or pyrolysis gas surrogate was introduced through injectors embedded in these plugs as indicated in Fig. 1. Injection into the recirculation zones allowed waste surrogates to be trapped for relatively long residence times under potentially high temperature and/or relatively oxygen rich conditions so that they could be destroyed more efficiently. For the pyrolysis gas experiments described below, no auxiliary fuel was required in the inlet and only air was injected into the plenum. Water-cooled stainless steel injectors were used in all cases here to introduce gaseous surrogates into the cavity[11, 13]; there were 40 0.3 mm diameter holes in the spanwise direction along each injector. Acoustic data were taken using pressure transducers located in the plenum and inlet.

External acoustical forcing was accomplished in the present experiment using a loudspeaker situated at the bottom of the plenum section of the device. Using a signal generator it was possible to produce a sine wave of varying frequency, then to amplify the signal and pass it to the speaker. This enabled a sweep through a range of input forcing frequencies from 0 to 1000 Hz to be performed, with forcing amplitude variation up to 150 dB, although frequencies below 200 Hz were difficult to attain consistently with the present speaker. Thus it became possible to force the loudspeaker at frequencies corresponding to the natural ("resonant") modes of the device as well as other ("non-resonant") frequencies.

To continue to evaluate the performance of this dump combustor as a potential incinerator or pyrolysis gas afterburner, the gas phase surrogates methyl chloride and a mixture of ethylene, benzene, and nitrogen (EBN) were used in the present study. CH_3Cl is a gas which has been ranked as one of the thirty RCRA Appendix VIII compounds which are most difficult to destroy[18]. The difficulty in incinerating CH_3Cl results from the fact that chlorine scavenges hydrogen in the flame, thus reducing the radical pool and acting as a flame inhibitor. Hence CH_3Cl is a surrogate whose destruction is sensitive to the presence of radical species formed at high temperatures, so that hot recirculation zones created by premixed flames at the dump plane are required for adequate destruction. The EBN mixture has been identified by the NAWC China Lake as a suitable surrogate for pyrolysis off gases from a plasma arc pyrolysis system. The proportions of ethylene:benzene:nitrogen used in the mixture were 12:1:20 by volume. In contrast to CH_3Cl, the EBN mixture required the presence of high concentrations of oxygen for complete burning; this mixture burned as a

diffusion flame in the recirculation zones, again, requiring no auxiliary fuel in the core flow at all.

Detection of waste destruction in the present device was made using a gas chromatograph equipped with an electron capture detector to measure CH_3Cl destruction (sensitive to 100 ppb), yielding a maximum detectable DRE of approximately 5.6 nines. A flame ionization detector was used to detect ethylene (to 100 ppb or 7 nines DRE) and benzene (to 0.1 ppb or 5.5 nines DRE). In addition to DREs, unburned hydrocarbons were measured for the EBN mixture.

A chemiluminescence $NO - NO_x$ analyzer (Thermo Environmental 10AR Chemiluminescence $NO - NO_x$ Gas Analyzer) was used to measure the NO emissions from the combustor. The analyzer measured NO by reacting ozone O_3 with the sampled gases and measuring the resulting chemiluminescence. After being generated in the analyzer, O_3 was mixed to react with the sampled gases in a reaction chamber. The resulting chemiluminescence signal resulted from the decay of electronically excited NO_2 molecules produced in the reaction,

$$NO + O_3 \rightarrow NO_2 + O_2 \qquad (2)$$
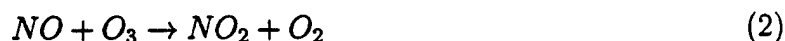
and was monitored through a filter by a high sensitivity photomultiplier. The output of the photomultiplier was linearly proportional to the NO concentration. For this reason, a one point calibration with a sample of known concentration suffices as a calibration. For the present experiments, a gas cylinder of 19.2 ppm NO in N_2 from Matheson Gas Products was used as the calibrating gas.

4   Results and Discussion

Results for the destruction of the two surrogates examined here, methyl chloride and the ethylene/benzene/nitrogen mixture, are quantified in terms of the DRE. CH_3Cl DREs are shown in Figure 2 as a function of the equivalence ratio in the inlet core flow, with overall equivalence ratios (based on both the C_3H_8 in the inlet flow and the CH_3Cl surrogate) also shown. As one would expect, with increasing equivalence ratio (accomplished here by increasing the propane fuel flow rate) in the absence of external acoustic forcing, the primary reaction at the dump plane produced a hotter reaction, closer to stoichiometric, resulting in an increase in the rate of destruction of methyl chloride in the recirculation zones. Interestingly, at a relatively low overall equivalence ratio which nominally produced low DREs without forcing ($\phi = 0.75$), acoustic excitation via the loudspeaker at the 295 Hz mode showed a dramatic improvement in DREs, by nearly three orders of magnitude, to 5.6 nines. Since this was the detection limit of the GC for CH_3Cl, it is quite possible that acoustic excitation produced even higher destruction under these conditions. These observations suggested that the effect of acoustical excitation on CH_3Cl destruction was to cause the device to behave as if it were actually operating as if in a *richer* (closer to stoichiometric) combustion environment. Based on the destruction mechanism for CH_3Cl, Figure 2 suggests that external acoustical excitation at this natural mode enhanced the

5

transfer of heat and radicals from the flames to the recirculation zones, which in turn became better able to destroy CH_3Cl. Acoustical forcing thus had the benefit of requiring less auxiliary fuel for very high surrogate destruction, as similarly seen for SF_6 destruction in prior experiments[1].

Destruction and removal efficiencies for the EBN mixture are shown in Figures 3ab. As noted previously, this mixture did not require any auxiliary propane fuel in the inlet core flow. Its combustion was dependent on the transport of oxygen from the core to the region of surrogate injection, in this case, to the recirculation zones. In all cases, diffusion flame structures were observed in the recirculation zones. Here again it was found that acoustic excitation at the 295 Hz natural mode produced much higher DREs than without excitation for both benzene and ethylene. With the air flow rate fixed in the inlet, increases in the surrogate injection rate (to increase ϕ) without external forcing produced somewhat degraded destruction (Fig. 3a), indicating that higher rates of injection of the fuel source required a greater degree of entrainment of oxidizer to the recirculation zones for more complete combustion. Yet under the same flow conditions but with external acoustical forcing, substantial increases in DREs for both benzene and ethylene were seen; in fact, the percentage increase in DREs with acoustic forcing was generally higher for the higher equivalence ratios. This suggested that not only was the transport of oxygen from the core to the recirculation zones increased with acoustic forcing, but that entrainment of oxidizer into the jet of surrogate within these zones was enhanced as well. This improvement in DREs was observed until a critical equivalence ratio was reached ($\phi \approx 0.45$), above which the DREs dropped, eventually to unforced levels. Clearly, this critical equivalence ratio reflected a need for entrainment of oxygen into the recirculation zones and into the surrogate jet that even acoustical forcing could not accomplish.

With the surrogate injection rate fixed at the maximum shown in Figure 3a, air flow rate in the core was then increased to verify this conjecture. As shown in Figure 3b, even without acoustical excitation, an increased inlet velocity increased the oxygen available for combustion in the recirculation zones, and surrogate DREs increased. With external forcing at 295 Hz, the improvements in destruction rates were dramatic, bringing both benzene and ethylene DREs to their detection limits. Augmentation of transport of oxygen to the recirculation zones and into the surrogate jet in particular appeared to result from the acoustic forcing. Hence from this set of results it became apparent that the effect of acoustical forcing for EBN destruction was to cause the device to behave effectively as if combustion were occurring under *leaner* conditions overall.

The effect of acoustical forcing on jet entrainment within the recirculation zones was observed visually as well. As indicated in the photograph in Figure 4a, without acoustical forcing the sooting diffusion flames were long, circulating within the recirculation zones and filling the entire combustion cavity. Under the same flow conditions but with acoustical forcing at the 295 Hz natural mode (Figure 4b), the diffusion flame was dramatically shortened, indicating substantial augmentation of transport of oxygen to the recirculation zones and in turn into the vicinity of the "waste" jet, where the reaction was completed and the flame ended in a much shorter distance. There was a clear visual augmentation of transport of

gases from the inlet core to the recirculation zones during on-resonance acoustic excitation.

Emissions of unburned hydrocarbons during combustion of the EBN mixture further confirmed this effect of external forcing. As shown in Figures 5ab, under conditions corresponding to those in Figures 3ab, respectively, HCs were substantially reduced with acoustic excitation at 295 Hz, bringing levels nearly to 0 ppm. Again, this forcing appeared to have the effect of causing the combustor to behave as if operating under *leaner* conditions.

NO emissions from the combustor, with a propane-air mixture in the inlet core and no surrogate injection into the recirculation zones, further demonstrated the desirability of external acoustic driving. Figure 6a shows a plot of NO emissions from the combustor (corrected to 3% oxygen) as a function of forcing frequency, for flow conditions given in the caption. These conditions were the same baseline conditions (equivalence ratio, inlet velocity, cavity length) that produced extremely high DREs for SF_6 with acoustic forcing at natural modes[1]. Remarkably, at natural frequencies at which SF_6 (as well as CH_3Cl) DREs were very high, nitric oxide production actually dropped compared to the unforced condition, in some cases by more than 50%, below 20 ppm. Even with external excitation at non-natural frequencies (e.g., 400 Hz), NO emissions were reduced compared with the unforced (0 Hz) case. Figure 6b shows NO emissions from the combustor as a function of equivalence ratio, for unforced conditions and forced conditions at 295 Hz. Excitation at this frequency appeared to reduce NO emissions significantly, by nearly 60% in some cases, especially at moderate equivalence ratios ($0.80 \leq \phi \leq 0.85$). Even at stoichiometric conditions the external forcing reduced NO by 40%. These results appear to be consistent with the observations of Keller, *et al.*[7] who suggest that NO reduction during acoustical excitation in general occurs due to shorter gas residence times at higher temperatures. That the present NO emissions drop even further, to a significant degree, at natural frequencies could indicate enhanced residual gas mixing as well at these frequencies.

The results described above clearly indicate that very efficient combustor operation is achieved during external acoustic excitation at a natural frequency of the system. These extremely high destruction rates and low unburned hydrocarbon and NO emissions suggest that the transport of mass and energy between core/reaction zones and recirculation zones may be strongly enhanced during external forcing. Recent optical diagnostics by our group, described in [1, 19, 20], as well as pointwise temperature measurements within the device, appear to confirm this enhancement of transport.

Figure 7 shows transverse temperature distributions under hot combustion conditions (with propane and air in the inlet core) as measured by a Type B thermocouple introduced into the cavity at a location 2 cm above the dump plane. The frequency response of the thermocouple in its ceramic jacket was considerably slower than the unsteady oscillations in the present flowfield (i.e., slower than 300 Hz), hence only time-averaged temperatures were obtained from the thermocouple. The thermocouple was introduced from the right, and essentially estimated average temperatures in the recirculation zone, flame, and jet core regions for different conditions of forced and unforced operation. Interestingly, the temperature profiles for unforced and 430 Hz externally forced (non-natural mode) cases were nearly identical. In contrast, for 295 Hz excitation (a natural mode in the larger

combustor), the temperatures in the recirculation zones, flames, and inner core regions all increased. Actual increases in recirculation zone temperatures during the 295 Hz excitation were of the order 30-50 degrees. According to a simple pyrolysis model[20], this temperature rise could be sufficient to explain the increase in destruction rates experienced by SF_6[1] during the 295 Hz excitation. The increased temperatures quantified in the recirculation zones are also consistent with prior OH^* chemiluminescence images in this device[1] which suggested that average flame liftoff distances decreased during the 295 Hz excitation as well as during excitation at other resonant modes.

That the average temperature in the flame zone increased with the 295 Hz excitation was not necessarily inconsistent with lowered NO production at this condition. Recent phase-locked, planar laser-induced fluorescence (PLIF) imaging of temperature in the combustor[20] indicated that temperature in the central (core) region of the combustor oscillated significantly, by as much as 700 degrees during one acoustic cycle at the 295 Hz excitation. Hence the flame could possibly be experiencing high temperatures for relatively short periods of time, too short for significant thermal NO production to occur.

5 Conclusions

The present studies continue the evaluation of the acoustically driven dump combustor as a potential hazardous waste incinerator/afterburner, demonstrating remarkable overall performance with external forcing at specific resonant modes. Destruction rates for thermodynamically dissimilar waste/off gas surrogates (SF_6, CH_3Cl, and a ethylene/benzene/nitrogen mixture) were found to reach detection limits (of 5.5 to 8 nines) with external acoustic forcing at desirable natural frequencies. Simultaneously, NO emissions as well as unburned hydrocarbons were seen to diminish significantly under these same acoustic conditions. These results suggest the tremendous potential that this device has as a thermal destruction system, in addition to its suitability for active control of combustion performance via external acoustic forcing.

6 Acknowledgements

7 References

References

[1] Pont, G., Willis, J. W., Karagozian, A. R., and Smith, O. I., *26th Symp. (Intl.) on*

Comb. 2463-2470 (1996).

[2] Rayleigh, Lord, *The Theory of Sound, Vol II*, Dover Publications, 227 (1945).

[3] Putnam, A. A., *Combustion-Driven Oscillations in Industry*, American Elsevier, New York (1971).

[4] McManus, K. R., Poinsot, T., and Candel, S. M., *Prog. Energy Combust. Sci.* 19: 1-12 (1993).

[5] Stewart, C. R., Lemieux, P. M., and Zinn, B. T., *Combust. Sci. Tech.* 94: 427-446 (1993).

[6] Bai, T., Cheng, X. C., Daniel, B. R., Jagoda, J. I., and Zinn, B. T., *Combust. Sci. Tech.* 94: 245-258 (1993).

[7] Keller, J. O., Barr, P. K., and Gemmen, R. S., *Combust. Flame* 99: 29-42 (1994).

[8] Barr, P. K. and Keller, J. O., *Combust. Flame* 99: 43-52 (1994).

[9] Putnam, A. A., *Prog. Energy Comb. Sci.* 12: 1 (1986).

[10] Logan, P., Lee, J. W., Lee, L. M., Karagozian, A. R. and Smith, O. I., *Combust. Flame* 84:93-109 (1991).

[11] Smith, O. I., Marchant, R., Willis, J., Lee, L. M., Logan, P. and Karagozian, A. R., *Combust. Sci. Tech.* 74:199-210 (1990).

[12] Cadou, C., Logan, P., Karagozian, A., Marchant, R., and Smith, O., *Environ. Sensing and Comb. Diagnostics, SPIE Proc. Series* 1434:67-77 (1991).

[13] Marchant, R., Hepler, W., Smith, O. I., Willis, J., Cadou, C., Logan, P. and Karagozian, A. R., *Combust. Sci. Tech.* 82:1-12 (1992).

[14] Willis, J. W., Lee, L.-M., Karagozian, A. R. and Smith, O. I., *Combust. Sci. Tech.* 94:469-481 (1993).

[15] Willis, J. W., Cadou, C., Mitchell, M., Karagozian, A. R., and Smith, O. I., *Combust. Flame* 99:280-287 (1994).

[16] Oppelt, T., *J. Air Pollut. Control Assoc.* 37:558 (1987).

[17] Zukoski, E. E. and Marble, F. E., *Proc. Gas Dynamics Symp. on Aerothermochemistry*, Northwestern University Press, 205-210, (1956).

[18] Taylor, P. H., Dellinger, B., and Lee, C. C., *Environ. Sci. Technol.* 24(3):316-328 (1990).

[19] Kang, Yungmo, "Dump Combustor Flowfield Investigation using Particle Image Velocimetry", Ph.D. thesis, University of California, Los Angeles (1997).

[20] Cadou, C. P., "Two-Dimensional, Time Resolved Temperature Measurements in a Resonant Incinerator using Planar Laser-Induced Fluorescence", Ph.D. thesis, University of California, Los Angeles (1996).
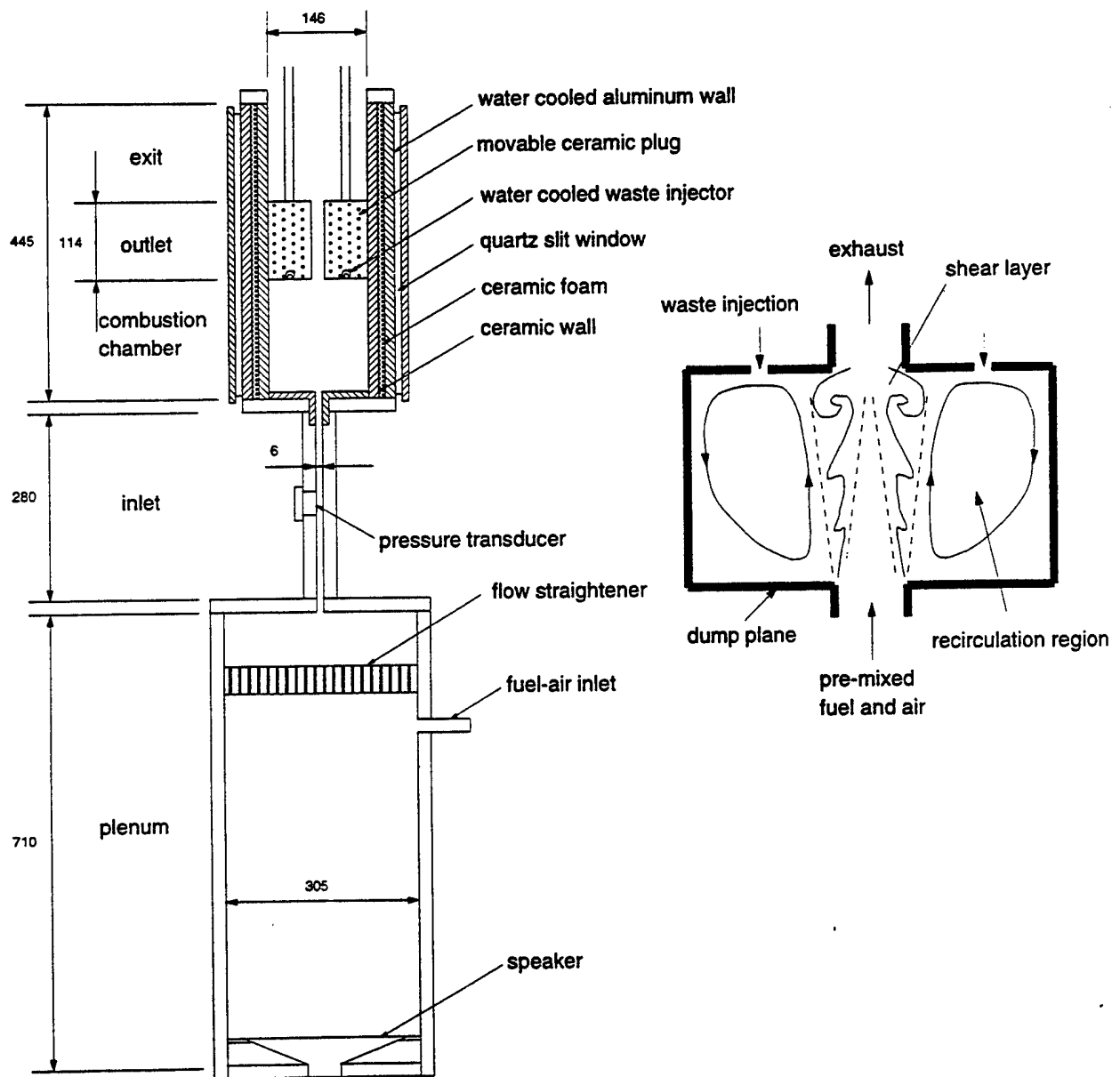
Figure 1. Schematic of the dump combustor, including features of the combustion chamber cavity. Dimensions are given in units of mm.
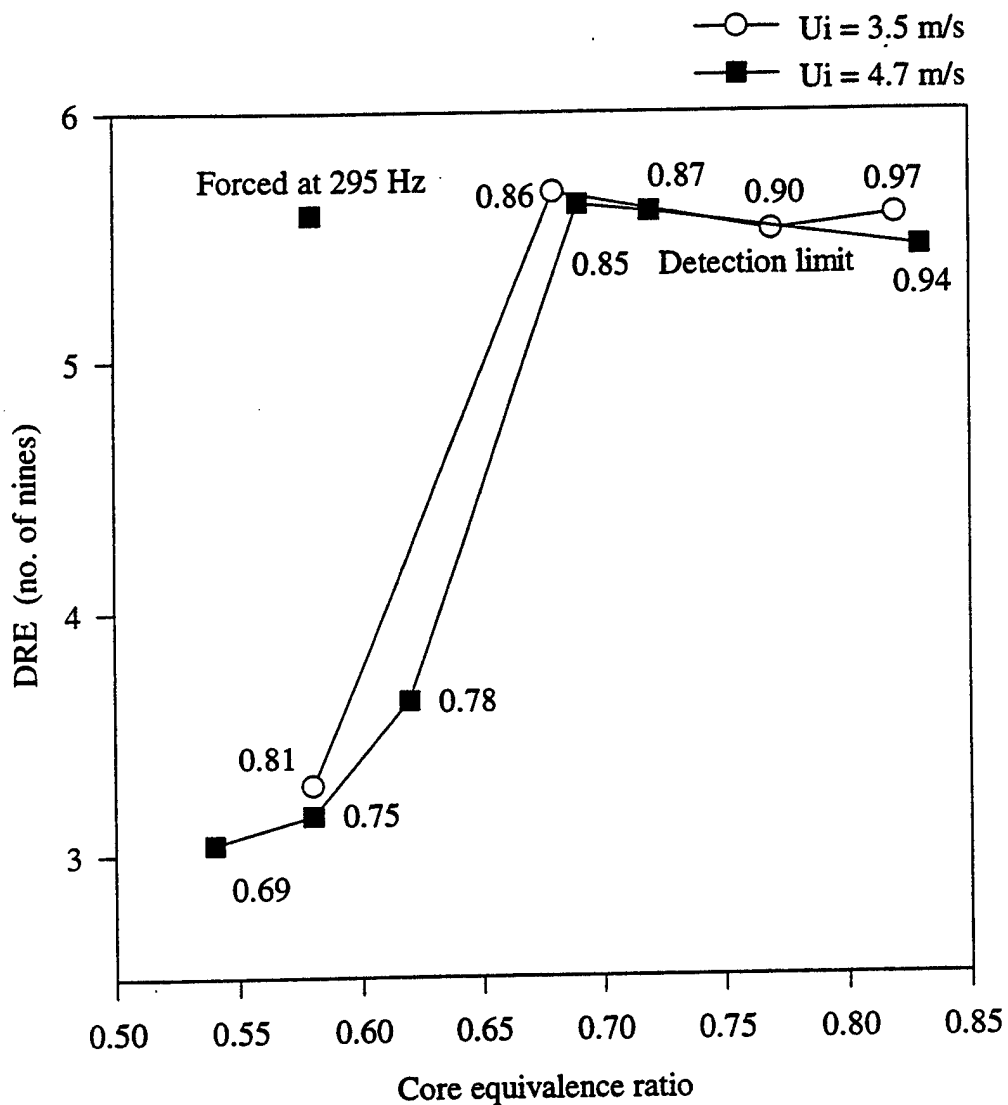
Figure 2. Destruction and Removal Efficiencies (DREs) of CH_3Cl in the dump combustor during externally forced acoustical excitation as a function of core (inlet) equivalence ratio for two different inlet velocities U_i, and cavity length 10.2 cm. All conditions shown are for the case without external acoustical forcing except for that labeled "forced at 295 Hz"; overall equivalence ratios are shown next to each data point.
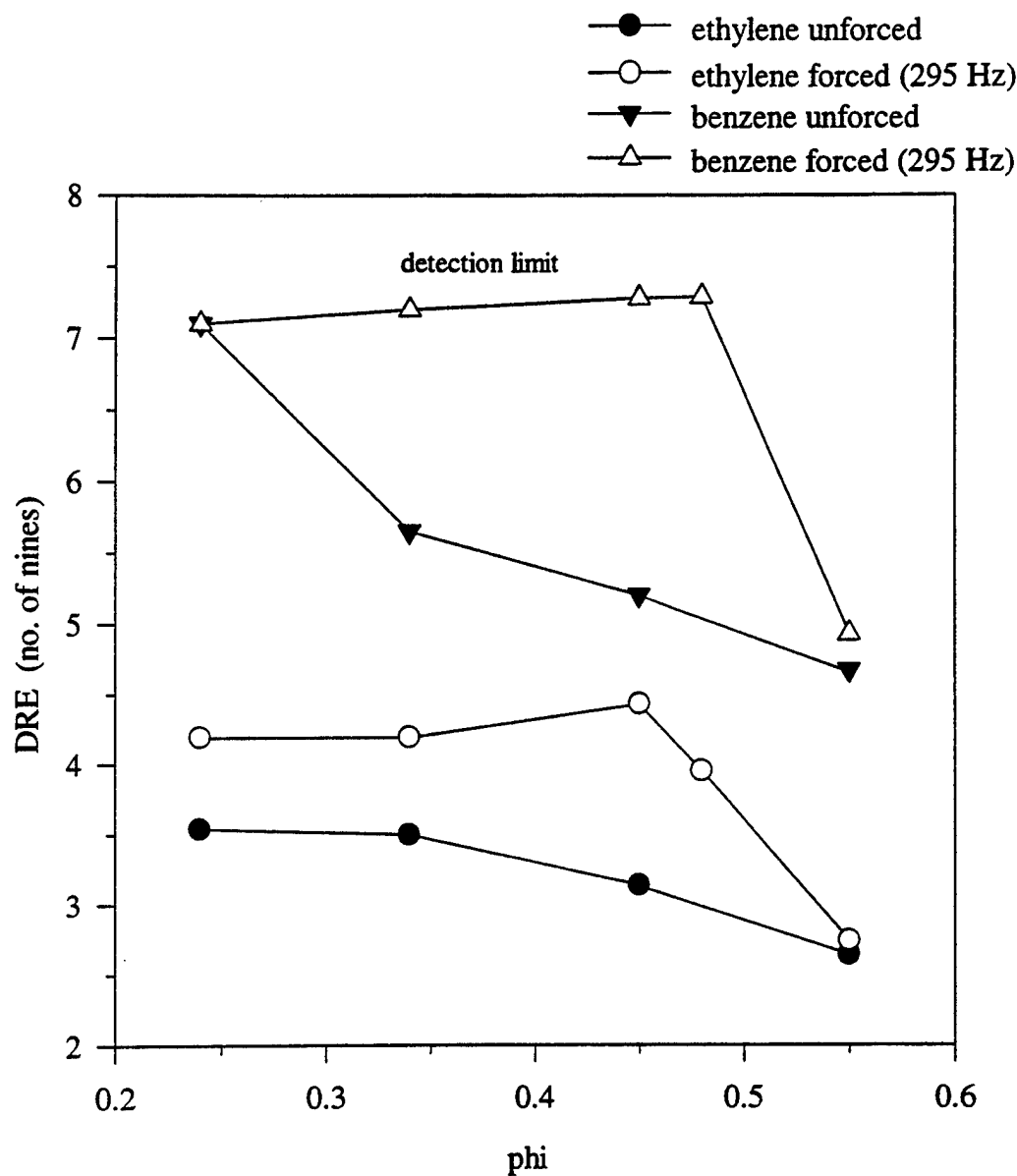
Figure 3a. Destruction and Removal Efficiencies (DREs) for the ethylene/benzene/nitrogen (EBN) mixture during unforced and 295 Hz externally forced acoustical excitation as a function of equivalence ratio based on EBN as the sole fuel source. DREs for both ethylene and benzene are shown. Only air is injected in the core flow, so that equivalence ratio is increased by increasing the EBN injection rate. The cavity length is 10.2 cm.
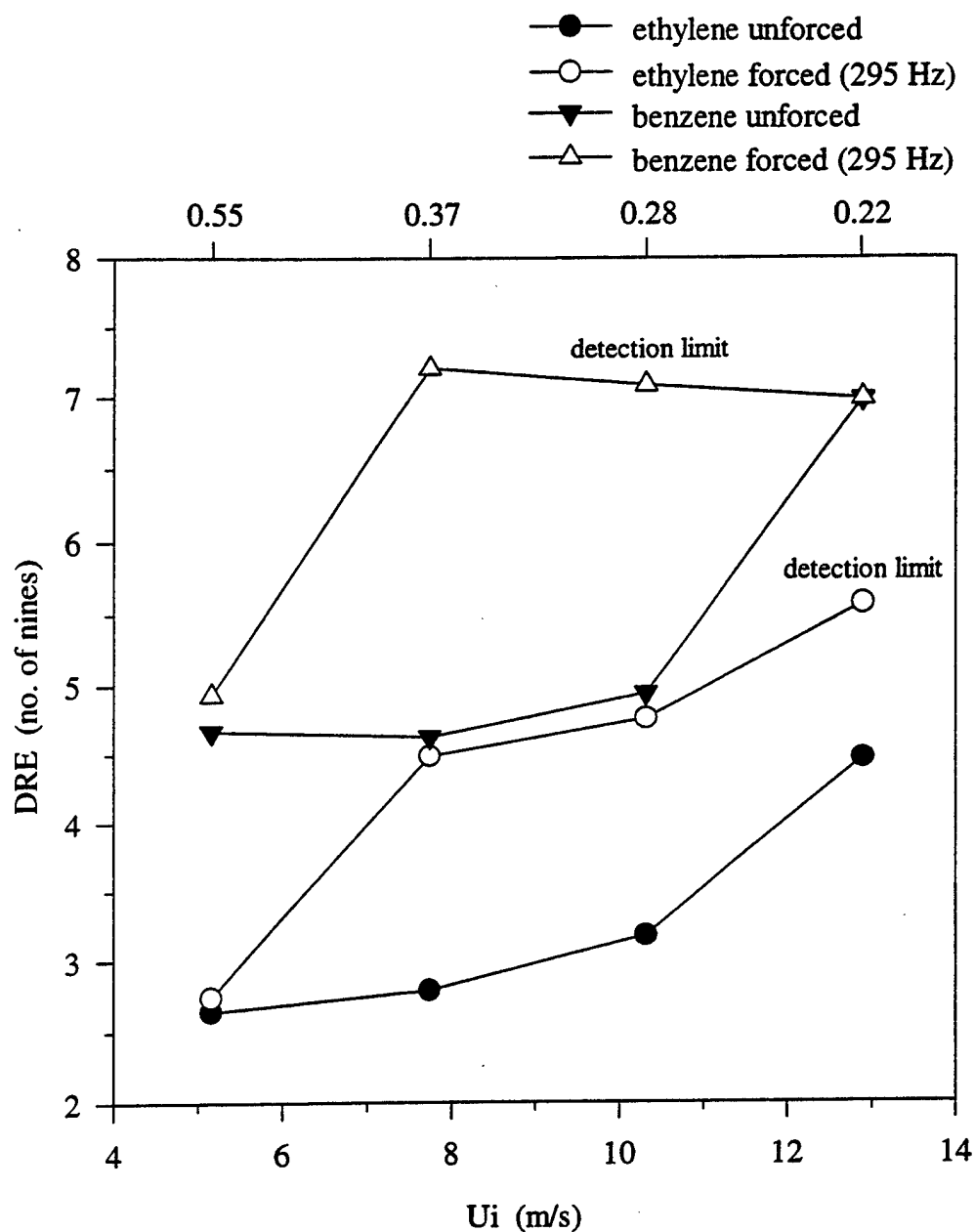
13

Figure 3b. Destruction and Removal Efficiencies (DREs) for the ethylene/benzene/nitrogen (EBN) mixture during unforced and 295 Hz externally forced acoustical excitation as a function of air flow rate in the core. DREs for both ethylene and benzene are shown. The EBN injection rate is fixed at that yielding the maximum equivalence ratio in Figure 3a. The cavity length is 10.2 cm. The scale at the top of the figure provides the corresponding values of equivalence ratio.
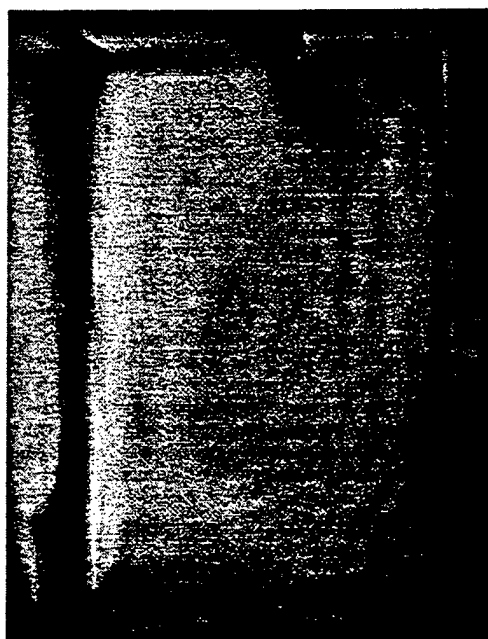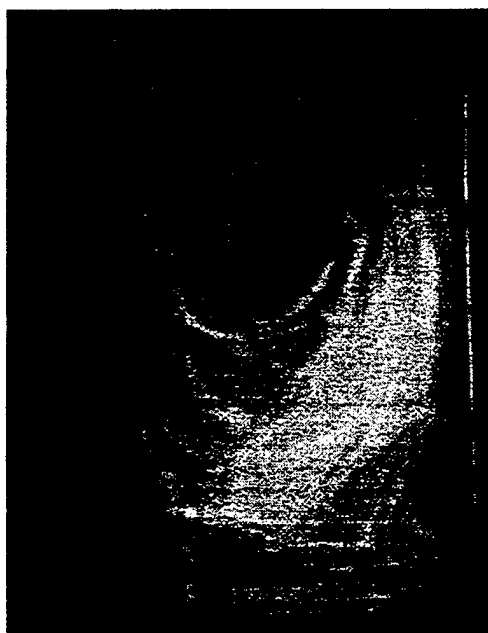
Figure 4a)

Figure 4b)

Figure 4. Photograph of sooting flame structure in the right half of the combustion cavity during destruction of the EBN mixture, for overall equivalence ratio 0.23 and cavity length 10.2 cm. Photos shown are for cases: a) in the absence of external acoustical forcing, and b) with external forcing at 295 Hz.
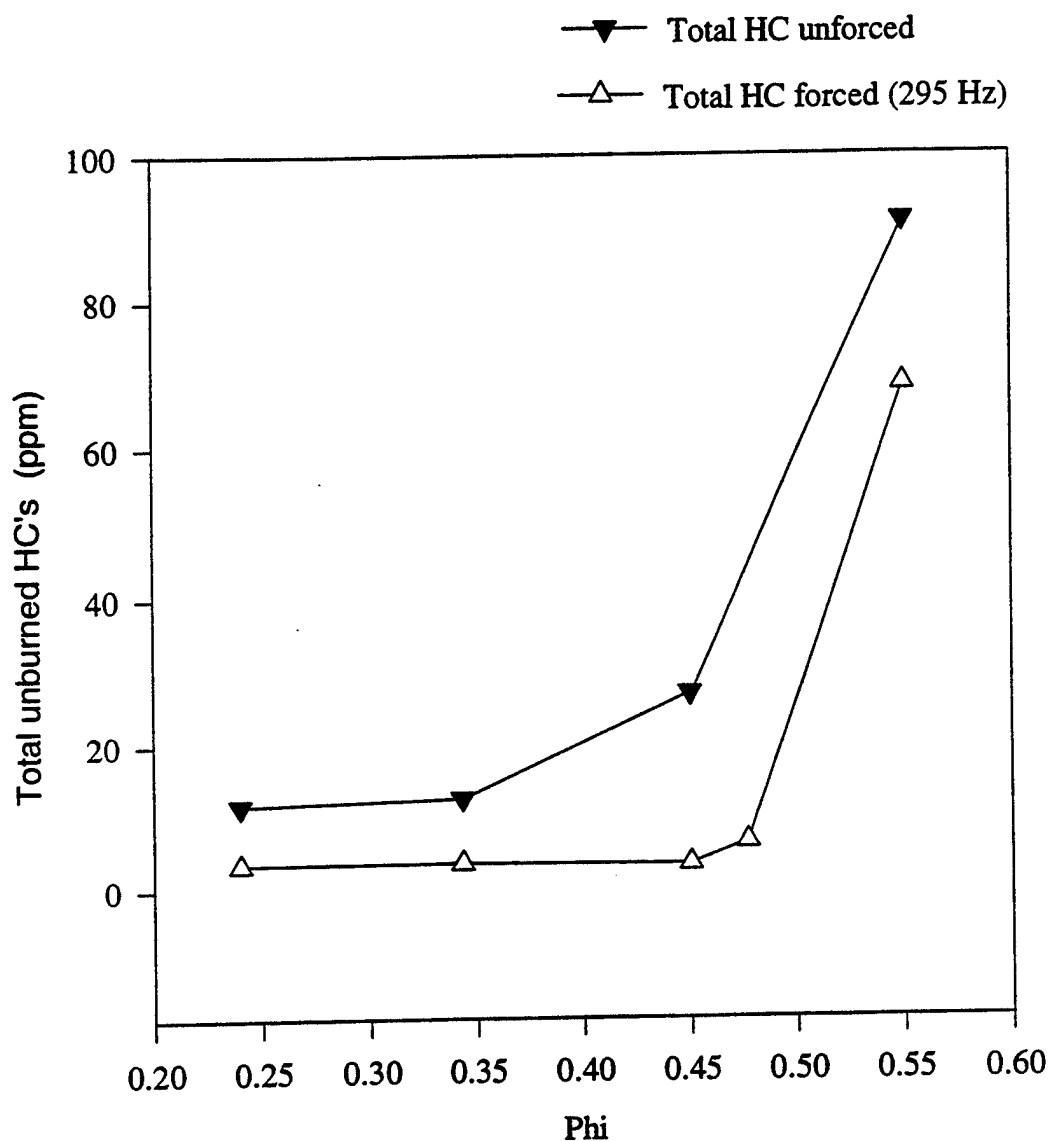
15

Figure 5a. Unburned hydrocarbon emissions from the ethylene/benzene/nitrogen (EBN) injection case during unforced and 295 Hz externally forced acoustical excitation as a function of equivalence ratio based on EBN as the sole fuel source. Only air is injected in the core flow, so that equivalence ratio is increased by increasing the EBN injection rate. The cavity length is 10.2 cm.
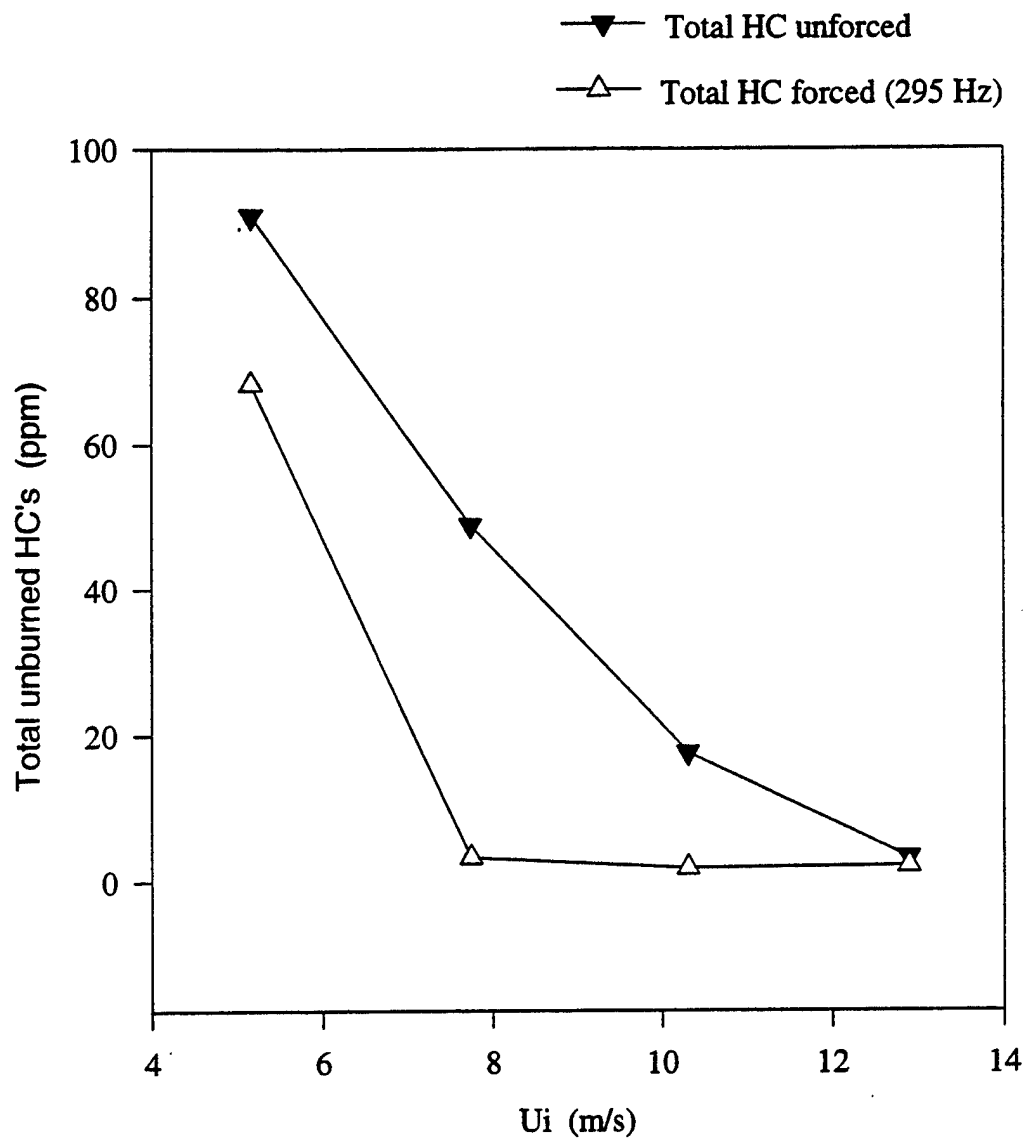
Figure 5b. Unburned hydrocarbon emissions from the ethylene/benzene/nitrogen (EBN) injection case during unforced and 295 Hz externally forced acoustical excitation as a function of air flow rate in the core. The EBN injection rate is fixed at that yielding the maximum equivalence ratio in Figure 5a. The cavity length is 10.2 cm.
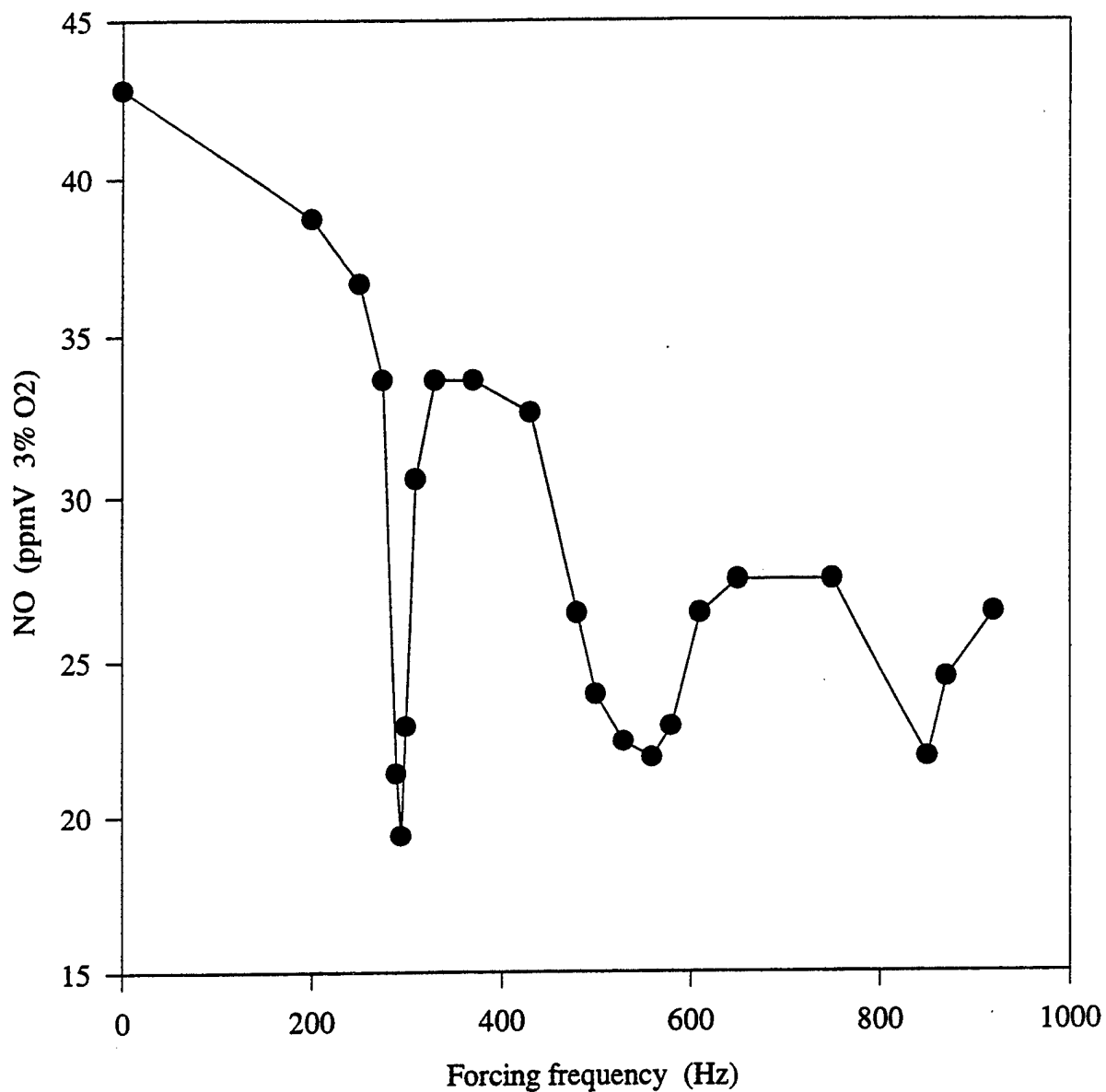
Figure 6a. Nitric oxide emissions in the dump combustor during externally forced acoustical excitation for the case where equivalence ratio $\phi = 0.83$, inlet velocity $U_i = 4.7$ m/sec, and cavity length is 10.2 cm. No surrogate is injected into the recirculation zones here. Zero forcing frequency refers to the unforced case.
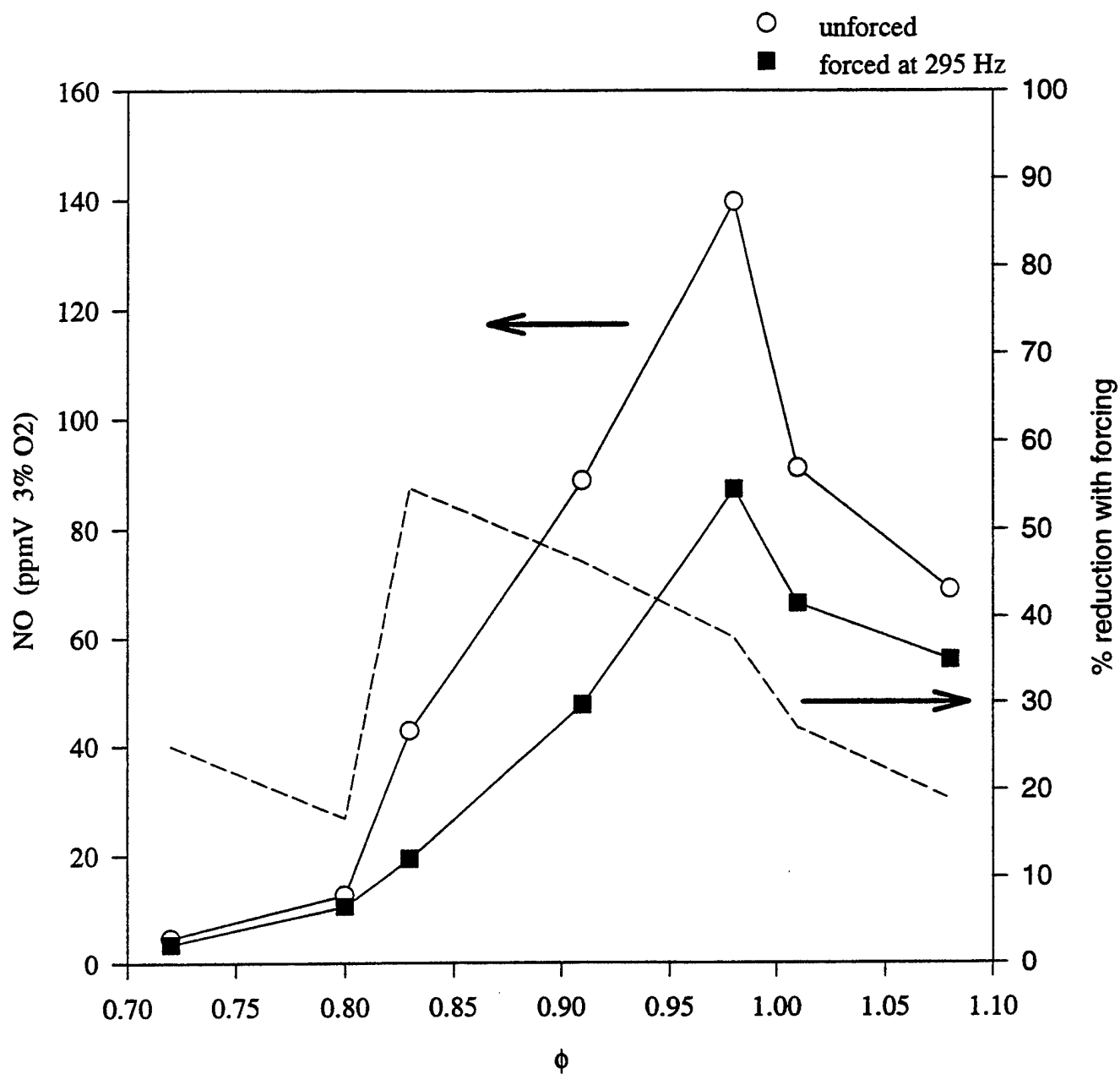
Figure 6b. Nitric oxide emissions as a function of equivalence ratio in the dump combustor during externally forced acoustical excitation at 295 Hz for the case where inlet velocity U_i = 4.7 m/sec and cavity length is 10.2 cm. No surrogate is injected into the recirculation zones here.

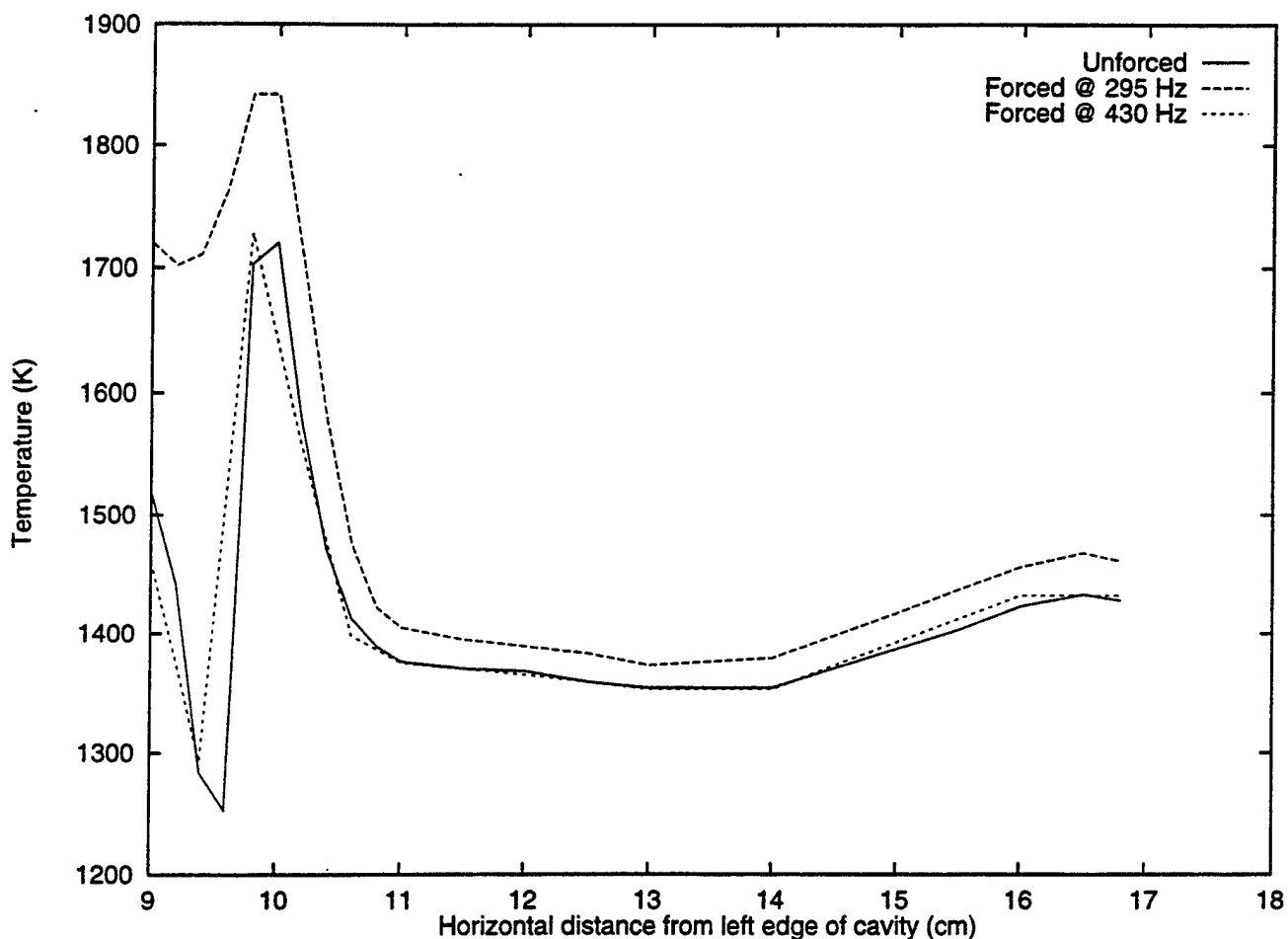Figure 7. Averaged temperatures measured by a Type B thermocouple for a horizontal slice taken through the combustor cavity at a height of 2 cm above the dump plane. At the dump plane, the inlet is situated approximately between 9.4 and 10.0 cm, and the right combustor wall is situated at 17 cm. Here the inlet velocity $U_i = 5.6$ m/sec, equivalence ratio $\phi = 0.83$, and cavity length $= 10.2$ cm.

REFERENCE [5]

UNIVERSITY OF CALIFORNIA

Los Angeles

Effects of External Acoustic Excitation

on Waste Surrogate Destruction
in a Resonant Combustor

A thesis submitted in partial satisfaction

of the requirements for the degree

Master of Science in Chemical Engineering

by

Guillermo Pont

1996

REFERENCE [6]

UNIVERSITY OF CALIFORNIA

Los Angeles

Two-Dimensional, Time Resolved Temperature Measurements in a Resonant Incinerator using Planar Laser-Induced Fluorescence

A dissertation submitted in partial satisfaction

of the requirements for the degree

Doctor of Philosophy in Mechanical Engineering

by

Christopher P. Cadou

1996

REFERENCE [7]

UNIVERSITY OF CALIFORNIA

Los Angeles

Dump Combustor Flowfield Investigation using Particle Image Velocimetry

A dissertation submitted in partial satisfaction

of the requirements for the degree

Doctor of Philosophy in Mechanical Engineering

by

Yungmo Kang

1997

REFERENCE [9]

Numerical Simulation of Steady-State Dump Combustor Operation with Auxiliary Fuel Injection

WILLIAM HEPLER and OWEN SMITH   *Department of Chemical Engineering, University of California, Los Angeles*

ABSTRACT—Solutions of the steady, two-dimensional Navier-Stokes, thermal energy and species conservation equations have been computed for a low-speed dump combustor geometry with a downstream constriction. The equations are solved in the conservative finite-difference form on a nonuniform rectilinear grid of sufficient resolution to accurately capture the momentum/thermal boundary layers and. with somewhat lower accuracy, the flame structure. The chemistry is represented by a finite-rate reduced methane-air mechanism involving seven species. The computed flame shapes for different cavity lengths and mixture equivalence ratios are compared to those determined experimentally by OH(A) chemiluminescence. Except for the leanest mixture studied, the computed and experimental flame lengths agree to within a few percent. In general. the computed flame lengths depend more strongly on equivalence ratio than does the experimental. The dependence of computed flame shape on cavity length generally agrees with that determined from experiment. Computations indicate that the structure of the recirculation zone is similar to that of a nonreacting flow for short cavities, but is qualitatively different for longer cavities. These differences are a consequence of the heat release in the flame front. Simulations with additional fuel (representing a hydrocarbon waste) injected into the recirculation zone show two stages of heat release. The first is associated with premixed burning of the primary fuel-air mixture. while the second is associated with a diffusion flame at the interface between the oxygen-starved recirculation zone and the comparatively oxygen-rich combustion products from the primary flame. These simulations indicate that excess oxygen from a lean primary flame can be effectively utilized for waste destruction. even for very lean core flames resulting from oxygen enrichment. Oxygen utilization is seen to be somewhat better for longer cavities.

Key Words: Dump combustor, incineration. injection model

INTRODUCTION

Over the past several years we have conducted experimental and numerical investigations of the operating characteristics of the bench-scale dump combustor (Logan *et al.*, 1991) shown schematically in Figure 1. The device has planar symmetry allowing convenient optical access to the combustion cavity for experimental characterization of the flame front and flow-field structures (Cadou *et al.*, 1991). A premixed methane-air mixture is admitted to the plenum chamber where it passes through a flow-straightener. into the inlet section, then into the combustion cavity. Hot combustion products in the recirculation zone of the combustion cavity stabilize a laminar flame that attaches to the inlet at the dump plane. Very high volumetric heat release rates may be obtained. The combustor can be operated so that flame front instabilities excite one of several acoustic modes of the system, leading to resonances (Logan *et al.*, 1991). Alternatively. it can be operated in such a manner as to suppress flame front instabilities. leading to steady behavior (hereafter referred to as the "quiet mode"). The actual operating mode

TO EXHAUST

CERAMIC LINER
WATER-COOLED STEEL PLATE
ALUMINUM HOUSING

MOVABLE
CERAMIC
PLUG

EXIT

COMBUSTOR

RECTANG-
ULAR
CROSS-
SECTION

INLET
SECTION

CIRCULAR
CROSS-
SECTION

PLENUM
CHAMBER

MOVABLE
FLAME-
ARRESTOR

PERFORATED
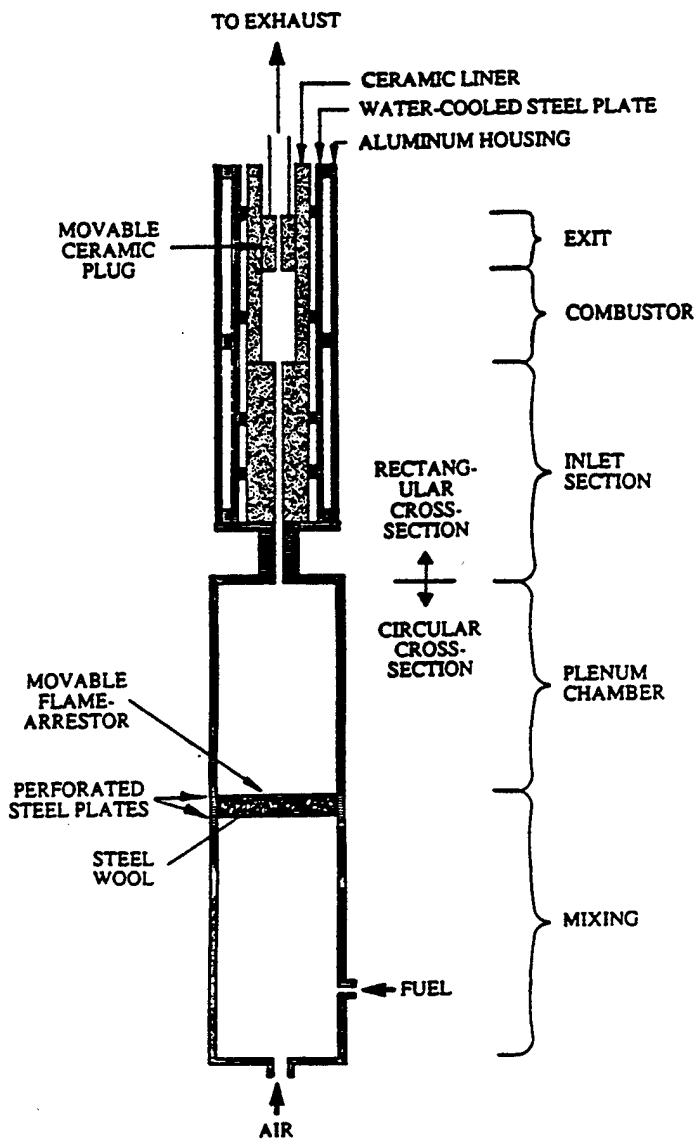STEEL PLATES

STEEL
WOOL

MIXING

FUEL

AIR

FIGURE 1   Schematic of the dump-combustor.

depends on the equivalence ratio, inlet velocity and the combustion cavity aspect ratio (the ratio of cavity length to step width).

We are interested in utilizing the large hot recirculation zones in the dump cavity as oxidizing chemical reactors for the destruction of hazardous wastes. Hence, we are concerned with the residence time of wastes and rate of entrainment of oxidizing species within the recirculation zone, and with the effect on both of the location and rate of

waste injection. Past tests have shown quiet mode operation to be highly effective in destroying surrogate wastes (Smith *et al.*, 1990), apparently due to the stability of the recirculation zone.

In this paper we report the construction of a steady two-dimensional model of the combustor with realistic chemical kinetics, and its use in characterizing the structure of the flame front and recirculation zone under conditions known to lead to quiet mode operation. Successful prediction of the flame front location, indicating that heat release and transport processes are correctly accounted for, is of great importance in understanding the complex dynamic behavior this device can exhibit. We are currently in the process of extending the model to simulate the unsteady operation of this device, including the acoustic interactions affecting the flow-field and chemistry.

EXPERIMENTAL MEASUREMENTS

The location of the flame front can be identified experimentally using planar imaging of OH chemiluminescence. The image results from the radiative decay of electronically excited radicals (OH*), thought (Gaydon, 1974) to be produced by the reaction between CH and O_2

$$CH + O_2 \rightarrow CO + OH^*$$
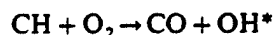
In premixed hydrocarbon flames, the peak in the product of the CH and O_2 concentrations is nearly coincident with the peak in the heat release rate.

For the OH chemiluminescence images, light is collected at right angle to the plane of symmetry, passed through a bandpass filter centered around 312 nm, and imaged onto the S20 photocathode of an image intensifier coupled to a CCD camera. The bandpass filter is used in an attempt to isolate fluorescence from the $X^2\Pi \leftarrow A^2\Sigma(0,0)$ transition of OH. Individual images were acquired with 50 µs integration times, which is short enough to show flame instabilities, if present. Very little variation in flame position or intensity was noted, indicating steady operation.

Four premixed methane–air flames were examined in this manner, each at two cavity aspect ratios. In each case the mean inlet velocity at the dump plane was 2.7 m/s. Equivalence ratios of 0.7, 0.8, 0.9 and 1.0 were examined.

NUMERICAL MODEL

The literature has numerous two-dimensional transport calculations, but most utilize either one-step global reaction expressions or the flame sheet approximation. Detailed chemical kinetic calculations have been largely limited to one-dimensional premixed or diffusion-counterflow flames. Problems cast in a streamfunction boundary layer formulation are somewhat more difficult, but are only applicable when the streamwise diffusion term is negligible or when the flow does not recirculate.

Most of the previous fully two-dimensional calculations of deflagrations with complex chemical kinetics are for unconfined flames, or in geometries which lead to relatively simple flow-fields (Smooke *et al.*, 1989, 1990; Fukutani *et al.*, 1990; Patnaik

and Kailasanath, 1990; Patnaik *et al.*, 1988). The calculation of Burke–Schumann methane–air diffusion flames by Smooke *et al.* (1989,1990) provides an excellent example of the application of the streamfunction-vorticity approach. Both confined and unconfined simulations were performed with a 15 species, 42 reaction mechanism. Recirculation was observed under certain conditions. Fukutani *et al.* (1990) solved the two-dimensional transport equations with a full H_2–O_2 chemical mechanism for the Burke–Schumann problem, but in the primitive variable formulation. These results compare well with experiment. Patnaik and Kailasanath (1988,1990) have used unsteady, two-dimensional simulations with complex chemistry to address the stability of unconfined premixed laminar H_2–O_2 flames.

Although our device can exhibit very complex fluid dynamic behavior, often with significant flame strain, the pressure oscillations are on an acoustic scale of the order of $100\,dynes/cm^2$, or about $114\,dB$. The operation of our dump combustor is exclusively in the low speed regime, with the Mach number always less than 0.07. Except for the effect of heat release, the flow is essentially incompressible. The principal effect of heat release is to change the density; small changes in pressure balance the acceleration of the flow. We solve the conservation equations in the form listed below.

Mass Continuity:

$$\frac{\partial(\rho u)}{\partial x} + \frac{\partial(\rho v)}{\partial y} = 0 \tag{I}$$

X-Momentum:

$$\frac{\partial}{\partial x}(\rho u u) + \frac{\partial}{\partial y}(\rho u v) = -\frac{\partial p}{\partial x} + \frac{\partial}{\partial x}\left(\mu \frac{\partial u}{\partial x}\right) + \frac{\partial}{\partial y}\left(\mu \frac{\partial u}{\partial y}\right) + \rho g_x$$

$$+ \nabla \cdot \left(\mu \frac{\partial \mathbf{u}}{\partial x}\right) - \frac{2}{3}\frac{\partial}{\partial x}(\mu \nabla \cdot \mathbf{u}) \tag{II}$$

Y-Momentum:

$$\frac{\partial}{\partial x}(\rho u v) + \frac{\partial}{\partial y}(\rho v v) = -\frac{\partial p}{\partial y} + \frac{\partial}{\partial x}\left(\mu \frac{\partial v}{\partial x}\right) + \frac{\partial}{\partial y}\left(\mu \frac{\partial v}{\partial y}\right) + \rho g_y$$

$$+ \nabla \cdot \left(\mu \frac{\partial \mathbf{u}}{\partial y}\right) - \frac{2}{3}\frac{\partial}{\partial y}(\mu \nabla \cdot \mathbf{u}) \tag{III}$$

Thermal Energy:

$$\rho u c_p \frac{\partial T}{\partial x} + \rho v c_p \frac{\partial T}{\partial y} = \frac{\partial}{\partial x}\left(\kappa \frac{\partial T}{\partial x}\right) + \frac{\partial}{\partial y}\left(\kappa \frac{\partial T}{\partial y}\right)$$

$$- \sum_{k=1}^{K} h_k \dot{\omega}_k W_k - \rho \sum_{k=1}^{K} c_{p,k} Y_k \mathbf{V}_k \cdot \nabla T \tag{IV}$$

Species Continuity:

$$\frac{\partial}{\partial x}(\rho u Y_k) + \frac{\partial}{\partial y}(\rho v Y_k) + \frac{\partial}{\partial x}(\rho Y_k U_k) + \frac{\partial}{\partial y}(\rho Y_k V_k) = \dot{\omega}_k W_k \quad k = 1, K-1 \quad \text{(V)}$$

$$Y_K = 1 - \sum_{k=1}^{K-1} Y_k \qquad \text{(Diluent)}$$

State:

$$\rho = \frac{p}{RT}$$

This formulation of the problem is designed to be readily extendible to unsteady calculations in enclosures where the pressure perturbations are not large. One major difficulty with the slightly compressible (or incompressible) problem is calculation of the pressure field. In principle, the pressure could be obtained from the density, which is obtained by solving Equation (I), but because the velocity of sound is much greater than the mean flow velocity, small density perturbations can result in large pressure changes with disastrous consequences for the momentum equations. For this reason, among others, the problem is notoriously difficult to solve numerically.

Models for fully two-dimensional, nearly incompressible flows may be formulated in terms of streamfunction-vorticity, or primitive variables. The streamfunction-vorticity approach eliminates the pressure, while the primitive variable formulation requires derivation of a PDE for the pressure. For unconfined flames, the effect of small perturbation pressures (≈ 100 dynes/cm^2) can generally be ignored, so that the stream-function-vorticity formulation is particularly convenient. However, where the pressure perturbations are important, as for the acoustic resonances which can exist in our system and which we hope to model in the future, this advantage disappears. To recover the pressure in the streamfunction-vorticity formulation, we must solve an additional Poisson equation at each iteration.
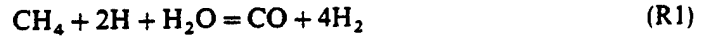
A further disadvantage of the $\psi-\omega$ formulation for confined flows is that we must derive boundary conditions for vorticity as part of the solution: ω is not constant on the boundaries. To be sure, the primitive variable formulation suffers the same problem with respect to the derived pressure equation. However, the specifics of our implementation offer a way around this. Finally, the streamfunction-vorticity formulation is somewhat more difficult to extend to three dimensions, requiring the solution of three equations for the vorticity and three more for the vector potential. Only four fluid dynamic equations need to be solved in the 3-D primitive variable formulation. In more practical axisymmetric configurations, dump combustors can have important 3-D effects under certain conditions. Thus we choose to model the dump combustor in primitive variables.

Thermodynamic and transport properties are found using the CHEMKIN package (Kee et al., 1980) and mixture averaging rules (Kee et al., 1983) respectively. Diffusion velocities are evaluated from the mole-fraction and temperature gradients by

$$Y_k V_k = \frac{D_k W_k}{\overline{W}}\left(-\nabla X_k + \frac{k_{T,k}}{T}\nabla T\right)$$

The code is constructed so as to use either a full mechanism or reduced mechanisms that are now being published. In this work, we use a reduced methane–air mechanism (Paczko et al., 1986) that contains seven species:
O_2, CH_4, CO, CO_2, H_2O, H_2, H and four global reactions[*].

$$CH_4 + 2H + H_2O = CO + 4H_2 \qquad \text{(R1)}$$

$$CO + H_2O = CO_2 + H_2 \qquad \text{(R2)}$$

$$2H + M = H_2 + M \qquad \text{(R3)}$$

$$O_2 + 3H_2 = 2H + 2H_2O \qquad \text{(R4)}$$

The rates of these global reactions are expressed as linear combinations of the rates of elementary reactions in the full (23 species) mechanism. This and similar mechanisms have been shown to satisfactorily model the heat release rate in strained and unstrained premixed flames. Since our primary interest is in obtaining the correct (strained) flame speed and shape of the major species profiles, use of a reduced mechanism is justified. As noted elsewhere (Peters and Kee, 1987), we use filters to prevent spurious species creation or destruction rates under certain special conditions. These filters do not change the flame speed or species profiles in the converged solutions.

We discretize the conservation Equations (I–V) on a staggered grid (Harlow and Welch, 1965) so as to eliminate the decoupling of the cell-pressure from the discretized momentum equation that occurs on the non-staggered grid. This also makes it unnecessary to specify the pressure on the combustor walls. Convection terms are upwinded while diffusion terms are evaluated from central differences. We solve the discretized equations in residual form. For example, for the species continuity equation. we write the implicit linearization as follows:

$$\left(A_t - \frac{\partial \dot{\omega}_k}{\partial Y_k} \right) \delta Y_k = (A_x + A_y) \delta Y_k + B(Y_k)$$

where $B(Y_k)$ is the residual of the discretized conservation Equation (V), A_x and A_y are the linearized coefficients that arise from the convective and diffusive transport. This equation is penta-diagonal, necessitating use of a factorization solution method (Peaceman and Rachford, 1955). A pseudo-transient term A_t has been added to speed convergence. We solve the species equations in a decoupled manner, i.e., we do not use a full chemical Jacobian. In fact it is often possible to solve this system of equations without utilizing the diagonal part of the chemical Jacobian. A delta form of the pressure equation is derived in a manner similar to that used in the SIMPLER method (Patankar, 1980). This pressure equation is iterated approximately 20 times. Iteration of the pressure correction equation only a few times often results in divergence due to failure to satisfy continuity from step to step.

---

[*] We have applied small corrections to what appear to be typographical errors in the original formulation. Specifically, $w_{IV} = w_1 + w_6 + w_8 + w_{23} - w_{27} - w_{32} + w_{37} - w_{39} - w_{45} + w_{46} + w_{47} - w_{48} - w_{50}$. Also, $[C_2H_2] = w_{30}/(k_{30b}[H] + (k_{35} + k_{36})[O] + k_{37}[OH]Z_{44})$ and, $w_{45} = k_{45}[C_2H][H_2]$.

CALCULATIONS

The nonuniform, orthogonal computational grid used for the unit aspect ratio ($A = L/S$) simulations is shown in Figure 2. Boundary conditions and physical dimensions are as indicated in the figure. Wall temperatures were measured with an optical pyrometer for the $A = 1, 2$, $\phi = 0.8, 1.0$ cases. Wall temperatures used for the calculations are given in Table 1. The combustor exhausts to atmospheric pressure. Coordinate stretching has been employed to increase the grid density near the dump and outlet planes because we expect fluid dynamic effects to be important there. Grid compaction is employed in the core flow to accurately capture the flame. The grid size for the unit
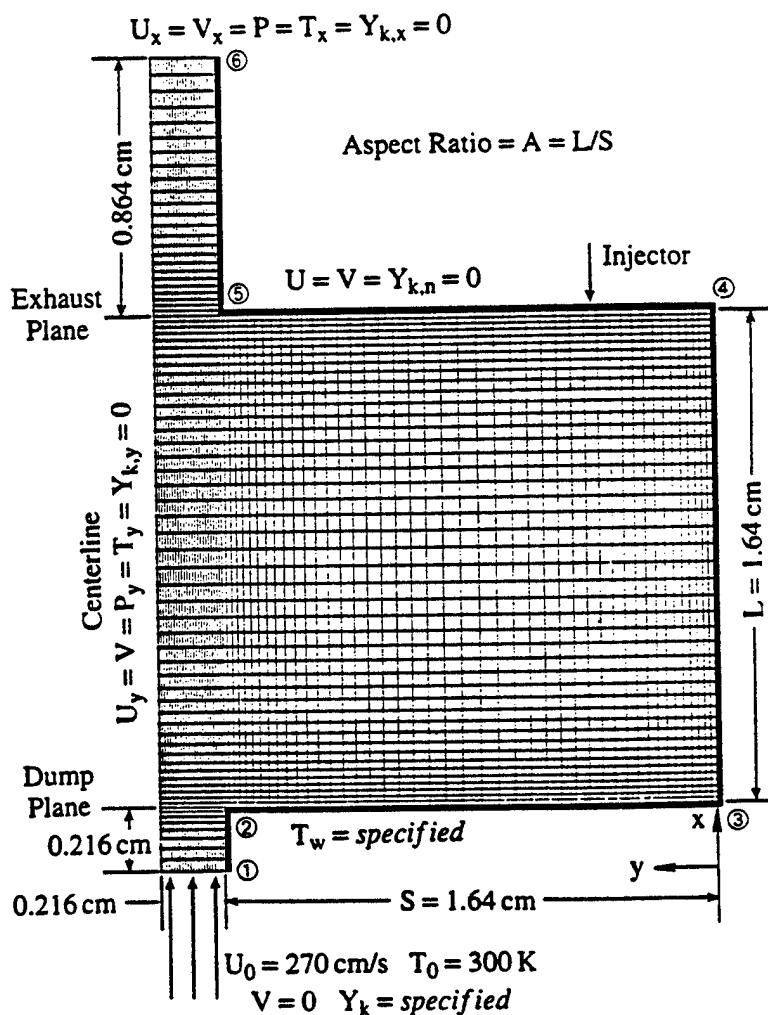

FIGURE 2 Computational grid with boundary conditions and physical dimensions. Wall temperature is based on linear interpolation of experimental measurements.

TABLE 1

Wall temperature (K) used in the calculations were linearly interpolated from these values. Subscripts refer to locations shown in Figure 2

A	ϕ	T_1	T_2	T_3	T_4	T_5	T_6
1	0.7	300	1315	1315	1315	1410	1450
1	0.8	300	1370	1370	1370	1450	1510
1	0.9	300	1400	1400	1400	1470	1540
1	1.0	300	1425	1425	1425	1490	1570
2	0.7	300	1265	1265	1265	1330	1420
2	0.8	300	1330	1330	1330	1390	1470
2	0.9	300	1365	1365	1365	1420	1500
2	1.0	300	1395	1395	1395	1450	1530

aspect ratio simulations is 78×70 while a 122×70 grid is used for an aspect ratio of two. The exhaust section was extended and additional grid points were added for the $A = 1$, $\phi = 0.7, 0.8$ calculations to obtain complete fuel burnout. Calculations have been performed for premixed methane–air mixtures of $\phi = 0.7, 0.8, 0.9, 1.0$ entering the combustor at 300 K and a velocity of 270 cm/s. These conditions correspond to those in the experiment, resulting in a cold-flow duct Reynolds number of 738 and a cavity Reynolds number of 2805 and 5610 for the aspect ratio one and two respectively. The duct Reynolds number is based on the full width of the entrance section (0.432 cm), and the cavity Reynolds numbers are based on the cavity length (L). The flow in a unit aspect ratio cavity is thought to become unsteady somewhere around a Reynolds number of 5000 (Vanka, 1985). Zhang (1990) reported no instability in aspect ratio two calculations at Reynolds numbers of 5000. Hence, our $A = 1$ flow-field is certainly steady, while for cold-flow at $A = 2$ some degree of instability cannot be ruled out. Our principal interest is in reacting flow, and here the cavity Reynolds numbers are substantially less than the corresponding cold-flow values due to the increase of viscosity at high temperatures. No instability is expected for the reacting flow, and our experimentally determined flame front intensity or position shows none.

Choosing $A_t = \rho / \Delta t$ with $\Delta t = 1 \mu s$ gave good performance. On each grid, the $\phi = 0.8$ simulation was started by setting plug flow in the core, stagnant fluid in the cavity, and superimposing a triangular flame from the lip of the dump plane to the centerline at the exhaust plane. The mixture outside the flame front was set to the adiabatic equilibrium composition. The other cases were restarted from the $\phi = 0.8$ solutions after making appropriate changes in the inlet conditions.

RESULTS WITHOUT WASTE INJECTION

Cavity Hydrodynamics

Figure 3 depicts the velocity fields for $\phi = 0.8$ reacting flows and corresponding cold, nonreacting flows at aspect ratios of 1 and 2. Significant differences in velocity fields exist between the reacting and nonreacting cases. Similarly, the cavity hydrodynamics

depends strongly on the aspect ratio. However, for a fixed cavity aspect ratio the velocity fields for reacting mixtures depend only weakly on equivalence ratio (or on the shape of the flame front). At unit aspect ratio, the nonreacting flow calculations show a single large recirculation cell filling most of the cavity. At an aspect ratio of two, there is also a second, large, but weaker counter-rotating recirculation zone in the bottom portion of the dump cavity. The corresponding reacting flows at unit aspect ratio show a somewhat smaller, weaker, primary recirculation zone, resulting from the divergence in velocity across the flame front. At an aspect ratio of two, however, the primary recirculation cell is larger for the reacting flow, now extending to the bottom of the cavity. This recirculation zone is also weaker than its inert counterpart. We also note the secondary recirculation zones (in the corners) are smaller for the reacting flow, consistent with the weaker primary recirculation zone and with nonreacting flow calculations at much lower cavity Reynolds numbers.
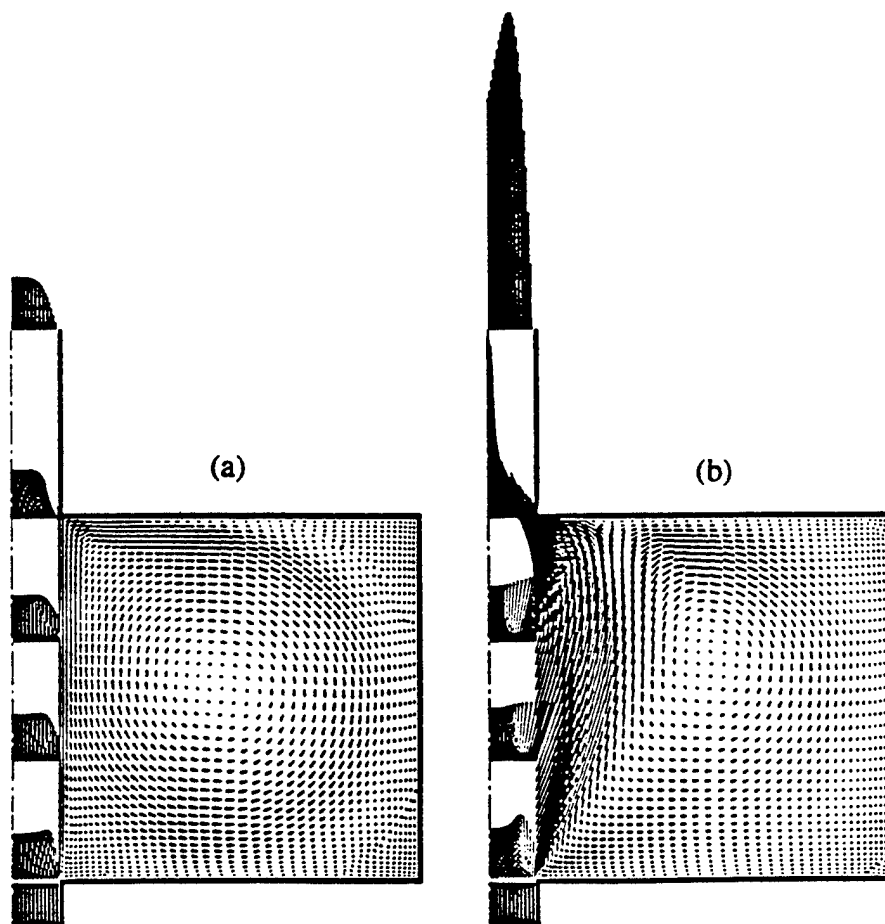

FIGURE 3 Calculated velocity fields for $\phi = 0.8$ methane–air mixtures in the combustor for inlet velocity of 270 cm/s: (a) Non-reacting, $A = 1$; (b) Reacting, $A = 1$ (c) Non-reacting, $A = 2$; (d) Reacting, $A = 2$.
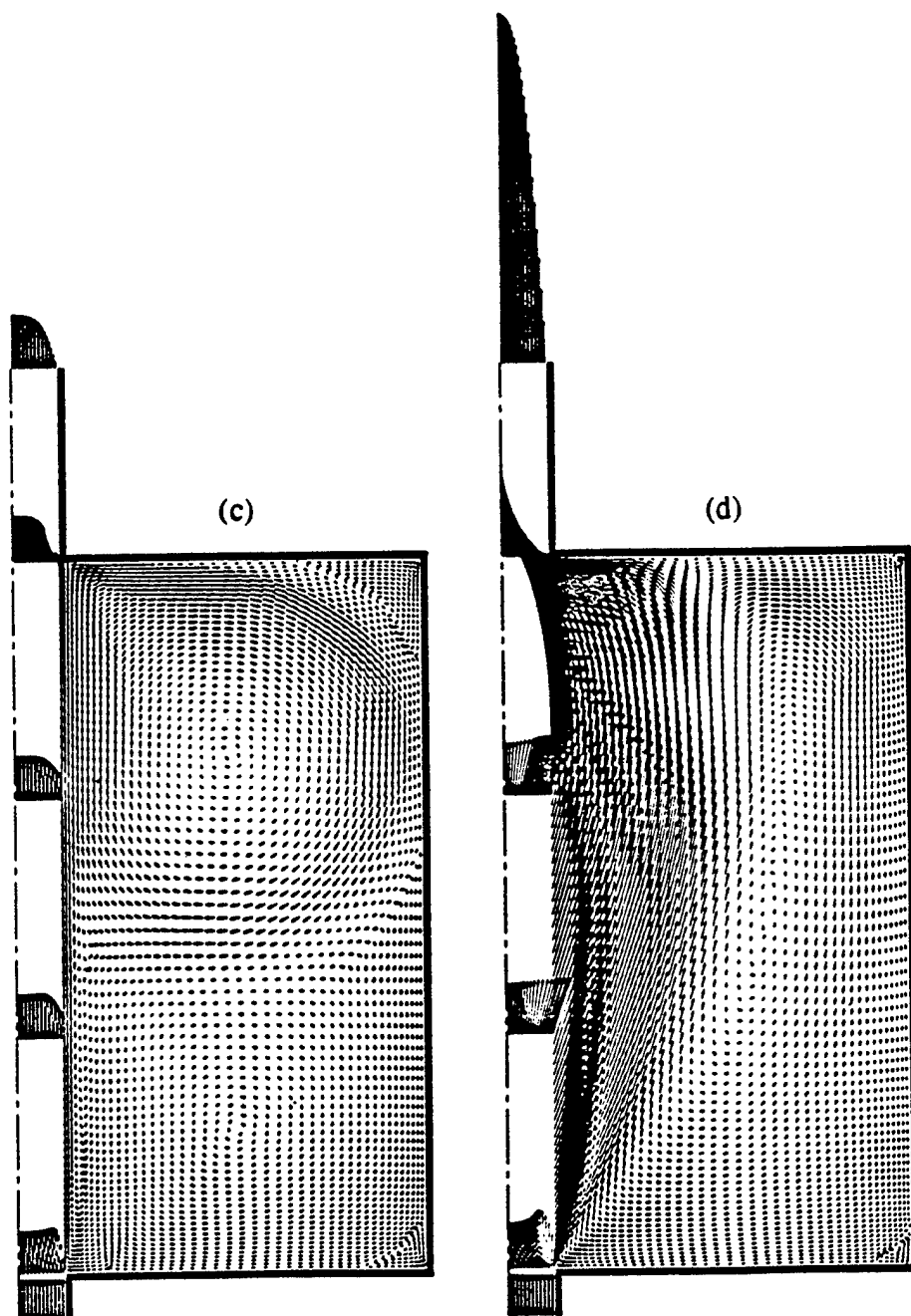
(c)   (d)

FIGURE 3   *(Continued)*

Reacting flow hot-cavity Reynolds numbers are about 750 and 1500 for $\phi = 0.8$ and aspect ratios of one and two, respectively. Constant property simulations at these Reynolds numbers fail to predict the changes in the flow field between nonreacting and reacting flows. Thus, these changes are not so much a consequence of the different viscosities but rather of the heat release within the flame front. This illustrates that the nonreacting velocity fields can fail to exhibit, even qualitatively, some the features present in reacting flows.

Flame Structure

Figure 4 presents selected results for the $\phi = 0.8$, unit aspect ratio case corresponding to Figure 3b. Except for Figure 4f, which depicts the experimentally determined OH* chemiluminescence, all results are from the calculations. The shape of the experimental chemiluminescence image agrees well with the distribution of the calculated heat production rate $(- \sum_{k=1}^{K} h_k \dot{\omega}_k W_k)$ shown in Figure 4d and with the numerical convolution [CH] [O_2] depicted in Figure 4e. Th concentration of CH is calculated from the steady-state relation in the reduced mechanism.

The mass fraction of fuel and that of a typical chain carrier (H-atoms) are presented in Figures 4a and 4b respectively. Methane is essentially completely consumed at the flame front. Two regions of high H-atom mass fraction are apparent. The first exists near the dump plane, where hot products in the recirculation zone impinges on the unreacted jet. This also corresponds to the area of highest local heat release. and the result is largely responsible for flame stabilization. The second exists at the tip of the flame, where flame front curvature is high.

The temperature field is given in Figure 4c. The highest temperatures are found between the flame front and the streamline separating the core flow from the recirculation zone. The latter is fairly uniform in temperature. The streamfunction corresponding to this calculation is given in Figure 6a.

In Figure 5, we compare the experimentally determined flame length (by chemiluminescence) to the numerically calculated flame length based on the convolution of [CH] [O_2] for several equivalence and aspect ratios. The uncertainty associated with the experimental equivalence ratios is attributable primarily to the 3% uncertainty in flowmeter readings. For $\phi \geq 0.8$, uncertainty in experimental flame length spans the height of the data points. For $\phi = 0.7$, some ambiguity is introduced by a slight lengthening of the flame in the colder region near the windows. which thickens the region of luminescence at the flame tip.

At $\phi \geq 0.8$, agreement between the experimental and calculated flame shapes and heights is generally good. The calculations correctly predict a shortening of the flame when going from lean towards stoichiometric. Computed flame lengths show only slight sensitivity to cavity length. The calculated $A = 2$ flames are 4–8% shorter than those for unit aspect ratio. Within the error of the experimental data. no dependence of measured flame length on aspect ratio is discernible. Figure 5 shows that the calculations are slightly more sensitive to equivalence ratio than are the experimental results. The error associated with this trend is not serious for $\phi \geq 0.8$. but grows rapidly below $\phi = 0.8$. At $\phi = 0.7$. the calculated flame lengths are about 18% longer than those measured.
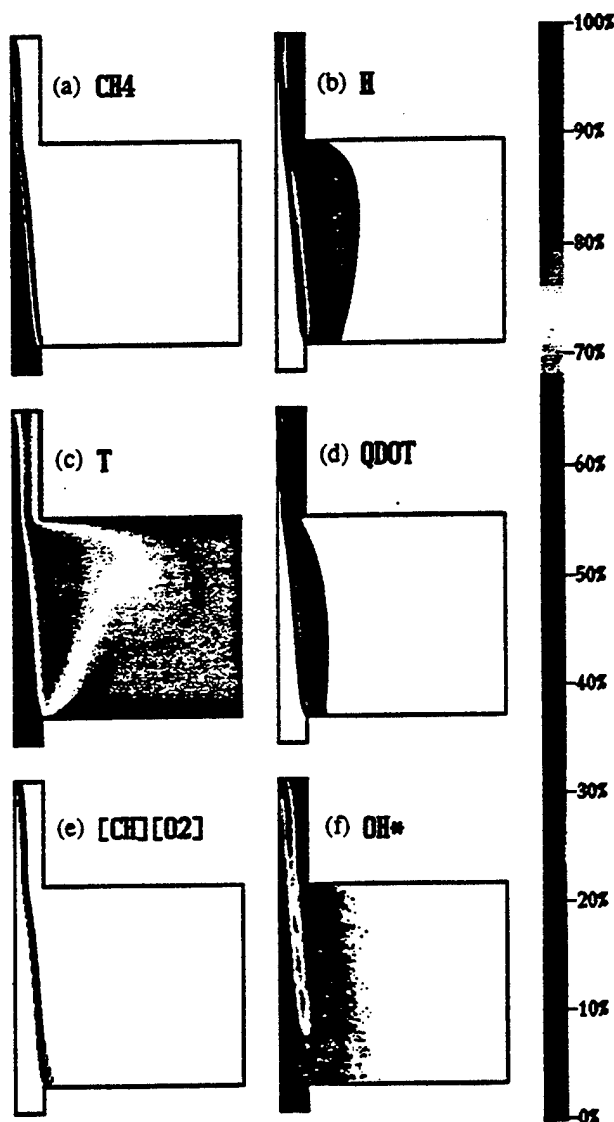
FIGURE 4　Selected solution components for a unit aspect ratio calculation at $\phi = 0.8$. The top of the bar (red) corresponds to the value indicated as follows: (a) CH_4 mass fraction, $4.46 \cdot 10^{-2}$; (b) H mass fraction, $1.68 \cdot 10^{-4}$; (c) Temperature, 2200 K, Minimum = 300 K; (d) Heat production rate $(-\sum_{k=1}^{K} h_k \dot{\omega} W_k)$, $2.50 \cdot 10^{10}$ erg/cm^3/sec; (e) Convolution of [CH][O$_2$], $1.75 \cdot 10^{-18}$ mol^2/cm^6; (f) OH* chemiluminescence, maximum pixel value. See COLOR PLATE I.

As part of the construction and verification of a reduced mechanism, it is usual to perform some one-dimensional laminar premixed flame calculations to compare adiabatic burning velocities and major species profiles. In this work we are primarily interested in obtaining the correct rate of heat release. Hence, we compare the burning
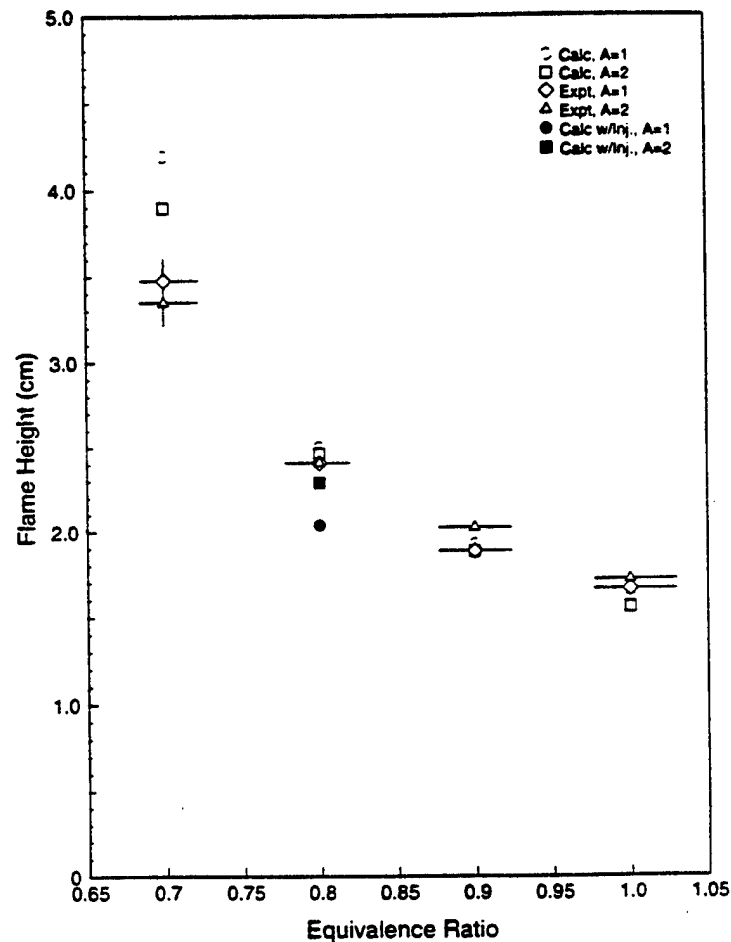
FIGURE 5 Experimental and calculated flame heights based on OH* chemiluminescence for equivalence ratios from 0.7 to 1.0.

velocity of the reduced mechanism on a coarse grid, equal to the transverse grid spacing used in the two-dimensional calculations, to the burning velocity calculated on a very fine grid using the full and reduced mechanisms. We also compare these results to experimental values determined by Egolfopoulos *et al.* (1989) to elucidate errors inherent in the full mechanism, those introduced in the reduction of the mechanism, and those associated with the coarse grid.

The full mechanism very slightly overpredicts the burning velocity as compared to experiment at $\phi = 0.7$. This overprediction increases monotonically to 9.3% as the mixture becomes stoichiometric. The reduced mechanism calculated on a fine grid underpredicts the burning velocity as compared to experiment by 12.6% at $\phi = 0.7$ and over-predicts it by 15.9% at $\phi = 1.0$. The overprediction of burning velocity at equivalence ratios of $\phi = 0.7, 0.8$ has also become larger with the introduction of the

reduced mechanism. Thus, the reduced mechanism is closest to predicting the burning velocity at $\phi = 0.8$ but somewhat exaggerates the dependance of burning velocity on equivalence ratio.

Comparing the coarse-grid reduced mechanism results to experiments showed the reduced mechanism over-predicts the burning velocity by 10.9% at $\phi = 1.0$, 6.9% at $\phi = 0.9$, 0.2% at $\phi = 0.8$ and underpredicts it by 12.8% at $\phi = 0.7$. Evidently the use of the reduced mechanism is primarily responsible for the relative "steepness" in the calculated flame height curve in Figure 5 as compared to the experiment. The effect of the coarse grid on the burning velocity is negligible for the leanest flame examined in the calculations but becomes progressively more pronounced as the mixture is enriched. The decrease in burning velocity predicted by the reduced mechanism on the coarse grid compared to the fine grid is probably due to poorer resolution of gradients within the flame because the flame will tend to become thinner as the mixture is enriched from $\phi = 0.7$ to $\phi = 1.0$.

Accuracy of the Results

To assess the accuracy of the calculations, we take two approaches. First, there exists a large body of results with which we can compare fluid dynamics for completely incompressible flows on a domain similar to ours, the lid-driven cavity (Gatski et al., 1982; Ghia et al., 1982; Schreiber and Keller, 1983; Vanka, 1986; Zhang, 1990). We have performed numerous fluid flow calculations on the lid-driven cavity using grids identical to those used for the reacting shear-driven cavity described earlier. Qualitatively, we find there exists one large recirculation zone for low cavity Reynolds numbers ($Re = \rho U_x L/\mu = 100$), with very weak secondary cells of nearly equal size for both the aspect ratios $A = 1$ and $A = 2$. As the Reynolds number is increased, the primary cell strength increases as do the secondary cells. The secondary cells grow in size, the downstream cell more so in the $A = 1$ case, but more so for the upstream cell in the $A = 2$ case. For the long cavity ($A = 2$) the secondary zone becomes very large at $Re = 1000$ and by $Re = 5000$ it is very similar to that shown for the shear-driven cavity at $Re = 5610$ in Figure 3c. These double counter rotating recirculation zones have been reported in the literature (Gatski et al., 1982; Zhang, 1990).

Quantitatively, the location and maximum streamfunction value for the shallow cavity ($A = 2$) agree with Zhang (1990) to within 4.4% at $Re = 5000$. This discrepancy decreases with the Reynolds number, reaching exact agreement at $Re = 100$. Similar accuracy is achieved for the secondary zones. We find similar agreement with the maximum streamfunction value and location given by the average of values reported by Zhang (1990), Ghia et al. (1982), Schreiber and Keller (1983), and Vanka (1985) for the unit aspect ratio problem. Our values are within 5% at $Re = 5000$ and within 0.2% at $Re = 100$. We note that the grids used in the literature calculations are somewhat finer than ours.

Second, we can examine important features of the solution and attempt to determine whether the grid is sufficient to resolve those features. The flame structure is of major concern. For the stoichiometric flame the initial O_2 mass fraction is about 0.22. If we consider the flame to be the region where the O_2 mass fraction decreases from 0.20 to 0.02, we find six grid points within the flame. Discrepancies in the flame heights other

than those attributable to the reduced mechanism (described earlier) must be assigned to the model: e.g., having only six grid points within the flame, small deviations from the experimental geometry or boundary conditions, etc.

To accurately capture the laminar flow structures, it is necessary to resolve the boundary layer. Gatski *et al.* (1982), in assessing the accuracy of their lid-driven cavity simulations, ran finite difference simulations on a model problem with successively finer grids. They report that having two grid points within the boundary layer is sufficient to predict the velocity to within one percent and the shear stress to within "engineering accuracy" or 10%. In our calculations there exist regions which clearly can be approximated by a flat plate; the inlet section and the exhaust section from the contraction to the exit of the computational domain. These two regions have fast moving fluid near the wall; other regions have slower moving fluid near the wall. Thus we apply a flat plate boundary layer test to these regions. If the test is satisfied here. it is expected to hold throughout the entire computational domain. The boundary layer thickness for flow over a flat plate is given by $\delta = 5\sqrt{\nu l/U_x}$. A severe test is to take $l = \Delta x$, the grid size at the wall. Using this test, we find two cross-stream direction grid points within the boundary layer for the first step downstream from the inlet boundary. At the cavity exhaust plane, the situation is more favorable: there are three grid points within the boundary layer. Inspection of the solution at these regions confirms these conclusions. The thermal boundary layer lies outside the momentum boundary layer as a consequence of the Prandtl number being less than one. As we do not account for reactions at the boundaries, species boundary layers are expected to be still thicker.

We find satisfactory agreement of the model's cold-flow calculations with the literature and the grid resolution to be adequate to resolve boundary layers to "engineering accuracy". The general agreement of experimental and calculated flame lengths indicates the model satisfactorily accounts for the heat release rate and transport processes of a methane–air flame in the combustor.


RESULTS WITH WASTE INJECTION

As stated in the introduction, we are evaluating the use of the recirculation region within the cavity as an oxidizing chemical reactor for the destruction of hazardous wastes. Incineration systems are generally designed to use time. temperature. and mixing (with sufficient oxygen) to effect destruction. Inadequate mixing cannot be corrected by increasing oxygen content, temperature, or residence time. Viewing the recirculation zone as a stirred reactor, the ratio of the volume to the injection rate will determine the residence time. For steady operation (as opposed to operation at a resonance), oxidizing species must be supplied by diffusion across the streamline separating the recirculation zone from the core flow. An estimate of the rate of supply of oxidizing species and of the reactor (recirculation zone) size is very useful in identifying factors which limit the rate of waste injection, and therefore the process economics.

The size of the reactor can be calculated directly from the streamfunction. The normalized streamfunction for $A = 1, 2$, $\phi = 0.8$ calculations are shown in Figures 6a and b respectively. Negative values of the streamfunction define the recirculation zone.

This excludes the secondary zones in the corners. The dependence of the recirculation zone volume for a unit depth reactor on the equivalence and aspect ratios is shown in Figure 6c. As expected, the aspect ratio is the principal factor influencing the reactor volume, but equivalence ratio also has a significant effect, especially for an aspect ratio of two.

Estimation of the rate of supply of oxidizing species is more difficult. We address this issue directly by computing a series of cases with lean core flames, but for which additional methane (representing a hydrocarbon waste) is injected into the recirculation cell. The injector is located in the top of the cavity 3/4 of the way towards the outer wall (see Fig. 2). This location was chosen so as to minimize disruption of the recirculation cell structure at high injection rates. Two cases were examined at each aspect ratio. The first utilizes a $\phi = 0.8$ methane–air flame in the core, as described previously. In the second, we augment the oxygen volumetric flow rate in the core flame
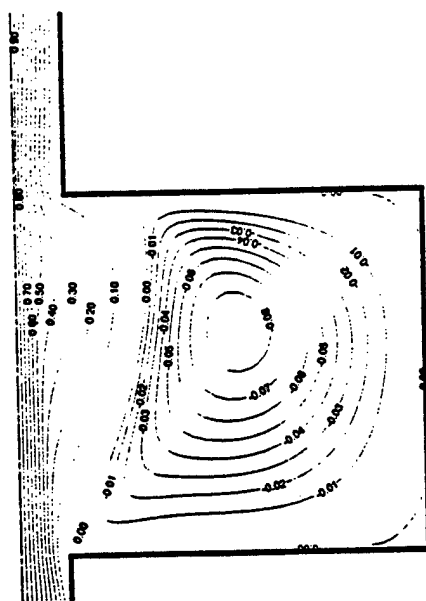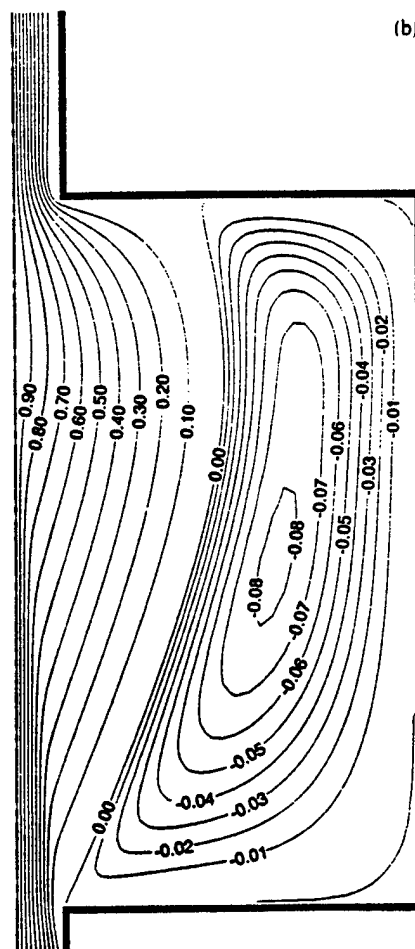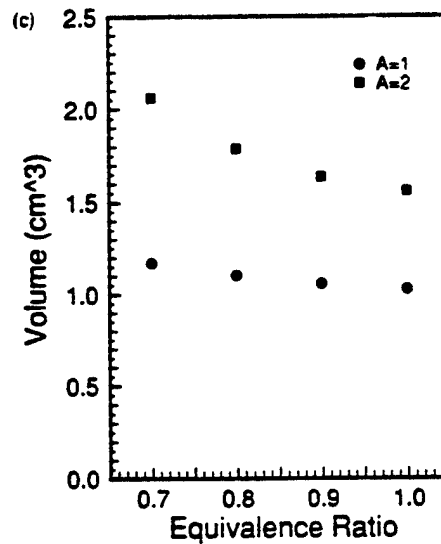
FIGURE 6   (a) Normalized streamfunction for A = 1, ϕ = 0.8; (b) Normalized streamfunction for A = 2, ϕ = 0.8; (c) Recirculation zone volume determined from the streamfunction.

by 50% and reduce the nitrogen by a corresponding amount, leaving the fuel and overall flow rates unchanged. This enhanced oxygen core flame burns at an equivalence ratio of 0.533. However, since oxygen and nitrogen have nearly the same heat capacities, the adiabatic flame temperature is not significantly different from the ϕ = 0.8 case. For both cases, methane is injected at a rate sufficient to raise the overall equivalence ratio to one. For the enhanced oxygen case, the rate of methane injection is about four times that for the methane–air case (3.85% and 1.12% of the inlet mass flow rates, respectively). The core equivalence ratio ultimately dictates the maximum rate at which hydrocarbon wastes can be injected. Hence, operation with enhanced oxygen may be desirable in an incineration application, provided that the additional oxidizing capacity can be effectively utilized.

Selected results for injected cases at unit aspect ratio are presented in Figure 7. The left column depicts the results for a ϕ = 0.8 core flame. The right-hand column depicts the results for oxygen enriched (ϕ = 0.533) core flame. Corresponding data without injection are shown in Figure 4.

Streamfunction plots are shown in Figures 7k and 7l. Streamlines associated with injected jet originate from the upper cavity wall. For the ϕ = 0.8 methane–air flame with 1.12% injection, injection streamlines span the range $0 \leq \Psi \leq -0.0112$. For the oxygen enhanced flame, injection streamlines span the range $0 \leq \Psi \leq -0.0385$. The interface between the core and recirculation cell is depicted by the stagnation stream-line (Ψ = 0.0) originating at the dump plane just outside the inlet. The higher core flow rate associated with the oxygen enhanced system displaces the core/recirculation cell interface into the cavity, resulting in minor enlargement of the interfacial area and consequent reduction in recirculation cell volume.

Higher temperatures are expected in the enriched oxygen case since this system is less dilute. The temperature fields (Figs. 7e and 7f) indicate that peak temperature is 450 K higher in the enriched oxygen case, but this differential attenuates rapidly towards the center of the recirculation region. Most of each recirculation cell is of nearly uniform temperature.

Figures 7g and 7h reveal the presence of two distinct flame fronts. A primary premixed flame is established in the core and a secondary diffusion flame separates the high temperature, oxidizer-rich products in the outer core flow from the fuel-rich
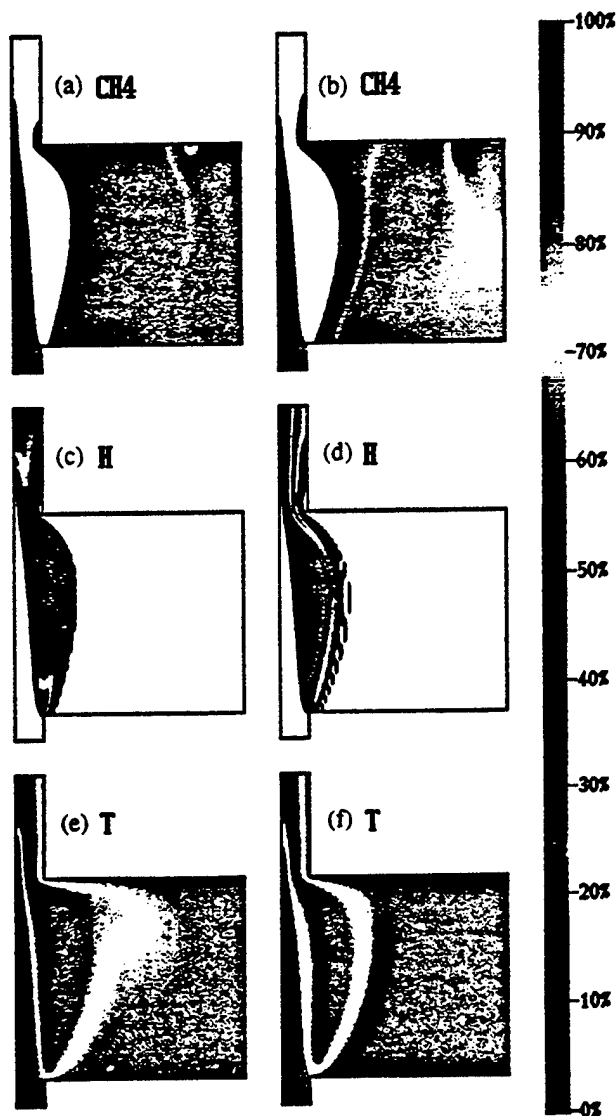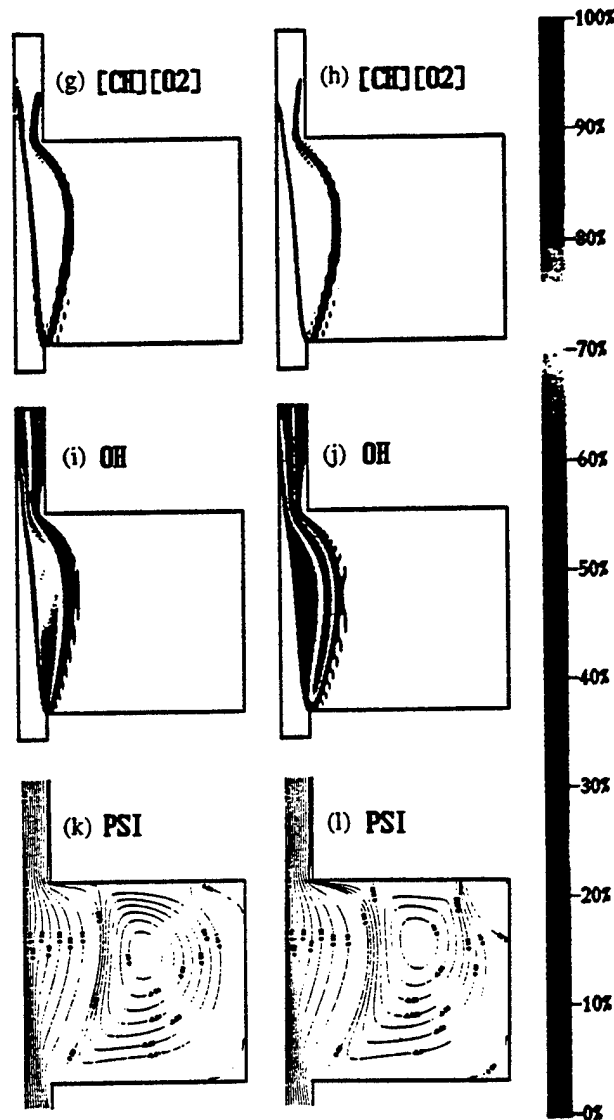
FIGURE 7 Selected solution components for two injected flames at unit aspect ratio. The left-hand column is for a $\phi = 0.8$ core methane–air flames. The right-hand column depicts results for an oxygen enriched ($\phi = 0.533$) core flame. In both cases the overall equivalence ratio is one. (a) CH_4 mass fraction, 1.0; (b) CH_4 mass fraction, 1.0; (c) H mass fraction, $3.38 \cdot 10^{-4}$; (d) H mass fraction, $5.00 \cdot 10^{-4}$; (e) Temperature, 2200 K. Minimum = 300 K; (f) Temperature, 2650 K, Minimum = 300 K; (g) [CH][O_2] concentration product, $6.31 \cdot 10^{-18} mol^2/cm^6$; (h) [CH][$O_2$] concentration product, $1.62 \cdot 10^{-17} mol^2/cm^6$; (i) OH mass fraction, $6.41 \cdot 10^{-3}$; (j) OH mass fraction, $1.60 \cdot 10^{-2}$; (k) Streamfunction; (l) Streamfunction. See COLOR PLATE II.

recirculation zone. The secondary flame front originates at the dump plane coincident with the stagnation streamline, but for the most part lies well inside the stagnation streamline, in the core region. Secondary flames are also observed in experiments in which combustible waste surrogates (methyl chloride and acetonitrile) are injected

(Willis *et al.*, 1994). Methane injection shortens the $\phi = 0.8$ core flame significantly, but it still extends into the exhaust section. The flame length with injection is still 27% greater than the length of a core flame of unit equivalence ratio, as shown in Figure 5. Adding fuel in the recirculation zone does increase the core flame speed, but not to the extent it would if added to the core. Higher temperatures in the oxygen enriched case result in minor reduction in core flame length. The length is still 16% greater than for a stoichiometric core methane–air flame.

The OH mass fraction fields (Figs. 7i and 7j) also distinctly show the presence to two flame fronts. Note that as the injection rate is increased there is quantitatively more OH and the peak moves from the core flame toward the secondary flame. This is most likely due to the shifting location of the temperature maxima in the combustor.

The methane mass fraction fields (Fig. 7a and 7b) also show two distinct regions. Fuel introduced through the inlet is confined to the cold side of the core flame. That injected into the cavity is confined to the fuel-rich side of the secondary diffusion flame. For both the air and oxygen enriched cases oxidizer is not supplied fast enough to confine the secondary flame front to the combustion cavity, hence a small amount of waste surrogate is still present in the lower part of the exhaust section. Waste surrogate penetrates further into the exhaust section in the oxygen enriched case, indicating that oxygen utilization within the cavity is lower. At the end of the computational domain, essentially all the methane is reacted.

Another interesting aspect of the methane field is the existence of very high mass fractions in the upper right corner of the cavity. Figures 7k and 7l show that injection results in the formation of secondary recirculation zones here. As expected, the size increase at higher injection rates. Since these cells exchange mass with the primary recirculation zone very slowly, this essentially reduces the cavity volume available for waste pyrolysis and oxidation.

Figure 7c depicts the H-atom mass fraction for the $\phi = 0.8$ case. Comparison with Figure 4d indicates that injection significantly raises the H-atom concentration, particularly in the impingement area just past the dump plane. This serves to attach the flame front much more securely at the cavity entrance, an observation which is again in accord with experiment (Willis *et al.*, 1994). This attachment tends to attenuate low frequency 'chugging' resonances which are prevalent in these combustors at low core equivalence ratios and large aspect ratios. We have shown previously that this instability results in very poor levels of waste destruction (Smith *et al.*, 1990; Marchant *et al.*, 1992). Comparison of Figures 7c and 7d indicates that increasing the rate of fuel injection does not significantly increase the H-atom concentration in the impingement region. The principal pyrolysis/partial-oxidation products formed in the recirculation zone (CO and H_2) are first exposed to oxygen at this point. The lack of increased reaction rate may be due to an observed decrease in the H_2/CO ratio at this point with increasing injection rate.

Finally, we note that the enriched oxygen case shows significantly higher levels of H in the secondary flame in the exhaust section. This is apparently due to the higher temperatures observed in this system, and to the fact that a greater portion of the heat release is associated with the secondary flame. The generic recombination reaction (R3) proceeds in the reverse direction in the high temperature region between the primary and secondary flame fronts; some of the resulting H-atoms participate in the destruc-

tion of methane by R1. The resulting consumption of H_2 accounts for the increase in the CO/H_2 ratio in the higher temperature, oxygen enriched flames. However, there is more H_2 in the oxygen enriched flame than the methane-air flame. The increase in H-atom levels in the exhaust section is due to the action of the generic H_2-O_2 branching reaction (R4) when the very lean core flame products are forced close to the rich secondary flame recirculation zone products.

In experiments, we frequently establish high frequency (200–500 Hz) resonances when enriching the core equivalence ratio from 0.8 to 1.0 at short cavity lengths. However, raising the total equivalence ratio from 0.8 to 1.0 by injection of acetonitrile into the cavity never establishes such resonances and, if already established at $\phi = 0.8$, frequently reduces their intensity (Willis *et al.*, 1994). It is expected that energy released in the secondary flame will be less effective in exciting this mode, since the driving instability is associated with the primary flame front (Willis *et al.*, 1993). However, we were somewhat surprised to see such resonances damped in those experiments. It may be that the additional heat release in the exhaust section has something to do with this.

We have determined the residence time distribution of mass in the core flow and of the surrogate waste by evaluating trajectories of massless particles initially distributed across the combustor inlet and the injector. With one exception noted later, computed residence times were strongly bimodal; mass belonging to the core flow has relatively short residence times and mass originating from the injector has longer residence time. We find the average residence time in the $A = 1$, $\phi = 0.8$ injection case to be about 5.58 ms for the core flow with a significant fraction of that spent at low temperature. The minimum residence time for the core flow is 4.0 ms. Injecting the waste into the slower moving high temperature recirculation zone results in very significant lengthening of the minimum residence time (by more than 25 times); furthermore, this mass is subjected to high temperature for essentially the entire time of flight. Residence times were shorter for injected mass in the enhanced oxygen cases because of the increased injection rate. The minimum residence time of injected mass in the enhanced oxygen case was still 11.4 times that of the core flow. Thus, by careful design, relatively long residence times at high temperature may be obtained in a compact device.

The features of the injected air and enriched oxygen systems at $A = 2$ are generally the same as described previously at unit aspect ratio. Injection results in the establishment of a secondary diffusion flame and stabilization of the core flame at the dump plane. Oxygen enrichment increases the total heat release (as well as the fraction associated with the secondary flame front) and moves the region of peak H-atom concentration into the exhaust section.

Selected fields at an aspect ratio of two are displayed in Figure 8. The left- and right-hand columns depict results for the methane-air and oxygen enriched core flames, respectively. Comparison of Figures 7k and 7l and 8k and 8l shows that increasing the aspect ratio displaces the stagnation streamline towards the cavity wall. This is consistent with the behavior observed for non-injected systems (Figs. 3b and 3d). The high injection rate with oxygen enhancement causes an additional secondary recirculation cell to form along the top wall just toward the centerline from the injector location. The streamlines associated with the injected fluid bifurcate about $\Psi \approx -0.025$, with those trajectories in the range $-0.0385 \le \Psi \le -0.025$ (representing approximately 1/3 of the fluid) exiting the cavity without passing around the primary recirculation cell.

Although it occupies a smaller fraction of the cavity, the increase in cavity size with aspect ratio causes the volume of the primary recirculation cell to increase. This trend agrees with that established by Figure 6.

As expected, the residence time of injected mass increases with increasing cavity length. As noted earlier, the injected mass in the enhanced oxygen case suffers from bifurcation and hence, part of this mass had significantly shorter minimum residence time (2.75 times the core flow) than the remainder.
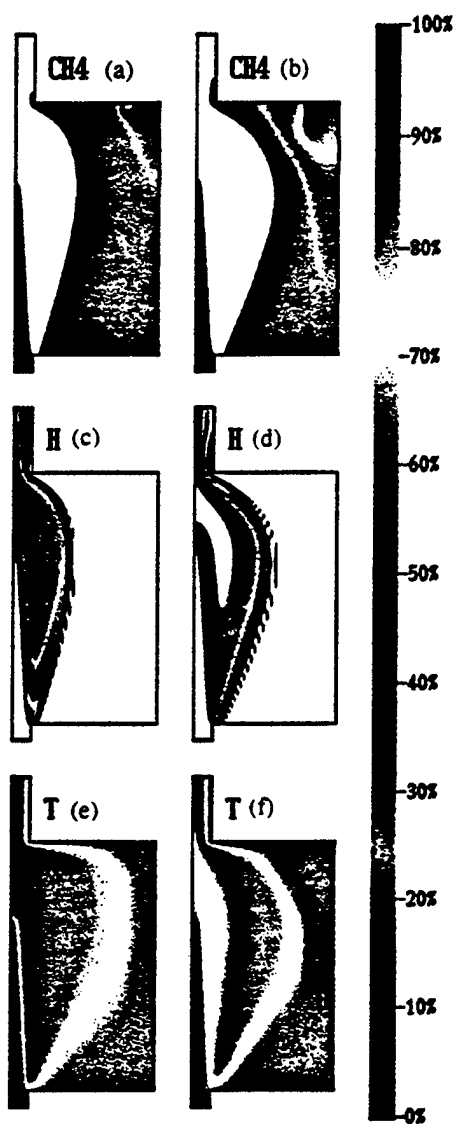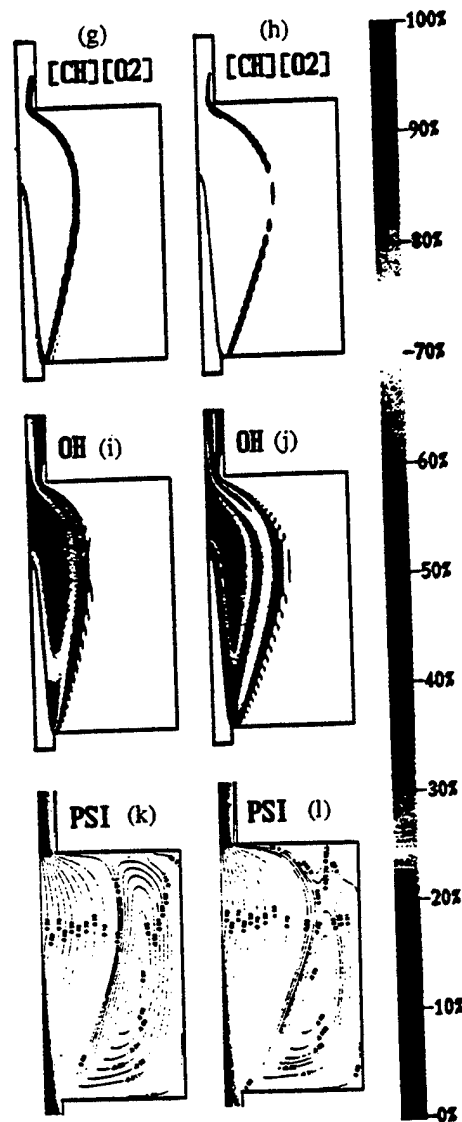
FIGURE 8 Selected solution components for two injected flams at an aspect ratio of two. The left hand column is for a $\phi = 0.8$ core methane–air flames. The right hand column depicts results for an oxygen enriched ($\phi = 0.533$) core flame. In both cases the overall equivalence ratio is one. (a) CH_4 mass fraction, 1.0; (b) CH_4 mass fraction, 1.0; (c) H mass fraction, $2.84 \cdot 10^{-4}$; (d) H mass fraction, $4.29 \cdot 10^{-4}$; (e) Temperature, 2200 K, Minimum = 300 K; (f) Temperature, 2650 K, Minimum = 300 K; (g) $[CH][O_2]$ concentration product, $4.67 \cdot 10^{-18} \, mol^2/cm^6$; (h) $[CH][O_2]$ concentration product, $1.77 \cdot 10^{-17} \, mol^2/cm^6$; (i) OH mass fraction, $5.96 \cdot 10^{-3}$; (j) OH mass fraction, $1.46 \cdot 10^{-2}$; (k) Streamfunction; (l) Streamfunction. See COLOR PLATE III.

The secondary flame front (Figs. 8g and 8h) also moves outward with increasing aspect ratio, following the displacement of the stagnation streamline. This causes the area of the secondary flame front to scale nonlinearly with aspect ratio. As expected, based on the results without injection, increasing the aspect ratio has

little effect on the length (Fig. 5) of the primary flame, which is now confined well within the combustion cavity. The H-atom (Fig. 8c and 8d) and OH radical (Fig. 8i and 8j) peaks are now quite removed from the core flame in the enhanced oxygen–methane injection cases. The mechanism previously described accounts for the increase in H-atom levels in the oxygen enhanced case as compared to injection into the methane–air flame.

Figures 8a and 8b indicate that, as for the unit aspect ratio cases, a small amount of injected methane escapes from the cavity into the lower part of the exhaust section. Comparison with Figs. 7a and 7b shows that the minimum CH_4 mass fraction depicted (0.00394) does not penetrate as far into the exhaust section as the aspect ratio is increased. This is not surprising, since the larger area of the secondary flame front and longer mean residence time of injected fluid at $A = 2$ would be expected to result in more complete consumption. However, at fixed aspect ratio, oxygen enrichment (along with the corresponding increase in injection rate) is seen to increase the degree of methane penetration into the exhaust. For the enhanced oxygen case, the tri-modal residence time distribution resulting from injection streamline bifurcation probably plays a role in this.

INCINERATION IMPLICATIONS

In incineration applications, the overriding concern is achieving an adequate degree of waste destruction at the exhaust of the combustor. Depending on the nature of the waste, so called "destruction and removal efficiencies" (DREs) from 99.99% to 99.9999% may be required. Secondary concerns include by-product formation, economics, and others. In our device, the economics are influenced by the rate at which waste can be introduced while maintaining adequate levels of destruction. For combustible wastes, a key factor is the mixing of excess oxidizer from the fuel-lean core with the products of oxidative pyrolysis formed within the recirculation zones.

One way to quantify performance in the above areas is to examine the ratio of molecular flux at the various points within the domain to that at the inlet. In Table 2 we report the computed integrated mass flux for selected species at two points within the device. *End* refers to the end of the combustion cavity or entrance to the exhaust section, i.e., the location where the duct contracts. *Exit* refers to the end of the computational domain, as indicated in Figure 2. The columns labeled CH_4 report the ratio of methane mass flow rate to the total rate at which methane is introduced into the cavity. For cases without injection, this corresponds to the inlet methane mass flow rate. Where injection occurs, the denominator includes both methane introduced at the inlet and that injected into the recirculation cell, except as noted below. In some modes of operation (for example if the primary flame is fueled with waste), it would be appropriate to interpret these entries in terms of DREs. In other modes (e.g., where the primary flame is fueled conventionally), a distinction needs to be made between the methane introduced at the inlet and the methane injected into the recirculation cell. We accomplish this by solving a separate conservation equation for the injected species, termed H_4C, with identical chemical and physical properties as methane. An additional

TABLE 2

Ratio of outlet to inlet mass fluxes of methane and oxygen in the calculations

A	ϕ_c	ϕ	CH$_4$		O$_2$		O$_{2,eq}$
			End	Exit	End	Exit	
1	0.7	0.7	5.221E-01	3.513E-01	6.740E-01	5.655E-01	3.004E-01
2	0.7	0.7	1.574E-01	1.866E-07	4.161E-01	3.014E-01	3.004E-01
1	0.8	0.8	3.167E-01	6.278E-03	4.769E-01	2.462E-01	2.021E-01
2	0.8	0.8	5.781E-12	8.192E-18	1.948E-01	1.951E-01	2.021E-01
1	0.9	0.9	1.479E-01	6.810E-18	2.802E-01	1.331E-01	1.092E-01
2	0.9	0.9	1.140E-18	3.354E-27	1.013E-01	1.011E-01	1.092E-01
1	1.0	1.0	6.174E-05	1.794E-23	8.471E-02	6.199E-02	3.312E-02
2	1.0	1.0	2.866E-26	0.000E+00	3.067E-02	2.933E-02	3.312E-02
1	0.8	1.0	1.948E-01	9.092E-15	2.979E-01	9.362E-02	3.312E-02
2	0.8	1.0	2.625E-02	1.998E-12	8.990E-02	6.729E-02	3.312E-02
1	0.533	1.0	1.761E-01	6.982E-14	3.457E-01	1.554E-01	1.048E-01
2	0.533	1.0	7.409E-02	1.190E-15	2.183E-01	1.416E-01	1.048E-01

propagation reaction

$$H_4C + 2H + H_2O = CO + 4H_2 \qquad \text{(R1a)}$$

is added to the reduced mechanism. The CH_4/H_4C product distribution in the reaction of $CO + 4H_2$ (the reverse of reactions (R1) and (R1a) is arbitrarily set to the local $[CH_4]/([H_4C] + [CH_4])$ concentration ratio. (An alternative, less conservative approach might set the product distribution ratio to one, indicating that waste, once destroyed by reaction, is never re-formed.) Results for the destruction of injected waste are presented in the columns labeled H_4C in Table 3. For these cases, entries in the CH_4 columns are normalized by the inlet methane mass flow rate.

Oxygen utilization data are presented in the columns labeled O_2. Since oxygen is never injected, the ratio denominator represents the inlet oxygen mass flow rate. The ratio of oxygen mass flow rate at equilibrium to that at the inlet is presented in the last column. The equilibrium calculation is based on the overall equivalence ratio and an

TABLE 3

Ratio of outlet to inlet mass fluxes of methane and H$_4$C in the calculations

A	ϕ_c	ϕ	CH$_4$		H$_4$C	
			End	Exit	End	Exit
1	0.8	1.0	1.775E-01	1.434E-17	1.362E-01	1.031E-17
2	0.8	1.0	2.389E-05	3.263E-18	1.092E-01	1.458E-14
1	0.533	1.0	1.379E-01	3.280E-19	1.899E-01	1.882E-15
2	0.533	1.0	6.229E-05	1.258E-19	1.667E-01	3.259E-16

adiabatic system. This represents the theoretical lower limit for the entries in the preceding two columns, and thus the maximum possible oxygen utilization.

Tables 2–3 reveal some interesting generalizations. First, we see that adequate DREs for injected wastes are never obtained within the cavity. DREs for waste surrogate (H_4C) at the end of the cavity increase slightly as far as the aspect ratio is increased. For the oxygen enriched case this occurs in spite of the injected streamline bifurcation, indicating that the shortened minimum residence time is not a serious problem, at least for a surrogate as reactive as methane. DREs at the end of the exit section are dramatically higher, indicating that mixing and reaction in the exit section play a critical role in the overall performance. Exit DREs for the injected cases indicate that destruction is essentially complete, a fact we attribute to high oxidation rates achieved when the recirculation and primary flame front gases are forced into the proximity in the exit section.

While we observe high DREs at both aspect ratios, we observe higher degrees of oxygen utilization in the longer cavity. This is a result of the increased surface area available for diffusive transport of oxygen across the stagnation streamline. Oxygen utilization actually comes closer to the theoretical maximum for the oxygen enriched core flame, indicating that waste incineration capcacity can be effectively increased by oxygen enrichment. If DREs are essentially complete but oxygen utilization is not. it is clear that products of incomplete combustion (PICs) must be formed. The generic PIC in the reduced mechanism is CO. Table 4 shows that this is indeed the case. We observe higher mass fractions of CO in the exhaust for shorter aspect ratios, indicating that while impingement of the primary and secondary flame fronts in the exit section is very effective in oxidizing CH_4 to CO, it is less effective is oxidizing CO to CO_2. This is reasonable because the oxidation of CO by OH (included in the gas–water shift reaction (R2) is very slow even if there are no other reactions effectively competing for OH and the time available for reaction is short.

TABLE 4

Comparison of outlet CO mass fraction to equilibrium

A	ϕ_c	ϕ	Y_{CO}		
			End	Exit	Eq.
1	0.7	0.7	5.264E-03	8.679E-03	9.302E-05
2	0.7	0.7	5.998E-03	3.851E-03	9.302E-05
1	0.8	0.8	7.973E-03	1.287E-02	5.621E-04
2	0.8	0.8	7.278E-04	5.380E-04	5.621E-04
1	0.9	0.9	1.272E-02	8.371E-03	2.501E-03
2	0.9	0.9	1.687E-03	1.410E-03	2.501E-03
1	1.0	1.0	2.045E-02	1.494E-02	8.931E-03
2	1.0	1.0	8.231E-03	7.622E-03	8.931E-03
1	0.8	1.0	2.693E-02	2.119E-02	8.931E-03
2	0.8	1.0	1.808E-02	1.616E-02	8.931E-03
1	0.533	1.0	5.543E-02	4.439E-02	3.941E-02
2	0.533	1.0	4.793E-02	4.011E-02	3.941E-02

SUMMARY AND CONCLUSIONS

We have developed a model capable of predicting flame shape/speed, and by implication heat release rate, under steady conditions in the relatively complex hydrodynamic environment of a dump combustor. Comparison of reacting and non reacting simulations indicates that the core flame has a very significant impact on the structure of recirculation cell, in some cases completely changing the nature of the flow within the cavity. Hence nonreactive simulations, which are frequently used due to the ease of computation, can be misleading where the structure of the recirculation cell is of interest.

We find that injection of additional fuel into the recirculation cell tends to stabilize a very lean core flame at the dump plane, effectively suppressing low frequency instabilities which, under resonant conditions, can result in highly strained, intermittent flames. Simulations indicate that in the absence of acoustic resonances, satisfactory destruction or removal efficiencies for injected, readily combustible wastes (e.g., those with oxidation kinetics similar to methane) can be expected. Very good DREs are obtained regardless of aspect ratio, but better oxygen utilization is obtained for longer aspect ratios due to increased surface area for mass transport. Adequate transport of excess oxygen from the fuel-lean core with the fuel-rich recirculation zone can be expected at the scale of the simulation, even for laminar flow. Therefore, it appears that oxygen enrichment may be effective strategy for increasing the capacity of an incinerator based on this type of device.

REFERENCES

Cadou, C., Logan, P., Karagozian, A., Marchant, R. and Smith, O. (1991). Laser Diagnostic Techniques in a Resonant Incinerator. *Environmental Sensing and Combustion Diagnostics. SPIE Proceedings Series,* 1434, 67, The Int. Society for Optical Engineering. Bellingham, WA.

Egolfopoulos, F. N., Cho, P. and Law, C. K. (1989). Laminar Flame Speeds of Methane-Air Mixtures Under Reduced and Elevated Pressures. *Combust. Flame.* 76, 375.

Fukutani, S., Kunioshi, N. and Jinno, H. (1990). Flame Structure of an Axisymmetric Hydrogen-Air Diffusion Flame. *Twenty-Third Symposium (International) on Combustion,* The Combustion Institute. p. 567.

Gatski, T. B., Grosch, C. E. and Rose, M. E. (1982). A Numerical Study of the Two-Dimensional Navier-Stokes Equations in Vorticity-Velocity Variables. *J. Comp. Phys.,* 48, 1.

Gaydon, A. G. (1974). *The Spectroscopy of Flames.* 2nd ed., John Wiley and Sons. New York. p. 287.

Ghia, U., Ghia, K. and Shin, C. T. (1982). High-Re Solutions for Incompressible Flow Using the Navier-Stokes Equations and a Multigrid Method, *J. Comp. Phys.,* 48, 387.

Harlow, W. H. and Welch, J. E. (1965). Numerical Calculation of Time-Dependent Viscous Incompressible Flow of Fluid with Free Surface. *Phys. Fluids,* 8(12), 2182.

Kee, R. J., Miller, J. A. and Jefferson, T. H. (1980). CHEMKIN: A General Purpose, Problem Independent, Transportable, Fortran Chemical Kinetics Code Package, Sandia National Laboratories Report SAND80-8003.

Kee, R. J., Warnatz, J. and Miller, J. A. (1983). A FORTRAN Computer Code Package for the Evaluation of Gas-Phase Viscosities, Conductivities and Diffusion Coefficients. Sandia National Laboratories Report SAND83-8209.

Logan, P., Lee, J. W., Lee, L. M., Karagozian, A. R. and Smith, O. I. (1991). Acoustics of a Low-Speed Dump Combustor, *Combust. Flame*, **84**, 93.

Marchant, R., Hepler, W., Smith, O. I., Willis, J., Cadou, C., Logan, P. and Karagozian, A. (1992). Development of a Two-Dimensional Dump Combustor for the Incineration of Hazardous Wastes. *Combust. Sci. Tech.*, **82**, 1.

Paczko, G., Lefdal, P. M. and Peters, N. (1986). Reduced Reaction Schemes for Methane, Methanol and Propane Flames, *Twenty-First Symposium (International) on Combustion*, The Combustion Institute, p. 739.

Patankar, S. V. (1980). *Numerical Heat Transfer and Fluid Flow*, McGraw-Hill, New York.

Patnaik, G., Kailasanath, K. and Oran, E. S. (1988). Detailed Numerical Simulations of Cellular Flames. *Twenty-Second Symposium (International) on Combustion*, The Combustion Institute. p. 1517.

Patnaik, G. and Kailasanath, K. (1990). Effect of Gravity on the Stability and Structure of Lean Hydrogen-Air Flames. *Twenty-Third Symposium (International) on Combustion*. The Combustion Institute. p. 1641.

Peaceman, D. W. and Rachford, H. H. (1955). The Numerical Solution of Parabolic and Elliptic Differential Equations. *J. Soc. Indust. Appl. Math.*, **3**(1), 28.

Peters, N. and Kee, R. J. (1987). The Computation of Stretched Laminar Methane–Air Diffusion Flames Using a Reduced Four-Step Mechanism. *Combust. Flame*, **68**, 17.

Schreiber, R. and Keller, H. B. (1983). Driven Cavity Flow by Efficient Numerical Techniques. *J. Comp. Phys.*, **49**, 310.

Smith, O. I., Marchant, R., Willis, J., Lee, L. M., Logan, P. and Karagozian, A. R. (1990). Incineration of Surrogate Wastes in a Low-Speed Dump Combustor. *Combust. Sci. Tech.*, **74**, 199.

Smooke, M. D., Lin, P., Lam, J. K. and Long, M. B. (1990). Computational and Experimental Study of Laminar Axisymmetric Methane–Air Diffusion Flame, *Twenty-Third Symposium (International) on Combustion*. The Combustion Institute, p. 575.

Smooke, M. D., Mitchell, R. E. and Keyes, D. E. (1989). Numerical Solution of 2-Dimensional Axisymmetric Laminar Diffusion Flames. *Combust. Sci. Tech.*, **67**(4), 85.

Vanka, S. P. (1986). Block-Implicit Multigrid Solution of Navier–Stokes Equations in Primitive Variables. *J. Comp. Phys.*, **65**, 138.

Willis, J. W., Lee, L-M., Karagozian, A. R. and Smith, O. I. (1993). Acoustic Alteration in a Dump Combustor Arising from Halon Addition. *Combust. Sci. Tech.*, **94**, 469.

Willis, J. W., Cadou, C., Mitchell, M., Karagozian, A. R. and Smith, O. I. (1994). Destruction of Liquid and Gaseous Waste Surrogates in an Acoustically Excited Dump Combustor. *Combust. Flame*. **99**(2), 280.

Zhang, L. B. (1990). A Second-Order Upwinding Finite Difference Scheme for the Steady Navier–Stokes Equations in Primitive Variables in a Driven Cavity with a Multigrid Solver. *Math. Modelling and Num. Anal.*, **24**(1), 133.
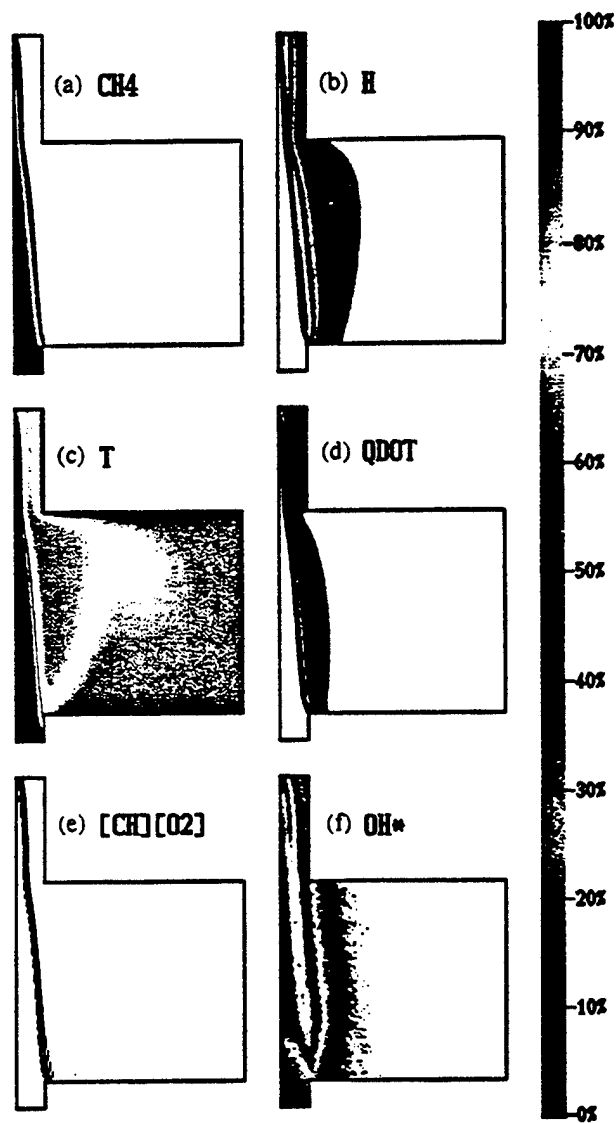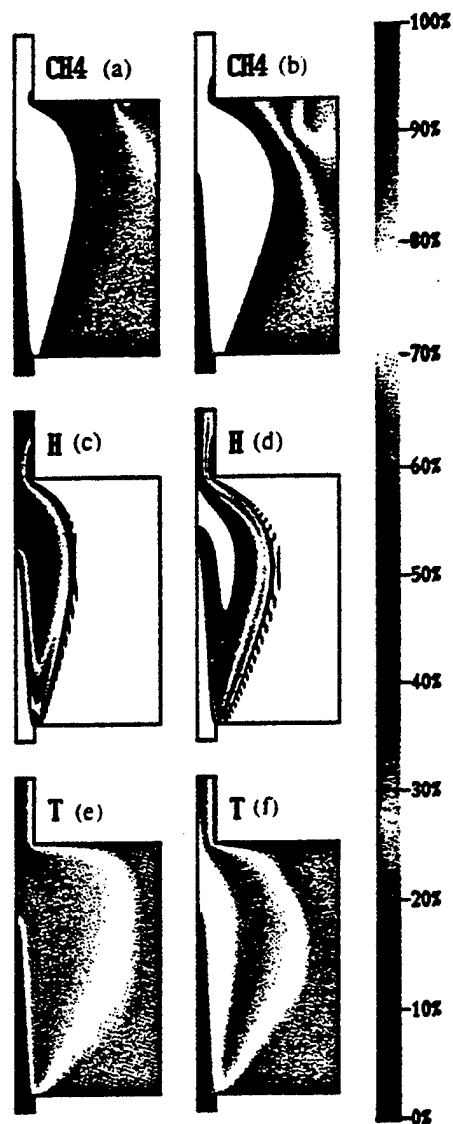
COMBUSTION SCIENCE AND TECHNOLOGY, Vol. 107/1-3. COLOR PLATE I.
See W. Hepler and O. Smith, Figure 4.
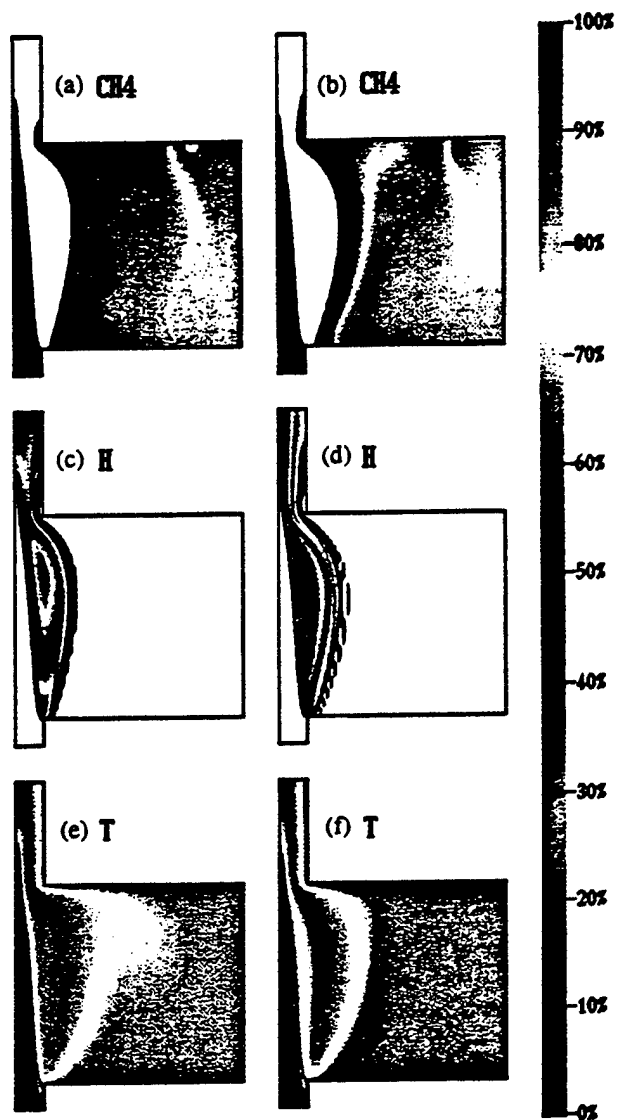
COMBUSTION SCIENCE AND TECHNOLOGY, Vol. 107/1-3. COLOR PLATE II.
See W. Hepler and O. Smith, Figure 7.
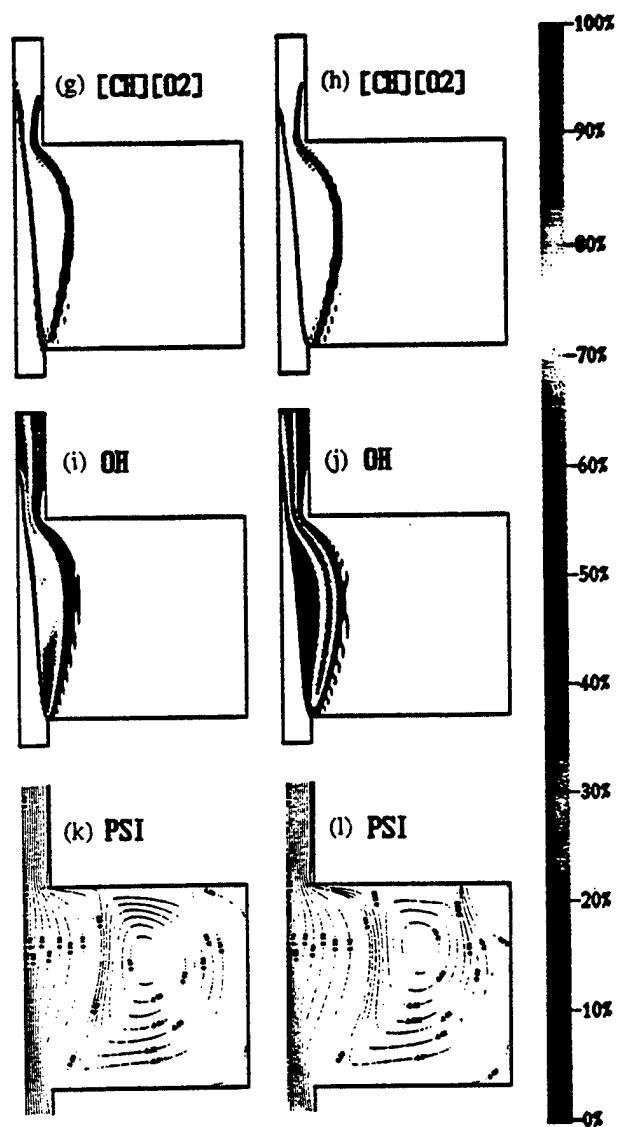
COMBUSTION SCIENCE AND TECHNOLOGY, Vol. 107/1-3. COLOR PLATE II.
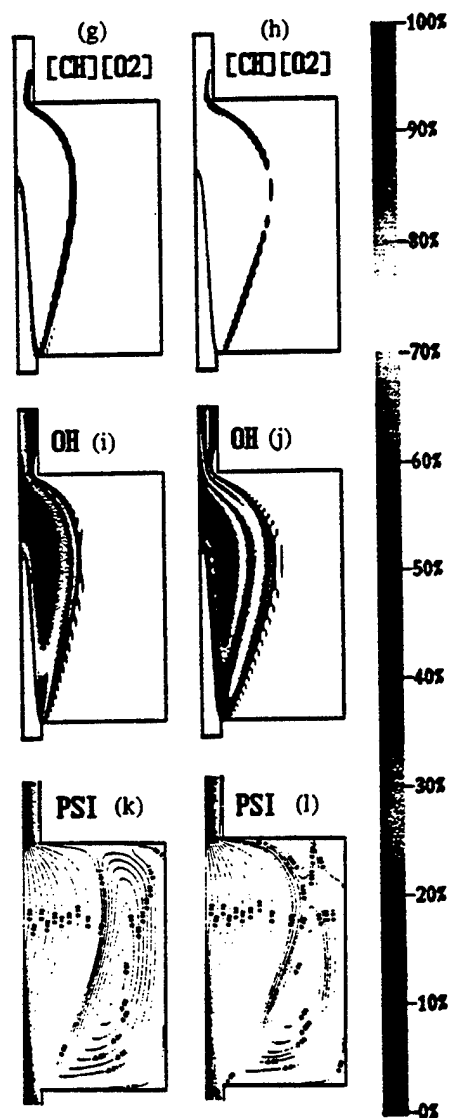See W. Hepler and O. Smith, Figure 7 (Continued).

COMBUSTION SCIENCE AND TECHNOLOGY, Vol. 107/1-3. COLOR PLATE III.
See W. Hepler and O. Smith, Figure 8.

COMBUSTION SCIENCE AND TECHNOLOGY, Vol. 107/1-3. COLOR PLATE III.
See W. Hepler and O. Smith, Figure 8 (Continued).

REFERENCE [10]

UNIVERSITY OF CALIFORNIA

Los Angeles

A Numerical Model

for

Turbulent Jets and Sprays

A thesis submitted in partial satisfaction of the

requirements for the degree Master of Science

in Aerospace Engineering

by

Mark Gustaf Mitchell

1996

REFERENCE [13]

Mixing enhancement in a lobed injector

L. L. Smith, A. J. Majamaki, I. T. Lam, O. Delabroy, A. R. Karagozian,[a] F. E. Marble, and O. I. Smith
Mechanical and Aerospace Engineering Department, University of California, Los Angeles, California 90095-1597

An experimental investigation of the non-reactive mixing processes associated with a lobed fuel injector in a coflowing air stream is presented. The lobed fuel injector is a device which generates streamwise vorticity, producing high strain rates which can enhance the mixing of reactants while delaying ignition in a controlled manner. The lobed injectors examined in the present study consist of two corrugated plates between which a fuel surrogate, CO_2, is injected into coflowing air. Acetone is seeded in the CO_2 supply as a fuel marker. Comparison of two alternative lobed injector geometries is made with a straight fuel injector to determine net differences in mixing and strain fields due to streamwise vorticity generation. Planar laser-induced fluorescence (PLIF) of the seeded acetone yields two-dimensional images of the scalar concentration field at various downstream locations, from which local mixing and scalar dissipation rates are computed. It is found that the lobed injector geometry can enhance molecular mixing and create a highly strained flowfield, and that the strain rates generated by scalar energy dissipation can potentially delay ignition in a reacting flowfield. © *1997 American Institute of Physics.* [S1070-6631(97)01003-9]

INTRODUCTION

The enhancement of fuel-air mixing processes in combustion systems can have substantial benefits with respect to combustion or incineration completeness[1] as well as NO_x or other toxic emission reduction[2-7] due to the reduced likelihood of the formation of stoichiometric diffusion flames. Rapid mixing associated with high fluid mechanical strain rates can suppress the ignition of diffusion flames,[8-10] instead forming premixed or partially premixed regions that can be made locally lean. When strain rates relax, ignition then occurs in a premixed mode, allowing a more complete consumption of the fuel species while reducing NO formation via the well known Zeldovich or thermal mechanism.[2] NO formation can then be limited to the (normally less important) "prompt" mechanism, suggesting the potential for significant NO emissions reduction.

The present study examines the flow and mixing processes associated with a fuel injector configuration which has the potential for such enhanced fuel-air mixing. This configuration, the "lobed" injector, is designed to generate very rapid initial mixing of reactants through streamwise vorticity generation[11] and associated high strain rates. A schematic diagram of the generic lobed injector is shown in Fig. 1. The injector consists of two initially flat, parallel plates which "grow" downstream into corrugated lobes as shown. Fuel is injected from between the plates into an axially coflowing airstream. The oppositely oriented secondary flows which develop along the sides of each of the lobes roll up into counter-rotating vortical structures oriented in the streamwise direction. The array of counter-rotating vortices strains fluid interfaces, in this case, those separating fuel and air.

The general principle of the lobed or louvered geometry has been applied to two-stream mixing in turbofan engines using a single corrugated plate or interface to mix initially separated fluids.[12-21] Skebe *et al.*[18] report that the secondary (cross-stream) flow induced by the lobed mixer is generated inviscidly by the mixer shape. As a consequence the streamwise circulation generated at each half of a lobe wavelength at the exit plane of the mixer may be predicted by inviscid analysis. This streamwise circulation Γ is shown to take the form[18]

$$\Gamma \approx C_1 \bar{U} h (\tan \alpha), \tag{1}$$

where C_1 is a constant which is sensitive to the specific lobe corrugation geometry, $\bar{U}$ is the mass-averaged streamwise velocity, h is the peak-to-peak lobe height, and α is the lobe half-angle (see Fig. 1). Vortex strength predicted by equation (1) is consistent with the experimental results in Ref. 18 as well as with those of McCormick and Bennett.[17] Recent numerical simulations by O'Sullivan *et al.*[21] in fact confirm that the estimate in (1) for vortex strength can even be extended to cases where the flow has separated, for lobe half-angles α as high as 25°.

Further experiments by Eckerle *et al.*[16] demonstrate strong secondary velocities near the exit plane of a lobed mixer which evolve into a sheet of streamwise vorticity and eventually coalesce into distinct streamwise counter-rotating vortices, with scales on the order of the mixer lobe width. Further downstream, turbulent breakdown of the streamwise vortices occurs, the location of which is dependent on the ratio of axial velocities on either side of the mixer. Vortex breakdown is seen by Eckerle *et al.*[16] to be the critical phenomenon that significantly enhances turbulent mixing due to the generation of smaller scale turbulence at breakdown. Yet Yu *et al.*[19] find that enhanced mixing can actually occur upstream of the region in which vortex breakdown occurs, due to the localized, rapid production of turbulent kinetic energy. Skebe *et al.*[18] and Yu *et al.*[19] further note that sinusoidally shaped lobes tend to produce lower secondary flow velocities

[a] Author to whom correspondence should be addressed: Phone: (310) 825-5653; Fax: (310) 206-4830; Electronic mail: ark@seas.ucla.edu
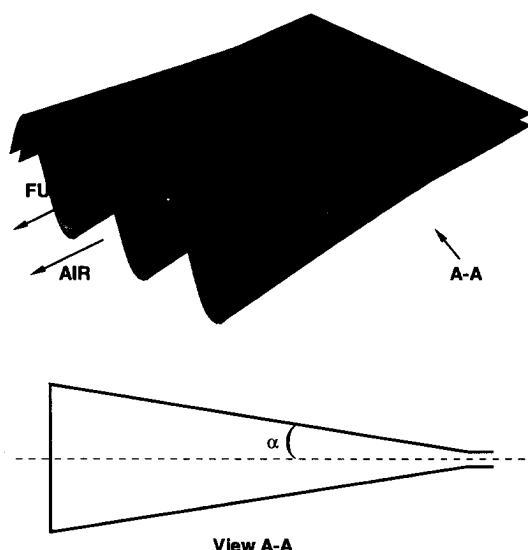
FIG. 1. Schematic of the general lobed injector geometry.

For combustor applications, the lobed injector (Fig. 1) reported in the present paper has several potential advantages over the lobed mixer. In the lobed injector, fuel is injected directly into the region of highest strain rates and highest streamwise vorticity. As a consequence, all of the fuel begins to be mixed with oxidizer within a rapidly strained flowfield, so that mixing may occur under conditions which delay ignition.[8-10] Further, when a thin "strip" of fuel is sandwiched between the oxidizer streams, ignition delay can occur at smaller strain rates than when fuel and oxidizer meet at only one independent interface,[29] hence ignition delay can be easier to achieve in a lobed injector rather than a lobed mixer geometry. The lobed injector also has an advantage over other types of fuel injection schemes in that energy losses and pressure drop are small, while mixing takes place over a comparatively short distance.[15]

The present study investigates mixing in a chemically nonreacting, isothermal flow downstream of two alternative lobed injector geometries, and compares mixing characteristics for each of these injectors with those for a straight (non-lobed) injector. The measured parameters of greatest interest for combustion applications are the scalar dissipation rate (from which the local strain rate may be estimated) and mixedness or unmixedness. These preliminary measurements were made in nonreacting flow in order to remove the effects of chemical reaction and heat release when comparing the net effect of streamwise vorticity generation on mixing and strain rate. It has also been suggested[30] that the local strain field in a cold, non-reacting turbulent flow may be used to predict local reactive flow quantities in an equivalent combusting flow, irrespective of the extent of chemical equilibrium in the reacting flowfield. Thus the present results have broader implications for the processes of mixing and ignition delay in a reacting flowfield associated with the lobed fuel injector.

and to mix less efficiently than a geometry with parallel lobe sidewalls due to the merger of sidewall boundary layers in the troughs of the former geometry. Flow instabilities in plane wakes and shear layers have been studied for a lobed mixer type geometry with small lobe ramp angles ($\alpha < 1°$) and moderate Reynolds numbers;[22,23] an uncoupled development of streamwise and spanwise vorticity by the lobed trailing edge is seen here. Axisymmetric lobed or corrugated mixer geometries have also been investigated;[24,25] these also demonstrate the propensity for streamwise vorticity generation.

Combustion in a lobed mixer geometry, with roughly equal regions of fuel and oxidizer initially separated by a single lobed splitter plate, has also been studied.[26-28] When using a lobed splitter plate, the flame spread angle is double the flame spread angle of a flat splitter plate, indicating enhanced mixing and an increased rate of flame propagation.[26] Mixing rate augmentation due to the addition of streamwise vorticity was found to be less sensitive to the detrimental effects of heat release than the mixing rate for a planar shear layer configuration.[28]

EXPERIMENTAL FACILITY AND METHODS

In the present experiments, three different fuel injector geometries were each studied in a low speed wind tunnel with a square test section having 9.5 cm sides, as shown schematically in Fig. 2. A blower at the wind tunnel exit drew air through the wind tunnel at speeds between 1 and 12
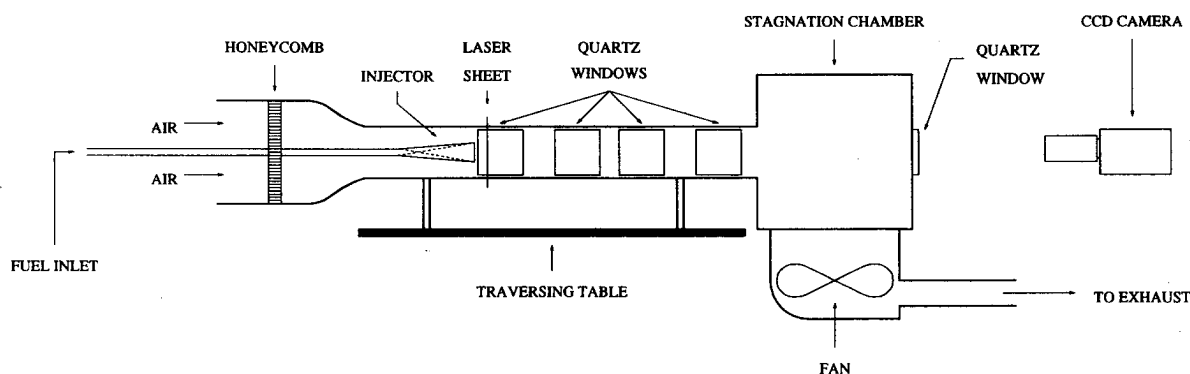

FIG. 2. Schematic of the wind tunnel and experimental apparatus.

Smith *et al.*

WALL THICKNESS 0.038 cm

INJECTOR A

GAP WIDTH
0.071 cm

λ = 1.905 cm

3.721 cm

WALL THICKNESS 0.076 cm

INJECTOR B

GAP WIDTH
0.056 cm

λ = 3.175 cm

3.518 cm

INJECTOR C

GAP WIDTH
0.056 cm

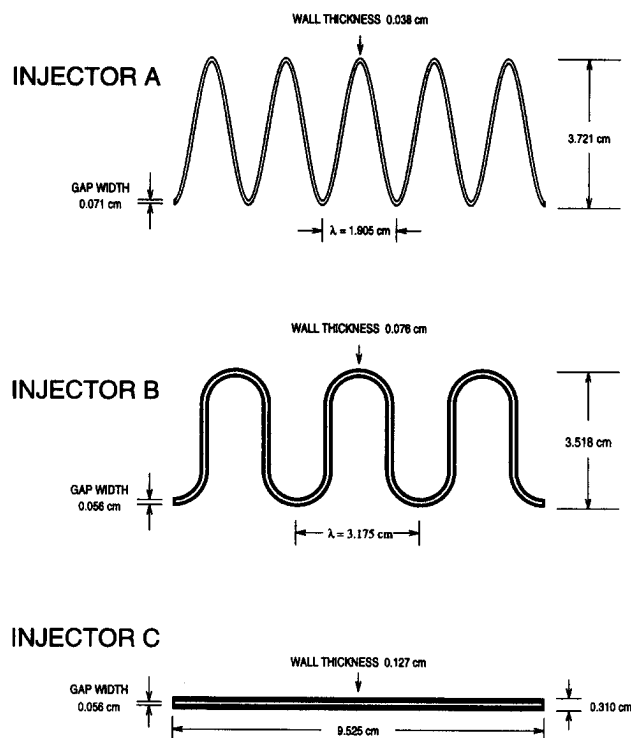WALL THICKNESS 0.127 cm

9.525 cm

0.310 cm

FIG. 3. Comparison of exit plane geometries for the three injectors examined in the present experiments.

m/s. The wind tunnel entrance contained a honeycomb section to straighten the flow, followed by a contraction section of 4:1 area ratio. Hot-wire measurements in the empty wind tunnel (injector removed) confirmed that the velocity profile was uniform in the test section and that turbulence levels were less than one percent of the free stream velocity, except within 1.2 cm of the wind tunnel walls. Quartz windows were fitted in the two vertical side walls of the test section and at the downstream end of the wind tunnel (in a plane perpendicular to the bulk flow) for optical access. The wind tunnel was attached to a traversing table to allow movement of the tunnel relative to a laser sheet passing through the side wall windows (see optics description below).

Three different fuel injectors were studied in this wind tunnel; exit plane geometries are shown schematically in Fig. 3. The lobed injectors were constructed of aluminum using an electron discharge machining or EDM device. Lobed injector A was constructed of two plates which were planar and parallel at the upstream edge and sinusoidally corrugated (lobed) at the downstream edge. The plates were separated by a small gap (on average, 0.071 cm at the downstream exit plane) through which fuel surrogate flowed; the wall thickness at the exit was approximately 0.038 cm. It should be noted that, due to machining inaccuracies, the gap width and wall thickness of this injector did vary along the exit plane lobes. Both thicknesses became more than twice the nominal value at the peaks and troughs of the sine wave. The wavelength λ of the lobes was 1.905 cm, and the peak-to-peak amplitude at the exit was 3.721 cm. The injector had five lobes and spanned the width of the wind tunnel; it was 15.2 cm in length (in the direction of flow), so that the lobes grew

at a constant ramp half-angle α of approximately 7°.

Lobed injector B had a wavelength of 3.175 cm, a peak-to-peak amplitude of 3.518 cm, a ramp half-angle of 6.6°, a slot width of 0.056 cm, and a wall thickness of approximately 0.076 cm at the exit plane. Wall thickness and slot width were much more uniform along the lobes in injector B than in injector A. In injector B, the three lobes were designed as rounded square waves with parallel side walls. The different geometry and larger wavelength-to-amplitude ratio were chosen in an attempt to reduce the boundary layer thickness in the injector troughs and to examine this effect on vortex roll-up and mixing effectiveness. Streamwise vortex strength Γ for injectors A and B was estimated using equation (1), with coefficients $C_1 = 2.4$ for injector A and $C_1 = 4.0$ for injector B, per the conclusions of Skebe et al.[18] for alternative lobe geometries.

Finally, injector C was a straight slot injector with the same slot width as in injector B, but with a wall thickness of 0.127 cm at the exit plane. There was no aerodynamic loading for injector C, and hence the principal mechanism for streamwise vorticity generation was removed. We examined this configuration in an attempt to isolate the effects of the lobes' streamwise vorticity generation on mixing from the effects of spanwise vorticity generation when the upper and lower air flow velocities were unequal and from the wakes caused by the finite thickness of the injector walls. Although the injector wall thicknesses differed on average between the lobed geometries and the straight geometry, for the flow conditions studied, this difference had little effect on mixing characteristics[31] as compared with the effect of slot width, which was on average about the same among the three injectors.

Carbon dioxide (CO_2) was used in the present experiments as a fuel surrogate because of its similarities to propane fuel in terms of molecular weight and diffusivity. Air was passed above and below the injector. CO_2 was supplied to the injector by a rectangular pipe of the same dimensions as the upstream edge of each injector. The pipe passed through the entrance and contraction sections of the wind tunnel, and was fastened flush with the upstream surfaces of the injector. This pipe separated the wind tunnel into two halves in the section between the contraction and the injector exit.

Each of the three injectors was tested for different sets of operating conditions. In flow set I, the axial velocities of all the streams (v_f for fuel, v_{aa} for the air flow above the injector, and v_{ab} for the air flow below the injector) were matched as closely as possible, although due to nonuniformities in the lobed injector geometry, the fuel velocities were not precisely matched with airflow, especially at the peaks and troughs in injector A. Flow set II involved matched air velocities but with a quantifiably higher fuel exit velocity. The last set of flow conditions, set III, consisted of mismatched upper and lower air velocities, with the fuel velocity set at the mean of the upper and lower air stream velocities. These flow conditions, appropriate for each of the three injectors, are summarized in Table I.

For the flow conditions outlined above, the momentum thicknesses above and below the lobe peaks (at the injection

Phys. Fluids, Vol. 9, No. 3, March 1997

Smith et al. 669

Flow condition set	Velocity range, m/s			Velocity ratio range	
	v_f	v_{aa}	v_{ab}	v_{ab}/v_{aa}	$2v_f/(v_{aa}+v_{ab})$
I	1–11.5	1–11.5	1–11.5	1	1
II	9–13.5	4.5	4.5	1	2–3
III	$\dfrac{v_{aa}+v_{ab}}{2}$	3–5	15–18	3–6	1

plane) were measured using a pitot probe. A summary of momentum thicknesses θ for the range of bulk airflow conditions examined is shown in Table II. Velocity measurements were made from the top of the wind tunnel to the bottom, vertically passing through the central peak of each lobed injector. The lobed shape clearly thins the boundary layer above the upper plate at the lobe peak and thickens the boundary layer below the lower plate at the lobe peak when compared with values for the flat injector C. While the differences in θ for the lobed injectors A and B were not as large as were expected, the differences may have been sufficient to have had an effect on downstream mixing characteristics. The momentum thicknesses for the lobe side walls, also shown in Table II, indicated a consistently thinner sidewall boundary layer thickness for injector B than for injector A, as would be expected from the design.

Scalar mixing was studied in the present experiments using planar laser-induced fluorescence (PLIF) imaging of acetone seeded in the CO_2 supply as a tracer. Acetone was excited with 308 nm laser light from a XeCl excimer laser, pumping several lines in the acetone $A \leftarrow X$ system, resulting in fluorescence proportional to the acetone concentration.[32] The 300 mJ, 25 ns laser beam was formed into a 5 cm tall sheet, passing through the wind tunnel test section perpendicular to the direction of bulk flow, with a sheet thickness of 600 μm or less. By moving the laser sheet along the streamwise axis of the tunnel, the evolution of the CO_2 or "fuel" concentration field driven by the developing vortices was visualized. Nonresonant fluorescence of acetone occurred over a broad spectrum from 350 to 650 nm, peaking at about 435 nm.

Acetone fluorescence was detected and imaged by an intensified CCD camera located outside the wind tunnel's downstream end window. Long-pass optical filters were placed in front of the imaging lens to prevent elastically scattered laser light from reaching the intensified CCD array. Acetone phosphorescence (200 μs lifetime) was rejected by gating the image intensifier on for a period of 500 ns. The CCD array contained 610×492 pixels, and the imaging lens and CCD array combination gave a pixel resolution of better than 200 μm.

To obtain quantitative measurements of acetone concentration, it was desirable to operate in the regime of linear fluorescence. Lozano et al.[32] give the fluorescence lifetime for acetone as 2.7 ns, and the absorption cross-section σ for 308 nm light as 1.6×10^{-20} cm^2. This gives a saturation photon flux density of $N_{sat}=2.3\times10^{19}$ photons/(cm^2−ns). In the present experiment the photon flux density was less than 1.2×10^{17} photons/(cm^2−ns), or more than 2 orders of magnitude smaller than the saturation photon flux density. The fluorescence signal was therefore linear in acetone concentration and linear in laser energy in the present experiments. While the acetone concentrations introduced into the injectors were about 90 000 ppm, the average concentration of acetone downstream in the test section was well below 90 000 ppm, and beam absorption was negligible.

All PLIF images of acetone (including calibration images) were normalized by laser pulse energy to correct for shot-to-shot variations in laser energy. The normalized PLIF images of mixing were corrected for intensity nonuniformity in the laser sheet and imaging optics and simultaneously calibrated for acetone concentration by dividing by the normalized calibration image on a pixel-by-pixel basis. Pixel values in the scalar concentration images varied between 0 and 1, representing the mass fraction Y of CO_2 at each pixel location.

These PLIF images were converted from CO_2 mass fraction (Y) images to mixture fraction (ξ) images using the relation $\xi = Y/Y_f$, where Y_f represents the maximum CO_2 ("fuel") mass fraction in the flowfield, at injection. Mixture fraction gradients $\nabla\xi$ were calculated from the pixel values using central differencing with a low-pass spatial filter. The scalar dissipation rate[9] χ was then calculated as $\chi = 2\mathscr{D}\nabla\xi\cdot\nabla\xi$, where D is the average mass diffusivity; in the present experiments, gradients were calculated in two dimensions only, since instantaneous images were obtained in relatively widely spaced two-dimensional planes at different points in time. While this evaluation clearly does not produce the complete value of scalar dissipation rate χ, it is reasoned that the component of χ arising from the streamwise or axial gradient in ξ should be roughly the same among the three different injectors for the same flow conditions. Hence *comparisons* of χ among the three injectors

TABLE II. Momentum thicknesses at exit plane for each injector.

Injector	Air speed (m/s)	Momentum thickness θ (cm)			
	$v_{aa}=v_{ab}$	θ above peak	θ below peak	θ left lobe	θ right lobe
A	4.7	0.0061	0.203	0.035	0.024
A	11.5	0.0092	0.179	0.033	0.024
B	4.9	0.011	0.198	0.024	0.018
B	12.1	0.013	0.148	0.018	0.019
C	4.4	0.081	0.095	–	–
C	11.4	0.072	0.132	–	–

should yield useful information with respect to the potential for ignition delay.

Following descriptions in Refs. 9, 30, and 33, it is possible to relate the scalar dissipation rate χ to strain rate ϵ at stoichiometric contours in a reactive flow, assuming the interfaces between fuel and air to behave as locally steady, opposed flow diffusion flames. In a flowfield in which only molecular mixing occurs at strained fluid interfaces, the relationship between strain rate and the dissipation rate of the conserved scalar takes the same form when applied at local maxima in χ or "strained dissipation layer" contours. This relationship between strain rate ϵ and scalar dissipation rate χ at a dissipation layer contour ξ_{st} is given by[30]

$$\epsilon = \frac{\pi\chi}{(\xi_+ - \xi_-)^2} \cdot \exp\left[2\left(\text{erf}^{-1}\left[\frac{\xi_{st} - \frac{1}{2}(\xi_+ + \xi_-)}{\frac{1}{2}(\xi_+ - \xi_-)}\right]\right)^2\right]. \quad (2)$$

As pointed out by Bish and Dahm,[30] the values of the conserved scalar well above and below the mixing interface, ξ_+ and ξ_-, can have a critical effect on the magnitude of the local strain rate experienced by the interface. This is especially important, yet is difficult to quantify, as dissipation layers are brought close together in a strain field as occurs in the present situation. In the present study, an automated technique was used[34] in which the dissipation layer contours ξ_{st} were determined by searching for local maxima in the scalar gradient field; it was at these locations that χ was computed. ξ_+ and ξ_- were then estimated locally by a curve fit to the error function solution.

The degree of molecular mixing within a flowfield may be quantified using the concept of mixedness[35,36] as well as the concept of unmixedness.[37,38] Both concepts quantify mixing in terms of the second moment of the scalar concentration field, enabling comparisons of the local scalar field to be made with the scalar field that would be present if the fluids were completely mixed or completely unmixed. In the present analysis the concept of unmixedness is used to quantify molecular mixing processes; this is defined as follows, after Dimotakis and Miller:[38]

$$U = \frac{\int_{Y_0}^{Y_1} (Y - \bar{Y})^2 \cdot p(Y) dY}{(Y_1 - \bar{Y})(\bar{Y} - Y_0)}, \quad (3)$$

where Y_0 and Y_1 are the minimum and maximum CO_2 mass fractions present within a given interrogation area, respectively, $p(Y)$ is the probability density function of the mass fraction, and the mean value of the mass fraction within the local interrogation area, $\bar{Y}$, is given by

$$\bar{Y} = \int_{Y_0}^{Y_1} Y \cdot p(Y) dY. \quad (4)$$

It is noted that the unmixedness U approaches unity for the case of completely non-molecularly mixed fluids, i.e., the second moment in the numerator of Eq. (3) approaches the denominator, and U approaches zero for complete molecular mixing of two fluids, i.e., a local mass fraction of $\bar{Y}$ everywhere within the integration region.

The degree of mixedness or unmixedness in a flowfield is sensitive to the integration area over which the second moment is evaluated, as pointed out by Marble.[35] For application of the present flowfield to combustion systems, the *global* mixing of all fuel and air present at each cross-section of the wind tunnel is not the most useful information, since ignition is not dependent on complete mixing of fuel with air far above and below the injector. It is the *local* degree of fuel-air mixing at strained stoichiometric interfaces that determines the local "equivalence ratio" (fuel-air ratio compared with stoichiometric) that would be present when ignition occurs in a reacting case, from which reactant consumption rates and local NO concentrations, for example, may be estimated. As a consequence, in quantitatively comparing mixing characteristics among the three injectors, we chose an integration area which included (at the injection plane) only a single side of each of the lobes for injectors A and B, with equivalent areas of surrounding air; a strip of injector C of equal length and surrounding area was chosen for comparison. Initial fluid interface lengths, areas of pure "fuel," areas of pure air, and total integration areas were also kept constant among the three injectors. Hence comparisons of unmixedness among the three injectors yielded differences which arose mostly from secondary flows along the lobes and subsequent streamwise vorticity generation and which were not due to increased interfacial length at injection.

The integration area and location for the evaluation of unmixedness were maintained as constants with downstream location. This is another difficulty with the concept of mixedness or unmixedness: As the integration area (laser sheet location) is moved downstream, new, entrained fluid is counted within the integration area, while some fluid originally present at injection may have been lost from the integration area. Yet as noted above, using the entire cross-sectional area of the wind tunnel (in which no fluid is gained or lost) as the integration area would yield nonuseful mixing information from a combustion perspective.

RESULTS

Flow visualization by smoke from $TiCl_4$ as well as acetone PLIF was performed in laminar flow with airstream velocities of 1 m/s in order to examine flow path and vortex rollup. Acetone PLIF images for the three-lobed injector B are shown in Fig. 4 for different downstream locations within the mixing tunnel. For these and all test conditions shown, effective streamwise circulation Γ was estimated using equation (1), with $C_1 = 2.4$ for injector A and $C_1 = 4.0$ for injector B, as suggested in Ref. 18. Figure 4 shows that, close to the injector exit, CO_2 remained concentrated within the region of injection, while further downstream, Kelvin-Helmholtz vortical structures formed along the injector lobes which eventually rolled up further downstream into large scale vortical structures, becoming concentrated near the injector inflection points. The vortical structures near the inflection points appeared to draw injector fluid from the peaks and troughs of the injector toward the center of the flowfield. The secondary, cross-stream velocities induced by the lobed
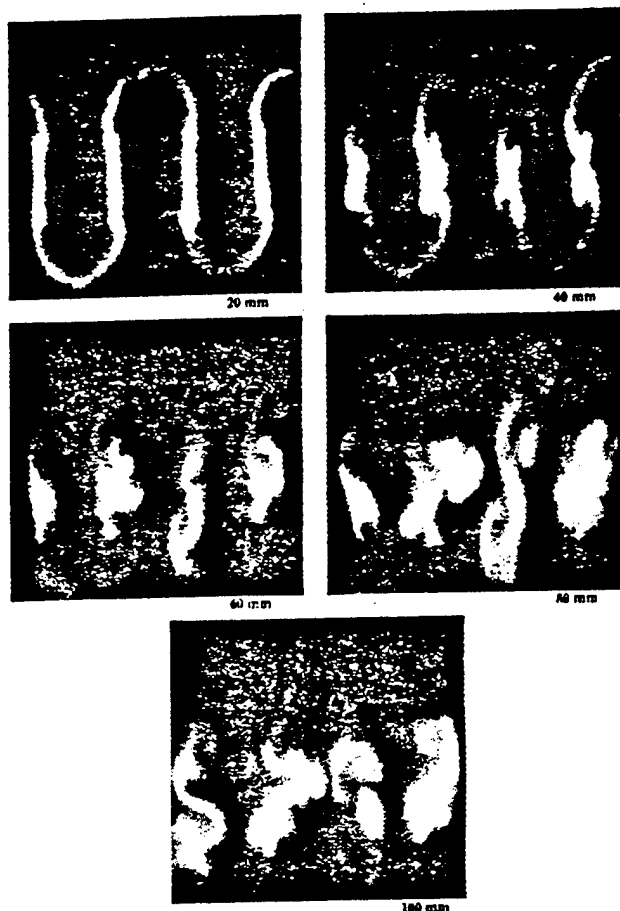
Phys. Fluids, Vol. 9, No. 3, March 1997

Smith *et al.*   671

FIG. 4. PLIF images of the mixture fraction of CO_2 for the 3-lobed injector B under flow condition I with low speed air flow at 1 m/s and estimated streamwise circulation $\Gamma \approx 0.016$ m²/s. Images are shown at locations 20, 40, 60, 80, and 100 mm downstream of injection.

FIG. 5. PLIF images of the mixture fraction of CO_2 for the 5-lobed injector A under flow condition I with high speed air flow at 11.5 m/s and estimated streamwise circulation $\Gamma \approx 0.132$ m²/s. Images are shown at locations 20, 40, 60, and 80 mm downstream of injection.

injector were also clearly visible in smoke images (not shown here), with a magnitude roughly 1/7th of the primary velocity.

Instantaneous acetone PLIF images in Figs. 5, 6, and 7 show flow evolution at higher speed air streams for injectors A, B, and C, respectively, again for flow condition I. As with the low speed flow, CO_2 remained concentrated within the region of injection close to the exit plane, later experiencing distortion by small scale vortical structures along the injector lobes (Figs. 5 and 6). Pairing and merger of these structures into larger vortical structures were observed to occur downstream, although evolution of the vortices into single large scale streamwise structures was not as obvious in these instantaneous images of the turbulent flow as in the laminar flow. Neither was any significant breakdown in the streamwise vortical structures noted within 100 mm of injection for flow condition I. Lobed injector B did demonstrate the ability of the streamwise vortical structures to draw injector fluid from the peaks and troughs toward inflection points; this was not observed in injector A, possibly due to the somewhat smaller effective circulation for injectors of this type as well as the injector's larger gap width at the peaks and troughs.

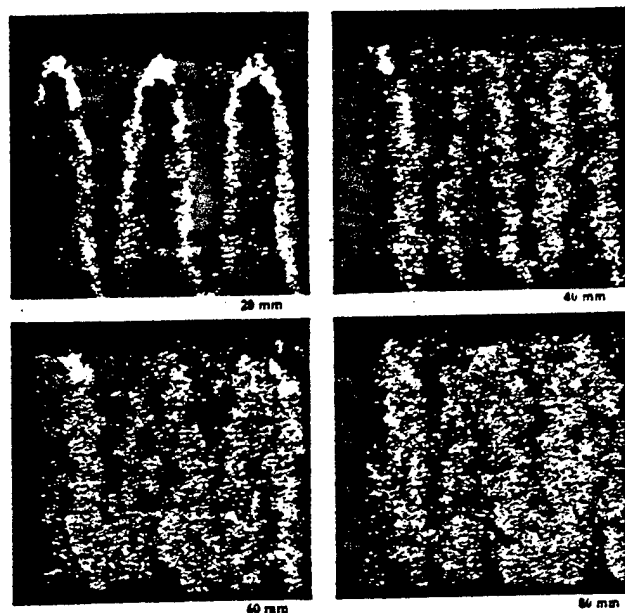Figures 8(a)–(c) and Figs. 9(a)–(c) show acetone PLIF images at a specific downstream location (60 mm) for each

injector at flow conditions corresponding to case III (at high speed) and case II (at moderate speed), respectively. The images in Fig. 8 for mismatched upper and lower air speeds are similar to those for matched air speeds in Figs. 5–7 and for other air velocity ratios examined.[39] Lobed injector B did appear to draw fluid from peaks and troughs toward injector inflection points more efficiently for this flow condition [Fig.
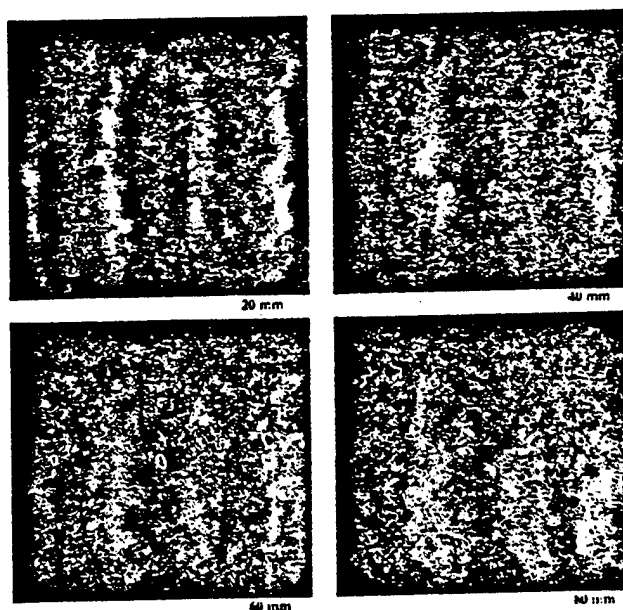

FIG. 6. PLIF images of the mixture fraction of CO_2 for the 3-lobed injector B under flow condition I with high speed air flow at 11.5 m/s and estimated streamwise circulation $\Gamma \approx 0.195$ m²/s. Images are shown at locations 20, 40, 60, and 80 mm downstream of injection.
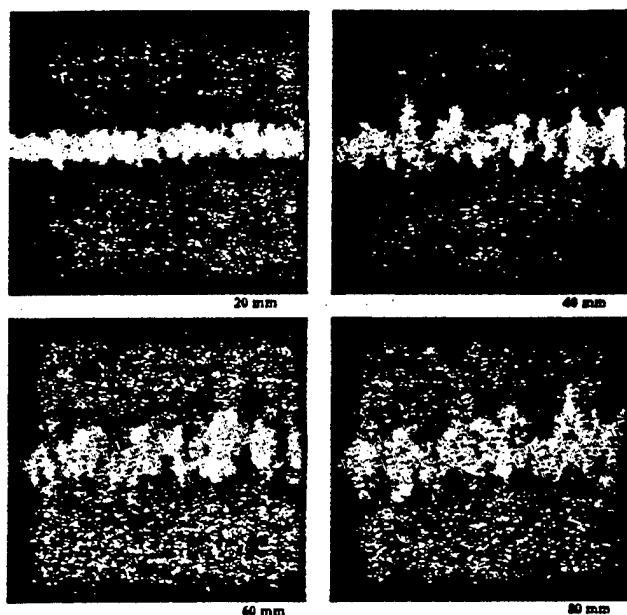
Smith *et al.*

FIG. 7. PLIF images of the mixture fraction of CO_2 for the straight injector C under flow condition I with high speed air flow at 11.5 m/s. Images are shown at locations 20, 40, 60, and 80 mm downstream of injection.

8(b)] than for flow condition I with equal air flow rates (Fig. 6), despite a somewhat higher estimated streamwise circulation in case I. Since the effective air speed mismatch was higher at the injector troughs than at the peaks for case III, one might expect a non-symmetric mixing of CO_2 and air between peaks and troughs, but this did not appear to have taken place for either lobed injector to any significant degree. The images in Fig. 9 for a moderate air speed ($v_{aa} = v_{ab} = 4.5$ m/s) and higher injectant velocity ($v_f/v_{aa} = 2$) in general are similar to PLIF images for other flow conditions, but there are a few important differences. Because the flow rate of CO_2 injectant is higher than that of air, injectant in the peaks and troughs of the lobed injectors persisted much further downstream in case II flows than in cases I or III. This is especially evident in Fig. 9(b) for lobed injector B. The higher injectant flow rate also acts to increase the generation of vorticity oriented normal to the streamwise direction; this can also assist with fuel-air mixing.

Quantitative mixing and strain field data may be extracted from mixture fraction images such as those shown in Figs. 5–9. Figures 10(a)–(d) show the downstream evolution of unmixedness U for several different cases of matched and unmatched air and fuel flow rates. As noted above, the interrogation areas for the computation of unmixedness were chosen to include one sidewall of each lobed injector, for comparison with unmixedness in an equal length of the straight injector C. Results for interrogation areas which included the whole injector flowfield (with differing interrogation widths to match interfacial lengths and fluid areas) gave similar results for unmixedness. Each data point in Figs. 10(a)–(d) is an average of four to six instantaneous PLIF images for the same flow conditions.

In all high flow rate cases [Figs. 10(a)–(c)], the lobed injectors appeared generally to produce a lower overall un-

mixedness (i.e., greater mixing) at each downstream location compared with the straight injector. Interestingly, for these high flow rate cases, the unmixedness for both lobed injectors was roughly the same near the exit [in Fig. 10(b) injector A had a somewhat higher unmixedness] and the unmixedness for the lobed injectors was generally lower than for the straight injector in the farfield. This suggests that initial streamwise vorticity generation by the lobed injectors did assist in increased initial mixing of injectant with surrounding air. Near a downstream location of $x = 35-45$ mm, however, the five-lobed injector A consistently produced a more rapid drop in U than did the three-lobed injector B. Acetone PLIF images (e.g., in Figs. 5 and 6) indicated that, upstream of roughly 40 mm, "fuel" injectant in each side lobe mixed with air fairly independently of the fuel in adjacent side lobes, whereas downstream of 40 mm, fuel from adjacent side lobes in injector A appeared to interact. The fuel in the more widely separated side lobes in injector B did not exhibit such interaction until much further downstream, if at all. Thus the sudden increase in mixing exhibited by injector A could have arisen from the transport of fuel from an adjacent lobe into the interrogation area of a given lobe. Airflow velocity mismatch [Figs. 10(b) and 10(c)] appeared to yield somewhat greater mixing than for equal upper and lower air speeds in both lobed injector geometries. This finding may be consistent with the observations of Yu et al.[19] that high turbulence generation occurs much sooner for mismatched air flows in lobed mixers (especially for sawtooth geometries similar to injector A) than for matched air flows.

Lower airspeeds and higher injectant velocities [Fig. 10(d)] were found to actually produce lower downstream fluid mixing (increased unmixedness) for the lobed injector geometries than for the straight injector. The lower axial air speeds for the flow condition here reduced the magnitude of secondary velocities in the lobes, apparently reducing the initial degree of mixing by streamwise circulation for the lobed injectors. Beyond this, the fuel-air velocity mismatch acted to increase spanwise vorticity generation, particularly for the straight injector, increasing its overall degree of fluid mixing. It is possible that the increase in spanwise vorticity for the lobed injectors was inhibited by the lobed shape, and hence was not sufficient to increase their overall mixing as compared with that for injector C.

It should be noted that for all three injectors the unmixedness U was less than 0.4 at the first measurement location, 20 mm downstream of the injector exit, for all flow conditions. This indicated very rapid initial mixing. In this respect the lobed injector geometry is different from the lobed mixer geometry studied by previous researchers.[12-21] In the lobed mixer geometry the stirring action generated by the lobe shape must penetrate well into both fluid streams before significant mixing occurs. In the lobed injector geometry, however, fuel is injected directly into the region of streamwise vorticity generation, and is rapidly mixed with and diluted by coflowing air. For this reason, the scalar boundary conditions for the dissipation layers must be carefully evaluated when estimating fluid mechanical strain rates, as noted previously.

The local scalar dissipation rate χ along strained dissipation contours ξ_{st} was determined as described previously

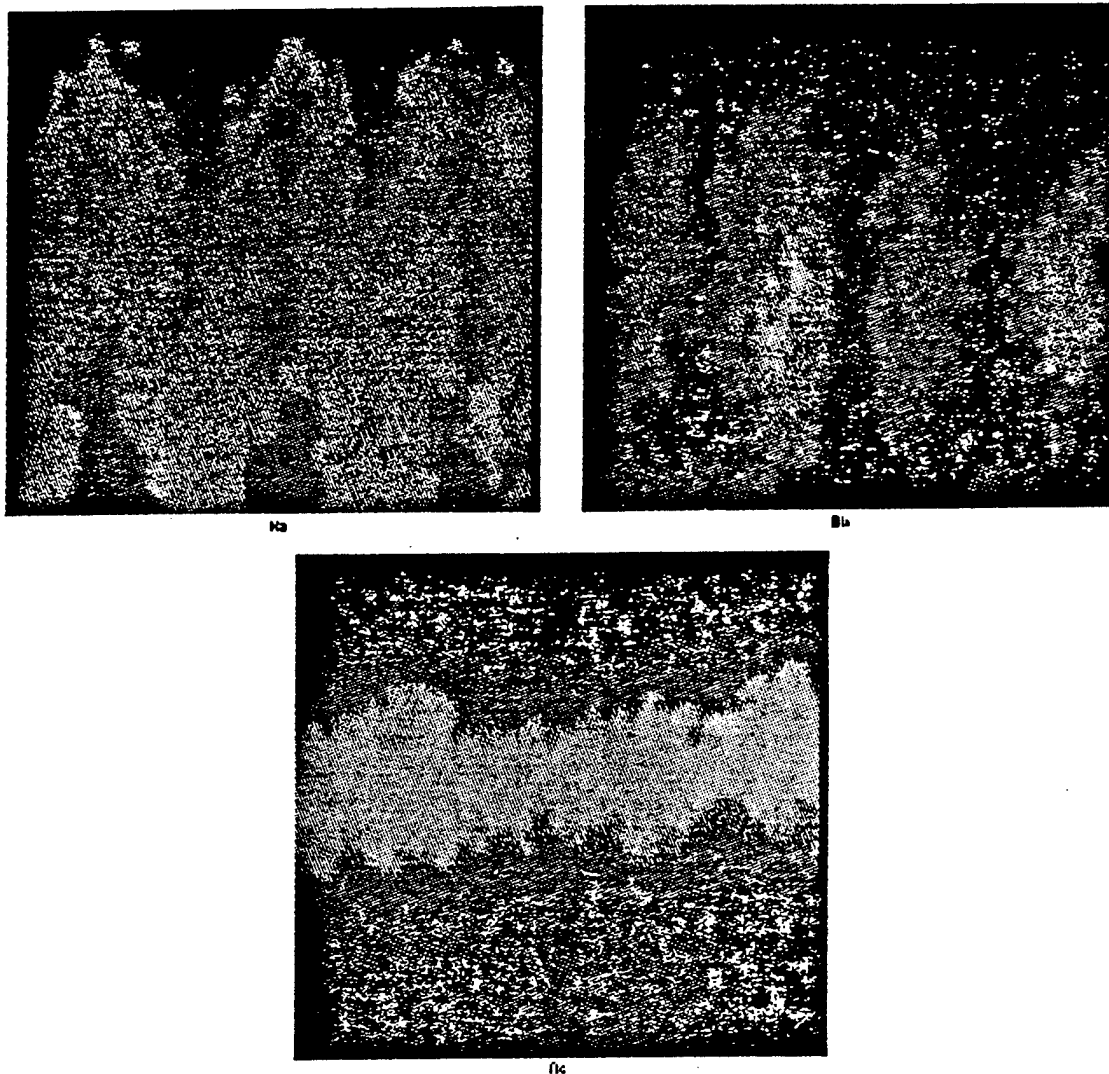Phys. Fluids, Vol. 9, No. 3, March 1997

Smith et al.   673

FIG. 8. PLIF images of the mixture fraction of CO_2 at the downstream location $x=60$ mm for flow condition III with high speed flow at an airflow velocity ratio $v_{ab}/v_{aa}=6$ with $v_{ab}=18$ m/s. Comparisons are made among injectors A (a), B (b), and C (c). Estimated streamwise circulations are 0.115 and 0.171 m^2/s for injectors A and B, respectively.

from acetone PLIF images. The average diffusivity D in the present experiments was taken to be 1.5×10^{-5} m^2/s. Plots of the *mean* value of χ along this contour of maximum scalar gradient at a given downstream location are shown in Figs. 11(a)–(d), for flow conditions corresponding to those in Figs. 10(a)–(d), respectively. It should be noted that in the nearfield ($x = 20$–40 mm downstream), each strained dissipation layer was resolved by 5–7 pixels, so that the gradient $\nabla \xi$, and hence χ, were probably underestimated. In the farfield ($x=60$–100 mm), layers were resolved by at least 20 pixels and hence χ values were probably more accurate. Again it should be noted that the scalar dissipation rates were calculated only from mixture fraction gradients in the planes of the PLIF images. As expected, for all flow conditions, scalar dissipation rates for the lobed injectors tended to start out relatively high, then to decay due to viscous dissipation with downstream distance. For straight injector C, χ did not vary substantially with downstream distance, suggesting no

significant rollup of spanwise vorticity into streamwise vortical structures by this injector.

In contrast to the results for unmixedness, at high as well as low speeds the three-lobed injector B appeared to create a much higher mean scalar dissipation rate than did either lobed injector A or straight injector C in nearly all cases [a notable exception being the equal flowrate case in Fig. 11(a)]. This observation is consistent with the generally higher effective streamwise circulation associated with rounded square wave lobes as in injector B as compared with the sinusoidal injector of type A for the same flow conditions.[18] The fact that injector B tended to draw fluid from the peaks and troughs toward the inflection points more effectively (in the PLIF images) provided further evidence of the higher degree of streamwise vorticity that was generated and thus the higher local strain rate. That the average scalar dissipation rate χ for injector A decayed to even lower levels in the farfield than for straight injector C for the airspeed
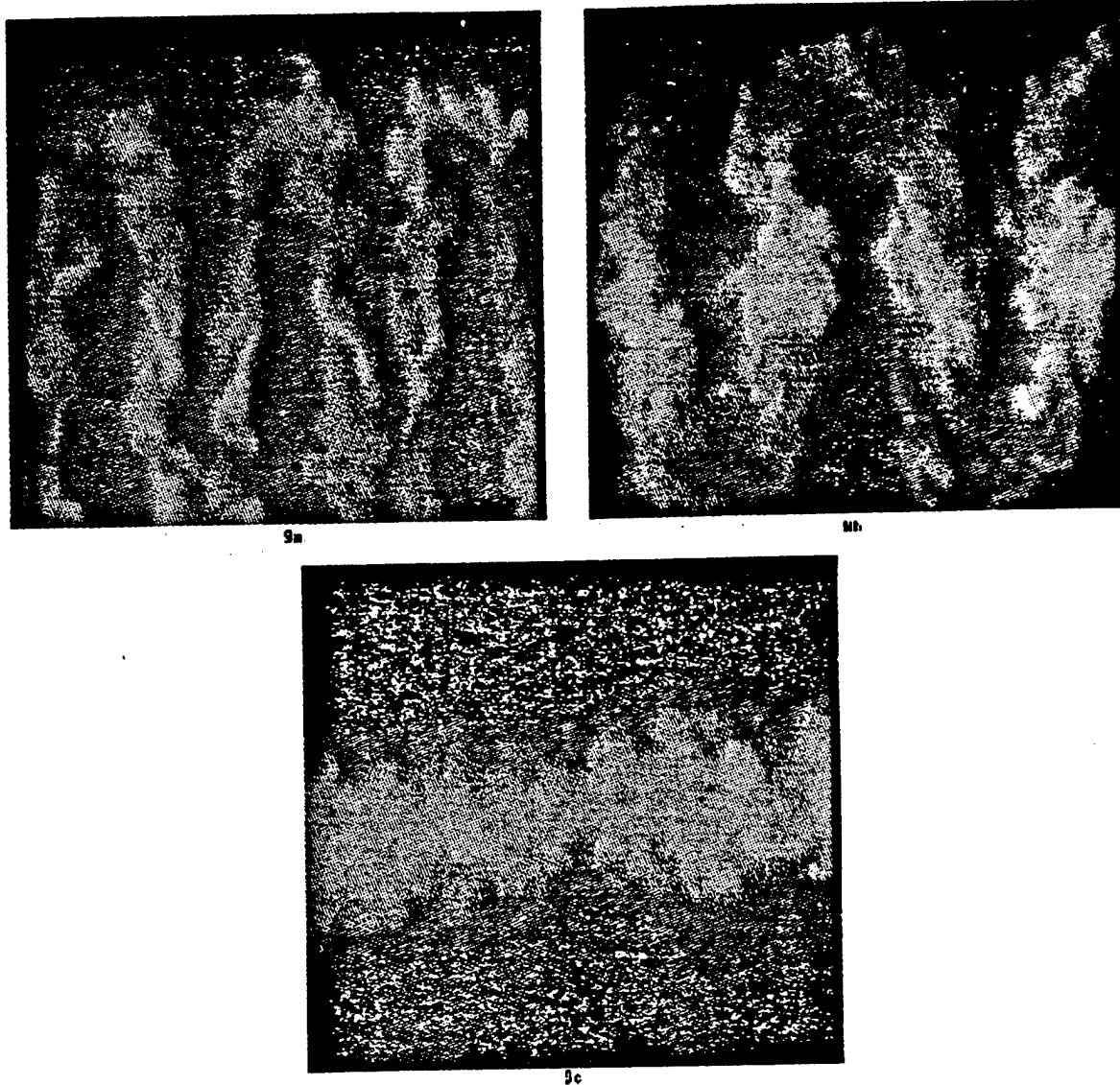
Smith *et al.*

FIG. 9. PLIF images of the mixture fraction of CO_2 at the downstream location $x = 60$ mm for flow condition II with low speed flow at a fuel-to-air velocity ratio $v_f/v_{aa} = 2$ with $v_{aa} = v_{ab} = 4.5$ m/s. Comparisons are made among injectors A (a), B (b), and C (c). Estimated streamwise circulations are 0.049 and 0.073 m²/s for injectors A and B, respectively.

mismatch cases [Figs. 11(b) and 11(c)] was unexpected. While airspeed mismatch appeared to assist lobed injector B with streamwise vorticity generation and vortex rollup [especially as seen in Fig. 11(b)], promoting the transport of injectant from peaks and troughs to inflection regions, airspeed mismatch appeared to inhibit initial streamwise vorticity generation and vortex rollup for injector A. A significant drop in χ is also generally seen for lobed injector B in the farfield. The very high initial scalar dissipation rates seen for both lobed injectors in Fig. 11(d) may be associated with the more coherent, laminar-like rollup of vortices seen in the PLIF images for this moderate flow condition (see Fig. 9).

The only case in which injector B did not create a higher mean scalar dissipation rate at high speeds is shown in Fig. 11(a) for flow condition I. As seen in the PLIF images, velocity mismatch in this flow regime (especially for condition III) seemed to augment the (initial) process of streamwise

vortex rollup for injector B and hence to augment fluid mechanical strain. This could explain the initial and overall drop in χ for injector B in Fig. 11(a) for matched airspeeds. The equal airspeed condition in Fig. 11(a) did cause the average scalar dissipation rate field generated by A to be increased above that for the other flow conditions shown, however. These findings for injector A may be consistent with the observations of Yu et al.[19] concerning the delay in vortex breakdown for matched air flows, yet the observations for injector B appeared to contradict Yu et al.'s results. The fact that Yu et al.'s results are for the lobed mixer rather than the lobed injector, however, may point to fundamental flowfield differences between the two configurations.

DISCUSSION

The results above provide information with respect to mixing and scalar energy dissipation characteristics for a
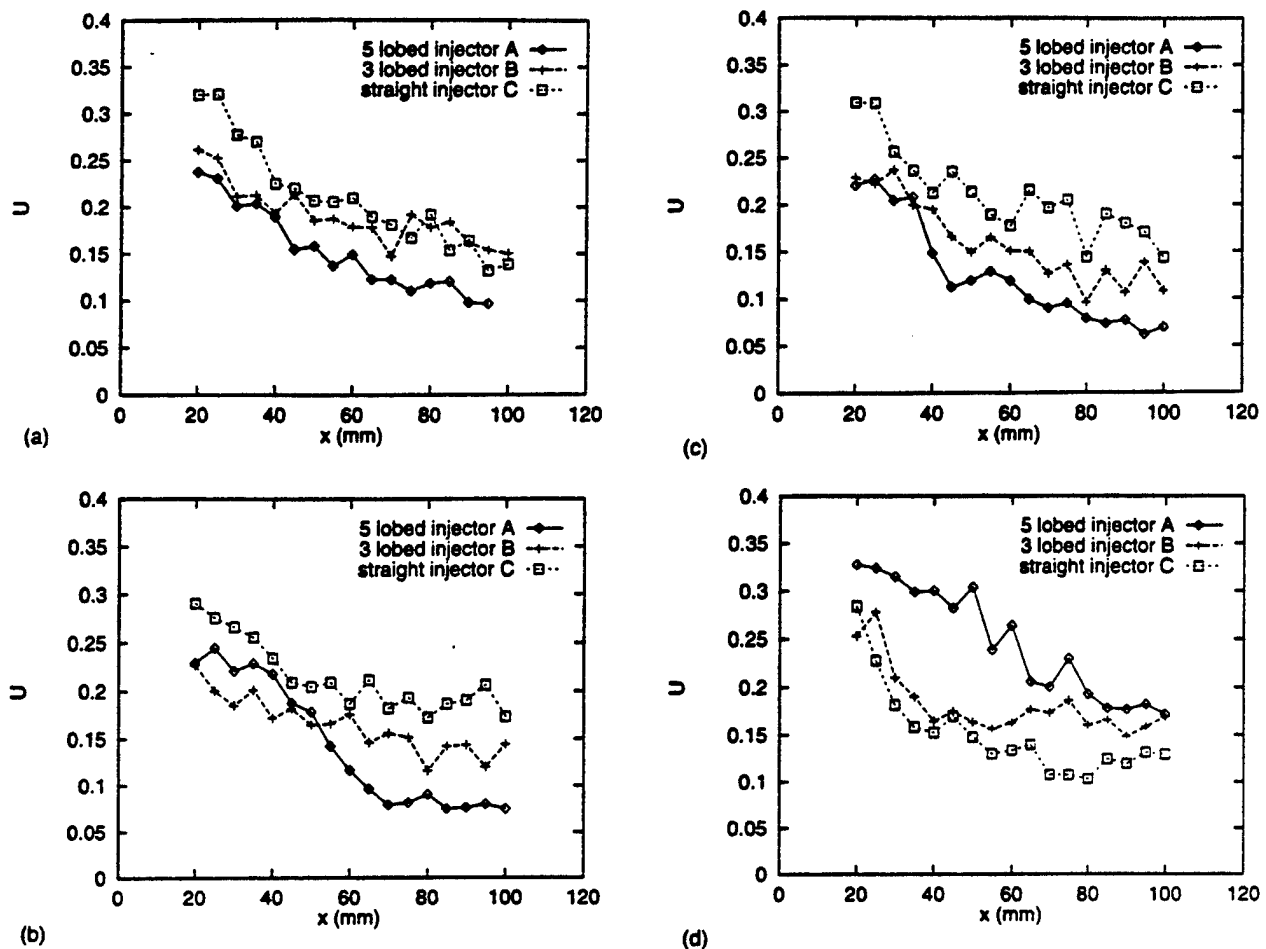
FIG. 10. Local unmixedness U as a function of downstream distance x (in mm) for different flow conditions, with comparisons made among injectors A. B. and C: (a) Flow condition I with high speed air flow at 11.5 m/s. Estimated streamwise circulations are 0.132 m²/s and 0.195 m²/s for injectors A and B. respectively. (b) Flow condition III with high speed flow at an airflow velocity ratio $v_{ab}/v_{aa}=4$ with $v_{ab}=16$ m/s. Estimated streamwise circulations are 0.110 m²/s and 0.163 m²/s for injectors A and B, respectively. (c) Flow condition III with high speed flow at an airflow velocity ratio $v_{ab}/v_{aa}=6$ with $v_{ab}=18$ m/s. Estimated streamwise circulations are 0.115 m²/s and 0.171 m²/s for injectors A and B, respectively. (d) Flow condition II with low speed flow at a fuel-to-air velocity ratio $v_f/v_{aa}=2$ with $v_{aa}=v_{ab}=4.5$ m/s. Estimated streamwise circulations are 0.049 m²/s and 0.073 m²/s for injectors A and B. respectively.

lobed injector configuration. It is seen that, for local fuel-air mixing along injector lobes, the five-lobed injector A consistently mixed fuel and air more rapidly than did the three-lobed injector B or straight injector C at high speeds, although transport of injectant from adjacent lobes clearly played a role in this quantification. Yet at high speeds the scalar dissipation rate, which is proportional to local strain rate, was in general substantially higher for injector B than for the other two injectors. If both rapid premixing and high strain rates are required for ignition delay and NO_x reduction in a combustion environment, the question arises as to which injector might be optimal.

In examining Eq. (2) relating strain rate and scalar dissipation rate, one finds that high strain rates can occur for large scalar dissipation rates χ but where values of (ξ_+, ξ_-) may be close to (1,0) or are roughly symmetric about $\xi_{st}=0.5$. High strain rates are also possible with smaller scalar dissipation rates if values of (ξ_+, ξ_-) differ more significantly from (1,0) or are more greatly skewed about the value of ξ_{st}. In the present study, both of these situations were observed for lobed injector geometries. The five-lobed

injector A mixed fluid more rapidly, diluting values of ξ_- and ξ_- downstream, but did not necessarily generate high values of χ, while the three-lobed injector B mixed less rapidly but could generate higher scalar dissipation rates. Estimates of strain rate at 80 mm (where there was sufficient dissipation layer resolution to compute ξ_+ and ξ_- with some confidence) confirmed the effects of these trends. For the high flow speed cases considered. the strain rates in the farfield were of the order 250–700 s⁻¹ for both lobed injectors A and B, and were of the order 300–400 s⁻¹ for the straight injector C. At 80 mm one would expect the average strain field to have relaxed due to viscous dissipation; this suggests that strain rates in the nearfield may have been higher, perhaps substantially so, than in the farfield.

The critical strain rate required for ignition delay of a 0.6 cm-thick propane fuel strip in air[29,40] for the present configuration is roughly of the order 400 s⁻¹. Recall that the strain rates estimated above for the present experiments were computed from only two components of the gradient in mixture fraction and as such should be regarded to be a minimal prediction of farfield strain rate. Hence it is reasonable to
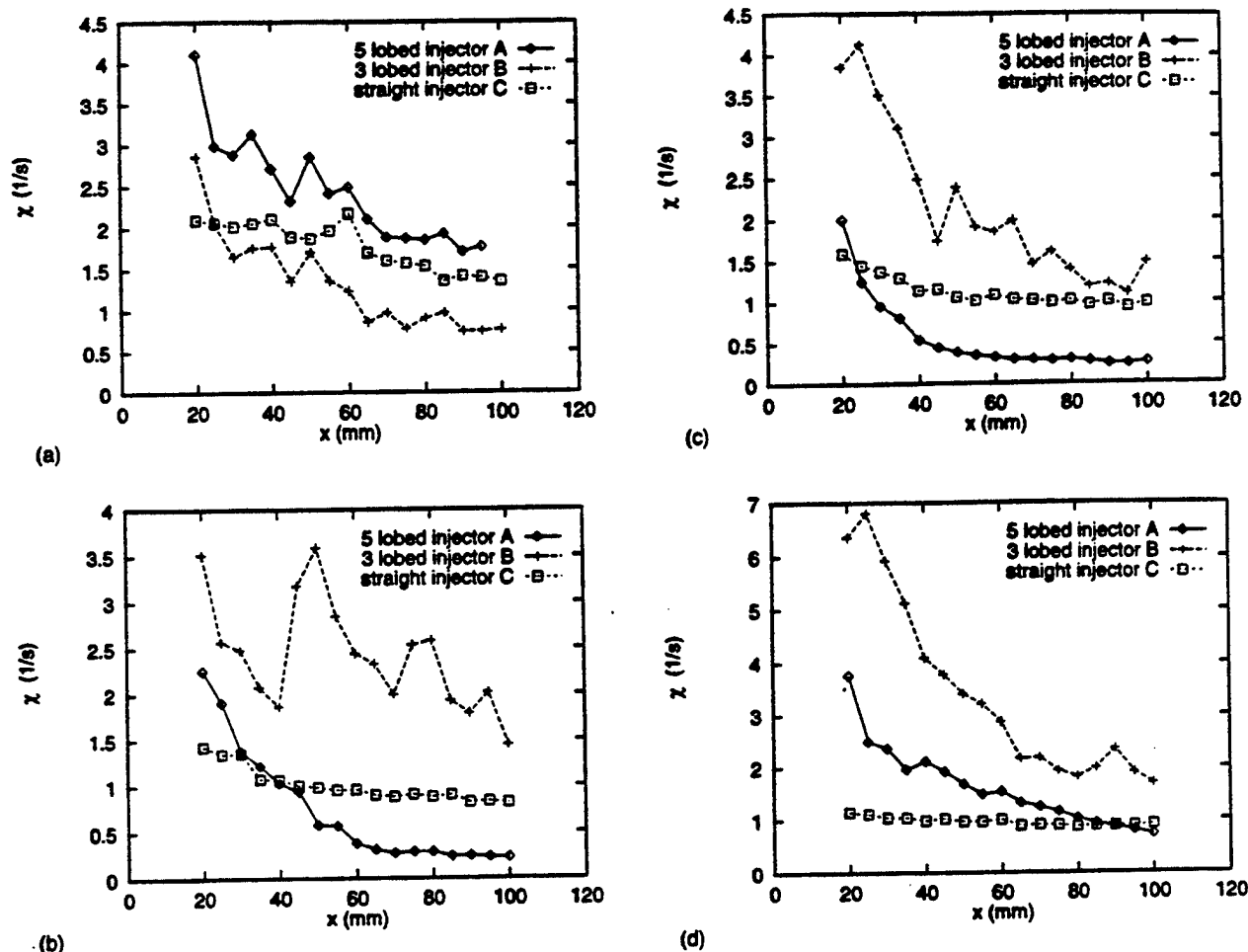
FIG. 11. Mean value of the scalar dissipation rate χ along the contours of maximum χ as a function of downstream distance x (in mm) for different flow conditions, with comparisons made among injectors A, B, and C: (a) Flow condition I with high speed air flow at 11.5 m/s. Estimated streamwise circulations are 0.132 m²/s and 0.195 m²/s for injectors A and B, respectively. (b) Flow condition III with high speed flow at an airflow velocity ratio $v_{ab}/v_{aa} = 4$ with $v_{ab} = 16$ m/s. Estimated streamwise circulations are 0.110 m²/s and 0.163 m²/s for injectors A and B, respectively. (c) Flow condition III with high speed flow at an airflow velocity ratio $v_{ab}/v_{aa} = 6$ with $v_{ab} = 18$ m/s. Estimated streamwise circulations are 0.115 m²/s and 0.171 m²/s for injectors A and B, respectively. (d) Flow condition II with low speed flow at a fuel-to-air velocity ratio $v_f/v_{aa} = 2$ with $v_{aa} = v_{ab} = 4.5$ m/s. Estimated streamwise circulations are 0.049 m²/s and 0.073 m²/s for injectors A and B, respectively.

estimate that there should be a delay of ignition in the nearfield region of a lobed fuel injector flowfield due to high fluid mechanical straining, and quite possibly further downstream as well, based on the present results. As seen in Figs. 10(a)–(c), this region just downstream of the injector is one during which fuel and air can strongly mix on a molecular level. Thus the present results suggest that a lobed fuel injector is likely to produce substantially premixed flame structures, more so than in a non-lobed injector, which is more likely to ignite stoichiometric diffusion flames.

CONCLUDING REMARKS

The present experimental study has demonstrated the potential of the lobed injector flowfield for applications to a low-NO$_x$ combustor. Both lobed injector designs under consideration demonstrated the possibility of an improvement in mixing over a straight (non-lobed) injector, in some cases by 30% or more. Fluid mechanical straining of the fuel-air interface, as evidenced by scalar dissipation rates, can be made significantly greater for the lobed injector geometries than

for non-lobed injection. Although accurate values of strain rate near the injection plane were not possible in the present experiments, farfield strain rates were sufficiently high to suggest that the nearfield strain rates (typically higher) will delay ignition of the fuel. It thus seems reasonable to expect that flame structures that form in the lobed fuel injector flowfield would be detached, locally premixed or partially premixed flames, with the potential for lowered NO production.

Phys. Fluids, Vol. 9, No. 3, March 1997

Smith et al.   677

[1]H.-H. Chen and J. F. Driscoll, "Nitric oxide levels of turbulent jet diffusion flames — effects of coaxial air and other mixing parameters," *Twenty-third Symposium (International) on Combustion* (The Combustion Institute, Pittsburgh, PA, 1990), pp. 281–288.

[2]C. T. Bowman, "Control of combustion-generated nitrogen oxide emissions: Technology driven by regulation," *Twenty-fourth Symposium (International) on Combustion* (The Combustion Institute, Pittsburgh, PA, 1992), pp. 859–878.

[3]J. F. Driscoll, R. H. Chen, and Y. Yoon, "Nitric oxide levels of turbulent jet diffusion flames — Effects of residence time and Damkohler number," *Combust. Flame* **88**, 37 (1992).

[4]S. R. Turns, F. H. Bandaru, and E. R. Maund, "Oxides of nitrogen emissions from turbulent jet flames — 2. Fuel dilution and partial premixing effects," *Combust. Flame* **93**, 255 (1993).

[5]G. Leonard and S. Correa, "NO$_x$ formation in premixed high-pressure lean methane flames," 2nd ASME Fossil Fuel Combustion Symposium, ASME/PD **30**, 69 (1990).

[6]T. F. Fric, "Effects of fuel-air unmixedness on NO$_x$ emissions," J. Propulsion Power **9**, 708 (1993).

[7]J. P. Gore and N. J. Zhan, "NO$_x$ emission and major species concentrations in partially premixed laminar methane/air co-flow jet flames," *Combust. Flame* **105**, 414 (1996).

[8]A. Liñan and A. Crespo "An asymptotic analysis of unsteady diffusion flames for large activation energies," *Combust. Sci. Tech.* **14** 95 (1976).

[9]N. Peters, "Local quenching due to flame stretch and non-premixed turbulent combustion," *Combust. Sci. Tech.* **30**, 1 (1983).

[10]D. Thévenin and S. Candel, "Effect of variable strain on the dynamics of diffusion flame ignition," *Combust. Sci. Tech.* **91**, 73 (1993).

[11]A. Roshko, "The mixing transition in free shear flows," in *The Global Geometry of Turbulence*, edited by J. Jimenez (Plenum, New York, 1991).

[12]T. G. Tillman, R. W. Paterson, and W. M. Presz, "Flow structure in a periodic axial vortex array," AIAA Paper No. 87-0610 (1987).

[13]J. K. Elliott, T. A. Manning, Y. J. Qiu, E. M. Greitzer, C. S. Tan, and T. G. Tillman, "Computational and experimental studies of flow in multi-lobed forced mixers," AIAA Paper No. 92-3568 (1992).

[14]A. K. S. Fung, "Modeling of mixer-ejector nozzle flows," M.S. thesis, Department of Aeronautics and Astronautics, Massachusetts Institute of Technology, February, 1995.

[15]W. M. Presz, B. L. Morin, and R. G. Gousy, "Forced mixer lobes in ejector designs," J. Propulsion Power **4**, 350 (1988).

[16]W. A. Eckerle, H. Sheibani, and J. Awad, "Experimental measurements of vortex development downstream of a lobed forced mixer," J. Eng. Gas Turbines Power **114**, 63 (1992).

[17]D. C. McCormick and J. C. Bennett, "Vortical and turbulent structure of a lobed mixer free shear layer," AIAA J. **32**, 1852 (1994).

[18]S. A. Skebe, R. W. Paterson, and T. J. Barber, "Experimental investigation of three-dimensional forced mixer lobe flow fields," AIAA Paper No. 88-3785-CP (1988).

[19]S. C. M. Yu, J. H. Yeo, and J. K. L. Teh, "Velocity measurements downstream of a lobed-forced mixer with different trailing-edge configurations," J. Propulsion Power **11**, 87 (1995).

[20]S. C. M. Yu, X. G. Xu, and T. H. Yip, "Effects of initial boundary layers to the lobed mixer trailing streamwise vorticity," J. Propulsion Power **12**, 440 (1996).

[21]M. N. O'Sullivan, J. K. Krasnodebski, I. A. Waitz, E. M. Greitzer, and C. S. Tan, "Computational study of viscous effects on lobed mixer flow features and performance," J. Propulsion Power **12**, 449 (1996).

[22]J. C. Lasheras and H. Choi, "Three-dimensional instability of a plane free shear layer: An experimental study of the formation and evolution of streamwise vortices," J. Fluid Mech. **189**, 53 (1988).

[23]E. Meiburg and J. C. Lasheras, "Experimental and numerical investigation of the three-dimensional transition in plane wakes," J. Fluid Mech. **190**, 1 (1988).

[24]V. M. Belovich, M. Samimy, and M. F. Reeder, "Dual stream axisymmetric mixing in the presence of axial vorticity," J. Propulsion Power **12**, 178 (1996).

[25]K. B. M. Q. Zaman, M. F. Reeder, and M. Samimy, "Control of an axisymmetric jet using vortex generators," Phys. Fluids **6**, 778 (1994).

[26]J. B. McVey, "Observation of the effect of streamwise vorticity on the spreading of flames in high speed flow," *Combust. Sci. Tech.* **60**, 447 (1988).

[27]J. B. McVey and J. B. Kennedy, "Flame propagation enhancement through streamwise vorticity stirring," AIAA Paper No. 89-0619 (1989).

[28]I. A. Waitz and D. S. Underwood, "Effect of heat release on streamwise vorticity enhanced mixing," AIAA Paper No. 95-2471 (1995).

[29]T. J. Gerk and A. R. Karagozian, "Ignition delay associated with strained fuel layers," *Twenty-sixth Symposium (International) on Combustion* (The Combustion Institute, Pittsburgh, PA, 1996), pp. 1095–1102.

[30]E. S. Bish and W. J. A. Dahm, "Strained dissipation and reaction layer analyses of nonequilibrium chemistry in turbulent reacting flows," *Combust. Flame* **100**, 457 (1994).

[31]R. D. Mehta, "Effect of velocity ratio on Plane mixing layer development: Influence of the splitter plate wake," Exp. Fluids **10**, 194 (1991).

[32]A. Lozano, B. Yip, and R. K. Hanson, "Acetone: A tracer for concentration measurements on gaseous flows by planar laser-induced fluorescence," Exp. Fluids **13**, 369 (1992).

[33]N. Darabiha and S. Candel, "The influence of the temperature on extinction and ignition limits of strained hydrogen-air diffusion flames," *Combust. Sci. Tech.* **86**, 67 (1992).

[34]I. Lam, "Computation of scalar dissipation rate and strain rate in lobed injector flowfields," M.S. thesis, University of California, Los Angeles, 1996.

[35]F. E. Marble, "Mixing, diffusion, and chemical reaction of liquids in a vortex field," *Chemical Reactivity in Liquids*, edited by M. Moreau and P. Turq (Plenum Press, New York, 1987), pp. 581–596.

[36]B. M. Cetegen and N. Mohamad, "Experiments on liquid mixing and reaction in a vortex," J. Fluid Mech. **249**, 391 (1993).

[37]P. V. Danckwertz, "The definition and measurement of some characteristics of mixtures," Appl. Sci. Res. A **3**, 279 (1952).

[38]P. E. Dimotakis and P. L. Miller, "Some consequences of the boundedness of scalar fluctuations," Phys. Fluids A **2**, 1919 (1990).

[39]A. J. Majamaki, "A mixing enhancement study in a lobed fuel injector," M.S. thesis, University of California, Los Angeles, 1996.

[40]T. J. Gerk, "Mixing, ignition, and burning processes in strained fuel layers," M.S. thesis, University of California, Los Angeles, 1996.

Smith *et al.*

REFERENCE [14]

UNIVERSITY OF CALIFORNIA

Los Angeles

A Mixing Enhancement Study in a Lobed Fuel Injector

A thesis submitted in partial satisfaction of the

requirements for the degree Master of Science

in Mechanical Engineering

by

Ari J. Majamaki

1996

REFERENCE [15]

UNIVERSITY OF CALIFORNIA

Los Angeles

Computation of Scalar Dissipation Rate and Strain Rate

in Lobed Injector Flowfields

A thesis submitted in partial satisfaction of the

requirements for the degree Master of Science

in Mechanical Engineering

by

Ivan Tinlung Lam

1996

REFERENCE [16]

NOx EMISSIONS FROM A LOBED FUEL INJECTOR/BURNER

M. G. Mitchell, L. L. Smith,
A. R. Karagozian, and O. I. Smith
Department of Mechanical and Aerospace Engineering
University of California
Los Angeles, CA 90095-1597

Corresponding Author:

Professor A. R. Karagozian
Department of Mechanical and Aerospace Engineering
46-147D Engineering IV, UCLA
Los Angeles, CA 90095-1597
U.S.A.
Phone: (310) 825-5653; FAX: (310) 206-4830
E-mail: ark@seas.ucla.edu

1

NOx EMISSIONS FROM A LOBED FUEL INJECTOR/BURNER

M. G. Mitchell, L. L. Smith, A. R. Karagozian, and O. I. Smith
University of California, Los Angeles, CA 90095-1597

Abstract

The present experimental study examines the performance of a novel fuel injector/burner configuration with respect to reduction in nitrogen oxide NO_x emissions. The lobed injector/burner is a device in which very rapid initial mixing of reactants can occur through strong streamwise vorticity generation, producing high fluid mechanical strain rates which can delay ignition and thus prevent the formation of stoichiometric diffusion flames. Further downstream of the rapid mixing region, this flowfield produces a reduced effective strain rate, thus allowing ignition to occur in a premixed mode, where it is possible for combustion to take place under locally lean conditions, potentially reducing NO_x emissions from the burner. The present experiments compare $NO/NO_2/NO_x$ emissions from a lobed fuel injector configuration with emissions from a straight fuel injector to determine the net effect of streamwise vorticity generation. Preliminary results show that the lobed injector geometry can produce lean premixed flame structures, while for comparable flow conditions, a straight fuel injector geometry produces much longer, sooting diffusion flames or slightly rich premixed flames. NO_x measurements show that emissions from a lobed fuel injector/burner can be made significantly lower than from a straight fuel injector under comparable flow conditions.

Introduction

The necessity to progressively reduce the production of nitrogen oxides in aircraft combustion processes arises both from legislated and anticipated environmental standards and from the need to meet public environmental concerns. Because NO_x formation rates in general are strongly temperature dependent, it becomes effectively prohibitive for the combustion of fuel to take place near its stoichiometric mixture ratio, a fact that may render nonpremixed combustion inappropriate because of the diffusion flames that are prevalent[1–5]. The capability to mix fuel and air very rapidly relieves this problem to some extent[3, 6]; with rapid mixing the formation of stoichiometric diffusion flames is discouraged in favor of premixed flames, which can be made locally lean or locally rich and thus reduce NO_x

emissions[5, 8]. The rapid mixing principle is, in fact, the basis of two low NO_x burners proposed for the High Speed Civil Transport (HSCT) turbofan engine under supersonic flight conditions[7]. Partial premixing of fuel and air can reduce NO emissions due to a reduction in flame temperature and reduction in species residence times[4, 6], but emissions can also increase with partial premixing due to reduced radiative heat loss, which effectively increases flame temperatures[6]. Thus there appear to exist optimal levels of partial premixedness for which NO_x emissions (as well as emissions of CO and other species) can be minimized, as recently shown by Gore and Zhan[8].

The rapid mixing rates required to accomplish overall NO_x reduction in combustors almost invariably necessitate pressure losses in both the fuel and air streams, which may present an undesirable consumption of pumping power. Moreover, ultra high pressure ratio engines (60:1 or greater) with turbine inlet temperatures around $3000°$ F, proposed for the Advanced Subsonic Transport Aircraft, could necessitate combustor equivalence ratios which are relatively high (approaching stoichiometric). Thus, rapid mixing could become essential in advanced aircraft in order to meet emissions goals.

The fundamental goal of the present research program is to examine the combustion performance of a novel fuel injector/burner which has the potential for significant reduction in nitrogen oxide emissions when compared with conventional aircraft burners. The lobed fuel injector, shown schematically in Figure 1, is a device in which very rapid initial mixing of reactants can occur through streamwise vorticity generation[9], producing high strain rates which can delay ignition[10–13]. This streamwise vorticity is created by oppositely oriented secondary flows which develop along the sides of each of the lobes; these flows roll up into counter-rotating vortical structures oriented in the streamwise direction. Further downstream of the development of the vortical structures, the strain field relaxes, producing a reduced effective strain rate and potentially allowing ignition to occur in a premixed or partially premixed mode, where it is possible for combustion to take place under locally lean conditions. This rapid premixing before ignition may potentially reduce NO_x emissions from the burner under specific critical conditions.

The general principle of the lobed or louvred geometry has been applied to two-stream mixing in turbofan engines using a single corrugated plate or interface to mix initially separated fluids[14–21]. Strong secondary velocities are observed near the exit plane of the lobed mixer, which evolve into a sheet of streamwise vorticity and eventually coalesce into distinct streamwise counter-rotating vortices[18]. Further downstream, turbulent breakdown of the streamwise vortices occurs, the location of which is dependent on the ratio of streamwise velocities on either side of the mixer. Vortex breakdown is seen by Eckerle et al.[18] to be the critical phenomenon that significantly enhances turbulent mixing due to the generation of smaller scale turbulence at breakdown. Yet Yu et al.[21] find that enhanced mixing can actually occur upstream of the region in which vortex breakdown occurs, due to the localized, rapid production of turbulent kinetic energy.

Combustion in a lobed mixer geometry, with fuel and oxidizer initially separated by a single lobed splitter plate, has also been studied to a limited extent[22–24]. When using a lobed splitter plate the flame spread angle is double that created by a flat splitter plate,

indicating enhanced mixing processes and an increased rate of flame propagation[22]. Mixing rate augmentation due to the addition of streamwise vorticity was found to be less sensitive to the detrimental effects of heat release than the mixing rate for a planar shear layer configuration[24].

For combustor applications, the lobed injector (Figure 1) reported in the present paper has several potential advantages over the lobed mixer. First, for stoichiometries which require greater proportions of air than of fuel (as with typical hydrocarbon fuels), the lobed injector allows large flow area differences between fuel and air without loss of symmetry or mixing effectiveness of the lobes. Second, because in the lobed injector fuel is injected directly into the region of highest strain rates and greatest vorticity, all of the fuel is mixed with oxidizer in a rapidly straining flow field, so that mixing may occur under conditions near flame extinction or ignition delay. Third, when a thin "strip" of fuel is sandwiched between the oxidizer, ignition delay can occur at smaller strain rates than when fuel and oxidizer meet at only one independently igniting interface[25]; hence ignition delay could be easier to achieve in a lobed injector rather than a lobed mixer geometry. The lobed injector also has an advantage over other types of strongly mixed nonpremixed combustors in that energy losses and pressure drop are small, while mixing takes place over a comparatively short distance[17].

Recent mixing studies for the non-reactive lobed injector flowfield by our group indicate significant increases in mixedness and scalar dissipation or strain rates over a planar geometry[26]. These studies employ planar laser-induced fluorescence (PLIF) imaging of seeded acetone to generate spanwise mixture fraction images at various locations downstream of the injector; from these images, local unmixedness[27] and average scalar dissipation rates are determined, from which strain rates may be estimated (after Bish and Dahm[28]). The mixing studies show that strain rates can be created in the farfield of the injector that exceed those required for ignition prevention; this implies that strain rates in the near field of the injector could be even higher, potentially able to delay ignition during rapid mixing. Yet the mixing studies also show that, depending on the specific lobed geometry, the mixing and strain field characteristics may be altered substantially for a given injector for different flow conditions. The purpose of the present work is to examine the behavior of the lobed injector under combustion conditions, specifically monitoring NO_x emissions from the device to demonstrate its potential for mixing enhancement and emissions reduction.

Experimental Facility and Methods

In the present experiments, two different planar fuel injector geometries were studied in a low speed combustion tunnel. The tunnel's square test section had 9.5 cm sides; a schematic of the combustion tunnel is shown in Figure 2. A compressor was used to pass air through the combustion tunnel at speeds between 2 and 7 m/s in the test section. The tunnel entrance contained a honeycomb section to straighten the flow, followed by a contraction section of 4:1 area ratio. Quartz windows were fitted in the two vertical side walls of the test section and at the downstream end of the wind tunnel (in a plane perpendicular to the

bulk flow) for optical access. Movable rearward-facing steps were used in the combustion tunnel as flameholders; these steps were placed flush with the upper and lower walls of the test section and were oriented perpendicularly with respect to the fuel injector. The design of the flameholders was such that the rearward-facing steps could only be brought to within 6 cm of the fuel injector.

Two different fuel injectors were studied in this combustion tunnel; exit plane geometries are shown schematically in Figure 3. Propane fuel was used in all experiments described here. The **lobed injector A** was constructed of aluminum using an electron discharge machining (EDM) device. It was constructed of two plates which were planar and parallel at the upstream edge and sinusoidally corrugated (lobed) at the downstream edge. The plates were separated by a small gap (on average, 0.071 cm at the downstream exit plane) through which fuel surrogate flowed; the wall thickness at the exit was approximately 0.038 cm. It should be noted that, due to machining inaccuracies, the gap width and wall thickness of this injector did vary along the exit plane lobes. Both thicknesses became more than twice the nominal value at the peaks and troughs of the sine wave. The wavelength λ of the lobes was 1.905 cm, and the peak-to-peak amplitude at the exit was 3.721 cm. The injector had five lobes and spanned the width of the wind tunnel; it was 15.2 cm in length (in the direction of flow), so that the lobes grew at a constant ramp half-angle of approximately 7°. **Fuel injector B** was a straight slot injector with a slot width of 0.056 cm and with a wall thickness of 0.127 cm at the exit plane. There was no aerodynamic loading for injector B, and hence the principal mechanism for streamwise vorticity generation was removed. We examined this configuration in an attempt to isolate the effects of the lobes' streamwise vorticity generation on mixing from the effects of spanwise vorticity generation arising from the Kelvin-Helmholtz instability (when the upper and lower air flow velocities were unequal) and from the wakes caused by the finite thickness of the injector walls. The comparison of injectors A and B here is analogous to the comparison of a "petal" shaped fuel injector[29] with a circular fuel injector.

The two fuel injectors were each tested in the combustion tunnel for different sets of operating conditions. In the experiments described here, the axial velocities of the air streams (above and below the injector) were matched, where the fuel exit velocity was varied to produce different overall equivalence ratios for the tunnel. It should be noted that the overall equivalence ratio actually has little bearing on the injector performance since the local reaction takes place under *local* stoichiometric conditions; depending on the degree of entrainment of species, local stoichiometric conditiosn could be vastly different from global conditions.

A chemiluminescent $NO - NO_x$ analyzer (Thermo Environmental 10AR Chemiluminescent $NO - NO_x$ Gas Analyzer) was used to measure the NO and NO_2 emissions from the combustor. The analyzer generated ozone (O_3) and then mixed it with the sampled gases in a reaction chamber. As a result of the decay of electronically excited NO_2 molecules produced in the reaction

$$NO + O_3 \rightarrow NO_2 + O_2$$

a chemiluminescent signal was obtained and monitored through a filter by a high sensitivity photomultiplier tube (PMT). The output of the photomultiplier tube was linearly proportional to the NO concentration. In order to help minimize calibration drift, a two point calibration was performed at each combustor operating condition where NO_x emissions were measured. A gas cylinder of certified 99.999% N_2 was used as the zero gas and a gas cylinder of 19.2 ppm NO in He from Matheson Gas Products was used as the calibrating gas. NO_2 emissions were measured by thermally converting NO_2 into NO (prior to the reaction with O_3) then determining the difference between the strength of this PMT signal and the NO measurement which had no thermal conversion.

The probe from the NO_x analyzer was placed well into the exhaust, downstream of the flame zones. Standard normalization of the NO and NO_2 emissions was made per kg of fuel burned on a dry basis. The emissions index of NO_x was then assumed to be equal to the sum of those for NO and for NO_2 made in the emissions measurements. In the near future, planar laser-induced fluorescence (PLIF) imaging of OH in the reaction zone will also be performed in order to better quantify reactive processes in the flame zone.

Results

Preliminary results from the present combustion experiments show dramatic differences in the visual structure of the flames formed in the combustion tunnel. For identical flow conditions (bulk air speeds and equivalence ratios), the lobed injector flames were bright blue in color, spanning the entire width of the flameholders, indicating the presence of lean premixed flames. The flames associated with the straight injector consisted of two distinct diffusion flame sheets, spreading toward the walls to become yellow further downstream. Even the visible flame characteristics indicated a substantial degree of mixing of fuel and air downstream of the lobed fuel injector, creating locally lean premixed or partially premixed flame structures. No substantial fuel-air mixing is observable within the test section for the straight injector; the flames themselves exist well into the plenum and occasionally into the exhaust section of the combustion tunnel.

Figure 4 shows plots of the emission indices for NO, NO_2, and NO_x as a function of overall equivalence ratio for both injectors under low speed conditions. Again, the overall equivalence ratio ϕ was based on the mass flow rates of fuel and air that were introduced into the tunnel; ϕ actually had little relevance to the *local* stoichiometry of the flame structures that form since *local* ignition can potentially take place in diffusion flame, lean premixed, or rich premixed flame modes. Results in Figure 4 demonstrate that the lobed fuel injector could actually produce lower emissions of NO and overall NO_x than could a straight (non-lobed) fuel injector under equivalent conditions. At the same overall equivalence ratio, NO emissions from the lobed injector were substantially lower than from the straight injector, indicating a much greater degree of mixing of the fuel with air and, locally, a much leaner reaction. An overall equivalence ratio just above 0.5 appeared to produce a maximum in NO production for the lobed injector; this indicated that the *local* equivalence ratio associated with the strained flame structures was likely close to unity at this condition. NO emissions dropped

with decreasing overall ϕ for the straight injector as well, indicating that this reaction may have been slightly premixed, but the magnitude of the emissions index indicated that this premixing was not substantial.

As overall equivalence ratio was reduced in Figure 4 for the lobed injector, NO_2 production peaked and then dropped, while for the straight injector NO_2 increased monotonically. Assuming that NO_2 formed due to the reaction of NO with oxygen-containing species near the flame and in the post-flame regions, it appeared that the $\phi \approx 0.4$ condition may have maximized entrainment of air into the flame/mixing zones for the lobed injector, thus forming higher NO_2 concentrations. On the other hand, air entrainment into the flame zone simply continued to increase in the straight injector with a higher air/fuel velocity ratio, leading to a peak in NO_2 at lower values of ϕ. The nature of NO_2 production demonstrates the sensitivity of the fuel injector/burner system to the evolution of the mixing field and the specific tailoring of the emissions production that is possible with the lobed injector.

It should be noted that equivalent values of the "overall ϕ" for the two injectors do not mean equivalent injectant/air velocity ratios. In fact, at the lower overall ϕ conditions (ϕ near 0.35), the ratio of fuel to air velocity for the lobed injector A is approximately 1.0, while the ratio for the straight injector is about 2.5. At the highest overall ϕ conditions (ϕ near 0.6), the ratio of fuel to air velocity for the lobed injector A is approximately 1.5, while the ratio for the straight injector is about 4.0. Hence the local fluid mechanics of the mixing process, in particular the generation of spanwise vorticity, is unequal between the two injectors despite having the same overall equivalence ratio.

Figure 5 shows the emissions indices as a function of overall ϕ for the lobed fuel injector, with two different bulk air speeds. Interestingly, the emissions indices for all three species are nearly the same as a function of ϕ. While the strain field and degree of mixing may increase as the air speed increases from 4.8 m/s to 6.0 m/s, any additional mixing did not appear to have a significant effect on NO_x emissions. These two different conditions may also represent the self-similar regions of the flowfield, which could explain the similarities in the emissions characteristics.

Figure 6 shows emissions indices for the lobed injector under the same (higher speed) operating conditions but where the flame holder was moved from a position 6.0 cm downstream of the injector to a position 14.0 cm downstream. As the flameholder was moved downstream, the emissions curves actually seemed to shift to the right, indicating the greater degree of fuel-air mixing that appeared to take place further downstream. As more air was entrained into the fuel-air mixture with downstream distance, the mixture became more lean; hence when ignition occurred at the downstream flameholder, it was in a leaner premixed mode for the lobed injector. This condition also had the effect of slightly increasing NO_2 production, since the greater degree of air entrainment increased the NO_2 formed from NO. Nevertheless, at given operating conditions (i.e., flow conditions and overall ϕ), the lobed injector flowfield demonstrated an increased degree of mixing downstream, and hence a lowered rate of NO emissions.

Conclusions

The present experiments confirm the usefulness of the lobed fuel injector concept as a means of NOx emission reduction. For locally lean conditions, rapid fuel-air mixing by the lobed injector flowfield can cause lean premixed flame structures to ignite downstream, thus reducing flame temperatures and simultaneously reducing NO emissions. The alteration in the degree of local air entrainment by the lobed injector can also be used to maximize NO_2 production. Future work on this device will include investigation of combustion characteristics associated with an alternative lobed fuel injector (studied also in [26]) and detailed interrogation of the flowfield via laser diagnostics.

Acknowledgements

References

[1] Bowman, C. T., "Control of Combustion-Generated Nitrogen Oxide Emissions: Technology Driven by Regulation", *Twenty-fourth Symposium (International) on Combustion*, The Combustion Institute, Pittsburgh, PA, 859-878 (1992).

[2] Lyons, V. J., "Fuel/Air Nonuniformity - Effect on Nitric Oxide Emissions", *AIAA Journal*, Vol. 20, No. 5, 1981, pp. 660-665.

[3] Fric, T. F., "Effects of Fuel-Air Unmixedness on NO_x Emissions", *Journal of Propulsion and Power*, Vol. 9, Sept.-Oct. 1993, pp. 708-713.

[4] Driscoll, J. F., Chen, R. H., and Yoon, Y., "Nitric Oxide Levels of Turbulent Jet Diffusion Flames - Effects of Residence Time and Damkohler Number", *Combust. Flame*, Vol. 88, 1992, pp. 37-49.

[5] Leonard, G. and Correa, S., "NO_x Formation in Premixed High-Pressure Lean Methane Flames", 2nd ASME Fossil Fuel Combustion Symposium, ASME/PD Vol. 30, 1990, pp. 69-74.

[6] Turns, S. R., Myhr, F. H., Bandaru, R. V., and Maund, E. R., "Oxides of Nitrogen Emissions from Turbulent Jet Flames - 2. Fuel Dilution and Partial Premixing Effects", *Combust. Flame*, Vol. 93, 1993, pp. 255-269.

[7] Fiorentino, A. J., Green, W., Kim, J. C., and Mularz, E. J., "Variable Geometry, Lean, Premixed, Prevaporized Fuel Combustor Conceptual Design Study", *Transactions ASME, Journal of Engineering for Power*, Vol. 102, 1980, pp. 896-902.

[8] Gore, J. P. and Zhan, N. J., "NO_x Emission and Major Species Concentrations in Partially Premixed Laminar Methane/Air Co-flow Jet Flames", *Combust. Flame*, Vol. 105, 1996, pp. 414-427.

[9] Roshko, A., "The Mixing Transition in Free Shear Flows", in *The Global Geometry of Turbulence*, J. Jimenez, ed., Plenum Press, NY, 1991.

[10] Keller, J. O., Gemmen, R. S., and Barr, P. K., "Premixed Combustion in a Periodic Flow Field. Part I: Experimental Investigation", *Combustion and Flame*, Vol. 99, 1994, pp. 29-42.

[11] Peters, N., "Laminar Flamelet Concepts in Turbulent Combustion", *21st Symposium (Intl.) on Combustion*, 1987, pp. 1231-1250.

[12] Law, C. K., Zhu, D. L., and Yu, G., "Propagation and Extinction of Stretched Premixed Flames", *21st Symposium (Intl.) on Combustion*, 1987, pp. 1419-1426.

[13] Kee, R. J., Miller, J. A., and Evans, G. H., "A Computational Model of the Structure and Extinction of Strained, Opposed Flow, Premixed Methane-Air Flames", *22nd Symposium (Intl.) on Combustion*, 1989, pp. 1479-1494.

[14] Tillman, T. G., Paterson, R. W., and Presz, W. M., "Flow Structure in a Periodic Axial Vortex Array", AIAA Paper No. 87-0610, 1987.

[15] Elliott, J. K., Manning, T. A., Qiu, Y. J., Greitzer, E. M., Tan, C. S., and Tillman, T. G., "Computational and Experimental Studies of Flow in Multi-Lobed Forced Mixers", AIAA Paper No. 92-3568, 1992.

[16] Fung, A. K. S., "Modeling of Mixer-Ejector Nozzle Flows", M.S. Thesis, Department of Aeronautics and Astronautics, Massachusetts Institute of Technology, February, 1995.

[17] W. M. Presz, B. L. Morin, and R. G. Gousy, "Forced Mixer Lobes in Ejector Designs", *J. Propulsion and Power*, Vol. 4, July-August, 1988, pp. 350-355.

[18] W. A. Eckerle, H. Sheibani, and J. Awad, "Experimental Measurements of Vortex Development Downstream of a Lobed Forced Mixer", *Journal of Engineering for Gas Turbines and Power*, Vol. 114, January, 1992, pp. 63-71.

[19] D. C. McCormick and J. C. Bennett, "Vortical and Turbulent Structure of a Lobed Mixer Free Shear Layer", *AIAA J.*, Vol. 32, September, 1994, pp. 1852-1859.

[20] S. A. Skebe, R. W. Paterson, and T. J. Barber, AIAA Paper No. 88-3785-CP, 1988.

[21] Yu, S. C. M., Yeo, J. H., and Teh, J. K. L, "Velocity Measurements Downstream of a Lobed-Forced Mixer with Different Trailing-Edge Configurations", *Journal of Propulsion and Power*, 11, 87-97 (1995).

[22] McVey, J. B., "Observation of the Effect of Streamwise Vorticity on the Spreading of Flames in High Speed Flow", *Combustion Science and Technology*, Vol. 60, 1988, pp. 447-451.

[23] McVey, J. B. and Kennedy, J. B., "Flame Propagation Enhancement Through Streamwise Vorticity Stirring", AIAA Paper No. 89-0619, 1989.

[24] Waitz, I. A. and Underwood, D. S., "Effect of Heat Release on Streamwise Vorticity Enhanced Mixing", AIAA Paper 95-2471, 1995.

[25] Gerk, T. J. and Karagozian, A. R., "Ignition Delay Associated with Strained Fuel Layers", accepted for publication in the *Twenty-sixth International Combustion Symposium Volume*, 1996.

[26] Smith, L. L., A. J. Majamaki, I. T. Lam, O. Delabroy, A. R. Karagozian, F. E. Marble, and O. I. Smith, "Mixing Enhancement in a Lobed Injector", submitted to *Physics of Fluids*, 1996.

[27] Dimotakis, P. E. and Miller, P. L., "Some consequences of the boundedness of scalar fluctuations", *Phys. Fluids A*, Vol. 2, No. 11, 1990, pp. 1919-1920.

[28] Bish, E. S. and Dahm, W. J. A., "Strained Dissipation and Reaction Layer Analyses of Nonequilibrium Chemistry in Turbulent Reacting Flows", *Combust. Flame*, Vol. 100, 1994, pp. 457-466.

[29] K. B. M. Q. Zaman, M. F. Reeder, and M. Samimy, "Control of an Axisymmetric Jet using Vortex Generators", *Phys. Fluids*, Vol. 6, 1994, pp. 778-793.
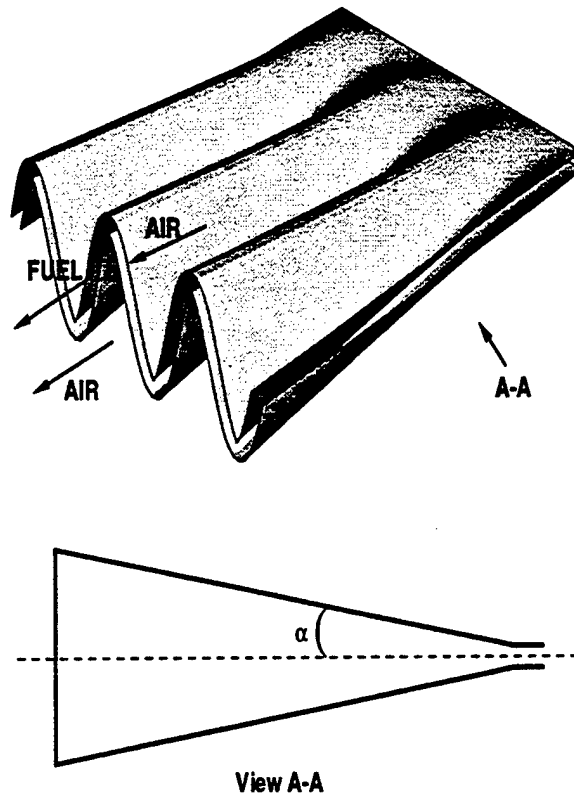
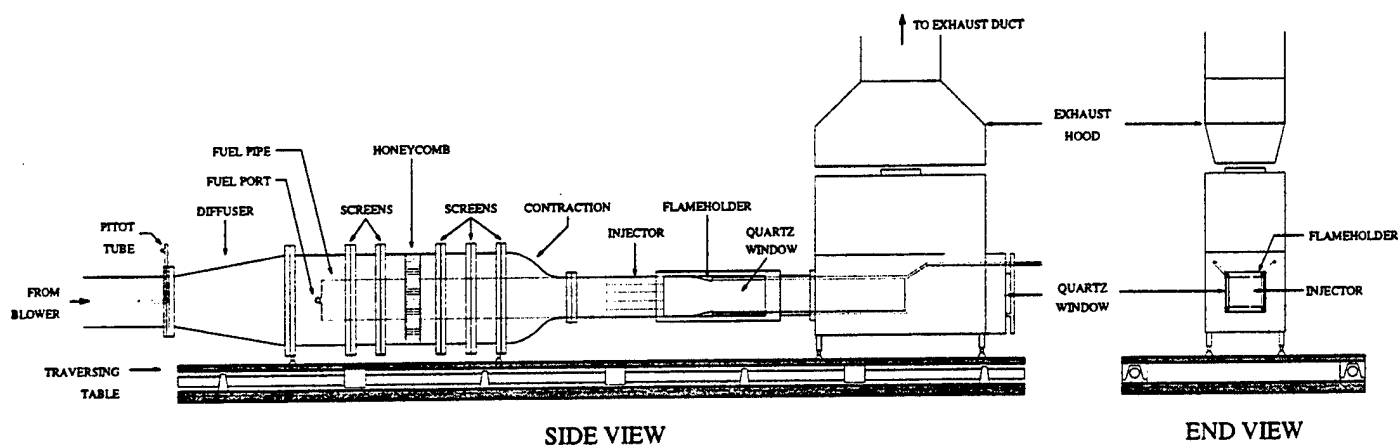Figure 1. Schematic of the general lobed injector geometry.

Figure 2. Schematic diagram of the combustor tunnel and experimental apparatus.

INJECTOR A

WALL THICKNESS 0.038 cm

GAP WIDTH
0.071 cm

3.721 cm

$\lambda = 1.905$ cm

INJECTOR B

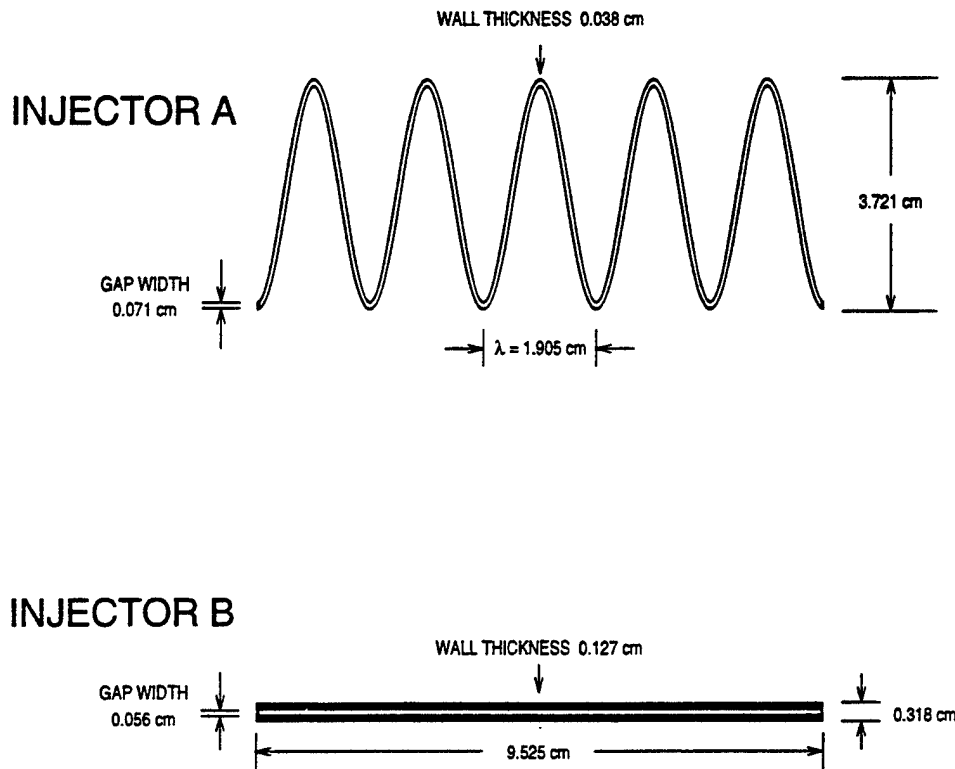WALL THICKNESS 0.127 cm

GAP WIDTH
0.056 cm

0.318 cm

9.525 cm

Figure 3. Comparison of exit plane geometries for the two injectors examined in the present combustion experiments: lobed fuel injector A and straight fuel injector B.
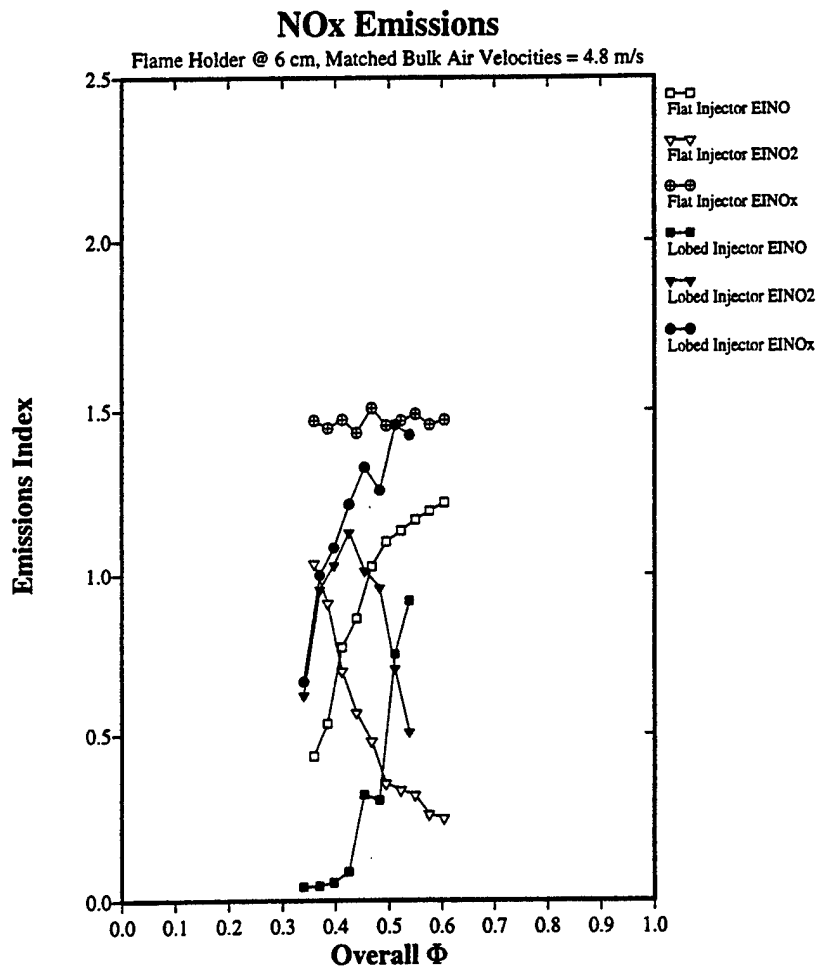
13

NOx Emissions

Flame Holder @ 6 cm, Matched Bulk Air Velocities = 4.8 m/s

Figure 4. Emissions indices for NO, NO$_2$, and NO$_x$ for the lobed fuel injector (A) and the straight fuel injector (B) as a function of tunnel overall equivalence ratio. The flameholder is situated 6.0 cm downstream of the injector, and the matched bulk air speeds are 4.8 m/s.

14

NOx Emissions

Lobed Injector with Flame Holder @ 6 cm
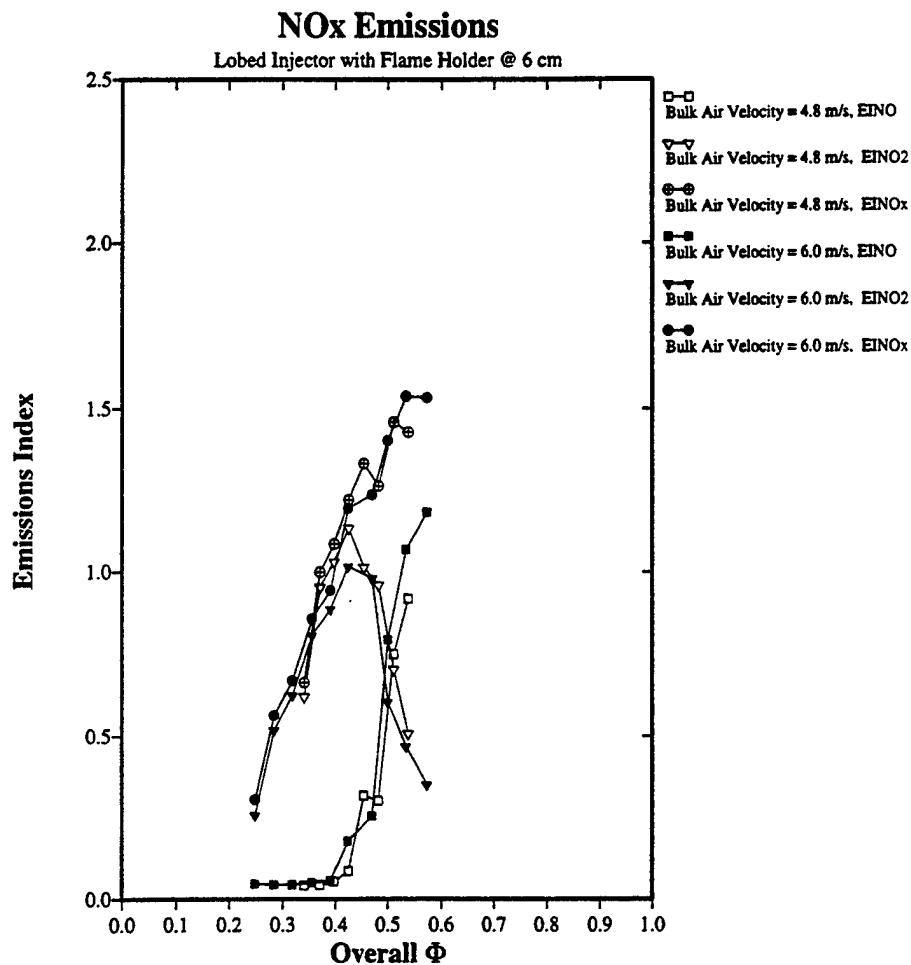
Figure 5. Emissions indices for NO, NO$_2$, and NO$_x$ for the lobed fuel injector (A) as a function of tunnel overall equivalence ratio for two different matched bulk air speeds: 4.8 m/s and 6.0 m/s. The flameholder is situated 6.0 cm downstream of the injector.

NOx Emissions

Lobed Injector with Matched Bulk Air Velocities = 6.0 m/s

Legend:
- Flame holder @ 14 cm, EINO
- Flame holder @ 14 cm, EINO2
- Flame holder @ 14 cm, EINOx
- Flame holder @ 6 cm, EINO
- Flame holder @ 6 cm, EINO2
- Flame holder @ 6 cm, EINOx

Y-axis: Emissions Index (0.0 to 2.5)
X-axis: Overall Φ (0.0 to 1.0)
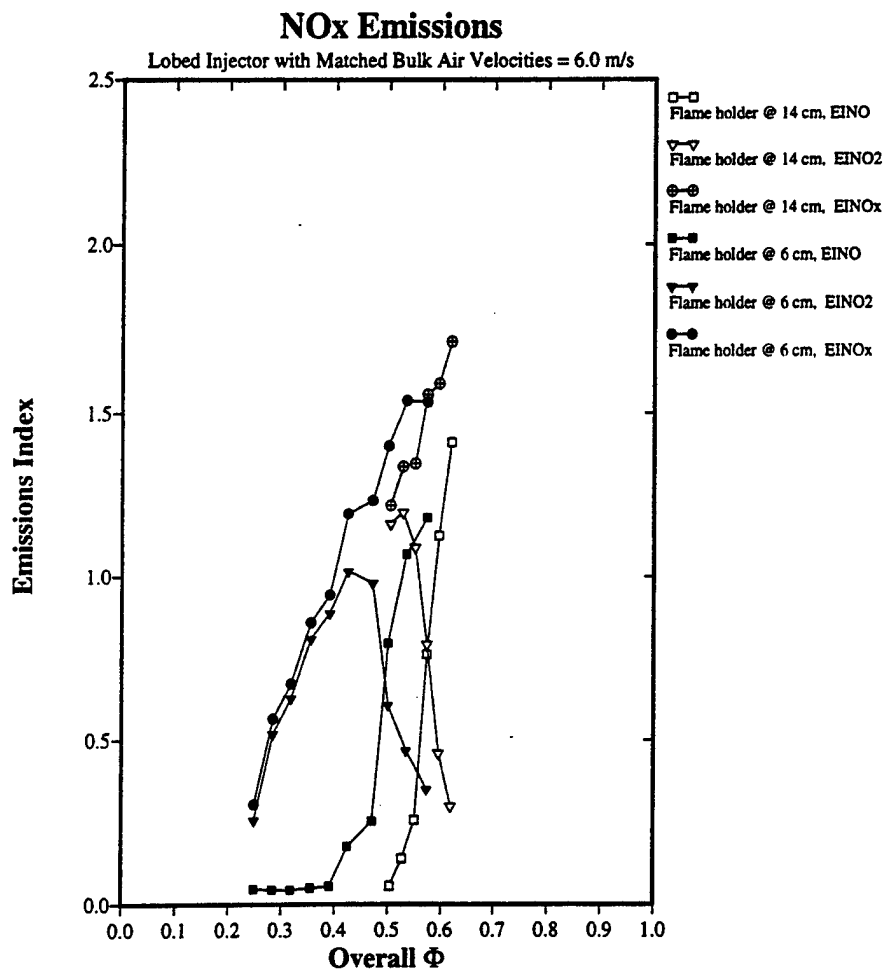
Figure 6. Emissions indices for NO, NO_2, and NO_x for the lobed fuel injector (A) as a function of tunnel overall equivalence ratio for two different locations of the flameholder: 6.0 cm and 14.0 cm downstream of the injector. The bulk air speed is 6.0 m/s.

16

REFERENCE [18]

UNIVERSITY OF CALIFORNIA
Los Angeles

Mixing, Ignition, and Burning Processes in Strained Fuel Layers

A thesis submitted in partial satisfaction of the requirements for the degree
Master of Science in Mechanical Engineering

by

Timothy J. Gerk

1996

REFERENCE [19]

IGNITION DELAY ASSOCIATED WITH A STRAINED FUEL STRIP

T. J. GERK AND A. R. KARAGOZIAN

Mechanical and Aerospace Engineering Department
University of California
Los Angeles, CA 90095-1597, USA

Ignition processes associated with two adjacent fuel-oxidizer interfaces bounding a strained fuel strip are explored here using single-step activation energy asymptotics. Calculations are made for constant as well as temporally decaying strain fields. Three possible modes of ignition are determined: one in which the two interfaces ignite independently as diffusion flames; one in which the two interfaces ignite dependently and in which ignition may be augmented by strain due to enhanced thermal feedback; and one in which ignition occurs to form a single, premixed flame at very high strain rates before ignition is completely prevented. In contrast to a single, isolated interface in which ignition can be prevented by overmatching heat production with heat convection due to strain, ignition of a strained fuel strip can also be prevented if the finite extent of fuel is diluted by oxidizer more quickly than heat production can cause a positive feedback thermal runaway. These behaviors are dependent on the relative sizes of timescales associated with species and heat diffusion, with convection due to strain, and with the chemical reaction. The results here indicate that adjacent, strained species interfaces may ignite quite differently in nature from ignition of a single, strained interface and that their interdependence should be considered as the interfaces are brought closer together in complex strain fields. Critical strain rates leading to complete ignition delay are found to be considerably smaller for the fuel strip than those for single interfaces as the fuel strip is made thin in comparison to diffusion and chemical length scales.

Introduction

Ignition and extinction processes associated with a single, strained fuel-air interface have been examined using single-step activation energy asymptotics [1–4] as well as reduced kinetics simulation [5–7] and full combustion chemistry simulation [8,9]. These processes may be understood in terms of the classic "S-shaped curve" [2,3,10], representing the thermal runaway leading to ignition as strain rate is relaxed and flame extinction as strain rate is increased. The concept of ignition delay due to straining has been applied to a variety of situations, including an understanding of flame liftoff [4,11] as well as ignition delay processes in jets, shear layers, and vortical structures [6,12–14].

In many complex flow situations, strained fuel-air interfaces form [15] and are brought closely together into layerlike turbulent flow structures, which may be viewed as alternating fuel-oxidizer strips undergoing local strain. These dissipation and reaction layers are comprised of laminar "flamelets," which are used to model turbulent non-premixed combustion [16]; it has been suggested that the existence of these layers is independent of the extent of chemical nonequilibrium in the flow [17].

Whereas extinction of the interfaces bounding finite regions of fuel has been considered in the fast chemistry limit [18,19] as well as using finite-rate chemistry [20] due to fuel burnout. the interesting problem of ignition delay associated with a strained fuel layer, bounded by oxidizing species. has not been explored to any significant degree. It is of interest to understand how the ignition process is affected as strained interfaces are brought closely together and behave dependently. If critical strain rates leading to ignition prevention in two adjacent species interfaces are different from those associated with a single isolated interface. the problem can have relevance to ignition delay (and eventually NO_x emissions reduction, for example [21]) for turbulent flows in which fuel and air mix and burn. These issues are what motivate the present study of ignition delay in strained fuel layers via activation energy asymptotics and a related, though preliminary, study using a full kinetics mechanism [22]. The strained fuel strip is in fact a component of a low-NO_x lobed fuel injector currently under examination [23].

Model Description and Solution Procedure

One-step activation energy asymptotics lends itself well to the problem of the ignition dynamics of the strained fuel strip or layer. Formulation of the problem may proceed in the same manner as in Ref. 6. with an alteration of the boundary conditions to represent the adjacent layers and finite extent of fuel present. The strained fuel strip problem is richer
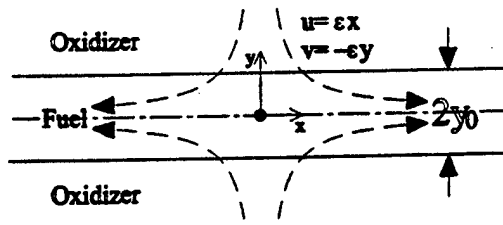
FIG. 1. Geometry of the strained fuel strip problem, where y_o is the initial strip thickness. The strip is exposed to the temporally evolving strain rate $\varepsilon(t)$ in general.

from a phenomenological point of view than is ignition of the single diffusion flame in that additional modes of ignition are possible, as will be described below.

As done by earlier researchers [2–4,6], a finite-rate, thermally controlled, single-step chemical reaction is assumed to follow an Arrhenius law for the reaction rate

$$\omega = \rho^2 k \frac{Y_F Y_O}{W_F W_O} e^{-T_A/T} \qquad (1)$$

This chemical model is adequate as a first approximation for ignition behavior even though transient ignition appears to be first controlled by elementary process initiation and radical pool formation reactions before thermal feedback ensues [9]. As noted by Thévenin and Candel [6], the reaction parameters may be estimated from the literature for premixed situations by matching flame propagation speeds from detailed kinetics computations to experiments [24]. In the present analysis, these parameters are used in scaling factors, so their numerical values are important in determining dimensional values for critical strain rates, critical strip widths, and ignition delay times. Although the actual values of activation energy and the pre-exponential Arrhenius factor are not accurately quantified due to strong variations with experimental conditions, the estimates should be adequate as a first approximation for ignition processes for two adjacent interfaces. Whereas specific quantitative results for critical strain rates, etc., may be specified more accurately using a full kinetics simulation [22], the fundamental modes of ignition of the fuel strip should be *qualitatively* the same as for an exact computation.

The governing equations for the present ignition problem consist of several species conservation equations and the energy conservation equation in thermal form. The geometry for the strained fuel strip is shown in Fig. 1, where the initial strip half-thickness is y_o, and the initial mass fractions of fuel within the strip and oxidizer surrounding the strip are Y_{F0} and Y_{O0}, respectively. The velocity field is specified as that of pure straining, with the strain rate $\varepsilon(t)$ prescribed; this is initiated at time $t = 0$. The

dimensional governing equations may be manipulated using the Howarth–Dorodnitzyn transformation [25,26] in order to eliminate density variations in the problem; in employing the transformation, the quantities $\rho^2 D$ and ρk are considered constants [27], whereas, in addition, the Lewis number is taken equal to one. The local mass fractions of fuel, oxidizer, and products are scaled by their initial conditions as $\hat{Y}_F = Y_F/Y_{F0}$, $\hat{Y}_O = (v_F W_F/v_O W_O)(Y_O/Y_{F0})$, and $\hat{Y}_P = (v_F W_F/v_P W_P)(Y_P/Y_{F0})$, respectively, and that for diluent is scaled as $\hat{Y}_N = [Y_N - (1 - Y_{O0})]/(1 - Y_{F0})$, where $Y_{N0} = (Y_{O0} - Y_{F0})/(1 - Y_{F0})$. The nondimensional temperature scale is chosen here to take the form $\theta = (T - T_{O0})(c_P/QY_{F0})$. With these transformations and scalings, the governing equations appear in vector form as

$$\left(\frac{\partial}{\partial t} + \mathbf{u}\cdot\nabla - D\nabla^2\right)\begin{Bmatrix}\hat{Y}_F\\\hat{Y}_O\\\hat{Y}_P\\\hat{Y}_N\\\theta\end{Bmatrix} = \begin{Bmatrix}-1\\-1\\1\\0\\1\end{Bmatrix}\frac{v_F W_F}{\rho Y_{F0}}\omega \qquad (2)$$

Four Zeldovich composite dependent variables may be constructed that are governed by the same homogeneous partial differential equation; these composite variables have closed-form solutions in terms of the error function. The variables are

$$Z_F = \frac{\hat{Y}_F + (\hat{Y}_{O0} - \hat{Y}_O)}{1 + \hat{Y}_{O0}}$$

$$Z_P = \frac{\theta - \hat{Y}_P}{B}$$

$$Z_O = \frac{\theta + \hat{Y}_O - \hat{Y}_{O0}}{B - \hat{Y}_{O0}}$$

$$Z_N = \frac{\hat{Y}_N}{\hat{Y}_{N0}}$$

where $B = [c_p(T_{F0} - T_{O0})]/(QY_{F0})$. These variables are each governed by the homogeneous form of Eq. (2), with the initial conditions $Z = 1$ within the fuel strip and $Z = 0$ in oxidizer regions for all species, that is, for all $Z = Z_F = Z_O = Z_P = Z_N$.

The equation governing temperature variation in the problem is

$$\frac{\partial\theta}{\partial t} + \mathbf{u}\cdot\nabla\theta - D\nabla^2\theta = \frac{v_F W_F}{\rho Y_{F0}}\omega \qquad (3)$$

with the initial conditions $\theta = \beta/\chi$ in the fuel strip and $\theta = 0$ in oxidizer regions, where a nondimensional heat release rate $\chi = QY_{F0}/c_P T_{O0}$ and nondimensional temperature difference $\beta = (T_{F0} - T_{O0})/T_{O0}$ are defined.

Scales of time, length, and velocity become important in the physical interpretation of the results. It is convenient here to assign a timescale t_{rxn} based on the chemical reaction and to use the diffusion coefficient to set the length scale: $l_{rxn} = \sqrt{Dt_{rxn}}$. The

chemical reaction time is taken here to be of the form

$$t_{rxn} = \frac{W_O e^{\alpha}}{\rho A v_F Y_{OO} \alpha \chi} \qquad (4)$$

where $\alpha = T_A/T_{OO}$. The velocity scale then can be defined to take the form $\sqrt{D/t_{rxn}} = D/l_{rxn}$.

It is now possible to evolve an asymptotic solution to the governing Eq. (3) by decomposing θ into a frozen-flow part and an increment in temperature due to heat release by the reaction. Liñan [2] determined that the temperature increment in the expansion is of order T^2_{OO}/T_A, so that the expansion may be written as

$$\theta = \frac{1}{\chi} \left(\beta Z + \frac{\vartheta}{\alpha} \right) \qquad (5)$$

A governing equation in the temperature variable ϑ may be simplified by expanding ϑ in increasing powers of T_A/T_{OO}, as described by Liñan and Crespo [3]. The final governing equation for the temperature variable ϑ then becomes

$$\frac{\partial \vartheta}{\partial \tilde{t}} + \tilde{u} \cdot \tilde{\nabla} \vartheta - \tilde{\nabla}^2 \vartheta = Z(1 - Z) e^{\alpha \beta Z} e^{\vartheta} \qquad (6)$$

where the temporal variable $\tilde{t} = t/t_{rxn}$, the spatial variable $\tilde{y} = y/l_{rxn}$, etc. In transformed coordinates, the governing equation in Z becomes

$$\frac{\partial Z}{\partial \tilde{t}} + u \cdot \tilde{\nabla} Z - \tilde{\nabla}^2 Z = 0 \qquad (7)$$

The governing Eqs. (6) and (7) may be solved subject to the flow, boundary, and initial conditions outlined previously. In the transformed coordinates for this one-dimensional problem, all spatial derivatives, except in the $\tilde{y}$ direction, are zero. A dimensionless strain rate may be defined as $\tilde{\varepsilon} = \varepsilon t_{rxn}$, while a nondimensional fuel strip thickness is $\tilde{y}_o = y_o/l_{rxn}$.

The solution for the homogeneous problem in Z, Eq. (7), is found by an analysis after Carrier et al. [15] and Marble [18], noting that a transformation for time is required for the imposed normal strain field:

$$Z(\tilde{y}, \tilde{t}) = \frac{1}{2} \left\{ erf\left(\frac{(\tilde{y} + \tilde{y}_o) \exp[\int_0^{\tilde{t}} \tilde{\varepsilon}(t) \, dt]}{2(\int_0^{\tilde{t}} \exp(2 \int_0^{\tilde{t}} \tilde{\varepsilon}(t) \, dt) \, d\tilde{t})^{1/2}} \right) \right.$$
$$\left. - erf\left(\frac{(\tilde{y} - \tilde{y}_o) \exp[\int_0^{\tilde{t}} \tilde{\varepsilon}(t) \, dt]}{2(\int_0^{\tilde{t}} \exp[2 \int_0^{\tilde{t}} \tilde{\varepsilon}(t) \, dt] \, d\tilde{t})^{1/2}} \right) \right\} \qquad (8)$$

The solution for Eq. (6) in ϑ must be found numerically due to the presence of the nonlinear thermal source term. This asymptotic form, in which the source varies like $\exp (\vartheta)$, will be described here, although the full form of the governing equation, in which the source term varies like $\exp (1 - 1/\vartheta)$, has also been solved numerically [28] and yields solutions that are within 30% of the asymptotic solution given below and qualitatively with the same features.

The asymptotic solution for the temperature increment ϑ (to the leading-order approximation) is computed by the Crank–Nicolson method, with a central difference approximation for the source term. The computational domain is defined using the cotangent transform from physical to computational coordinates in order to maintain appropriate conditions at infinity. For N grid points (characteristically 200 or 400), a tridiagonal set of N simultaneous, implicit algebraic equations is solved by Newton's method. Analysis shows the method is accurate to second order both in physical and temporal coordinates. A final tolerance parameter is used to test for thermal runaway at ignition or for the suppression of ignition by high straining: if $\Delta \max_x(\vartheta)/\Delta t > 10^{-6}$, the ignition condition is met; otherwise, the maximum temperature is level and ignition is observed to be suppressed.

Results

The present method is validated by examining the well-studied problem of a single flame in a field of constant straining, for example, as in Ref. 6. As expected, for increasing strain rates, increasing periods of time are necessary to generate a thermal runaway, and at critical strain rates, no thermal runaway is observed, and ignition is prevented.

Calculations for ignition of strained fuel strips of a given initial thickness and with a constant rate of straining produce time-dependent heat production distributions as plotted in Figs. 2a–2d for successively increasing rates of strain. A rough comparison of conditions leading to thermal runaway shows that increasing strain rate slightly increases ignition delay time and that above a critical rate of strain (here, $\tilde{\varepsilon} \approx 0.5$), ignition will not occur, as may be expected.

Closer examination of these results reveals interesting details. At zero or low rates of straining for the relatively thick fuel strip shown (Fig. 2a), there appear to be two independent ignition processes, exhibited in the thermal runaway that occurs at two distinct locations. Although the detailed processes leading to each ignition here may, depending on reaction and temperature parameters, involve the so-called triple flame structure [3,6], as found in numerical solution of this problem [28], each process eventually leads to ignition of two diffusion flames, each separated by fuel and oxidizer. As strain rate is increased (or as the strip is made thinner), ignition processes at either boundary of the fuel strip begin to interfere with each other, as shown in Fig. 2b. Heat produced at one boundary diffuses toward the other, creating more positive feedback in heat generation. Although there are two points of ignition, thermal runaway occurs in a dependent fashion. As
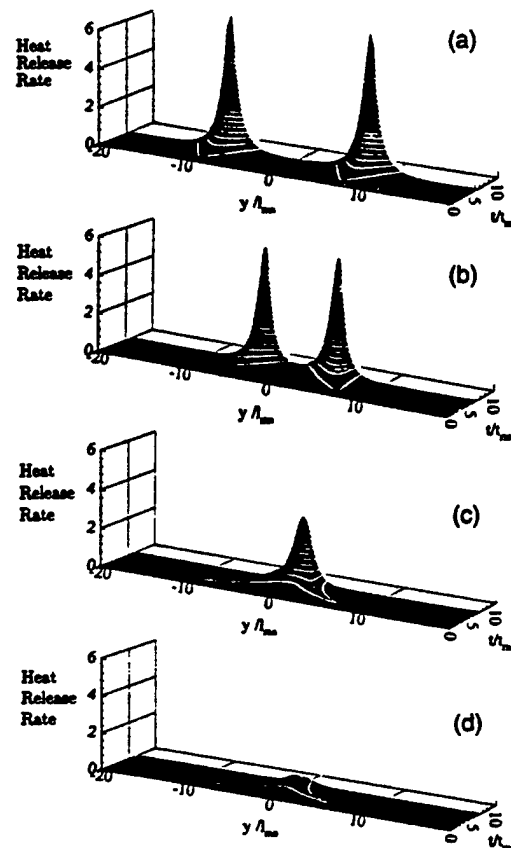
FIG. 2. Evolution of the nondimensional heat production rate (and possible thermal runaway) for the strained fuel strip with dimensionless thickness $y_o/l_{rxn} = 8$ and constant dimensionless strain rates $\bar{\varepsilon} = \varepsilon t_{rxn}$. Initial temperatures of reactants are equal. Cases shown are for (a) $\bar{\varepsilon} = 0$, no strain, yielding two independent ignition locations; (b) $\bar{\varepsilon} = 0.1$, yielding two ignition locations with interdependence of ignition boundaries; (c) $\bar{\varepsilon} = 0.3$, yielding one single (premixed) ignition point; and (d) $\bar{\varepsilon} = 0.5$, yielding strain rates too high to allow ignition to take place.

FIG. 3. Nondimensional time for ignition. t_{ign}/t_{rxn}. as a function of dimensionless initial fuel strip thickness y_o/l_{rxn}. for different nondimensional constant strain rate values $\bar{\varepsilon} = \varepsilon t_{rxn}$. The case shown is for identical initial fuel and oxidizer temperatures (i.e., $\beta = 0$).

strain rate is increased further (or strip thickness is reduced), this interdependence of the interfaces is so strong that thermal runaway can occur at a single point on the centerline of the strip (see Fig. 2c) rather than at two ignition points. This single ignition occurs at the centerline of the strip where the local fuel concentration is at a maximum; the ignition that follows must therefore be at least partially premixed, although it is possible that, after ignition, this single premixed flame may evolve into two flames that separate. Finally, for very high rates of strain and/or relatively thin fuel strips (Fig. 2d), complete suppression of ignition is observed, even when computed to nondimensional times of 50 (not shown). The results

shown in Figs. 2a–2d are pertinent to the case where fuel and oxidizer temperatures are initially equal ($\beta = 0$); similar behavior is observed for the case where $\beta \neq 0$.

These results have interesting implications with respect to ignition processes for adjacent fuel-oxidizer interfaces in a strain field. For a *single*, isolated interface, ignition can be prevented (according to the thermal model) by overmatching heat production with heat loss through convection due to straining. Ignition of the *two* interfaces bounding a fuel strip may be prevented by this means as well but may also be prevented if the fuel is diluted by the oxidizer more quickly than heat production can cause a positive feedback thermal runaway. This phenomenon is exhibited in Fig. 3. which plots dimensionless ignition time (t_{ign}/t_{rxn}) as a function of dimensionless initial fuel strip thickness (y_o/l_{rxn}) for several different constant strain rates. Even at zero straining, there is a minimum dimensionless strip thickness ($y_o/l_{rxn} \approx 0.6$) below which ignition does not occur: here, the fuel strip is mixed with oxidizer much more quickly than heat is produced for thermal runaway. In the same figure for zero strain rate, at large strip thicknesses (above $y_o/l_{rxn} \approx 5$), the nondimensional ignition delay time is approximately the same as that for an unstrained, single diffusion flame: $t_{ign}/t_{rxn} \approx 5.84$. Curves for zero as well as nonzero strain rates ($\bar{\varepsilon} = \varepsilon t_{rxn} = 0.1$ and 0.3) show a local minimum in ignition time that occurs as one reduces the strip thickness, for example, for $y_o/l_{rxn} \approx 1.8$ for the zero strain case in Fig. 3. This minimum is
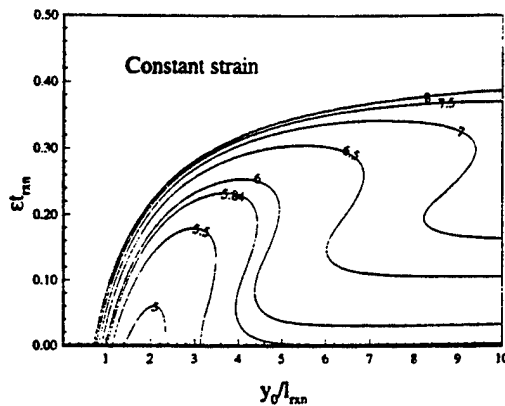
FIG. 4. Contours for constant nondimensional ignition time, t_{ign}/t_{rxn}, mapped on the strain rate–strip thickness plane, (et_{rxn}, y_o/l_{rxn}), for identical initial fuel and oxidizer temperatures (i.e., $\beta = 0$).

caused by augmentation of the thermal feedback cycle at each boundary of the strip due to heating by the opposite boundary as the boundaries approach each other. The phenomenon also produces the unusual result that. for certain ranges of strip thickness, ignition delay time *decreases* with increasing strain rate (see the crossover between $\bar{e} = 0$ and $\bar{e} = 0.1$ curves). The observation is unique to the fuel strip problem in which interfaces are close enough to each other to cause augmentation of thermal feedback.

The dependence of ignition delay on two independent variables, dimensionless strip thickness y_o/l_{rxn} and dimensionless strain rate $\bar{e} = et_{rxn}$, is shown in a plot of contours of constant ignition time in Fig. 4. The initial temperatures of the fuel and oxidizer streams are held identical ($\beta = 0$), but again, similar behavior is found when $\beta \neq 0$. The contour for $t_{ign}/t_{rxn} = 5.84$ corresponds to the ignition delay for an unstrained single interface, free of thermal augmentation effects of nearby boundaries. The contour near $t_{ign}/t_{rxn} = 8$ effectively represents the limit of maximum straining or minimum strip thickness that leads to ignition: larger ignition times produce contours coincident with this limit.

Several of the contours in Fig. 4 produce multiple values of strain rate for a given initial fuel strip thickness and a given ignition delay time. This result is consistent with intersecting points for the curves shown in Fig. 3. The contours in Fig. 4 indicate that, for certain *fixed* initial strip thicknesses (say $y_o/l_{rxn} = 5.0$), as one increases strain rate from zero, ignition begins to be delayed (reaching a local maximum ignition delay time), then is augmented (reaching a local minimum ignition delay time), then is further delayed before reaching complete ignition prevention.
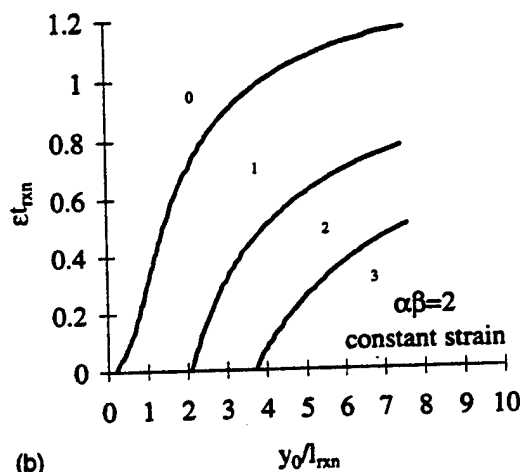
These local minima and maxima in ignition delay time are closely associated with the actual mode of ignition for the fuel strip. For a relatively large strip thickness, as strain rate begins to be increased from zero, the resulting ignition delay is phenomenologically the same as occurs in a strained, isolated interface; when ignition does occur, the flames quickly become diffusion flames, each separating reactants. Until the local maximum in ignition delay time is reached, the interfaces ignite mostly independently of each other, similar to the manner shown in Fig. 2a. After this local maximum is reached, as strain rate continues to be increased, ignition delay time is reduced due to the augmentation of thermal runaway by adjacent interfacial heating. Ignition occurring in this mode forms two diffusion flames that behave dependently, as shown in Fig. 2b. After a local minimum in ignition delay time is reached, increasing strain rates then cause an increase in ignition delay time again. The interfaces are now brought so closely together due to the strain field and fuel and oxidizer are so rapidly diffused into one another that ignition occurs and burning is sustained as a single. premixed flame surface (Fig. 2c). Finally, as strain rate is further increased, a critical strain rate is reached and ignition is completely prevented (Fig. 2d).

These four different modes of ignition/nonignition for the fuel strip exposed to a constant rate of strain are represented as a function of strain rate and initial fuel strip thickness in Fig. 5a. The modes delineated in the figure may be classified as no ignition (0), single, premixed flame ignition (1), double, dependent diffusion flame ignition (2), and double, independent diffusion flame ignition (3). Figure 5b plots the same parameters for the case where the initial fuel and oxidizer temperatures are unequal ($\alpha\beta = 2$): we see here a similar behavior to the $\alpha\beta = 0$ case. When the fuel temperature is increased above the fixed temperature of the oxidizer at a given fuel strip thickness, a comparison of Figs. 5a and 5b indicates that transitions from one ignition mode to another occur at increasingly large strain rates. This is an outcome of the enhancement of thermal feedback and runaway with increasing fuel temperature: the ignition process is sustained at higher strain rates (and thinner fuel strips) when the reactants are at unequal temperatures. When fuel temperature is fixed and oxidizer temperature is increased, similar enhancement of thermal feedback occurs, due to heating of the fuel by the oxidizer, extending the range of critical strain rates as in the single interface ignition problem [8].

Computations for a fuel strip exposed to a time-dependent rate of straining have also been made. Analysis of a flame deformed by a vortical flow field [18,29] shows that, following a short adjustment time, the rate of straining of any part of the flame interface decays like the inverse of time. Thus, in the interest of examining a temporally decaying strain
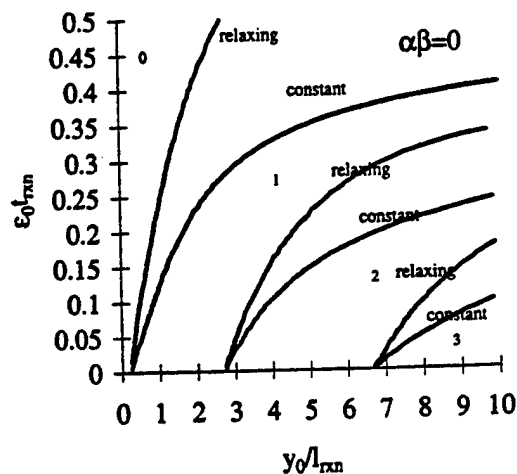
(a)

FIG. 6. Delineation of regions for different modes of ignition in a strained fuel strip with a *relaxing* strain rate for the case of identical initial fuel and oxidizer temperatures (i.e., $\beta = 0$). Regions shown distinguish conditions leading to mode 0 (ignition prevention), mode 1 (single, premixed ignition), mode 2 (two dependently igniting interfaces), and mode 3 (two independently igniting interfaces). Comparison is made to mode boundaries for the constant strain-rate case.

(b)

FIG. 5. Delineation of regions for different modes of ignition in a strained fuel strip. Regions shown distinguish conditions leading to mode 0 (ignition prevention), mode 1 (single, premixed ignition), mode 2 (two dependently igniting interfaces), and mode 3 (two independently igniting interfaces). The cases here are for (a) identical initial fuel and oxidizer temperatures, that is, $\alpha\beta = 0$, and (b) an initial fuel temperature greater than that of oxidizer, given by $\alpha\beta = 2$.

field relevant to complex, turbulent reacting flows, we consider the strain behavior

$$\varepsilon(t) = \frac{\varepsilon_0}{1 + t} \qquad (9)$$

in contrast to the constant strain-rate case considered previously. The analogous mode boundaries for the relaxing strain case are shown in Fig. 6, with comparison made to the constant strain boundaries with identical initial temperatures (Fig. 5a).

When the strain field relaxes for a single interface, ignition cannot be *completely* prevented by straining since at some time the rate of strain will have relaxed to the unstrained situation and ignition will occur. However, a fuel strip can be diluted to very low concentrations before the rate of strain significantly relaxes, hence, there remain limits on the maximum initial strain rate ε_0 that allow ignition in any of the particular modes. Thus, the result of allowing the strain rate to relax is, at any particular strip thickness, to increase the initial strain rate ε_0 possible for ignition as compared with strain rate for the constant strain case, as indicated in Fig. 6. As expected, the ignition of fuel strips of increasing width approaches that of an isolated boundary in the relaxing strain field; hence, the maximum initial strain rate ε_0 for ignition will increase as $y_o/l_{rxn} \to \infty$.

The different modes of ignition determined above depend on the relative sizes of timescales associated with the following processes: (1) the process of diffusion and heat conduction (timescale y_o^2/D), (2) the process of advection and convection (timescale $1/\varepsilon$), and (3) the process of nonlinear, positive feedback heat release (chemical timescale t_{rxn}). If the process of diffusion and heat conduction happens most quickly, that is, if the physical length scale y_o is small or the diffusivity D is large, the fuel of the strip is dispersed or the heat is dissipated before ignition can occur, leading to the "no-ignition" mode. Like-

wise, if the timescale associated with advection and convection is shortest, that is, if the strain rate is very high, no ignition occurs. If the heat-releasing feedback process is quickest, that is, if the chemical time t_{rxn} is small, the independent, double-diffusion flame ignition mode can occur. When the thermal feedback process, convection, and diffusion occur on similar timescales, the double-dependent or premixed ignition mode can occur due to augmentation of the thermal process caused by the proximity of the boundaries of the fuel strip and the resulting interdependence of heating due to diffusion. These scaling arguments are borne out in Figs. 5a and 5b; further details, including dimensional values for critical strain rates, may be found in Ref. 28.

Summary and Conclusions

Ignition delay associated with a strained fuel strip has been computed using single-step activation energy asymptotics, for constant as well as temporally decaying strain fields. Fuel strip ignition behavior may be compared qualitatively, as well as quantitatively, with the strained single-interface problem.

For a single, strained diffusion interface [2,3,6], ignition may be delayed or prevented by excessive convection of heat away from the interface due to strain, according to thermal theory, or due to greater convection of species than production of radicals at the interface, according to finite, multistep kinetics calculations [9]. For two strained interfaces bounding a fuel strip of finite extent, ignition may be delayed or prevented by the processes above, but they may also take place due to excessive diffusion of species at the interface when compared with heat or radical production.

This difference in the strained fuel strip problem leads to three possible modes of ignition: one in which the two interfaces ignite independently as diffusion flames; one in which the two interfaces ignite dependently and in which ignition may be augmented by strain due to enhanced thermal feedback; and one in which ignition occurs to form a premixed, single flame at very high strain rates before ignition is completely prevented. The relative timescales associated with diffusion, convection, and chemical reaction determine which mode is likely to occur under specified conditions.

Whereas the present analysis is approximate in terms of quantitative prediction of these physical scales due to the simplification in reaction kinetics, preliminary calculations with a full kinetic mechanism replicate the different modes of ignition observed here [22]. These calculations (either for simplified or full combustion chemistry) may be applied to more complex flow fields in which closely spaced, strained species interfaces ignite, burn, and extinguish dependently.

Nomenclature

c_p	specific heat
D	binary mass diffusivity of reactants into products
k	heat diffusion coefficient
$\hat{k}$	pre-exponential reaction rate coefficient
l_{rxn}	reaction length scale
Q	heat release rate
t	time
t_{ign}	time at which flame ignites or thermal runaway occurs
t_{rxn}	timescale associated with reaction
T	temperature
T_A	activation temperature
$\mathcal{W}$	molecular weight of species
y_o	initial fuel strip half-thickness
Y	mass fraction
$\hat{Y}$	local mass fraction scaled by initial conditions
Z	Zeldovich composite variable

Greek Symbols

α	T_A/T_{∞}
β	nondimensional temperature difference $(T_{F0} - T_{\infty})/T_{\infty}$
ε	strain rate
$\bar{\varepsilon}$	dimensionless strain rate $= \varepsilon t_{rxn}$
θ	nondimensional temperature scale
ϑ	temperature variable defined in Eq. (7)
ρ	gas density
ω	molar reaction rate

Subscripts

F	fuel
$F0$	initial fuel conditions
N	diluent
O	oxidizer
OO	initial oxidizer conditions
P	product

REFERENCES

1. Fendell, F. E., *J. Fluid Mech.* 21(2):281–303 (1965).
2. Liñan, A., *Acta Astronautica* 1:1007–1039 (1974).
3. Liñan, A. and Crespo, A., *Combust. Sci. Technol.* 14:95–117 (1976).
4. Peters, N., *Combust. Sci. Technol.* 30:1–17 (1983).

5. Dold, J. W., *Combust. Flame* 76:71–88 (1989).

6. Thévenin, D. and Candel, S., *Combust. Sci. Technol.* 91:73–94 (1993).

7. Seshadri, K. and Peters, N., *Combust. Flame* 73:23 (1988).

8. Darabiha, N. and Candel, S., *Combust. Sci. Technol.* 86:67–85 (1992).

9. Kreutz, T. G., Nishioka, M., and Law, C. K., *Combust. Flame* 99:758–766 (1994).

10. Law, C. K., *Twenty-Second Symposium (International) on Combustion*, The Combustion Institute, Pittsburgh, 1988, pp. 1381–1402.

11. Peters, N., *Twenty-First Symposium (International) on Combustion*, The Combustion Institute, Pittsburgh, 1986, pp. 1231–1250.

12. Grosch, C. E. and Jackson, T. L., *Phys. Fluids A* 3:3087–3097 (1991).

13. Macaraeg, M. G., Jackson, T. L., and Hussaini, M. Y., *Combust. Sci. Technol.* 87:363–387 (1992).

14. Thévenin, D. and Candel, S., *Phys. Fluids* 7:434–445 (1995).

15. Carrier, G. F., Fendell, F. E., and Marble, F. E., *SIAM J. Appl. Math.* 28:463–500 (1975).

16. Peters, N., *Prog. Energy Combust. Sci.* 10:319–339 (1984).

17. Bish, E. S. and Dahm, W. J. A., *Combust. Flame* 100:457–466 (1994).

18. Marble, F. E., *Recent Adv. Aero. Sci.* (C. Casci, Ed.), pp. 395–413 (1985).

19. Buckmaster, J. D. and Ludford, G. S. S., *Theory of Laminar Flames*, Cambridge Univ. Press, Cambridge, 1982, pp. 179–181.

20. Cetegen, B. M. and Bogue, D. R., *Combust. Flame* 86:359–370 (1991).

21. Bowman, C. T., *Twenty-Fourth Symposium (International) on Combustion*, The Combustion Institute, Pittsburgh, 1992, pp. 859–878.

22. Selerland, T., Ph.D. Prospectus, University of California, Los Angeles, 1996.

23. Smith, L. L., Majamaki, A. J., Delabroy, O., Lam, I. T., Karagozian, A. R., Marble, F. E., and Smith, O. I., "Mixing Enhancement in a Lobed Injector," *Phys. Fluids* (1996), submitted.

24. Coffee, T. P. and Heimerl, J. M., *Combust. Flame* 43:273–289 (1981).

25. Howarth, P. L., *Proc. Roy. Soc. (London)* 164A:547 (1938).

26. Dorodnitzyn, A., *Dokl. Akad. Nauk.* (SSSR) 34:213 (1942).

27. Karlovitz, B., Denniston, J. R., Knapschaefer, D. H., and Wells, F. E., *Fourth Symposium (International) on Combustion*, The Williams and Wilkins Co., Baltimore, 1953, pp. 613–635.

28. Gerk, T. J., Master's Thesis, University of California, Los Angeles, 1996.

29. Karagozian, A. R. and Marble, F. E., *Combust. Sci. Technol.* 45:65–84 (1986).

COMMENTS

A. Ghoniem, MIT, USA. Did you find a relationship between the characteristic extinction strain of an isolated flame and that of interacting flames surrounding a fuel strip?

In a study of interacting premixed flame done at Sandia, they reported the significant role of H_2 concentration and the H radicals in enhancing the burning rate before total annihilation. Did you observe a similar effect in your detailed chemistry computations?

Author's Reply. The relationship between a characteristic strain rate for complete ignition prevention in an isolated interface and that for two adjacent interfaces can be seen to an extent (non-dimensionally) in Figures 5ab. In Figure 5a, for example, for the limit of large initial strip thicknesses (y_0/l_{rxn}), the boundary adjacent to the "no ignition" (0) mode may be interpreted to represent the condition of ignition prevention for the isolated interface; the other curves, of course, will intersect this upper boundary prior to the asymptote (i.e., at smaller strip thicknesses). The shape of this upper boundary in Figure 5a may be viewed as a rough approximation, to the level of accuracy of the asymptotic solution, of the relationship between the critical non-dimensional strain rate which prevents ignition

for the fuel strip and that for the isolated interface. An approximate curve fit for this upper boundary (for the case of equal initial temperatures as in Figure 5a) takes the form

$$\frac{y_0}{l_{rxn}} = \exp\left[b + m\left((ct_{rxn})\left(\frac{t_{ign}}{t_{rxn}}\right) + \frac{1}{2}\ln\frac{t_{ign}}{t_{rxn}}\right)\right]$$

where b = −0.858 and m = 0.487 for the constant strain case in Figure 5a. This functional form, with different constants, also describes the other boundaries in Figures 5ab; the relation effectively represents conditions where the dynamic thickness of the fuel strip is of the order of the diffusion and/or reaction thickness.

In more recent numerical simulations of the strained fuel strip problem using a full propane-air mechanism [22], we do see evidence that relatively thin fuel strips (e.g., y_0 = 0.25 mm) at moderate constant strain rates (e.g., c = 500 sec^{-1}) ignite in a dependent fashion as shown in the present asymptotic study. Under specific conditions, interfaces which ignite dependently can exhibit a runaway in the H concentration before thermal runaway occurs. While a drop in H concentration occurs at fuel strip burnout or diffusion flame annihilation, there is simultaneously a sharp dropoff in the burning rate prior to burnout, consistent with classical studies [18].

REFERENCE [20]

IGNITION, BURNING, AND EXTINCTION OF A
STRAINED FUEL STRIP
WITH COMPLEX KINETICS

T. Selerland and A. R. Karagozian
Mechanical and Aerospace Engineering Department
University of California, Los Angeles

Corresponding Author:

Professor A. R. Karagozian
Department of Mechanical and Aerospace Engineering
46-147D Engineering IV, UCLA
Los Angeles, CA 90095-1597
U.S.A.
Phone: (310) 825-5653; FAX: (310) 206-4830
E-mail: ark@seas.ucla.edu

1

IGNITION, BURNING, AND EXTINCTION IN A STRAINED FUEL STRIP WITH COMPLEX KINETICS

T. Selerland and A. R. Karagozian
Mechanical and Aerospace Engineering Department
University of California, Los Angeles

1 Abstract

Flame structure and ignition and extinction processes associated with a strained fuel strip are explored numerically using detailed transport and complex kinetics for a propane-air reaction. Ignition modes are identified that are similar to those predicted by one-step activation energy asymptotics, i.e., modes in which diffusion flames can ignite as independent or dependent interfaces, and modes in which single premixed or partially premixed flames ignite and burn. These ignition modes are found to be dependent on critical combinations of strain rate, fuel strip thickness, and initial reactant temperatures. The formation of NO/NO_2 is found to be strongly dependent on strain rate and the local mixing of reactants which occurs as a consequence of strain. Extinction in this configuration is seen to occur due to fuel consumption by adjacent flames, although viscosity is seen to have the effect of delaying extinction by reducing the effective strain rate experienced by the flames. Response of the flames to oscillatory strain rates is seen to be strongly dependent on the amplitude and frequency of the oscillation.

2 Nomenclature

D_{ij} binary mass diffusivity of species i into j
NS number of species
Q_x x-component of heat flux vector
Q_y y-component of heat flux vector
T temperature
W_i molecular weight of species k
Y_i mass fraction of species i
c_p specific heat at constant pressure for the mixture
$c_{p,i}$ specific heat at constant pressure for species i
e energy of the mixture per unit volume
h_i enthalpy per unit volume of species i
p pressure
t time
u velocity in x-direction
v velocity in y-direction

x	spatial coordinate along the strip
y	spatial coordinate normal to the strip
γ	ratio of specific heats of the mixture
ϵ	strain rate
ϵ_0	mean strain rate for oscillatory straining
ϵ_1	amplitude of the oscillatory strain rate
λ	thermal conductivity of the mixture
ρ	mixture density
τ	stress tensor
ω	frequency
$\dot{\omega}_i$	mass production rate of species i

3 Introduction

Ignition and extinction processes associated with a single strained fuel-air interface have been examined extensively using single step activation energy asymptotics[1–4] as well as reduced kinetics simulation[5, 6] and full combustion chemistry simulation[7, 8]. These processes may be understood in a global sense in terms of the "S-shaped curve"[2, 3, 9], representing the thermal runaway leading to ignition as strain rate is relaxed and flame extinction as strain rate is increased. The concept of ignition delay due to straining has been applied to a variety of situations, including an understanding of flame liftoff[4, 10] as well as ignition delay processes in jets, shear layers, and vortical structures[6, 11–13].

In many complex reacting flow situations, strained fuel-air interfaces form[14] and are brought closely together into layer-like turbulent flow structures which may be viewed as alternating fuel-oxidizer strips undergoing local strain (e.g., as represented in Figure 1). These dissipation and reaction layers are comprised of laminar "flamelets" which have been used to model turbulent non-premixed combustion[15]; it has been suggested that the existence of these layers is independent of the extent of chemical non-equilibrium in the flow[16]. Further, the temporal evolution of the strain field has been shown to have a significant effet on the ignition and evolution of flame structures in complex flowfields[6]. Effective oscillations in the strain field, with frequencies of the order of the eddy turnover time, are thus particularly important in characterizing turbulent reactive flows.

The effect of a complex flowfield on distorted turbulent dissipation and reaction layers as shown in Figure 1 can be studied by examining the simpler geometry of the planar strained fuel strip surrounded by oxidizing species, shown schematically in Figure 2. While extinction of the interfaces bounding the strained or non-strained fuel has been considered[14, 17–19] due to fuel burnout, the interesting problem of ignition delay associated with a strained fuel layer has only recently been studied via single step activation energy asymptotics[20]. This study examined how the ignition process is affected as species interfaces are brought closely together due to straining. Three possible modes of ignition are determined: one in which the

two interfaces ignite independently to form diffusion flames, one in which the two interfaces ignite in a dependent fashion and in which ignition may be actually augmented by strain due to enhanced thermal feedback, and one in which ignition occurs to form a single, premixed flame at very high strain rates before ignition is completely prevented. In contrast to a single, isolated interface in which ignition can be prevented by over-matching heat production with heat convection due to strain, ignition of a strained fuel strip can also be prevented if the finite extent of fuel is diluted by oxidizer more quickly than heat production can cause a positive feedback thermal runaway. These behaviors are dependent on the relative sizes of time scales associated with species and heat diffusion, with convection due to strain, and with the chemical reaction. Critical strain rates leading to complete ignition delay can be considerably smaller for the fuel strip than those for single interfaces as the fuel strip is made thin in comparison to diffusion and chemical length scales.

When critical strain rates leading to ignition prevention for two adjacent species interfaces are smaller than those required to delay ignition of a single isolated interface, certain benefits may be derived. If ignition is delayed due to strain in a turbulent reactive flow, fuel and air can experience substantial mixing, so that when the strain field relaxes, ignition may occur in a locally premixed, potentially lean mode, reducing NOx production that would occur in stoichiometric diffusion flames[21]).

The strained fuel strip is in fact a component of a low NOx, lobed fuel injector currently under examination at UCLA[22, 23]. Streamwise vorticity generated by the injector creates a flowfield of high strain rate, acting to delay the ignition of injected strips of fuel into a coflowing airstream. If the critical strain rate to delay ignition is smaller for adjacent fuel-air interfaces than for isolated interfaces, then NO_x reduction could potentially be easier to achieve in this system than for a conventional fuel injector. These issues are what motivated the earlier study of ignition delay in strained fuel layers via activation energy asymptotics[20]; they continue to motivate the present, more quantitative study which examines ignition, burning, and extinction in a strained propane fuel strip surrounded by air using a full reaction mechanism.

4 Problem Formulation and Solution Procedure

The geometry of the strained fuel strip problem is shown in Figure 2. The strain rate $\epsilon(t)$ imposed in the problem is formulated through boundary conditions as $y \to +\infty$, that is, $u(x, y \to +\infty, t) = \epsilon x$ and $v(x, y \to +\infty, t) = -\epsilon y$. It should be noted that the boundary conditions as $y \to -\infty$ are the same as those at $y \to +\infty$ due to the presence of air in both limits, in contrast to the classical counterflow diffusion flame problem with differing initial densities of fuel and air. The strained fuel strip problem is actually richer from a phenomenological point of view than is ignition of the single diffusion flame in that additional modes of ignition are possible, as noted in [20].

The governing equations for the strained fuel strip problem (mass, momentum, energy, and species conservation) may be solved in general in the present scheme in conservative form:

$$\vec{U}_t + \left[\vec{F}(\vec{U})\right]_x + \left[\vec{G}(\vec{U})\right]_y = \left[\vec{F}_v(\vec{U})\right]_x + \left[\vec{G}_v(\vec{U})\right]_y + \vec{S} \tag{1}$$

where the vector $\vec{U}$, the convective flux vectors $\vec{F}$ and $\vec{G}$, the diffusive flux vectors $\vec{F}_v$ and $\vec{G}_v$, and the source vector $\vec{S}$ are defined as follows:

$$\vec{U} = \begin{pmatrix} \rho \\ \rho u \\ \rho v \\ e \\ \rho Y_1 \\ \rho Y_2 \\ \vdots \\ \rho Y_{NS-1} \end{pmatrix} \quad \vec{F}(\vec{U}) = \begin{pmatrix} \rho u \\ \rho u^2 + p \\ \rho u v \\ (e+p)u \\ \rho u Y_1 \\ \rho u Y_2 \\ \vdots \\ \rho u Y_{NS-1} \end{pmatrix} \quad \vec{G}(\vec{U}) = \begin{pmatrix} \rho v \\ \rho u v \\ \rho v^2 + p \\ (e+p)v \\ \rho v Y_1 \\ \rho v Y_2 \\ \vdots \\ \rho v Y_{NS-1} \end{pmatrix} \tag{2}$$

$$\vec{F}_v(\vec{U}) = \begin{pmatrix} 0 \\ \tau_{xx} \\ \tau_{xy} \\ u\tau_{xx} + v\tau_{xy} + Q_x \\ \rho D_{1m}(Y_1)_x \\ \rho D_{2m}(Y_2)_x \\ \vdots \\ \rho D_{NS-1m}(Y_{NS-1})_x \end{pmatrix} \quad \vec{G}_v(\vec{U}) = \begin{pmatrix} 0 \\ \tau_{xy} \\ \tau_{yy} \\ u\tau_{xy} + v\tau_{yy} + Q_y \\ \rho D_{1m}(Y_1)_y \\ \rho D_{2m}(Y_2)_y \\ \vdots \\ \rho D_{NS-1m}(Y_{NS-1})_y \end{pmatrix} \tag{3}$$

$$\vec{S} = \begin{pmatrix} 0 \\ 0 \\ 0 \\ 0 \\ \dot{\omega}_1 \\ \dot{\omega}_2 \\ \vdots \\ \dot{\omega}_{NS-1} \end{pmatrix} \tag{4}$$

Mass production rate terms $\dot{\omega}_i$ are evaluated in (4) in standard fashion, assuming an Arrhenius-type reaction rate coefficient dependence on temperature. Inviscid as well as viscous forms of the equations have been solved in one and two dimensions, respectively[24].

If a one–dimensional, inviscid formulation of the problem is made with a low Mach number simplification[25–27], so that spatial variation in pressure is assumed negligible in comparison with temporal variation, the problem essentially reduces to a set of energy and species conservation equations:

$$\vec{U}_t + \left[\vec{G}(\vec{U})\right]_y = + \left[\vec{G}_v(\vec{U})\right]_y + \vec{S} + \vec{C} \tag{5}$$

5

where

$$\vec{U} = \begin{pmatrix} e \\ \rho Y_1 \\ \rho Y_2 \\ \vdots \\ \rho Y_{NS} \end{pmatrix} \quad \vec{G}(\vec{U}) = \begin{pmatrix} (e+p)v \\ \rho v Y_1 \\ \rho v Y_2 \\ \vdots \\ \rho v Y_{NS} \end{pmatrix} \quad \vec{G}_v(\vec{U}) = \begin{pmatrix} Q_y \\ \rho D_{1m}(Y_1)_y \\ \rho D_{2m}(Y_2)_y \\ \vdots \\ \rho D_{NS,m}(Y_{NS})_y \end{pmatrix} \tag{6}$$

and

$$\vec{S} = \begin{pmatrix} 0 \\ \dot{\omega}_1 \\ \dot{\omega}_2 \\ \vdots \\ \dot{\omega}_{NS} \end{pmatrix} \quad \vec{C} = \begin{pmatrix} -\epsilon(e+p) \\ -\epsilon\rho Y_1 \\ -\epsilon\rho Y_2 \\ \vdots \\ -\epsilon\rho Y_{NS} \end{pmatrix} \tag{7}$$

where the heat flux component, neglecting radiative heat transfer, is given by:

$$Q_y = \lambda T_y + \rho \sum_{k=1}^{NS} h_k D_{km}(Y_k)_y \tag{8}$$

In these computations all physical properties of the various species are assumed to be functions of temperature and are obtained using a transport package within CHEMKIN II[28].

The above equations, either (1) for the viscous case or (5) for the inviscid case, may be solved numerically. The energy conservation equation is solved in terms of the energy per unit volume e (or actually, the enthalpy per unit mass, h). This is in *contrast* to the common assumption of a "locally" calorically perfect gas where $h = \bar{c}_p T$ is assumed in the governing equations, employing table look-ups to obtain the dependence of $c_{p,i}$ for each species on temperature in the governing equation and averaging to obtain $\bar{c}_p$. While for many combustion problems the usual approach yields accurate results, it has been recently shown[29] that such assumptions in the vicinity of sharp gradients such as flames can yield errors in wave speeds and hence in the solution of the problem. The present approach avoids this difficulty.

Formulation of the ratio of specific heats for the mixture of gases present in a given computational cell is done so as to avoid thermodynamic inconsistencies in the presence of contact discontinuities. These inconsistencies are known to generate temperature spikes and numerical oscillations[30–32]. In the present procedure we use the relation

$$\gamma = 1 + \frac{\sum\limits_{k=1}^{NS} \frac{Y_k}{W_k}}{\sum\limits_{k=1}^{NS} \frac{Y_k}{W_k(\gamma_k - 1)}} \tag{9}$$

for the ratio of specific heats of the gas mixture in a given cell; this assumes that all species Y_k with molecular weights W_k are at the same temperature within the cell. Although this assumption is not as accurate as evolving γ from partial pressures of the species, as done by Ton[32], experience has shown that if a sharp contact surface rapidly fades away due to the

presence of highly diffusive species, then using equation (9) will result in confined spikes in temperature for only very short periods of computational time.

The method of operator splitting via fractional steps, after Yamenko[33], is employed to solve the system of equations (1) or (5). This procedure enables the system to be split into two separate equations, one which only includes the advection-diffusion terms and one which only includes the reaction rate source terms, respectively:

$$\vec{U}_t + \left[\vec{F}(\vec{U})\right]_x + \left[\vec{G}(\vec{U})\right]_y = \left[\vec{F}_v(\vec{U})\right]_x + \left[\vec{G}_v(\vec{U})\right]_y \tag{10}$$

$$\vec{U}_t = \vec{S} \tag{11}$$

An equivalent form of equations (10) and (11) may be written for the inviscid formuation of the problem, equation (5). Each relation above represents a set of equations that has been studied extensively. The present method uses a first-order upwind scheme[34] to solve the inviscid form of the advection-diffusion equation (10) and the second-order McCormack predictor-corrector scheme[35] to solve (10) in the full viscous form. It employs a stiff ODE solver (VODE[36], an improved version of LSODE[37]) accompanied by the CHEMKIN-II package[28] to solve equation (11).

The above formulation has been demonstrated to be relatively efficient as well as accurate in its prediction of the structure of strained diffusion flames and fuel strips. Grid resolution studies in time and space have been conducted[24]. The general numerical methodology was validated by computing the steady state behavior of the strained, single hydrogen-air interface, with effectively "infinite" supplies of fuel and air in a counterflow configuration, and comparing results with the experimental results via UV Raman scattering by Trees, *et. al*[38]. The full H_2-air mechanism of Maas and Warnatz[39] was employed in this validation, which is slightly different from the mechanism used in the computations in [38]. Results of the predictions for the steady state temperature profile and species distributions are shown in Figures 3 and 4, the latter case representing a strain rate field near extinction. For both cases the species distributions are predicted extremely well and the temperature predictions in the flame zone are within 12%. This reasonable correspondence between the present predictions and experiments lends credence to the validity of the present computational procedure; to our knowledge, there are no comparable experimental results available for validation of propane-air flames.

The focus of the present computational study is for the full propane-air chemical mechanism of [40], with the additional thermal NO_x formation mechanism of [41], to study ignition, burning, and extinction of a strained propane fuel strip.

5 Results

Results for the transient ignition, burning, and extinction processes associated with a propane strip burning in air are shown in Figures 5 through 8 for the inviscid case. Figure 5 shows plots of temperature, OH and H concentrations, and fuel consumption rate as a

function of distance across the fuel strip and as a function of time, for a fuel strip of initial thickness 1 mm in heated air at a constant strain rate of 300 sec^{-1}. In all cases shown here, the initial temperature of the air was taken to be 1300° K and the initial temperature of propane was 400° K; these conditions very roughly corresponded to experimental conditions for the lobed fuel injector study[23], in that unheated fuel is injected into air which is preheated by downstream flame structures. For the relatively thick fuel strip in Figure 5, two independent ignitions are visible via thermal runaway at two distinct locations. Burning proceeds at each flame in an independent manner as well, evidenced by movement of each flame away from the strip, toward the adjacent oxidizer, in accordance with the stoichiometric requirements of the reaction. At later times the flames begin to move toward each other, burning out the intervening fuel. This ignition mode is consistent with the asymptotic analysis of ignition in [20], whereby relatively thick fuel strips at zero or relatively low rates of strain ignite independently. Figure 5 demonstrates that the interfaces can initially burn in an independent fashion as well prior to the beginning of fuel burnout.

Figure 6 shows the evolution of temperature, species concentrations, and fuel consumption associated with a fuel strip of the same initial thickness as in Figure 5 but exposed to a constant strain rate of 500 sec^{-1}. While only a slight delay in ignition is observed in comparison to that in Figure 5, there is more of an interdependence of the flames that do ignite in that the temperature and radical concentrations between the interfaces have increased above their initial values at ignition. The flames then proceed to move toward each other much sooner, rapidly depleting the intervening fuel and extinguishing at a short time later. This behavior is a quantitative confirmation of the enhancement of thermal feedback suggested by the single step asymptotic solution of this ignition problem[20] and the corresponding "dependent" ignition mode for the two fuel-air interfaces.

Figures 7 and 8 show temporal and spatial evolution of flame structure for the propane fuel strip of the same initial thickness as above but with successively higher constant rates of strain. In Figure 7 there is a greater ignition delay than in Figure 5, but with ignition at a single location, indicating that ignition and sustained burning occur in the premixed or partially premixed mode. Here the rate of strain is so high that the fuel-air interfaces are brought together very rapidly, and substantial interchange of mass occurs before the ignition process. This mode of ignition again is a quantitative confirmation of the single ignition mode observed in the single-step asymptotic solution of this problem[20]. As is expected, this flame consumes the existing fuel-air mixture and burns out very rapidly. Figure 8, at a constant strain rate of 1500 sec^{-1}, demonstrates that at extremely high rates of strain, ignition can be prevented in the strained fuel strip; no significant formation of radicals, rise in temperature, or fuel consumption occurs. This "non-ignition" mode occurs due to the ultra rapid mixing of fuel and air, so high that fuel is diluted beyond a level necessary for ignition of the mixture. This observation is also seen in the asymptotic solution of the problem[20], and differs from modes of ignition prevention seen for single fuel-air interfaces in which heat loss due to high strain prevents thermal runaway.

In several of the cases shown in Figures 5 through 7 radical runaway can precede the runaway in temperature during ignition of the fuel-air interfaces, similar to the observations

of Kreutz, *et al.*[8] for single strained fuel-air interfaces. This phenomenon is resolved in more detail in Figure 9, where the start of runaway in H and OH radicals occurs at a time prior to the initiation of a runaway in temperature.

As indicated in Figures 5 - 9, there is a strong dependence of the nature of the ignition process on the specific flow variable (ϵ) and geometric variable (initial strip thickness). A plot of the time to ignition as a function of the initial strip thickness for different constant rates of strain is shown in Figure 10. A similar type of plot, nondimensionalized in terms of a chemical time, is generated by the single step, asymptotic solution of fuel strip ignition in [20]. As seen in the asymptotic result, as initial strip thickness is reduced for a fixed strain rate, a reduction in the time to ignition is seen due to the thermal/radical feedback between the fuel-air interfaces. For very thin fuel strips, ignition delay time then increases with a reduction in initial strip thickness due to a more rapid mixing process than that of heat or radical production. While all strain rate contours exhibit this trend in Figure 10, there does appear to be a crossover in curves, demonstrating (as in [20]) the possibility that a fuel strip exposed to a higher strain rate can ignite sooner than an equivalent strip exposed to a lower strain rate, again due to the feedback mechanism.

The benefit of increased strain rate for NO_x reduction in complex flows in which strained interfaces are brought together (as in Figure 1) is also examined here. Figures 11 and 12 show concentrations of NO and NO_2 (in addition to temperature and OH distributions) produced by fuel strips exposed to constant strain rates of 100 sec^{-1} and 1000 sec^{-1}, respectively. At the lower strain rate, ignition of the fuel occurs in an independent fashion before the diffusion flames sense each others' presence and burn out the intervening fuel; for the higher strain rate, premixed ignition and relatively rapid burnout occur. The differences in NO and NO_2 production are quite significant here. At the lower strain rate (Figure 11) the initial NO concentrations can be over an order of magnitude greater than for the higher strain rate problem (Figure 12), while NO_2 concentrations can be nearly an order of magnitude higher at the low strain case. The small amount of NO_2 forming at ignition in Figure 11 appears to be associated with the rapid formation and depletion of a small amount of NO, smaller than would register on the NO plot in Figure 11. While the simple configuration of the planar fuel strip does not represent many of the complexities of turbulent reacting flows (Figure 1) the benefits of locally large strain rates for the ignition of adjacent reactant interfaces (as compared with a single interface) are quite profound precisely because ignition and burning can take place in a locally premixed mode rather than in a diffusion flame mode.

A sample result for solution of the viscous flow problem, represented by equation (1), is shown in Figure 13; comparison may be made to the equivalent inviscid problem, formulated in equation (5), with results shown in Figure 5. While the actual process of ignition and ignition times are the same for the two computations, the process of sustained burning of the fuel strip and eventual burnout is substantially longer for the viscous simulation than for the inviscid simulation. Clearly, the effect of viscosity is to reduce the effective velocity and strain field experienced by the species interfaces, transporting them more slowly toward each other and allowing for a reduced rate of consumption of intervening fuel.

The response of the fuel strip to a temporally oscillating strain rate in the absence of

viscous effects is also considered in this study. The temporal rate of strain experienced by the strip in the present formulation takes the form

$$\epsilon(t) = \epsilon_o + \epsilon_1 sin \left(2\pi\omega t\right) \tag{12}$$

Results for temperature contours for the case where $\epsilon_o = 300$ sec^{-1} are shown in Figures 5 ($\epsilon_1 = 0$), 14abc ($\epsilon_1 = 100$ sec^{-1}, $\omega = 25$, 250, and 1000 hz, respectively), and 15abc ($\epsilon_1 = 250$ sec^{-1}, $\omega = 25$, 250, and 1000 hz). For all cases of oscillatory strain the initial temperature contours (and species concentration contours, not shown) during ignition appear nearly identical, with nearly identical ignition times despite the fact that at the higher frequencies the fuel strip has been exposed to several oscillatory cycles in strain rate prior to ignition. In both Figures 14 and 15 there is an oscillatory response of the flame structure to the oscillations in strain rate. This response is somewhat out of phase with the local application of the strain rate, however, in that local increases in temperature seem to respond to a prior local increase in strain rate. In Figure 15, the low frequency oscillations at 25 hz are slow enough, and with a large enough amplitude of oscillation, that the flame experiences a sustained exposure to high strain rates according to equation (12) and thus burns out more quickly than for the higher frequency cases. In all cases at higher frequencies, the temperature (and species) distributions appear to oscillate about the "mean" profile exhibited in the non-oscillatory case (Figure 5). For this relatively thick fuel strip, the flames appear able to keep up with oscillations in strain even at high frequencies, in contrast to a lack of response in strained premixed flames at high frequencies of oscillation[42].

6   Summary and Conclusions

The present study demonstrates that a full numerical simulation of ignition of a strained fuel strip with complete combustion chemistry exhibits the same phenomenological modes of thermal/radical runaway that are seen in a single-step asymptotic simulation of the problem. Further, burning and extinction processes may be explored via numerical simulation; these calculations suggest the sensitivity of the combustion characteristics to the degree of straining, to the presence of viscosity in the flowfield, and to temporal oscillations in the rate of strain. The benefits of large strain rates in terms of NO and NO$_2$ reduction are demonstrated to occur in the present context as a result of enhanced fuel-air mixing during high strain which leads to premixed flame ignition and burning.

7   Acknowledgements

8 References

References

[1] Fendell, F. E. (1965). Ignition and extinction in combustion of initially unmixed reactants. *J. Fluid Mech.* 21 (Pt. 2), pp. 281-303.

[2] Liñan, A. (1974). The asymptotic structure of counterflow diffusion flames for large activation energies. *Acta Astronautica* 1, pp. 1007-1039.

[3] Liñan, A. and Crespo, A. (1976). An asymptotic analysis of unsteady diffusion flames for large activation energies. *Combust. Sci. Tech.* 14, pp. 95-117.

[4] Peters, N. (1983). Local quenching due to flame stretch and non-premixed turbulent combustion. *Combust. Sci. Tech.* 30, pp. 1-17.

[5] Dold, J. W. (1989). Flame propagation in a nonuniform mixture: analysis of a slowly varying triple flame. *Combust. Flame* 76, pp. 71-88.

[6] Thévenin, D. and Candel, S. (1993). Effect of variable strain on the dynamics of diffusion flame ignition. *Combust. Sci. Tech.* 91, pp. 73-94.

[7] Darabiha, N. and Candel, S. (1992). The influence of temperature on extinction and ignition limits of strained hydrogen-air diffusion flames. *Combust. Sci. Tech.* 86, pp. 67-85.

[8] Kreutz, T. G., Nishioka, M., and Law, C. K. (1994). The role of kinetics versus thermal feedback in nonpremixed ignition of hydrogen versus heated air. *Combust. Flame* 99, pp. 758-766.

[9] Law, C. K. (1988). Dynamics of stretched flames. *Twenty-second Symposium (International) on Combustion*, The Combustion Institute, Pittsburgh, PA, pp. 1381-1402.

[10] Peters, N. (1986). The laminar flamelet concept in turbulent combustion. *Twenty-first Symposium (International) on Combustion*, The Combustion Institute, Pittsburgh, PA, pp. 1231-1250.

[11] Grosch, C. E. and Jackson, T. L. (1991). Ignition and structure of a laminar diffusion flame in a compressible mixing layer with finite rate chemistry. *Phys. Fluids A* 3, pp. 3087-3097.

[12] Macaraeg, M. G., Jackson, T. L., and Hussaini, M. Y. (1992). Ignition and structure of a laminar diffusion flame in the field of a vortex. *Combust. Sci. Tech.* 87, pp. 363-387.

[13] Thévenin, D. and Candel, S. (1995). Ignition dynamics of a diffusion flame rolled up in a vortex. *Phys. Fluids* 7, pp. 434-445.

[14] Carrier, G. F., Fendell, F. E., and Marble, F. E. (1975). The effect of strain rate on diffusion flames. *SIAM J. Appl. Math.* 28, pp. 463-500.

[15] Peters, N. (1984). Local quenching fue to flame stretch and non-premixed turbulent combustion. *Prog. Energy Combust. Sci.* 10, pp. 319-339.

[16] Bish, E. S. and Dahm, W. J. A. (1994). Strained dissipation and reaction layer analysis of nonequilibrium chemistry in turbulent reacting flows. *Combust. Flame* 100, pp. 457-466.

[17] Marble, F. E. (1985). Growth of a diffusion flame in the field of a vortex. *Recent Adv. in Aero. Sci.*, C. Casci, Ed., pp. 395-413.

[18] Buckmaster, J. D. and Ludford, G. S. S. (1982). *Theory of Laminar Flames*, Cambridge University Press, pp. 179-181.

[19] Cetegen, B. M. and Bogue, D. R. (1991). Combustion in a stretched fuel strip with finite rate chemistry. *Combust. Flame* 86, pp. 359-370.

[20] Gerk, T. J. and Karagozian, A. R. (1996). Ignition delay associated with a strained fuel strip. *Twenty-Sixth Symposium (International) on Combustion*, The Combustion Institute, Pittsburgh, PA, pp. 1095-1102.

[21] Bowman, C. T. (1992). Control of combustion-generated nitrogen oxide emissions: technology driven by regulation. *Twenty-fourth Symposium (International) on Combustion*, The Combustion Institute, Pittsburgh, PA, pp. 859-878.

[22] Smith, L. L., Majamaki, A. J., Lam, I. T., Delabroy, O., Karagozian, A. R., Marble, F. E., and Smith, O. I., Mixing enhancement in a lobed injector. *Phys. Fluids* 9, pp. 667-678.

[23] Mitchell, M. G., Smith, L. L., Karagozian, A. R., and Smith, O. I. (1996). NO_x emissions from a lobed fuel injector/burner. Paper 96F-075, Western States Section/The Combustion Institute Fall Meeting, October, 1996.

[24] Selerland, T. (1996). Numerical simulation of ignition, burning, and extinction processes for strained flames. Ph.D. prospectus, University of California, Los Angeles.

[25] Majda A. and Sethian, J. (1985). The derivation and numerical solution of the equations for zero Mach number combustion. *Combust. Sci. Tech.* 42, p. 185.

[26] Majda A. and Lamb K. G. (1991). Simplified equations for low Mach number combustion with strong heat release. *Dynamical Issues in Combustion Theory*, Springer-Verlag.

[27] Darabiha, N. (1992). Transient behaviour of laminar counterflow hydrogen-air diffusion flames with complex chemistry. *Combust. Sci. Tech.* 86, pp. 163-181.

[28] Kee, R. J., Miller, J. A., and Jefferson, T. H. (1980). CHEMKIN: A general purpose, problem independent, transportable, Fortran chemical kinetics code package. Sandia National Laboratories Report SAND80-8003.

[29] Fedkiw, R. P., Merriman, B., and Osher, S. (1997). High accuracy numerical methods for thermally perfect gas flows with chemistry. *J. Computational Physics*, 132 (2), pp. 175-190.

[30] Abgrall, R. (1988). Generalization of the Roe scheme for computing flows of mixed gases with variable concentrations. *La Recherche Aerospatiale* 6, pp. 31-43.

[31] Larrouturou, B. (1991). How to preserve the mass fractions positivity when computing compressible multi-component flows. *J. Computational Physics* 95, pp. 59-84.

[32] Ton, V. T. (1996). Improved shock-capturing methods for multicomponent and reacting flows. *J. Computational Physics* 128 (1), pp. 237-253.

[33] Strikwerda, J. C. (1989). *Finite Difference Schemes and Partial Differential Equations*, Wadsworth and Brooks.

[34] LeVeque, R. J. (1992). *Numerical Methods for Conservation Laws*, Birkhauser, Basel, Switzerland.

[35] MacCormack, R. W. (1969). The effect of viscosity in hypervelocity impact cratering. AIAA Paper 69-354.

[36] Brown, P. N., Byrne, G. D., and Hindmarsh, A. C. VODE: A variable coefficient ODE solver. *SIAM J. Scientific Statistical Computing* 10, pp. 1038-1051.

[37] Hindmarsh, A. C. (1983). ODEPACK, a systematized collection of ODE solvers. In *Scientific Computing*, R. S. Stepleman, *et al.*, eds., North-Holland, Amsterdam, pp. 55-64.

[38] Trees, D., Brown, T. M., Seshadri, K., Smooke, M. D., Balakrishnan, G., Pitz, R. W., Giovangigli, V., and Nandula, S. P. (1995). The structure of nonpremixed hydrogen-air flames. *Combust. Sci. Tech.* 104, pp. 427-439.

[39] Maas U., and Warnatz J. (1991). Detailed numerical modeling of H2-O2 ignition by hot spots. In *Dynamics of deflagration and reactive systems: Flames*, Prog. Astro. Aero. 131: pp. 3-18.

[40] Warnatz, J. (1983). The mechanism of high temperature combustion of propane and butane. *Comb. Sci. and Tech.* 34, pp. 177 (1983).

[41] Chung, S. H., Lee, S. R., Mauss, F., and Peters, N. (1993). Reduced kinetic mechanisms and NOx formation in diffusion flames of CH4/C2H6 mixtures. *Reduced Kinetic Mechanisms for Applications in Combustion Systems*, Norbert Peters and Bernd Rogg, Eds., Lecture Notes in Physics V15, Springer-Verlag, pp. 308-328.

[42] Egolfopoulos, F. N. (1994). Dynamics and structure of unsteady, strained, laminar premixed flames. *Twenty-fifth Symposium (International) on Combustion*, The Combustion Institute, Pittsburgh, PA, pp. 1365-1373.
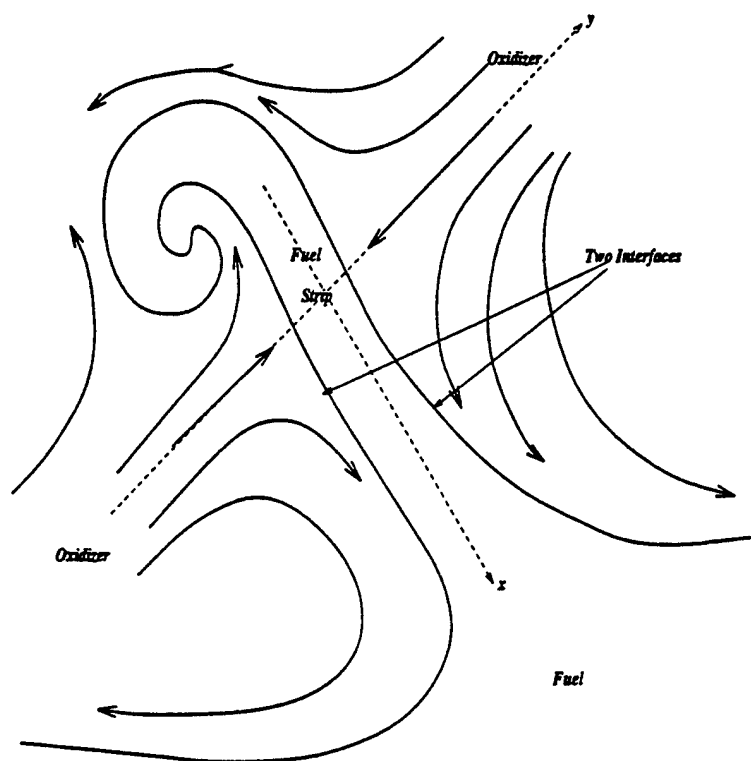
Figure 1: Local deformation and stretching of a strip of fuel in a complex flowfield
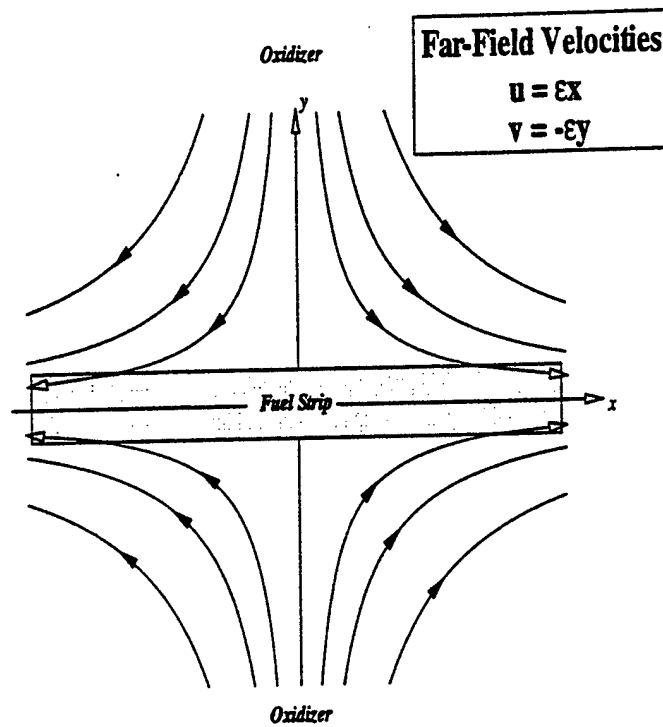
Figure 2: Geometry of strained fuel strip problem, where y_o is the initial strip thickness. The strip is exposed to the temporally evolving strain rate $\epsilon(t)$ in general.
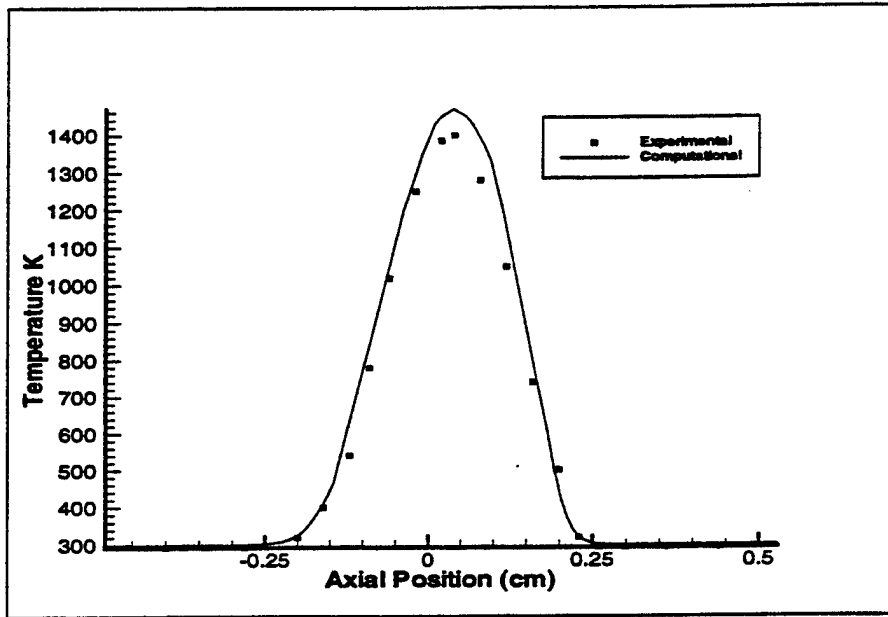
(a) Temperature distribution
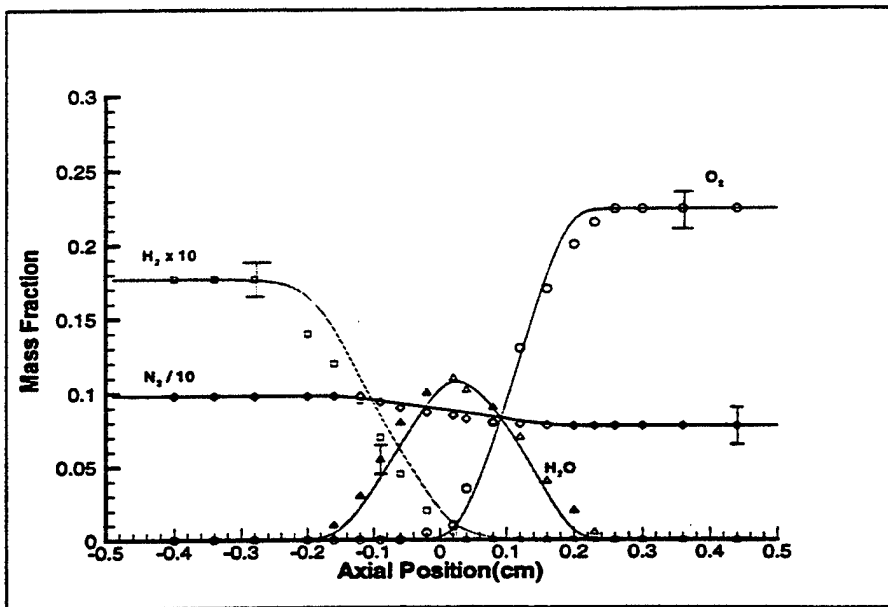
(b) Species concentrations

Figure 3: Results from the present computational method for the steady state structure of the single strained hydrogen-air diffusion flame. Comparisons are made with the experiments of Trees, *et. al*[38] for the effective strain rate $\epsilon = 134$ sec^{-1}. Error bars shown are for the experimental data.

17
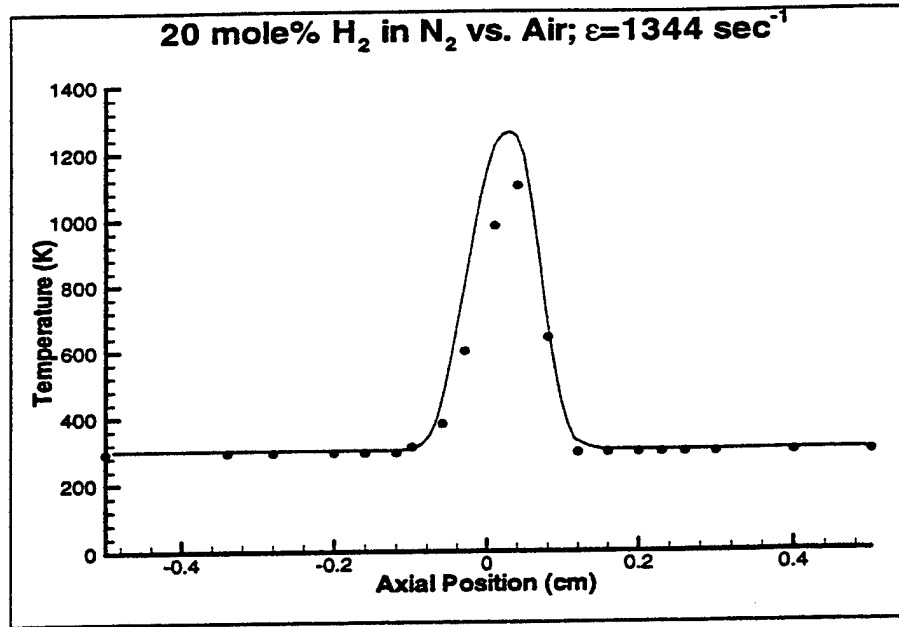
(a) Temperature distribution
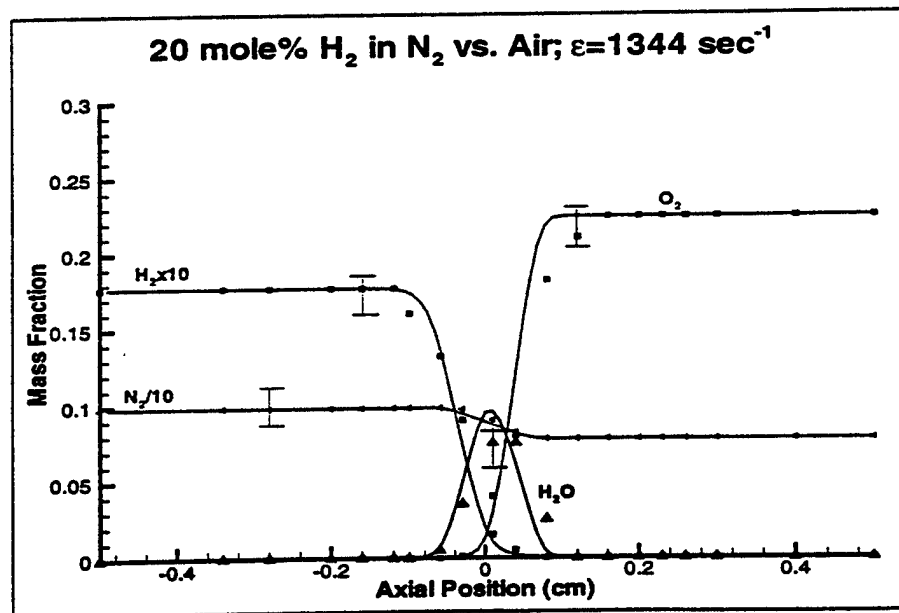
(b) Species concentrations

Figure 4: Results from the present computational method for the steady state structure of the single strained hydrogen-air diffusion flame. Comparisons are made with the experiments of Trees, *et. al*[38] for the effective strain rate $\epsilon = 1344$ sec^{-1} (near extinction). Error bars shown are for the experimental data.
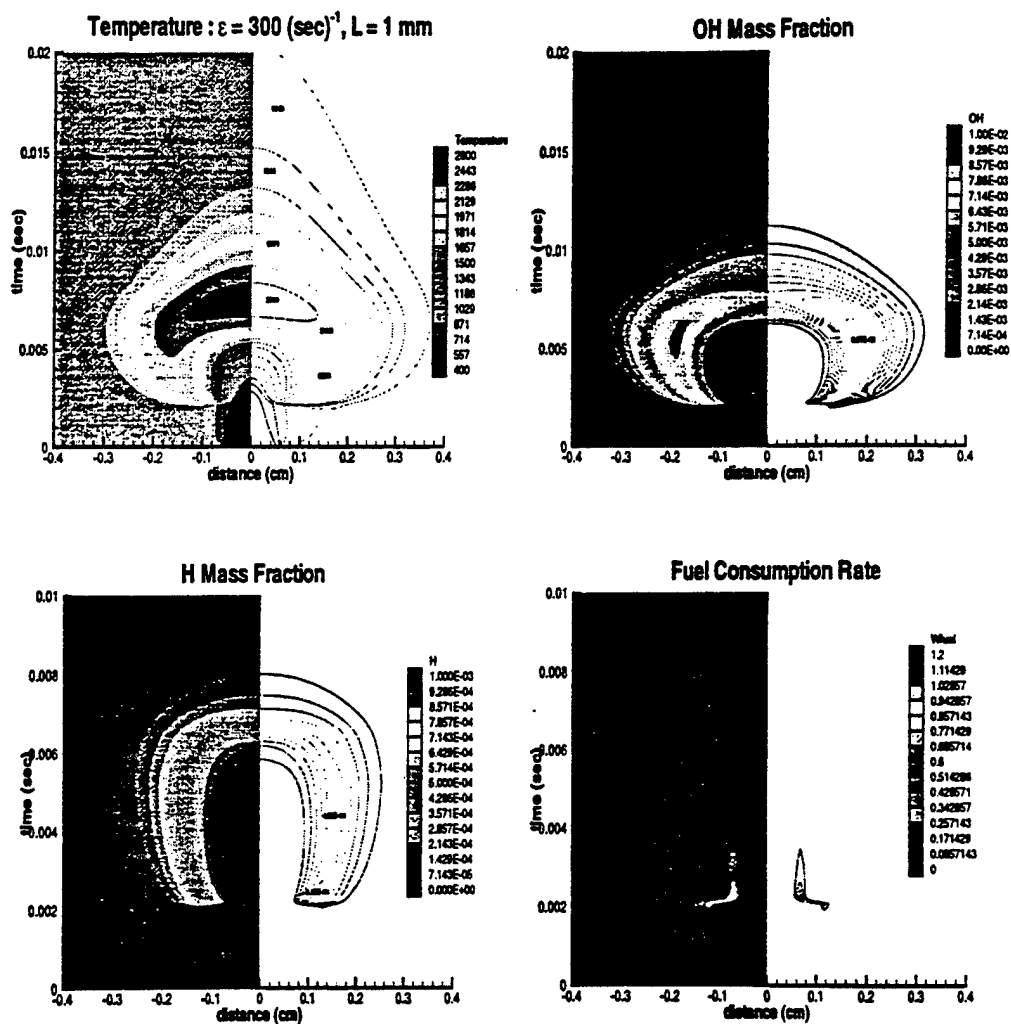
Figure 5: Temporal and spatial evolution of temperature, fuel consumption rate, and OH and H mass fractions for the strained fuel strip with initial thickness 1.0 mm and constant rate of strain 300 sec^{-1}.
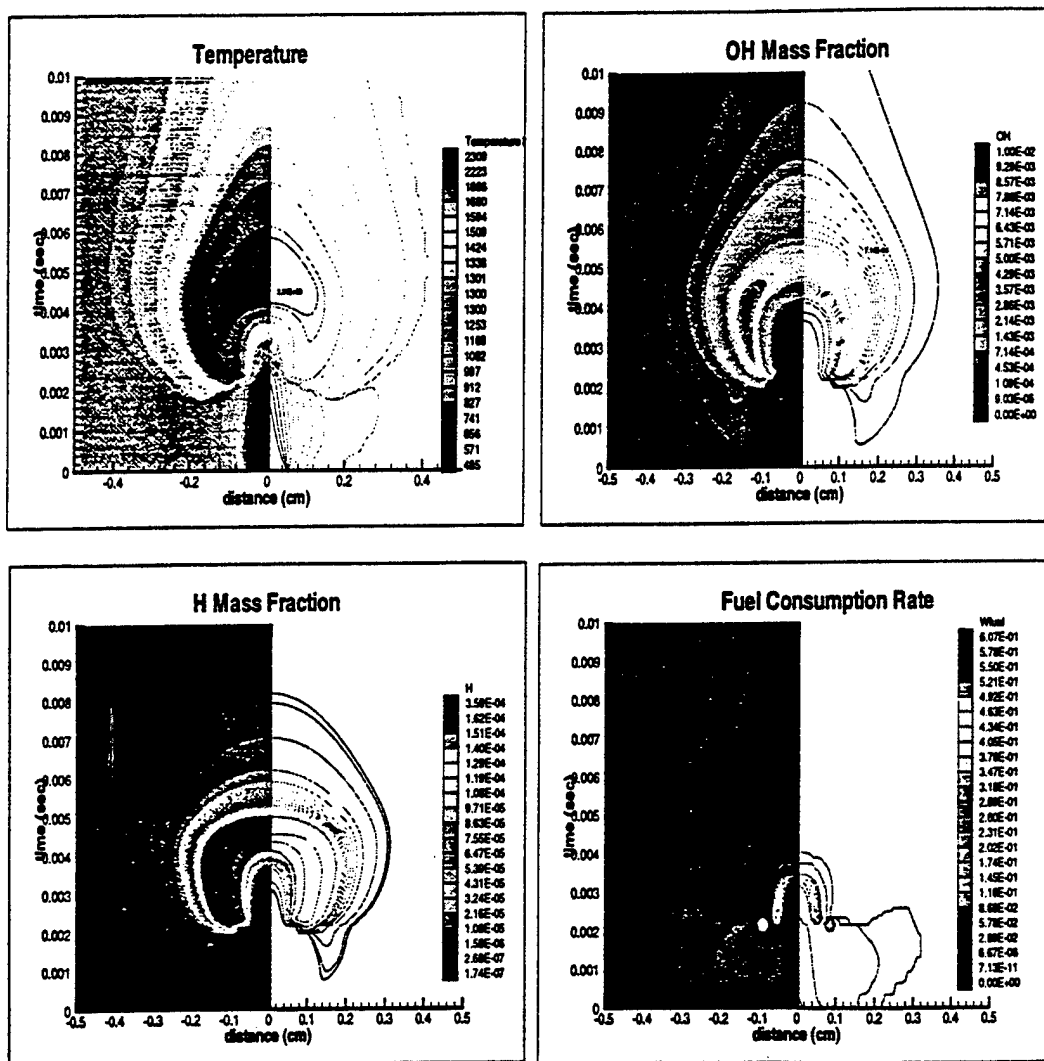
Figure 6: Temporal and spatial evolution of temperature, fuel consumption rate, and OH and H mass fractions for the strained fuel strip with initial thickness 1.0 mm and constant rate of strain 500 sec^{-1}.
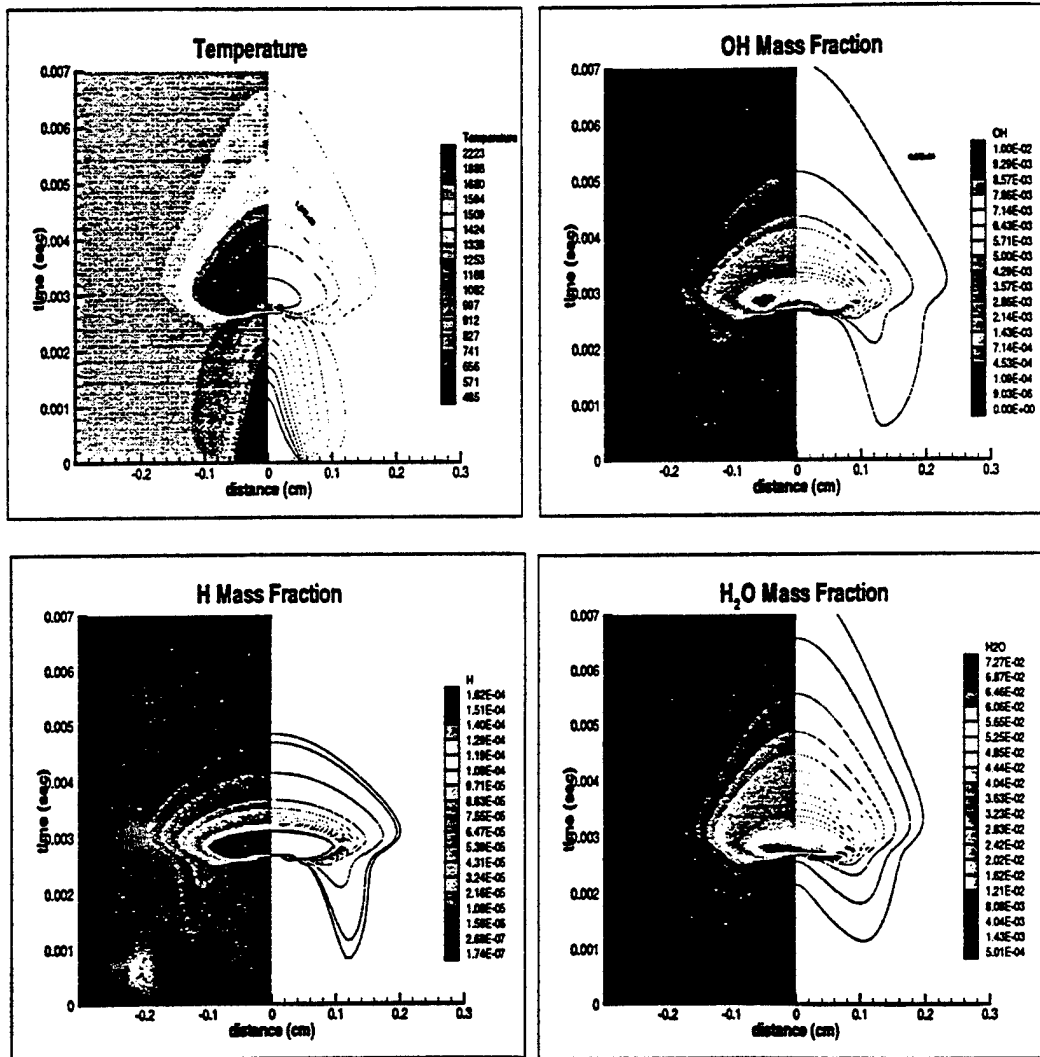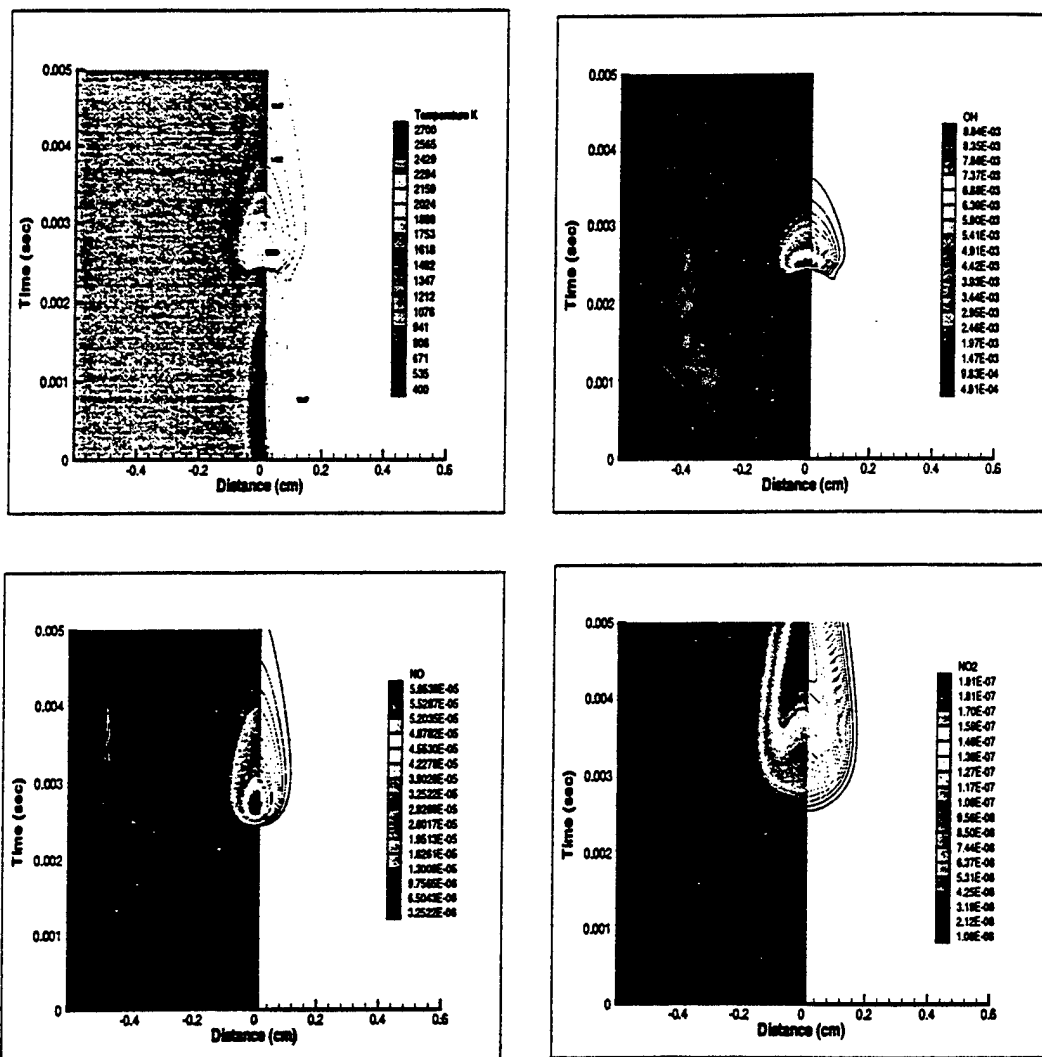
Figure 7: Temporal and spatial evolution of temperature, fuel consumption rate, and OH and H mass fractions for the strained fuel strip with initial thickness 1.0 mm and constant rate of strain 1000 sec^{-1}.
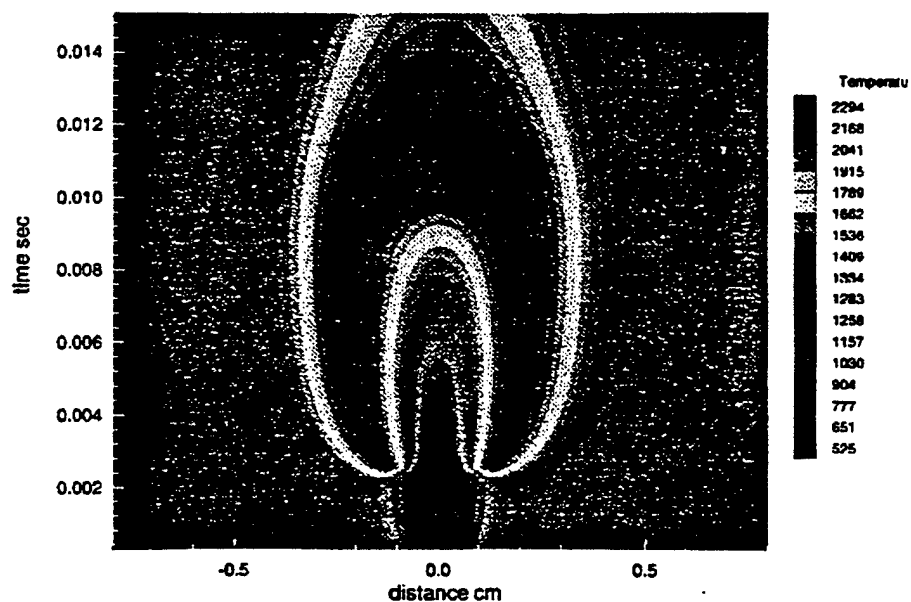
21
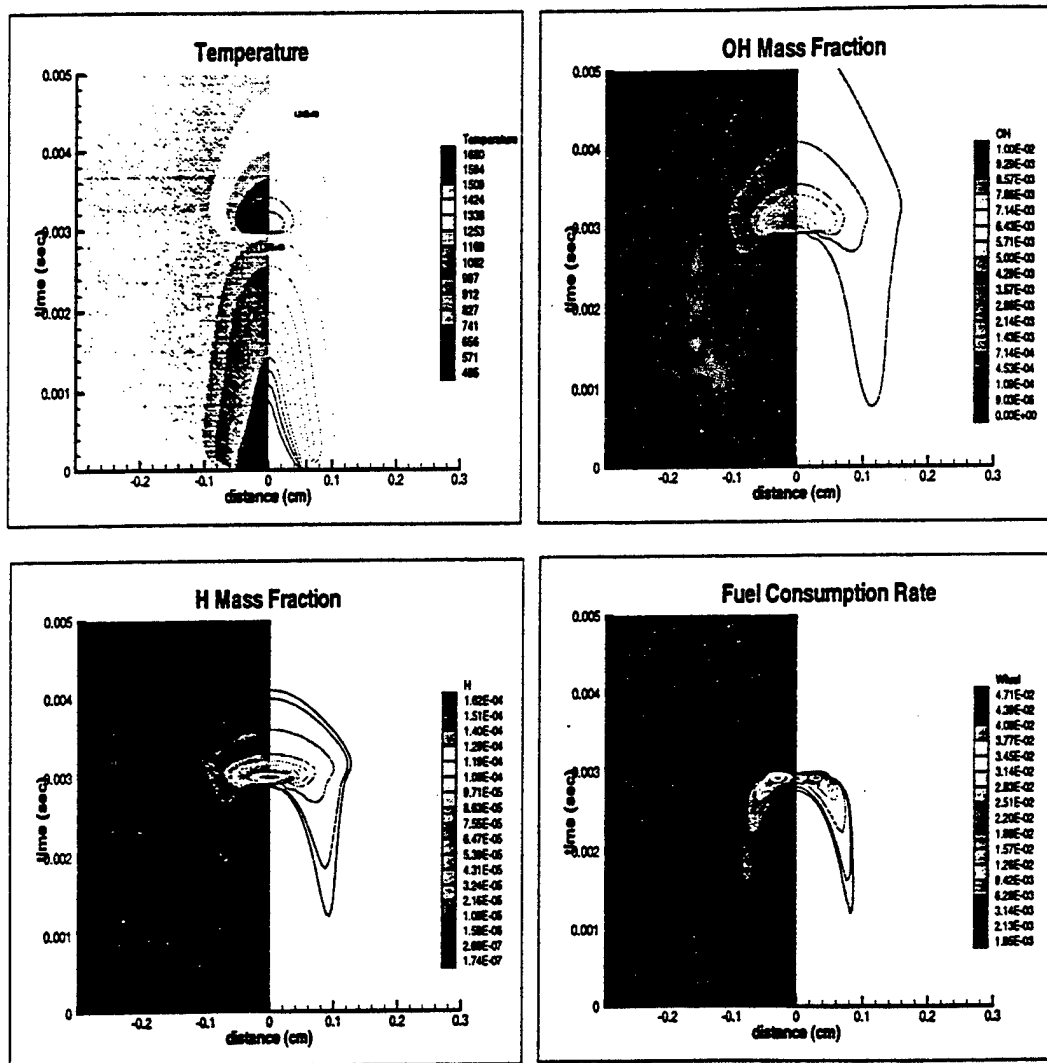
Figure 8: Temporal and spatial evolution of temperature, fuel consumption rate, and OH and H mass fractions for the strained fuel strip with initial thickness 1.0 mm and constant rate of strain 1500 sec^{-1}.
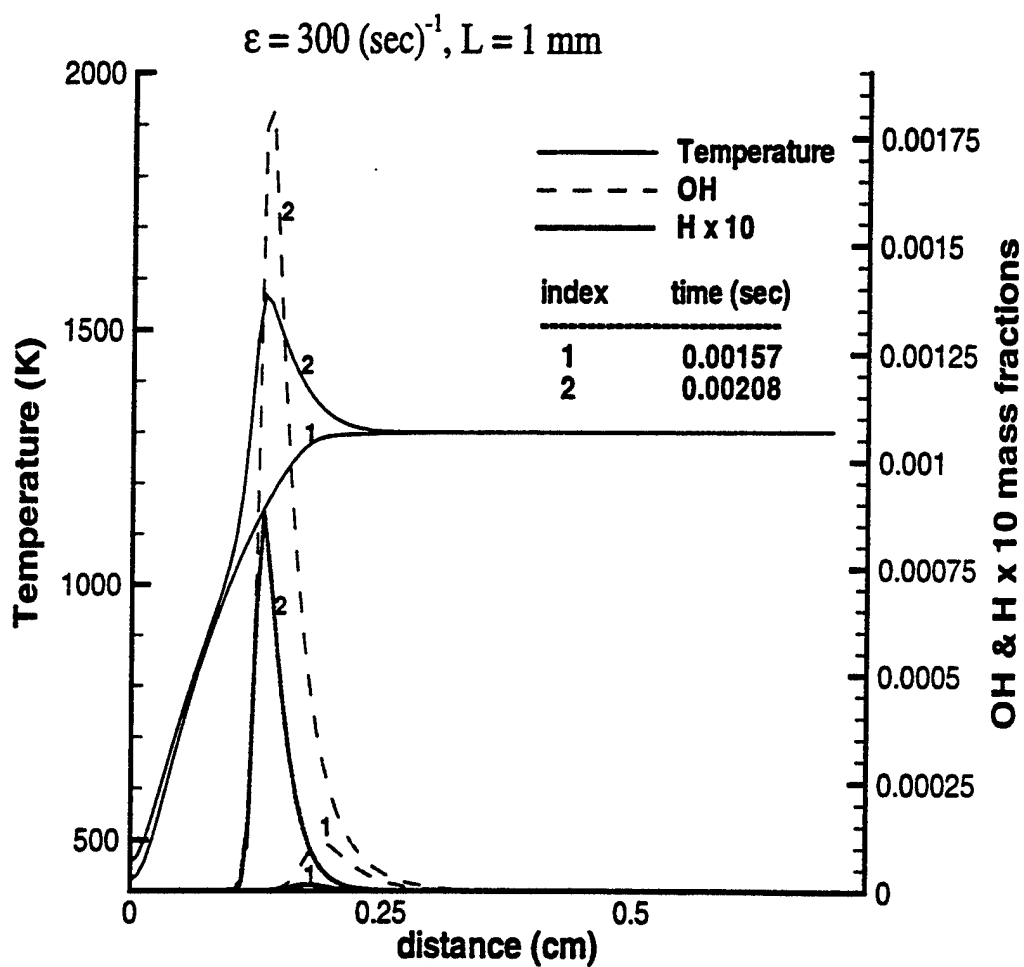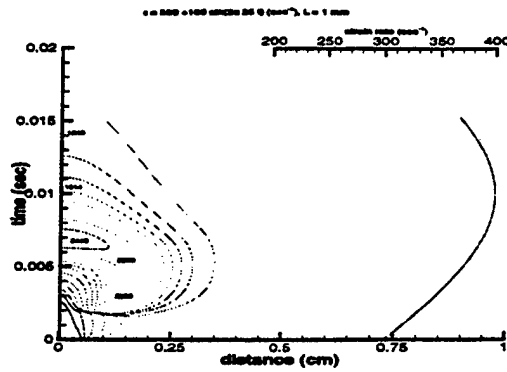
Figure 9: Spatial distribution of temperature, OH, and H mass fractions at two different times for the strained fuel strip with initial thickness 1.0 mm and constant rate of strain 300 sec^{-1}. Radical runaway is apparent prior to thermal runaway here.
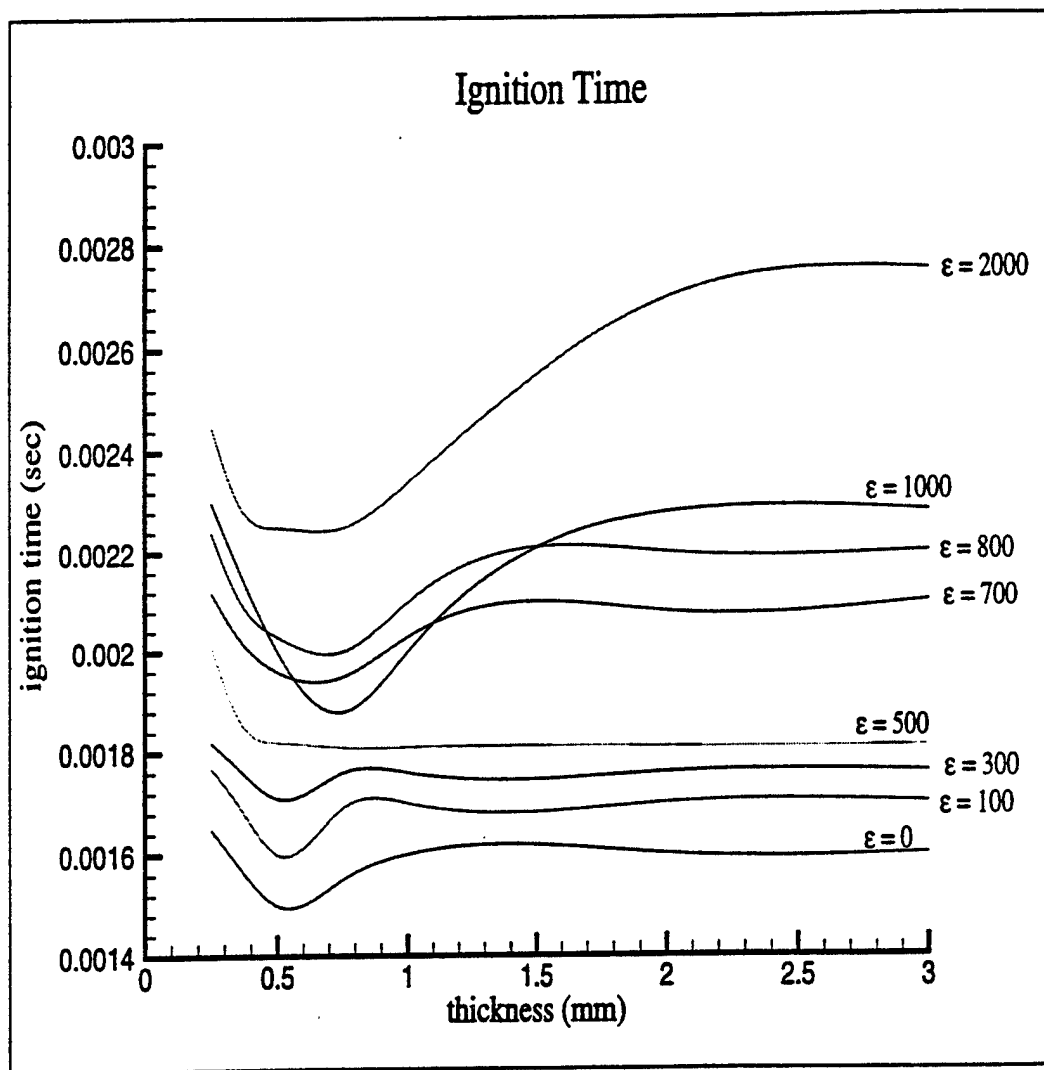
Figure 10: Time to ignition (determined via thermal runaway detection) as a function of initial fuel strip thickness for different constant rates of strain.
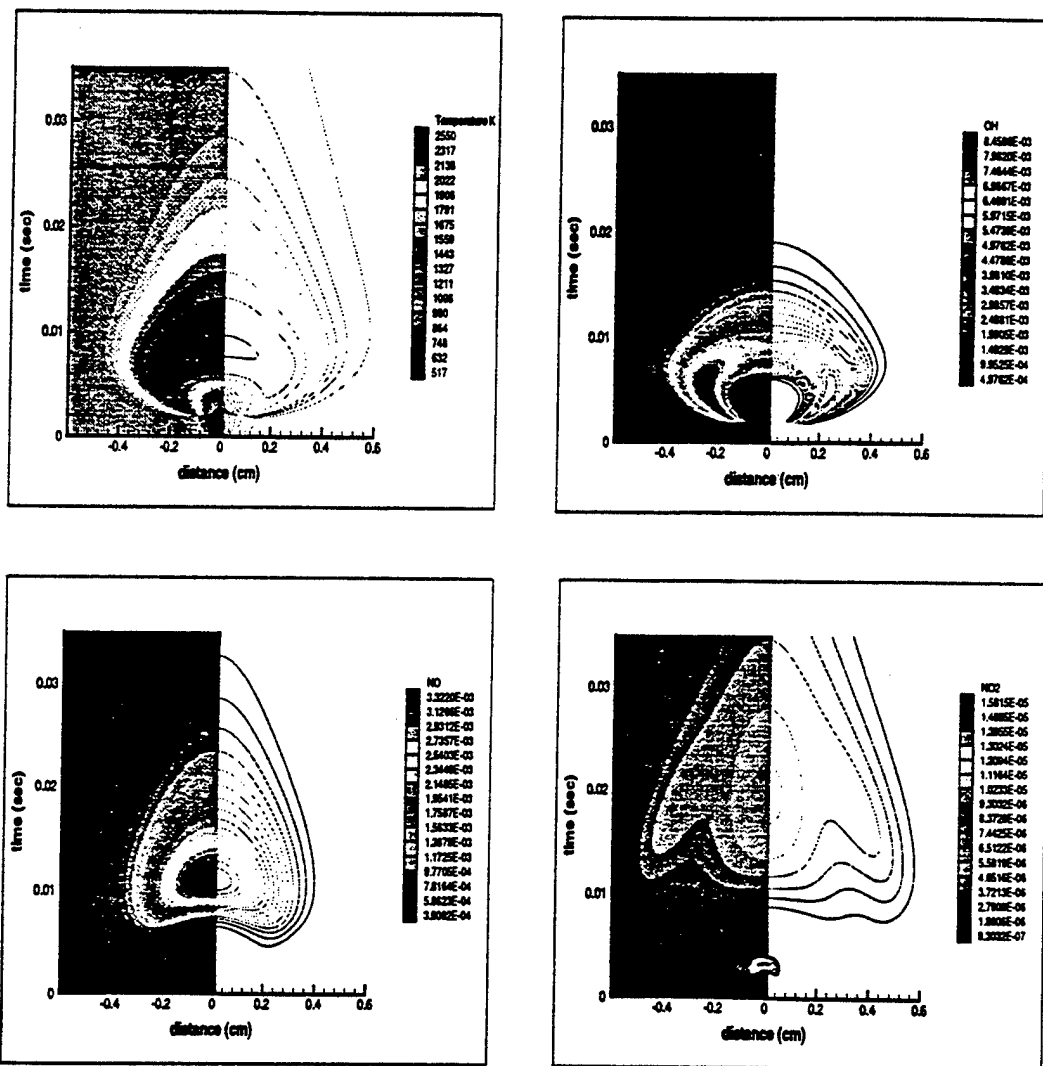
Figure 11: Temporal and spatial evolution of temperature, OH, NO, and NO_2 mass fractions for the strained fuel strip with initial thickness 0.35 mm and constant rate of strain 100 sec^{-1}.
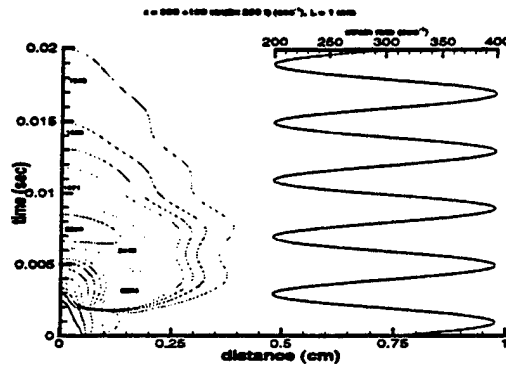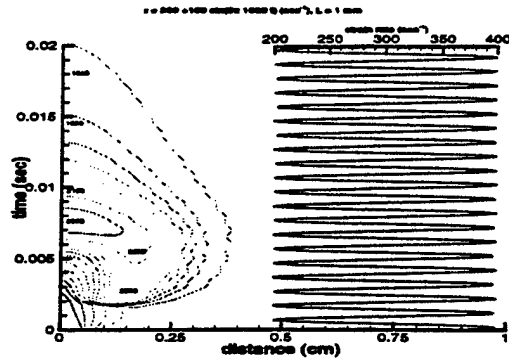
Figure 12: Temporal and spatial evolution of temperature, OH, NO, and NO_2 mass fractions for the strained fuel strip with initial thickness 0.35 mm and constant rate of strain 1000 sec^{-1}.

Figure 13: Temporal and spatial evolution of temperature for the strained fuel strip with initial thickness 1.0 mm and constant rate of strain 300 sec^{-1}. Result from the viscous computation is shown.
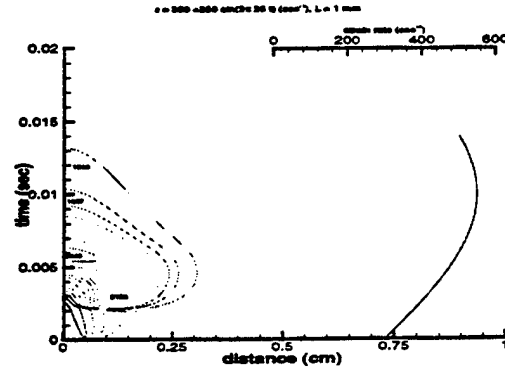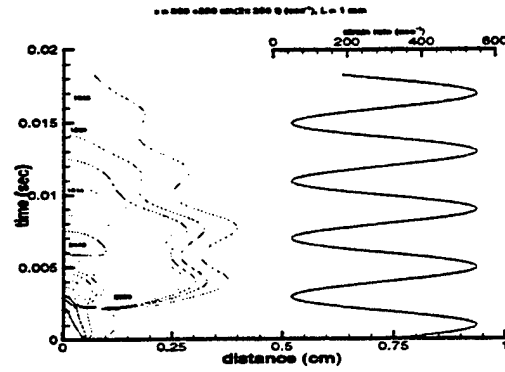
27

(a) $\omega = 25$ Hz
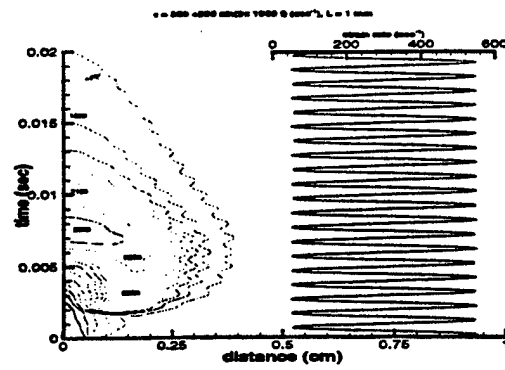

(b) $\omega = 250$ Hz

(c) $\omega = 1000$ Hz

Figure 14: Temporal and spatial evolution of temperature for the strained fuel strip with initial thickness 1.0 mm, mean rate of strain $\epsilon_o = 300$ sec^{-1}, and amplitude of oscillation $\epsilon_1 = 100$ sec^{-1}.

(a) $\omega = 25$ Hz

(b) $\omega = 250$ Hz

(c) $\omega = 1000$ Hz

Figure 15: Temporal and spatial evolution of temperature for the strained fuel strip with initial thickness 1.0 mm, mean rate of strain $\epsilon_o = 300$ sec^{-1}, and amplitude of oscillation ϵ_1 = 250 sec^{-1}.

29